



HAL
open science

Electrochimiluminescence : de la compréhension mécanistique aux applications bioanalytiques

Milica Sentic

► **To cite this version:**

Milica Sentic. Electrochimiluminescence : de la compréhension mécanistique aux applications bioanalytiques. Chemical Physics [physics.chem-ph]. Université de Bordeaux; Univerzitet u Beogradu, 2015. English. NNT : 2015BORD0307 . tel-01271592

HAL Id: tel-01271592

<https://theses.hal.science/tel-01271592>

Submitted on 9 Feb 2016

HAL is a multi-disciplinary open access archive for the deposit and dissemination of scientific research documents, whether they are published or not. The documents may come from teaching and research institutions in France or abroad, or from public or private research centers.

L'archive ouverte pluridisciplinaire **HAL**, est destinée au dépôt et à la diffusion de documents scientifiques de niveau recherche, publiés ou non, émanant des établissements d'enseignement et de recherche français ou étrangers, des laboratoires publics ou privés.

THÈSE

PRÉSENTÉE A

L'UNIVERSITÉ DE BORDEAUX
ÉCOLE DOCTORALE DES SCIENCES CHIMIQUES

Par Milica SENTIC
POUR OBTENIR LE GRADE DE
DOCTEUR
SPÉCIALITÉ : Chimie-Physique

Electrogenerated chemiluminescence: from mechanistic insights to bioanalytical applications

Sous la direction de Prof. Neso SOJIC et de Prof. Dragan MANOJLOVIC

Devant la commission d'examen formée de :

DE COLA Luisa	Professeur, Université de Strasbourg	Rapporteur
LACROIX Jean-Christophe	Professeur, Université Paris Diderot	Rapporteur
LIVACHE Thierry	Directeur de recherche CEA, Grenoble	Examineur
BASSANI Dario	Directeur de recherche CNRS, Bordeaux	Examineur
MANOJLOVIC Dragan	Professeur, Université de Belgrade	Co-directeur de thèse
SOJIC Neso	Professeur, INP Bordeaux	Co-directeur de thèse

Soutenue le 26.11.2015

Acknowledgement

I would like to thank my supervisors Prof. Dragan Manojlović and Prof. Neso Sojic for knowledge I gained during these four years, in scientific and quotidian life. I profoundly acknowledge Prof. Manojlović for his wisdom and bravery, as an unceasing inspiration to me. I am deeply grateful to Prof. Sojic for his wide scientific interest, curiosity and willpower, who will keep on influencing me. Посебно им се од срца захваљујем на указаном поверењу, подршци, залагању и што су ми отворили врата изазовног света науке.

The work presented in this doctoral dissertation was realized under the joint program between the group Analytical Nanosystems of the Institute of Molecular Sciences, University of Bordeaux in France and the Analytical department of the Faculty of Chemistry, University of Belgrade in Serbia.

A part of this thesis has been the result of different collaborations, within the Paris Diderot University and the University of Ca' Foscari in Venice.

I acknowledge all members of the jury committee of my defense, especially Dr. Jean-Christophe Lacroix, Dr. Luisa de Cola, Dr. Thierry Livache. Special thanks belong to Dr. Dario Bassani for accepting to be the president of the jury committee.

I also acknowledge Prof. Alexander Kuhn for the opportunity to expand my knowledge within exciting bipolar electrochemistry and for his enthusiasm, creativity and innovation in scientific research. Dankeschön.

I acknowledge Prof. Paolo Ugo for sharing his knowledge on electrochemistry at nano-scale and his passion in photography. Grazie mille for the joyful work we have done together.

Je voudrais remercier Dr. Frédéric Kanoufi pour l'important apport que ses simulations théoriques m'ont apporté lors de notre collaboration.

Je voudrais ensuite chaleureusement remercier Stéphane Arbault pour avoir collaboré avec moi. J'ai beaucoup appris de ses conseils et de nos discussions.

I would like to express the gratitude to all the people I have met as ancient or current members of the Nsysa group. All of you have special place in my heart.

Special acknowledgements go to the orange luminescent team: Dr. Milena Milutinović-Dumont for passing to me her ECL and experimental knowledge in such an altruistic manner; Dr. Catherine Adam for all the exciting moments in laboratory we have shared together and her positive personality; Dr. Habatmu Henok for his passionate research spirit; Dr. Anne de

Poulpiquet for her humorous soul and helpful presence. Lorenzo Russo for all interesting exchanges; Haidong Lee as the current capitan.

I would like to thank the sparkling bipolar team: Dr. Gabriel Loget for introducing me the world of bipolar "swimmers" and for great personality he possess at any level; Dr. Dodzi Zigah for his valuable presence and his frankness; Dr. Laurent Bouffier for the nice collaboration and the uncatchable "green swimmers". Dr. Zahra Fattah for the good atmosphere – Merhaba.

I acknowledge Dr. Valérie Ravaine and Dr. Florent Pinaut for sharing their knowledge on stimuli responsible micro-gels and for the opportunity to contribute in diverse ECL projects.

Je voudrais spécialement remercier Dr. Bertrand Goudeau pour toute l'aide qu'il a pu m'apporter, et pour avoir su me guider de façon pertinente durant mon travail.

Je voudrais également exprimer ma gratitude à Aline Simon-Lalande sans qui je n'aurais pu m'en sortir d'un point de vue administratif surtout au début de ma thèse. Merci pour sa disponibilité et sa patience à mon égard.

Véronique Lapeyre and Patrick Garrigue are acknowledged for their inputs and technical supports.

I strongly acknowledge the whole Nsysa family: my dear friend Dr. Suresh Vajrala, Dr. Emmanuel Suraniti (Merci beaucoup), Damla Keskin (Baby), Dr. Léa Messenger (Diamont), cara Serena Carrara, Dr. Aileen Justies, Dr. Michael Ongaro, Dr. Lisa Peyrard, Dr. Girard Emeline, Dr. Salem Ben Amor, Dr. Jérôme Roche, Dr. Nina Hüsken, Hannah Nas, Antoine Richieu, Alessandra Zanut, Dr. Sudarat Yadnum, Dr. Churalat Wattanakit, Dr. Chawanwit Kumsapaya, Thittaya Yutthalekham, Dr. Damien Quinton, Dr. Pascal Massé, Dr. Vasilica Lates, Dr. Stéphane Reculosa, Loïc Batot, Beatriz Diez Buitrago, Eugenio Gianessi, Héléne Labbie, Pauline Lefrancois, Gibran Hernandez Moreno.

I profoundly acknowledge Dr Aleksandar Karajić for invaluable friendship we have. Veliko ti hvala!

Takođe, htela bih da se zahvalim svim članovima laboratorije 538, kao i ostalim profesorima i istraživačima na Hemijskom fakultetu u Beogradu na pruženoj podršci tokom izrade doktorske disertacije.

Najpre bih se zahvalila prof. Goranu Rogliću na dugogodišnjoj podršci koja datira još iz vremena osnovnih studijama, kao i na konstruktivnim diskusijama i savetima.

Zahvaljujem se Anđeliji Milić, dr Tanji Verbić, dr Milici Jović, dr Marijani Marković, dr Biljani Matić, dr Jeleni Mutić, dr Jeleni Nešić, dr Tanji Ćirković, dr Daliboru Stankoviću, dr Ivanu Anđelkoviću, dr Vojinu Krsmanoviću, Bekiju, Hikiju, Branku!!! Hvala svima od srca na neponovljivo vesloj i prijateljskoj atmosferi!

Najtoplije i najiskrenije se zahvaljujem svojoj porodici, roditeljima Lepi i Novici, batu Vuku i dragim prijateljima, na njihovom razumevanju i pažnji koju si mi poklanjali i na bezgraničnoj podršci i podstreku koju su mi sve vreme nesebično pružali. Vama dugujem sve.

Na kraju bih se srdačno zahvalila Vladimiru Petroviću bez čije podrške i pomoći tokom dugog niza godina ne bih bila ovde gde jesam.

"What is greatest in human beings is what makes them equal to everybody else. Everything else that deviates higher or lower from what is common to all human beings makes us less. If we know this, we can develop a deep respect for every human being."

Bert Hellinger

Abstract

Electrogenerated chemiluminescence (ECL) is a powerful analytical technique exploited for clinical, industrial and research applications. The high sensitivity and good selectivity, makes ECL a tool-of-choice analytical method for a broad range of assays, most importantly for a large number of commercialized bead-based immunoassays. In the present thesis, we aimed to study the ECL phenomenon and its application in development of new analytical methods.

In the first part of this work, we used an imaging technique to investigate the ECL mechanisms operating in bead-based assays. Spatial reactivity mapping at the level of a single functionalised bead provides a new strategy to test the co-reactant efficiency and shows associated optical focusing effects.

In the second part, the design of a novel anti-transglutaminase ECL immunoassay for celiac disease diagnostic is shown using nanoelectrode ensembles as bioelectroanalytical platforms. We also studied the characteristics of ECL generated by arrays of boron-doped-diamond nanoelectrodes (BDD NEAs) as a promising materials for bioapplications. The ECL efficiency of two co-reactants at BDD NEAs was investigated.

Finally, bipolar electrochemistry is a “wireless” process that was exploited for the controlled motion of conductive objects exposed to an electric field in the absence of direct ohmic contact. In the third part of the thesis, we report ECL coupled to bipolar electrochemistry for tracking the autonomous trajectories of swimmers by light emission. We further expanded this concept for dynamic enzymatic sensing of glucose concentration gradient using ECL light emission as an analytical readout.

Key-words: Electrogenerated chemiluminescence, imaging, immunoassays, nanoelectrode array, bipolar electrochemistry, analytical swimmers

Résumé

La chimiluminescence électrogénérée (ECL) est une technique analytique puissante exploitée pour la détection autant au niveau industriel que dans le domaine de la recherche scientifique ou du diagnostic clinique. La sensibilité élevée et la bonne sélectivité de cette technique font de l'ECL une méthode analytique de choix pour un large éventail d'applications, dont la plus importante est son utilisation commerciale dans un grand nombre de tests immunologiques à base de billes fonctionnalisées. Dans cette thèse, nous avons cherché à étudier le phénomène ECL et son application pour le développement de nouvelles techniques analytiques.

Dans la première partie de ce travail, nous utilisons les techniques d'imagerie pour étudier les mécanismes ECL se produisant sur les billes utilisées pour les tests immunologiques. La cartographie de la réactivité au niveau d'une seule microparticule fonctionnalisée avec un complexe de ruthénium fournit une nouvelle stratégie visant à tester l'efficacité du co-réactif et montre des effets optiques associés de focalisation.

Dans la deuxième partie, la conception d'un test immunologique pour la détection de l'anti-transglutaminase pour le diagnostic de la maladie coeliaque est présentée en utilisant des ensembles de nanoélectrodes comme plates-formes bioélectroanalytiques. Nous avons également étudié les caractéristiques de l'ECL générée par des réseaux de nanoélectrodes dopées au bore-diamant en tant que matériaux prometteurs pour des applications biologiques ainsi que l'efficacité ECL de deux co-réactifs sur ces réseaux.

L'électrochimie bipolaire est un processus sans contact que nous avons exploité pour contrôler le mouvement d'objets conducteurs exposés à un champ électrique en l'absence de contact ohmique direct. Dans la troisième partie de ma thèse, nous présentons l'ECL couplée à l'électrochimie bipolaire pour le suivi d'objets autonomes luminescents. Nous avons élargi ce concept à la détection enzymatique dynamique de glucose en utilisant l'émission de lumière ECL comme signal analytique.

Mots-Clés: électrochimiluminescence, imagerie, immunodosage, réseaux de nanoélectrodes, électrochimie bipolaire, nageurs analytiques

2.1. Introduction	46
2.2. Reported mechanisms of Ru(bpy) ₃ ²⁺ / TPrA system	47
2.3. Reported mechanisms of Ru(bpy) ₃ ²⁺ / DBAE system	53
2.4. Bead-based Sandwich ECL immunoassay	55
2.4.1. 2D ECL Imaging	57
2.4.2. 3D ECL Imaging	59
2.5. Conclusions	65
References	66
 CHAPTER 3: Mapping the ECL generation with nanoelectrode ensembles and arrays for Immunosensing	 70
3.1. Introduction	71
3.2. Nano-Electrode Ensembles (NEEs) fabrication	73
3.3. Nano-Electrode Arrays (NEAs) fabrication	75
3.4. Electrochemistry at electrode ensembles and arrays	76
3.5. Bioelectroanalysis and biosensors with NEEs/ NEAs	81
3.6. Highly sensitive ECL Sensor for Celiac Disease Biomarkers	84
3.6.1. NEEs characterization	85
3.6.2. Voltammetric and ECL characterization of the immunosensor	87
3.6.3. Analytical performance study of the immunosensor	90
3.7. Tuning of induced luminescence with arrays of nanoelectrodes, NEAs	93
3.7.1. The MNEAPs were fabrication	94
3.7.2. Electrochemical characterization of the MNEAP	96
3.7.3. ECL measurements with the MNEAP	97
3.8. Conclusion	104
References	105
 CHAPTER 4: Electrogenerated chemiluminescent swimmers driven by bipolar electrochemistry	 109
4.1. Introduction	110
4.2. Bipolar electrochemistry	111
4.2.1. Definition of bipolar electrode	111
4.2.2. Polarization of a conducting object in an open configuration	112
4.2.3. The case of closed bipolar electrochemistry	114
4.3. Applications of bipolar electrochemistry coupled to ECL	115

4.4. Bipolar electrochemistry for motion generation	119
4.4.1. Translation, rotation and levitation of motors by BE	122
4.5. Lightening up bipolar swimmers	123
4.6. Light emitting swimmers for enzymatic glucose sensing	135
4.7. Conclusions	141
References	142
GENERAL CONCLUSION	147
PERSPECTIVES	152
APPENDIX	155

Abbreviations

Abbreviations	Meaning
AFP	alpha-fetoprotein
AgCl	silver chloride
AP	asymmetric particle
ATP	adenosine triphosphate
BDD	boron-doped diamond
BE	bipolar electrochemistry
BPE	bipolar electrode
BSA	bovine serum albumin
CCD	charge coupled device
CE	capillary electrophoresis
CL	chemiluminescence
CRP	C-reactive protein
CV	cyclic voltammetry
DBAE	2-(dibutylamino)ethanol
DC	direct current
DMSO	dimethylsulfoxide
DNA	deoxyribonucleic acid
DPA	9,10-diphenylanthracene
EBL	electron beam lithography
ECL	electrogenerated chemiluminescence
EF	electric field
EM	electromagnetic
EM-CCD	electron multiplying charge coupled device
ET	electron transfer
FIA	flow injection analysis
GC	glassy carbon
GDH	glucose dehydrogenase
GLC	glucose
HER2	human epidermal growth factor receptor
HOMO	highest occupied molecular orbital
HPLC	high performance liquid chromatography
HQ	hydroquinone
HRP	horseradish peroxidase
ICP	inductively coupled plasma
ITO	indium tin oxide
JP	Janus particle
LC	ligand centered excited states
LECs	light-emitting electrochemical cells
LED	light emitting diode
MNEAP	Multiple Nanoelectrode Array Platform

Abbreviations	Meaning
MWCNT	multi-walled carbon nanotube
NAD ⁺	nicotinamide adenine dinucleotide
NEA	Nano Electrode Array
NEE	Nano Electrode Ensemble
NP	nanoparticle
ox	oxidant
PBS	phosphate buffer saline
PC	polycarbonate
PDMS	polydimethylsiloxane
PMMA	poly(methyl methacrylate)
PMT	photomultiplier tube
PS	polystyrene
QD	quantum dot
red	reductant
Ru(bpy) ₃ ²⁺	ruthenium (II) tris(bipyridine)
SA	self-assembly
SAM	self- assembled monolayer
SEM	scanning electron microscopy
TEM	transmission electron microscopy
TPrA	tripropylamine
X-ray	X-ray spectroscopy

Symbols

Symbol	Meaning	Units
C	concentration	M
d	diameter or length of a bipolar electrode	cm
D	diffusion coefficient	cm ² s ⁻¹
E	potential	V
E	polarization potential	V
\mathcal{E}	imposed electric field	V cm ⁻¹
E^0	standard potential of the redox couple	V
E_a	anode potential	V
E_c	cathode potential	V
f	frequency	Hz
F	Faraday constant	C mol ⁻¹
h	height	cm
i	current	A
i_{be}	current flowing through the bipolar electrode	A
i_{bpe}	faradaic current through the bipolar electrode	A
i_{bps}	by-pass current	A
l	length of a bipolar electrode	cm
L	distance between the feeder electrodes	cm
n	stoichiometric number of electrons involved in a redox reaction	none
ϕ	rotation angle	rad
pK_a	acid dissociation constant	none
r	radius of the bipolar electrode	cm
R	resistance	Ω
T	temperature	K
t	time	s
t_0	initial time	s
U	measured potential difference	V
v	speed	m s ⁻¹
ΔV	maximum polarization potential	V
x	position on the bipolar electrode	m
Θ	angular position	rad
λ	wavelength	nm
σ	conductivity	S cm ⁻¹
ω	angular speed	rpm

Preface

Electrogenerated chemiluminescence (ECL) is a process which emits luminescent signals by converting electrochemical energy into radiative energy. It offers very sensitive detection of sub-picomolar concentrations with an extremely large dynamic range, greater than six orders of magnitude and almost zero background signal. The direct optical readout can be performed just with a photomultiplier tube (PMT) or inexpensive CCD cameras and therefore, easily combined with other technologies such as microfluidics and capillary electrophoresis to obtain complete detection systems. ECL detection is widely used in commercialized systems with an increasing trend. The present thesis is aimed at studying the fundamental ECL process and at developing new ECL systems for original bioanalytical applications.

Chapter one is dedicated to the general principles of ECL. Two different pathways to generate ECL, annihilation and co-reactant ECL, are explained in details. The most used ECL luminophores, based on ruthenium complexes, and co-reactants are also presented. In the last part of this chapter, the principal applications of ECL are briefly described.

In the second chapter, the study of ECL mechanisms used in bead-based immunoassays and their influence on ECL emission were investigated. Spectroelectrochemistry and ECL imaging was combined to observe the ECL generation from a single micro-bead, functionalized with ruthenium complex with two efficient co-reactants, by mapping the ECL reactivity in space. This new imaging approach provides insights into the ECL mechanistic route operating in such a commercialized bead-based bioassays and its extremely high sensitivity.

Chapter 3 addresses the electrochemical properties of nanoelectrode ensembles and arrays (NEEs / NEAs) with recent advances in bioelectroanalytical applications. The electrochemical characteristic that makes the NEEs and NEAs very useful in the development of chemical nanosensors is the dramatic lowering of capacitive currents (that are the largest component of the noise, or more properly the background signal of voltammetric measurements) allowing very sensitive detection of analytes of interest. Exploiting both gold NEEs as a sensor platform and generation of ECL at low oxidation potentials, a new sensitive and specific ECL immunosensor for diagnosis of celiac disease (CD) will be presented. Furthermore, ECL imaging was used for the characterization of ECL generation at boron-doped diamond (BDD) NEAs fabricated with different geometries of arrays. BDD electrodes have advantageous

properties including high reproducibility, stability, and robustness under extreme conditions with a wide potential window in aqueous solutions, without oxidation of the electrode itself. BDD NEAs with a very tiny background signal should be therefore applied in future developments of sensors with high sensitivity.

In the last chapter, principles of bipolar electrochemistry (BE) will be presented. This concept has been recently used to control the motion of autonomous microswimmers, breaking the symmetry on the surface of these conductive objects in a wireless manner. The strategy to trigger the motion relies on the generation and release of bubbles and was used for translation, rotation and levitation and it will be described in details. We will present the integration of ECL light emission process into this mechanism. Furthermore, we expanded this concept to develop sensing swimmers using ECL as an analytical signal. This approach, in which ECL is coupled to BE, offers a unique analytical approach based on the design of smart dynamic systems for a straightforward visual readout.

Chapter 1:
Fundamentals of Electrogenerated Chemiluminescence

1.1. Introduction

Electrogenerated chemiluminescence (ECL) is an electrochemical process, where light emission is initiated by an electron-transfer reaction occurring at an electrode surface¹⁻⁴. ECL is by essence a chemiluminescence reaction (CL), triggered by electrochemical methods⁵. This technique represents a marriage between electrochemistry and spectroscopy. The smart combination of two analytical methods offers to ECL unique superiorities over other optical sensing methods. As it does not require a light source, it simplifies the detection apparatus and most importantly invalidates background signals from scattered light and luminescent impurities, thus providing improved sensitivity^{1,6,7}. For instance, a tris(bipyridine)ruthenium(II), $\text{Ru}(\text{bpy})_3^{2+}$, can be detected at sub-picomolar concentrations with an extremely broad dynamic range, greater than six orders of magnitude³. Secondly, as the excited state of the luminophore can be regulated by alternating the applied potential, good selectivity is provided. This fact, coupled with the possibility to place the optical detectors very close to the electrode surface, allows accurate spatial and temporal control over the reaction. By controlling its initiation, light emission can be delayed until events such as immune or enzyme-catalyzed reactions have taken place.¹ Finally, ECL allows simultaneous measurements of two experimental parameters, the light intensity and the Faradaic current, as function of the potential, which facilitates the investigation of light emission mechanism and enables the ECL and electrochemical detections, simultaneously. Due to these properties, ECL has become an important detection method in analytical chemistry. Commercial immunoassays and deoxyribonucleic acid (DNA) probe assays have been widely used in the areas of clinical diagnostic, food and water testing, environmental monitoring, biowarfare agent detection and scientific research^{1,2,6,8-14}. ECL has also been exploited for the determination of numerous analytes when combined with high performance liquid chromatography (HPLC), flow injection analysis (FIA) and capillary electrophoresis (CE).¹⁵⁻

19

Since the work performed in this thesis is based on investigation of ECL mechanisms and ECL detection, the first chapter will present the principles of ECL and its applications.

1.2. Discovery of ECL and brief historical overview

ECL has been reported for the first time as the emission of light generated by relaxation of excited state molecules that are produced during an electrochemically-initiated reaction²⁰. Pioneer work on light generation following electrochemical reactions date back to early 1900's.^{21,22} In 1960s the first detailed ECL studies started reporting the luminescence of aromatic hydrocarbons and organometallic compounds.²³⁻²⁵ The first experiments done by applying alternating currents lead to the suggestion of a mechanism and the first theory about electron transfer in ECL. ECL actually provided the first evidence of the Marcus inverted region, where generation of the excited state rather than the energetically more favored ground state was observed.²⁶ In 1972, it has been reported that Ru(bpy)₃²⁺ species can also emit light under cycling of the potential on a Pt electrode with the maximum of emission at exactly the same wavelength as the maximum of emission observed upon photoexcitation.²⁷ Furthermore, organometallic compounds due to their ECL nature, have attracted continuous interest in development of ECL-emitting species. It was found in 1997, that characteristic emission occurs during the simultaneous oxidation of oxalate and some fluorophores such as rubrene, 9,10-diphenylanthracene and bipyridyl chelates of ruthenium(II) and osmium(II).²⁸ ECL generation by one direction scan of the potential in the presence of both luminophores and co-reactant species was a real breakthrough. Ten years later aliphatic amines especially tri-n-propylamine has been found to be one of the most efficient ECL co-reactants.^{5,29} Applications in bioassays started from 1990s and played a large part in fueling interest in the technique, resulting in commercialized ECL instrumentation in 1994. Thanks to its high sensitivity and good selectivity, ECL is now exploited in more than 30000 instruments worldwide as a powerful analytical technique, easily adapted to a broad range of applications.^{1,2,6}

1.3. Background

ECL is one of many forms of luminescence (light emission) and is triggered by the electrochemical reaction initiated on the electrode surface. To understand the principles of ECL emission and to differentiate it from other types of luminescence, the principles of photoluminescence (PL) and chemiluminescence (CL) are discussed.

1.3.1. Photoluminescence

Photoluminescence is the light emission by a molecule when raised at an excited state after a photon absorption (electromagnetic radiation). Absorption of energy occurs between the closely spaced vibrational and rotational energy levels of the excited states in different molecular orbitals. Various energy states available to a molecule and the transitions between them are illustrated by the so-called Jablonski-energy level diagram (Figure 1). It shows electronic and vibrational states (rotational energy states are ignored).³⁰ Once a molecule has absorbed energy in the form of electromagnetic radiation, there are numerous relaxation mechanisms by which it can return to ground state S_0 . The ground state of a large majority of molecules is a singlet state, meaning that the electrons are paired into a zero spin state. If the photon emission occurs between states of the same spin state (e.g. the first excited singlet state $S_1 \rightarrow S_0$), this is termed fluorescence. Another excited state at lower energy than the first excited singlet is the triplet state T_1 , with total spin of 1. In the case when the spin states of the initial and final energy levels are different (e.g. $T_1 \rightarrow S_0$), the emission is called phosphorescence. Transitions between singlet and triplet states are called intersystem crossing (ISC). The low probability of ISC arises from the fact that molecules must first undergo spin conversion to produce unpaired electrons, an kinetically unfavorable process. Here in contrast to fluorescence, molecules absorb light and form an excited state whose decay involves a spin flip, and is therefore “forbidden” by electric dipole transitions. As a result, the energy can become trapped in the triplet state with only "forbidden" $T_1 \rightarrow S_0$ transitions available to return to the ground energy state. Correspondingly, the lifetimes of fluorescent states are very short (1×10^{-6} to 10^{-9} seconds) while phosphorescence ones are longer (1×10^{-3} seconds).

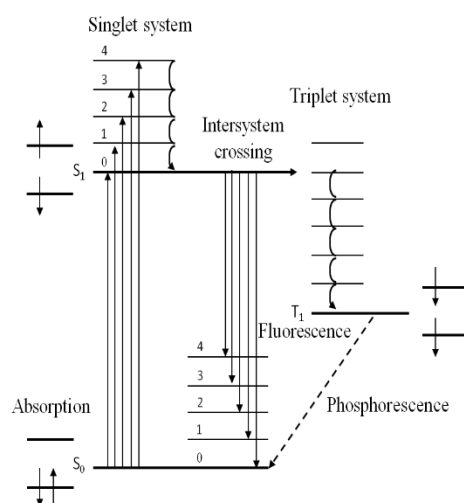


Figure 1. Jablonski energy level diagram during the absorption and emission of radiation.

Different fluorophores can absorb different spectra of lights, but each fluorophore absorbs light at a specific wavelength. This process is dominated by energy difference in between different energetic states of molecules and it can be seen in an excitation spectrum. Accordingly, they have a specific spectrum of light re-emission (usually called emission spectrum). Wavelengths of maximum excitation (~absorption) and emission (for example, absorption/emission = 485 nm/517 nm) are the terms used to refer to a given fluorophore. As electronic transitions are induced by electromagnetic irradiation, they are characterized by its frequency ν and a state of polarization. This provides the information about spatial direction of the electric field. When electrons diminish their energy from the excited state to the ground state, there is a loss of vibrational energy. The quantum of energy that the radiation field can exchange with matter is

$$E = h\nu \quad (1)$$

usually expressed in kJ/mol, eV/molecule, where h is the Plank constant (6.626×10^{-34} J·s), ν is frequency (Hz). It is also common to use a quantity proportional to E , such as the wavelength of the light:

$$\lambda = \frac{c}{\nu} \quad (2)$$

where c is speed of light ($2.99 \cdot 10^8$ m.s⁻¹) and λ is wavelength of emission (m). In absorption and emission spectra, light intensity is plotted as a function of one of the characteristics that identify photon energy. The equation 1 provides a bridge from the position of the observed spectral peaks to the energy difference between the initial and final state involved in a spectroscopic transition.³⁰ Obviously, the energy of emission is lower than energy of excitation and excitation wavelength is longer compared to the wavelength of absorption. The difference between the maximum excitation and maximum emission wavelengths is termed: the Stokes' shift. For example, the complex [Ru(bpy)₃]Cl₂ exposed to the white light absorbs blue light (450 nm)³¹ which enables the excitation on an electron. For this reason the complex is orange-red colored (610 nm).⁴

1.3.2. Chemiluminescence

CL is an homogeneous process compared to ECL, in which the light emission is obtained by highly energetic electron-transfer reactions between two reacting species. The reaction occurs in the homogenous phase.³² Besides, many conventional CL reactions can be initiated by

electrochemical means. The most studied and exploited reaction has been that involving luminol (Figure 2). CL reaction of luminol is an oxidation reaction which is carried out either in aprotic solvents (dimethyl sulfoxide, DMSO; *N,N*-dimethylformamide, DMF) or protic solvents (water, lower alcohols).²⁷ Oxidation in aqueous media gives rise to blue light emission 424 nm,²⁸ while in aprotic solvents this shifts to yellow-green. Luminol (LH_2) can be considered as a diprotic acid. To obtain chemiluminescence from luminol in an aqueous solution, an oxidizing reagent, such as hydrogen peroxide, is needed. Under basic conditions (pH 11–13) the prevalent luminol anion (LH^-) is oxidized to luminol radical anion (LH^{\bullet}). Others one-electron oxidants can catalyze this reaction (horseradish peroxidase, cobalt-complexes, copper, manganese, iron, etc.). In a second oxidation step LH is further oxidized to either aminodiazquinone (L) or directly (by superoxide anion) to hydroperoxide adduct (LO_2H). From this adduct, an endoperoxide species can be formed, from which molecular nitrogen is expelled, generating excited state 3-aminophthalate dianion (AP).

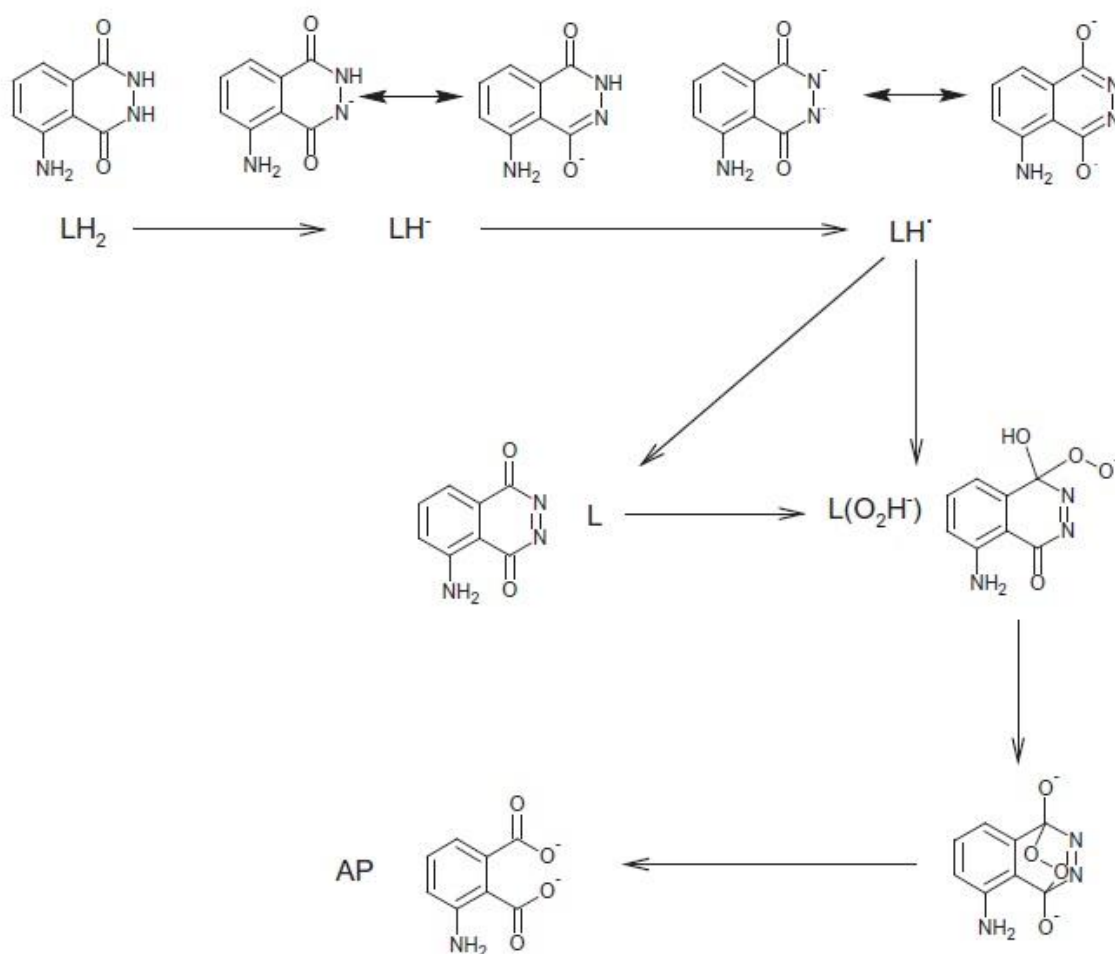


Figure 2. Mechanism of CL luminol oxidation.³³

In comparison with ECL reactions, the way to achieve excited state is different but the relaxation process and mechanism of light emission is the same. The ECL mechanisms will be discussed in detail in Chapter 2. However, in CL reactions the emitting species is an excited chemical product, such that the original CL reagent cannot be regenerated. Molecules as are ruthenium complexes, which can be regenerated after having emitted their photons, appeared to be more appealing luminescent reagents and therefore the main competitors to luminol in the field of electroanalytical chemistry. $\text{Ru}(\text{bpy})_3^{2+}$ for example, is the stable species in solution and the reactive species, $\text{Ru}(\text{bpy})_3^{3+}$, can be generated from $\text{Ru}(\text{bpy})_3^{2+}$ by oxidation. $\text{Ru}(\text{bpy})_3^{3+}$ can react with analytes containing tertiary, secondary and primary alkyl amine groups to form the excited state $\text{Ru}(\text{bpy})_3^{2+*}$, which will decay to the ground state emitting yellow-orange light.²⁹ Thus, in ECL reactions, ruthenium complexes are regenerated after light emission, making ECL methodology reusable and highly interesting from an analytical point of view.

1.3.3. Electrogenerated chemiluminescence

ECL is a controllable form of chemiluminescence where light emission is initiated by an electron transfer-reaction occurring at an electrode surface. The most common system used for analytical purposes consists of the luminophore species $\text{Ru}(\text{bpy})_3^{2+}$, or one of its derivatives, with tri-n-propylamine as a co-reactant. ECL reaction can be controlled and manipulated, since ECL reagents are generated *in situ* at the electrode by sweeping the applied potential, generally in cyclic voltammetry or chronoamperometry. The activated species formed upon the oxidation of both luminophore and co-reactant, further react together to form the excited state $\text{Ru}(\text{bpy})_3^{2+*}$ and thus the ECL emission. Actually, the intimate mechanism of presented ECL reaction is much more complex, and is still an active area of investigation.³⁴⁻³⁷ Proposed mechanisms in the literature will be presented in details in paragraph 1.4.

1.4. ECL mechanisms

The annihilation and co-reactant pathways are the two main pathways through which ECL can be generated. Although the analytical usefulness of co-reactant based ECL has been recognized and exploited to great extent, the first ECL study reported in the literature was based on ion annihilation ECL.

1.4.1. Organic ion annihilation ECL

High energy electron transfer reactions between electrochemically generated radical ions of aromatic hydrocarbons or their derivatives, produced by a potential step or sweep, are accompanied by the light emission due to the relaxation of excited species.^{1,2} Because of the solubility of aromatic hydrocarbons, these reactions are performed in organic solvents, in the presence of a supporting electrolyte such as tetrabutylammonium salt. The general mechanism is following:



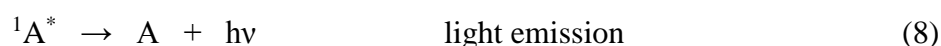
followed by either



or



ending by



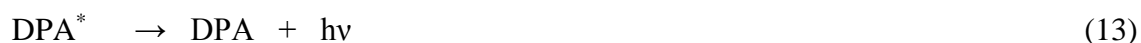
where A is an aromatic hydrocarbon and B is either the same or another aromatic hydrocarbon, ${}^1A^*$ is the singlet excited state and ${}^3A^*$ is the triplet excited state. If the potential of the working electrode is quickly changed between two different values, species A can be oxidized to $A^{\cdot+}$ (Eq. 3) and B reduced to $B^{\cdot-}$ (Eq. 4) at the same electrode. These species react in the Nernst diffusion layer and form an excited state A^* and thus produce the light emission (Eq. 8).² Depending on the energy available in the annihilation reaction, the produced A^* can be either in the lowest excited singlet state ${}^1A^*$ or in the triplet state ${}^3A^*$. In systems with sufficient energy, the light emission process is defined as “S-route” (excited singlet formation (3) - (5)). Most ECL systems based on aromatic compounds follow this mechanism. From the redox potential in Eq. 3 and 4, the enthalpy which is directly related to the energy available in Eq. 5 can be calculated (Eq. 9)¹ by:

$$-\Delta H_{\text{ann}} = \Delta G + T\Delta S = E_p(A/A^{\cdot+}) - E_p(A/A^{\cdot-}) - 0.16 \quad (9)$$

$-\Delta H_{\text{ann}}$ (in eV) is the enthalpy for ion annihilation, E_p is the peak potential for electrochemical oxidation or reduction. The value of 0.16 eV is the entropy approximation term ($T\Delta S$) estimated to be ~ 0.1 eV with an addition of 0.057 eV resulting from the difference between two reversible peak potentials of the redox reaction.^{1,38} If the enthalpy of annihilation is larger than the energy required to produce the lowest excited singlet state (E_s), it is possible to directly generate $^1A^*$, which is the case for ‘‘S-route’’.

In contrast, in lower energy systems, the triple state energy $^3A^*$ will be first produced (Eq. 7). From subsequent annihilation of $^3A^*$ (triplet–triplet annihilation), $^1A^*$ will be generated, and this reaction is said to follow the ‘‘T-route’’. This means that $-\Delta H_{\text{ann}}$ is smaller than the energy of singlet excited state E_s , but larger than the energy of triplet excited state (E_t)³. Emission from the triplet state is rarely seen because transition from triplet to the lower singlet energy state is quantum-mechanically ‘‘forbidden’’.

One of the first ECL system reported represents a classic example of energy sufficient system (‘‘S-route’’) and it involves 9,10-diphenylanthracene (DPA) in dimethylformamide (DMF) by applying alternating potential.²³ In the first experiments, the working electrodes were platinum coaxial helices or parallel pairs of gold foils. During potential changes DPA was oxidized and reduced. Formed DPA^+ and DPA^- react together, resulting in light emission.



The anodic and cathodic processes of DPA have been characterized by cyclic voltammetry showing the reduction peak at -1.95 V vs SCE and oxidation peak at +1.25 V vs. SCE. According to these results by applying equation (9), the enthalpy for the electron-transfer reaction can be calculated as 3.04 eV. When we compare this value with the energy of emitted light at 435 and 410 nm (2.85 and 3.02 eV), we can see that the emitting state is directly accessible.¹ DPA^* can be populated directly in the reaction so it follows S-route.

A typical example of triplet–triplet annihilation (‘‘T-route’’) is the ECL of DPA/TMPD (TMPD = N,N,N',N'-tetramethyl-p-phenylenediamine) system, generated from two different

precursors. ECL is achieved via a “cross-reaction” between the anion radical of DPA and the cation radical of N,N,N,N-tetramethyl-p-phenylenediamine (TMPD) in DMF:³⁹⁻⁴¹



The enthalpy for the electron-transfer reaction is 1.97 eV which is less than required to reach the emitting single state for DPA (3.02 eV). However, the emitted light generated via ECL is identical to DPA photoluminescence indicating that DPA^* is the ultimate product of charge transfer.⁴⁰ As a result, the singlet excited state is not accessible directly, but only via triplet-triplet annihilation where the energy from two electron-transfer reaction is pooled to provide sufficient energy (Eq. 18).⁴²



If the enthalpy of the electron-transfer reaction is marginal compared to the energy of singlet excited state, the T-route can contribute to the formation of ${}^1\text{A}^*$ in addition to the S-route, so called ST-route. A common example is the rubrene anion-cation annihilation.⁴³

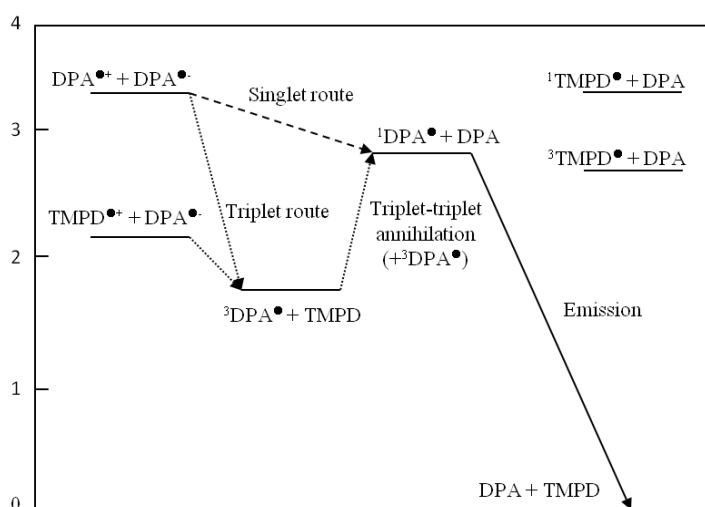
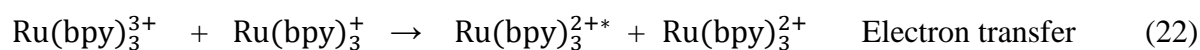


Figure 3. Energy level diagram for DPA-DPA and TMPD-DPA ECL systems.⁴

Despite being frequently used in light-emitting electrochemical cells (LECs) and the most studied case of ECL, regarding the mechanism and the nature of the excited state, annihilation ECL has not found significant application in direct analysis.³ Mostly, this is due to the fact that these reactions take place in organic solvents, such as acetonitrile, dimethyl-sulfoxide or methylene-chloride. While working in aprotic solvents, the potential window proceed the electrochemical reactions should be wide enough (from ~-3.3 to 2 V) (eq. 9), so that water and dissolved oxygen must be rigorously excluded to prevent quenching of the ECL reaction. Thus, cells and electrodes have to be constructed to allow transfer of solvent and degassing on high-vacuum line or in inert-atmosphere (glove-boxes).² Furthermore, generation of both radicals (anion and cation) at the electrode surface are required. For singlet systems, parent species in this type of reactions must undergo both oxidation and reduction within a potential range that is accessible in the employed solvent. Once formed, the radical ions must be sufficiently long-living to allow them to diffuse, encounter each others, and undergo electron transfer.

1.4.2. Inorganic annihilation ECL

The most studied and exploited inorganic ECL-generating compound to date is ruthenium(II) tris(2,2'-bipyridine), $\text{Ru}(\text{bpy})_3^{2+}$, although a broad range of inorganic complexes and clusters have been shown to generate ECL.⁴⁴ The reason lies in fact that it can undergo ECL in aqueous buffered solutions at easily attainable potentials at room temperature with very high efficiency. The compound exhibit ECL following ‘‘S-route’’, analogous to that of aromatic hydrocarbons above, as follows:



But its analytical usefulness stems from the fact that compounds which can act as a chemical reductant and replace the electro-reduction step are potential analytes, producing ECL at a single anode.

1.5. Co-reactant pathway

Co-reactant ECL technology is an essential part of all commercially available ECL analytical instrumentations. Finding new co-reactants with a high ECL efficiency for bioassays is a constant driving force in this area. The co-reactant route is an electrochemical (E) step followed by a chemical (C) one, which can be considered as an EC process. The co-reactant is a deliberately introduced species that, upon its oxidation or reduction, reacts with ECL luminophores to produce the excited state. Distinct from ion annihilation ECL, coreactant ECL is more comfortable for work not only in aqueous media but also in physiological conditions (pH ~ 7.4). Thus most of the applications of ECL are based on co-reactant ECL.

The main advantage over annihilation ECL which demands generation of both oxidized, A^+ and reduced, B^- , is that the co-reactant pathway follows electron transfer between either A^+ or B^- and the co-reactant. As a result, ECL emission features a single, unidirectional potential step where reagents are only oxidized or reduced. Depending on the polarity of the applied potential, both luminophore and co-reactant can be first oxidized or reduced at the electrode leading to anodic and cathodic ECL emission, respectively. The intermediate-formed radicals then decompose and provide a powerful reducing or oxidising species. These species react with the oxidized or reduced luminophore to produce the excited state that emit light.¹ Thus, ECL can be simply designed as “oxidative-reduction” for anodic ECL emission and “reductive-oxidation” for cathodic ECL emission (detailed in paragraph 1.5.1.1. and 1.5.1.2., respectively).

Taking into account a one potential step generation, co-reactant ECL is more easily applicable than annihilation ECL. First of all, it facilitates the generation of ECL in aqueous solution, opening up a wide range of opportunities for the use of ECL in chemical analysis. There is no need for wide potential window so other solvents with a narrow potential window and aqueous solution can be also used. Secondly, the oxygen quenching effect does not influence strongly the ECL signal, so ECL analysis can be still effective without degassing. Finally, the use of co-reactant can make ECL possible even for some fluorophores that have only a reversible electrochemical oxidation or reduction while annihilation ECL requires both of them.

1.5.1. ECL co-reactants-based systems and their mechanisms

An ECL co-reactant is a reagent that after oxidation or reduction can decompose forming highly reactive oxidative or reductive species which can undergo energetic electron-transfer reaction with oxidised or reduced luminophore to generate ECL, as explained in the above paragraph.

To find an efficient ECL co-reactant, a number of criteria need to be met which include solubility, stability, electrochemical properties, kinetics, quenching effect, ECL background etc.⁴⁵

Some typical ECL co-reactants are shown in Table 1.

Table 1. Typical co-reactant ECL systems

Type of co-reactant ECL	Luminophore	Co-reactant	main co-reactant intermediate
Oxidative reduction	$\text{Ru}(\text{bpy})_3^{2+}$	oxalate	$\text{CO}_2^{\cdot-}$
	$\text{Ru}(\text{bpy})_3^{2+}$	pyruvate	$\text{CH}_3\text{CO}^{\cdot}$
	$\text{Ru}(\text{bpy})_3^{2+}$	tri-(n)-propylamine	$\text{TPrA}^{\cdot+}$, TPrA^{\cdot}
Reductive-oxidation	$\text{Ru}(\text{bpy})_3^{2+}$	hydrazine	N_2H_2 , $\text{N}_2\text{H}_3^{\cdot}$
	$\text{Ru}(\text{bpy})_3^{2+}$	persulfate	$\text{SO}_4^{\cdot-}$
	aromatic hydrocarbons	benzoyl peroxide	PhCO_2^{\cdot}
	$\text{Ru}(\text{bpy})_3^{2+}$	hydrogen peroxide	OH^{\cdot}

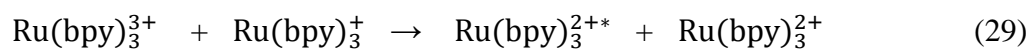
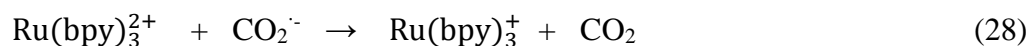
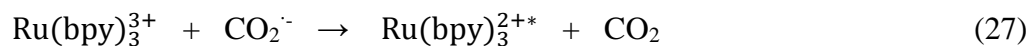
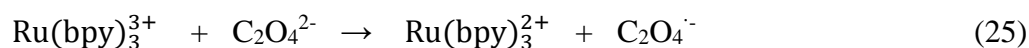
The first report that upon mixing $\text{Ru}(\text{bpy})_3^{3+}$ and aliphatic amines, the generation of light *via* CL reaction has been shown by Noffsinger and Danielson.²⁴ The reaction was explained by oxidation of aliphatic amines by $\text{Ru}(\text{bpy})_3^{3+}$ leading to the formation of short lived radical cation which then loses a proton giving a free radical. This free radical can then reduce $\text{Ru}(\text{bpy})_3^{3+}$ to the excited state $\text{Ru}(\text{bpy})_3^{2+*}$. Following this work and the idea that reactants in the presented reaction can be electrochemically generated, Leland and Powell reported a new ECL reaction based on TPrA and $\text{Ru}(\text{bpy})_3^{2+}$.⁵ The experiment was carried out on a gold electrode in a buffer solution of TPrA and $\text{Ru}(\text{bpy})_3^{2+}$ at physiological pH by recording the ECL curve and cyclic voltammograms, simultaneously. Further, a lot of work has been done

to correlate the co-reactant ECL efficiency with the amine structure. An important condition that should be met is that amine should have a hydrogen atom attached to the α -carbon so that upon oxidation newly formed radical can undergo reaction of deprotonation to form a strongly reducing free radical species. In general, it was found that ECL intensity increases following the order : primary < secondary < tertiary amines.^{5, 24,63,86} The efficiency of all other ECL systems are compared with the efficiency of Ru(bpy)₃²⁺/ TPrA system, thus it can be considered as an ECL standard.

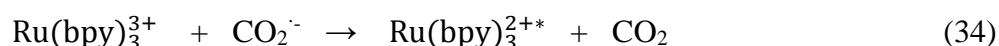
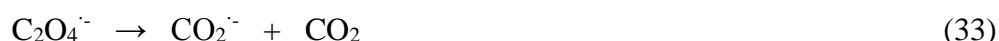
1.5.1.1. Oxalate (Ru(bpy)₃²⁺/ C₂O₄²⁻) System, example of oxidative-reduction ECL

Bard and co-workers discovered oxalate ion as the first ECL co-reactant.^{28,46-50} They demonstrated that silica nanoparticles (SiNPs) could achieve a higher ECL emission upon adding an excess of C₂O₄²⁻. The first experiments were performed in acetonitrile and later in aqueous solutions.

In an aqueous solution, Ru(bpy)₃²⁺ is first oxidised to Ru(bpy)₃³⁺ cation after applying the anodic potential, it is therefore an example of “oxidative-reduction” ECL. The cation is then capable to oxidize the oxalate (C₂O₄²⁻) in the diffusion layer close to the electrode surface and to form an oxalate radical anion (C₂O₄^{·-}). C₂O₄^{·-} decomposes to form the highly reducing radical anion CO₂^{·-} and carbon dioxide. In this reaction, the excited state is produced via direct reduction of Ru(bpy)₃³⁺ by the radical CO₂^{·-}, but also, a second mechanism *via* annihilation may occur. The ECL mechanism of this system is presented as follow:

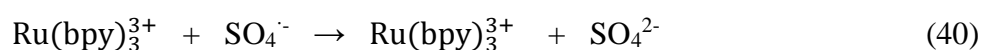
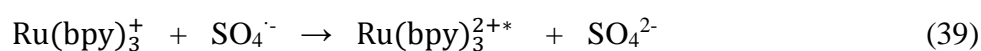
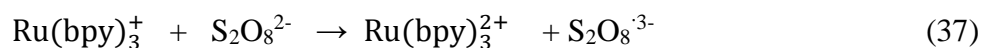


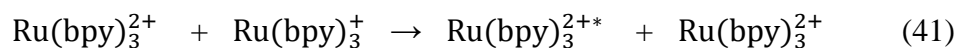
In the previous case, oxalate species was oxidized by a catalytic way. In acetonitrile oxalate may be oxidised directly on the electrode surface, thus the mechanism is more simple.²⁸ The oxalate ($C_2O_4^{2-}$) is oxidised to oxalate radical anion ($C_2O_4^{\cdot-}$) that decomposes to a reducing radical anion ($CO_2^{\cdot-}$) which then reacts with $Ru(bpy)_3^{3+}$ to form the excited states.



1.5.1.2. Peroxydisulfate ($Ru(bpy)_3^{2+}/S_2O_8^{2-}$) System, example of reductive-oxidation ECL

Persulfate is the first example of a so-called “reductive-oxidation” co-reactant ECL system produced by applying a cathodic potential.⁵¹ Since $Ru(bpy)_3^+$ is unstable in aqueous solutions while $(NH_4)_2S_2O_8$ has a low solubility in acetonitrile and reduction reaction is accompanied with serious hydrogen evolution, the reaction was carried out in acetonitrile- H_2O mixed solution. Upon the application of cathodic potential $S_2O_8^{2-}$ can be reduced directly at the electrode surface but also catalytically by $Ru(bpy)_3^+$ forming $S_2O_8^{\cdot 3-}$, that decomposes to intermediate $SO_4^{\cdot-}$ with a strongly oxidising capacity.⁴⁵ The radical then oxidises $Ru(bpy)_3^+$ to the excited state $Ru(bpy)_3^{2+*}$ or $Ru(bpy)_3^{2+}$ to $Ru(bpy)_3^{3+}$ that undergo annihilation giving $Ru(bpy)_3^{2+*}$.





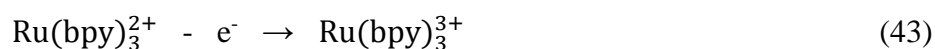
1.5.1.3. Tri-n-propylamine / Ru(bpy)₃²⁺ System, the model ECL system

Among organic amines, TPrA is a model co-reactant for anodic ECL systems through “oxidative-reduction” pathway.^{5,29} The system composed of Ru(bpy)₃²⁺, or its derivatives, with TPrA as co-reactant exhibits high ECL efficiency and has become the commercial benchmark for ECL immunoassays and DNA analysis.^{1,6,45} Understanding the complex mechanism of ECL reaction is a dynamic area of research.^{5,29,34,35,37,52-54} According to the first report of the ECL emission from Ru(bpy)₃²⁺/ TPrA tandem by Leland and Powell and some later works, the proposed mechanism can be represented by the following reactions:^{5,52,55}

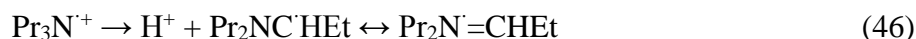
Acid-base equilibrium:



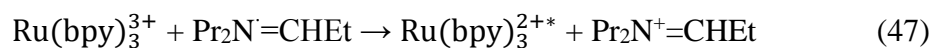
Oxidation step:



Deprotonation:



Excited state formation 1:



Light emission:



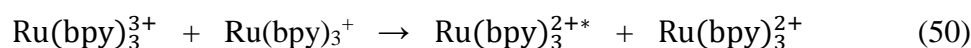
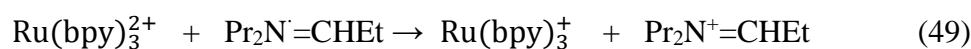
(Where Pr = CH₃CH₂CH₂- and Et = CH₃CH₂-)

The experiment was carried out on a gold electrode in a buffer solution of TPrA and Ru(bpy)₃²⁺.⁵⁶ In aqueous Ru(bpy)₃²⁺ ECL analysis, the optimum pH value of the TPrA buffer

solution is usually about 7-8. In anodic part of the scan, both $\text{Ru}(\text{bpy})_3^{2+}$ and TPrA (NPr_3) are oxidised (Eqs. 43-44). The oxidation of TPrA results in a broad wave due to preceding acid-base equilibrium (Eq. 42) (pK_a of ~ 10.4).⁵⁴ Comparing the ECL curve and cyclic voltammogram recorded simultaneously, they concluded that ECL emission also tracks the current for the oxidation of TPrA. Upon oxidation, the short-lived TPrA radical cation ($\text{TPrA}^{\cdot+}$) is losing a proton from an α -carbon to form the strongly reducing intermediate TPrA^{\cdot} (Eq. 44), and then reduces $\text{Ru}(\text{bpy})_3^{3+}$ to the excited state $\text{Ru}(\text{bpy})_3^{2+*}$ (Eq. 45). Despite it can be oxidised directly on the electrode surface (Eq. 44), oxidation *via* catalytic route involving homogeneous oxidation of TPrA with $\text{Ru}(\text{bpy})_3^{3+}$, can take place (Eq. 45). The relative contribution of both routes depends on relative concentration of $\text{Ru}(\text{bpy})_3^{2+}$ and TPrA and factors that affect the potential and rate of direct oxidation of TPrA at the electrode.^{52,46}

Further, highly reactive intermediate TPrA^{\cdot} can also reduce present $\text{Ru}(\text{bpy})_3^{2+}$ forming $\text{Ru}(\text{bpy})_3^+$ which can then react by annihilation pathway with $\text{Ru}(\text{bpy})_3^{3+}$ producing excited state $\text{Ru}(\text{bpy})_3^{2+*}$, as discussed in paragraph 1.3.2.

Excited state formation 2:

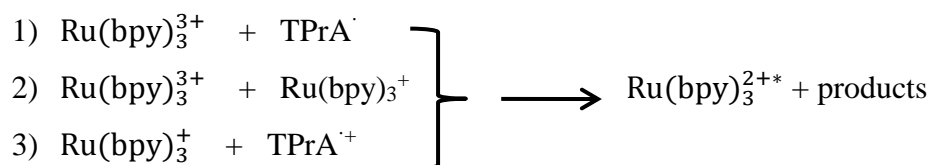


The contribution of this process to the overall ECL intensity depends upon the $\text{Ru}(\text{bpy})_3^{2+}$ concentration and is not favored when $\text{Ru}(\text{bpy})_3^{2+}$ concentrations are low. It was found that in the case of low concentration of $\text{Ru}(\text{bpy})_3^{2+}$ (nM- μM) and high concentration of TPrA (10-100 mM) the ECL emission *vs* potential curves showed two waves.³⁴ The second peak appears at the potential which corresponds to the oxidation of $\text{Ru}(\text{bpy})_3^{2+}$ but the first one could not be explained by mechanisms which consider only direct oxidation of $\text{Ru}(\text{bpy})_3^{2+}$ at the electrode surface.^{34,52}

Miao and Bard proposed a new mechanistic route considering the ECL emission at low oxidation potential.³⁴ The process occurs with the direct oxidation of TPrA at the electrode to generate $\text{TPrA}^{\cdot+}$ and TPrA^{\cdot} . The subsequent reaction between TPrA^{\cdot} and $\text{Ru}(\text{bpy})_3^{2+}$ generates $\text{Ru}(\text{bpy})_3^+$, which then reacts with $\text{TPrA}^{\cdot+}$ to form the excited state $\text{Ru}(\text{bpy})_3^{2+*}$. The initial ECL signal started at potential that is just positive enough to directly oxidize TPrA at the GC electrode while the second ECL signal occurs in the potential region of direct

oxidation of $\text{Ru}(\text{bpy})_3^{2+}$ at a GC electrode.^{34,52} It was found that dissolved O_2 could influence the ECL intensity when low concentrations (< 20 mM) of TPrA are used which is particularly remarkable for the first ECL wave.⁵² This behavior can be readily explained on the basis of the ECL mechanisms described above. A large excess of intermediate reducing radicals, TPrA^\cdot , was produced at high concentration of TPrA, and the dissolved O_2 within the ECL reaction layer was completely reduced by these radicals and exerted no quenching effect on the emission. However, at low TPrA concentration, co-reactant oxidation generated a relatively small amount of reducing intermediates, and O_2 acted as a quencher, destroying the intermediates before they participated in the ECL pathways, which led to the obvious reduction of the emission intensity.

To summarise, the excited state of $\text{Ru}(\text{bpy})_3^{2+}$ can be produced via three different routes: 1) $\text{Ru}(\text{bpy})_3^{3+}$ reduction by TPrA^\cdot ; 2) the $\text{Ru}(\text{bpy})_3^{3+}$ and $\text{Ru}(\text{bpy})_3^+$ annihilation reaction, and 3) $\text{Ru}(\text{bpy})_3^+$ oxidation by $\text{TPrA}^{\cdot+}$ radical cation:



The ECL intensity of both waves depends on different experimental conditions. pH is a crucial parameter in the ECL mechanism. Indeed, ECL is known to be effective at $\text{pH} > 5.5$, with a maximum intensity at $\text{pH} 7.5$. Solution pH should be sufficiently high to promote deprotonation of TPrA^+ to TPrA^\cdot .¹ However, pH value should not be higher than 9 because TPrA is insoluble and generated $\text{Ru}(\text{bpy})_3^{3+}$ on the electrode surface can react with hydroxide ions and to produce ECL background signal.⁴⁵

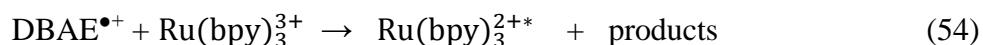
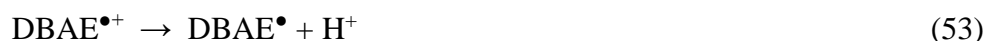
Direct oxidation of TPrA strongly depends on electrode material. On GC electrode, direct oxidation is evident while on Au and Pt electrodes, the formation of surface oxides can block it significantly.⁵² Therefore, the enhancement of the TPrA oxidation might lead to an increase in the ECL intensity. The electrode hydrophobicity has also effect on direct TPrA oxidation and ECL intensity. It was found that addition of some non-ionic surfactants such as Triton X-100 can significantly increase ECL intensity on Pt and Au electrodes.⁵⁷⁻⁶⁰ The mechanism of the surfactant effect appears to involve the adsorption of surfactant on the electrode surface,

which can make the electrode surface more hydrophobic and thus facilitates the direct oxidation of TPrA.

The ECL intensity of the first and second waves was found to be proportional to the concentration of both $\text{Ru}(\text{bpy})_3^{2+}$ and TPrA in a very large dynamic range^{5,34,52-54} with detection limits of 0.5 pM for $\text{Ru}(\text{bpy})_3^{2+}$ ⁶¹ and 10 nM TPrA^{62,63} being reported. Such performances allow to this system to find numerous analytical applications.

1.5.1.4. 2-(dibutylamino)ethanol / $\text{Ru}(\text{bpy})_3^{2+}$ System

As the $\text{Ru}(\text{bpy})_3^{2+}$ / TPrA system gives strong ECL response, most of the applications and commercial systems are base on it. Recently, a new co-reactant, 2-(dibutylamino)ethanol (DBAE), has been reported.⁶⁴ The ECL intensity of the $\text{Ru}(\text{bpy})_3^{2+}$ /DBAE system at Au and Pt electrode was found to be almost 10 and 100 times greater than with $\text{Ru}(\text{bpy})_3^{2+}$ / TPrA system, respectively. The very strong ECL efficiency was attributed to the catalytic effect of hydroxyethyl group toward the direct oxidation of DBAE at the electrode. Since DBAE is an aliphatic tertiary amine structurally similar to TPrA, it has been proposed to follow mechanisms analogous to TPrA with the formation of radical cation $\text{DBAE}^{\bullet+}$ and the reducing intermediate DBAE^\bullet by deprotonation.⁶⁵



DBAE is less toxic, more soluble and less volatile than TPrA and it could be promising co-reactant for ECL immunoassays and DNA probe assays.⁶⁶ The mechanism of $\text{Ru}(\text{bpy})_3^{2+}$ /DBAE system will be discussed in details in Chapter 2.³⁷

1.5.2. ECL Luminophores

In general, the luminophores that are used in ECL systems can be classified into three categories: 1) inorganic systems, which mainly contain organometallic complexes; 2) organic systems, which include polycyclic aromatic hydrocarbons (PAHs); and 3) semiconductor nanoparticle systems.

As discussed in paragraph 1.4.2., $\text{Ru}(\text{bpy})_3^{2+}$ is the first inorganic complex that shows ECL. Because of its excellent chemical, electrochemical and photochemical properties, it is still the most used ECL luminophore. $\text{Ru}(\text{bpy})_3^{2+}$ is soluble in a variety of aqueous and non-aqueous solvents at room temperature. It has ability to undergo reversible one electron-transfer reactions at mid potentials.²

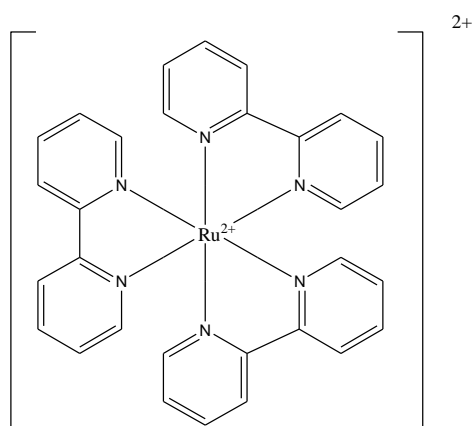


Figure 4. Structure formula of $\text{Ru}(\text{bpy})_3^{2+}$

To improve the light emission and the electron transfer performances, a lot of efforts were made to design or modify the ligands of the complex.⁶⁷ As the work of this thesis is not focused on finding and improving the ECL luminophore efficiency, the different examples will not be discussed in details, but some basics in the field are presented.

$\text{Ru}(\text{bpy})_3^{2+}$ is a yellow-orange coloured complex ($\lambda_{\text{abs}} = 454 \text{ nm}$, $\lambda_{\text{em}} = 607 \text{ nm}$).⁵⁷ Ru^{2+} is a d^6 system with electron configuration $[\text{Kr}] 4d^6$. In $\text{Ru}(\text{bpy})_3^{2+}$, it is surrounded with three bidentate polypyridine ligands that are usually colorless molecules possessing σ -donor orbitals localised on the nitrogen atoms and π -donor and π^* -acceptor orbitals more or less delocalised on aromatic rings.⁵⁸ Figure 5 shows a simplified representation of the electronic situation for a d^6 complex (such as $\text{Ru}(\text{II})$) in an octahedral microsymmetry (D_3).

One electron excitation from a π_M metal orbital to the π^*_L ligand orbitals gives rise to metal-to-ligand charge transfer (MLCT) excited states, whereas promotion of an electron from π_M to σ_M orbitals gives rise to metal centered (MC) excited states. Ligand centered (LC) excited states are obtained by promoting an electron from π_L to π^*_L .^{58, 59}

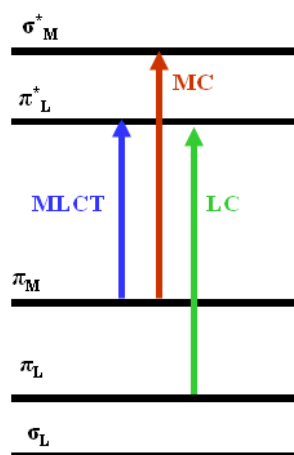


Figure 5. Simplified molecular orbital diagram for $\text{Ru}(\text{LL})^{2+}$ complexes in octahedral symmetry showing the three types of electronic transitions occurring at low energies.

The MC excited states of d^6 octahedral complexes are strongly displaced with respect to the ground state geometry along metal-ligand vibration coordinates. When the lowest excited state is MC, it undergoes fast radiationless deactivation to the ground state and/or ligand dissociation reactions. As a consequence, at room temperature, the excited state lifetime is very short and no luminescence emission is observed.⁵⁸ LC and MLCT excited states are usually not strongly displaced compared to the ground state geometry. Thus, when the lowest excited state is LC or MLCT, it does not undergo fast radiationless decay to the ground state and luminescence can usually be observed, except at high temperature when thermally activated radiationless deactivation via upper lying MC excited states can occur. The radiative deactivation rate constant is somewhat higher for $^3\text{MLCT}$ than for ^3LC because of the larger spin-orbit coupling effect (shift in an electron's atomic energy levels due to electromagnetic interaction between the electron's spin and the magnetic field generated by the electron's orbit around the nucleus). For this reason, the ^3LC excited states are longer living at low temperature in rigid matrix and the $^3\text{MLCT}$ excited states are more likely to exhibit luminescence at room temperature in solution where the lifetime of ^3LC and $^3\text{MLCT}$ is

shortened by activated surface crossing to short lived MC excited states or by bimolecular quenching processes.⁵⁸

$\text{Ru}(\text{bpy})_3^{2+}$, as the most used luminophore, is involved in a wide range of applications and it is often immobilised on the electrode surface, but it can be applied in the solution also. The ECL detection with TPrA as co-reactant is especially important because it allows efficient ECL not only in aqueous media but also at physiological pH (~ 7.4).^{38, 60-64} By attaching suitable groups to bipyridine moieties, $\text{Ru}(\text{bpy})_3^{2+}$ can be linked to biologically interesting molecules such as antibodies where it serves as a label for analysis. Some examples usually exploited for ECL labelling in clinical diagnostic assays are presented on Figure 6.

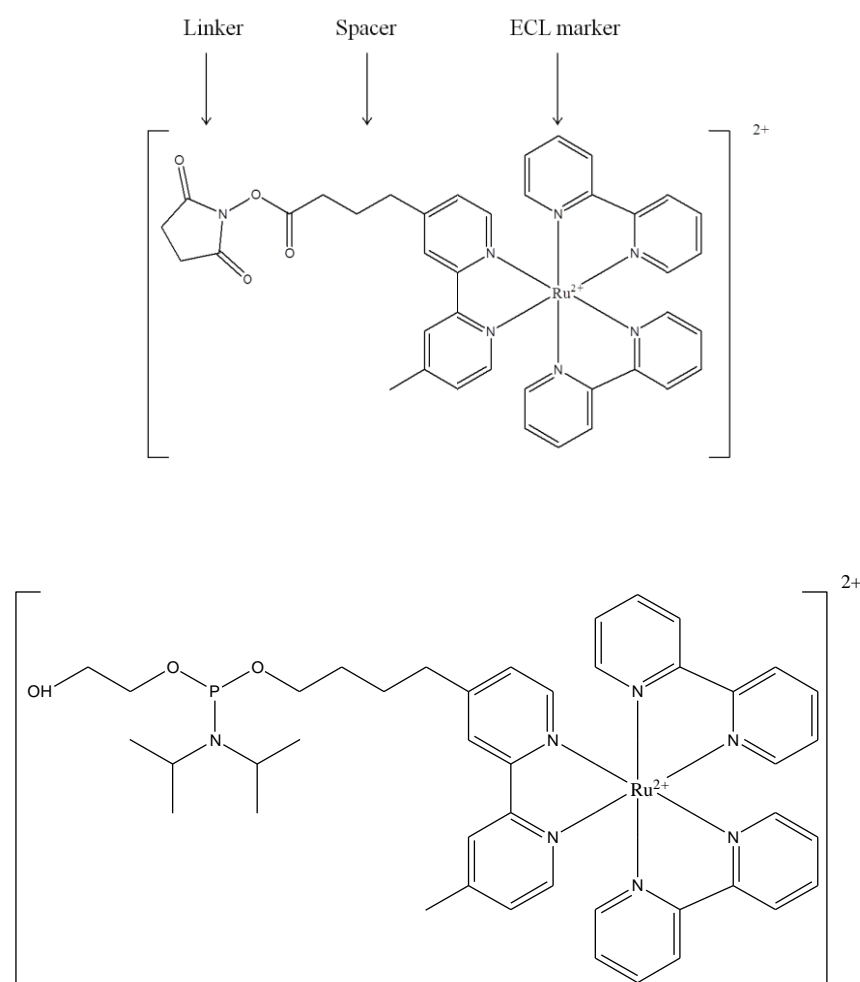


Figure 6. (Top) $\text{Ru}(\text{bpy})_3^{2+}$ - NHS ester for ECL labelling of biological molecules, (bottom) $\text{Ru}(\text{bpy})_3^{2+}$ - phosphoramidate linker for ECL for DNA and RNA.⁹

This ECL complex can directly detect different co-reactants such as amines, oxalate, pyruvate, peroxydisulfate, etc. but also for indirect detection of analytes that do not have co-reactant properties.^{1,2,65} Some analytes are detected after enzymatic reaction which involves transformation of NAD^+ to NADH acting also as a co-reactant.⁶⁶⁻⁶⁹ $\text{Ru}(\text{bpy})_3^{2+}$ -based ECL systems find good applications in flow systems such as high performance liquid chromatography (HPLC)⁷⁰, capillary electrophoresis (CE)^{14, 15, 17} and flow injection analysis (FIA).⁷¹

Even if the majority of ECL applications are based on $\text{Ru}(\text{bpy})_3^{2+}$ or its derivatives like a luminophore, other complexes can act as efficient ECL luminophores. Many metal complexes and clusters have electrochemical and spectroscopic qualities required for an ECL emitter. The ECL of complex or clusters containing Ag, Al, Au, Cd, Cr, Cu, Eu, Hg, Ir, Mo, W, Os, Pd, Pt, Re, Ru, Si, Tb, and Tl have been reported.²

The first reported osmium complex used in ECL was $\text{Os}(\text{phen})_3^{2+}$. The ECL was obtained in DMF with $\text{S}_2\text{O}_8^{2-}$ as co-reactant.⁶⁸ The development of osmium based systems would be advantageous because osmium systems are more photostable and usually oxidise at less anodic potentials than analogous ruthenium systems. However, the ECL application of osmium systems has been limited because of shorter excited state lifetimes and weaker emission efficiencies.⁶⁹

Complexes of iridium are also able to emit ECL. Depending on the structure, some of them are extremely efficient such as $(\text{pq})_2\text{Ir}(\text{acac})/\text{TPrA}$ (pq: 2-phenylquinoline, acac: acetylacetonate) which shows 77 times higher ECL efficiencies with TPrA as co-reactant than $\text{Ru}(\text{bpy})_3^{2+}$ under the same conditions.⁷⁰ But, ECL of $\text{Ir}(\text{ppy})_3$ that was reported using TPrA as co-reactant shows weaker ECL emission than of $\text{Ru}(\text{bpy})_3^{2+}$ under similar conditions. However, $\text{Ir}(\text{ppy})_3$ has green emission and its maximum compare to emission maximum of red/orange $\text{Ru}(\text{bpy})_3^{2+}$ is far enough so that it is possible to distinguish both signals in the single ECL experiment.⁷¹ Considerable attention has been focused on controlling the emission color, with the prospect of simultaneously detecting multiple, spectrally distinct electrochemiluminophores for multi-analyte quantification or internal standardization.⁷²⁻⁷⁶ Moreover, an important issue remains synthesis of water soluble Ir complexes with high yield.

Since ECL of silicon nanoparticles (NPs) was reported in 2002, miscellaneous nanomaterials with various sizes and shapes have been employed as ECL nanoemitters for bioanalysis. It was found that semiconductor NPs, (also known as quantum dots and

abbreviated QDs) can be involved in ECL reaction following both annihilation and co-reactant ECL pathways.^{77,78} Semiconductor nanoparticles have excellent luminescent properties including high quantum yields, stability against photobleaching and size-controlled luminescence properties. Additionally, the biocompatibility and low cost make them an attractive material for these applications.⁶ The ECL study of NPs was first reported for Si nanoparticles. Later, it was found that many semiconducting particle, such as CdS, CdSE and CdTe, can also produce ECL that can be electrochemically excitable in both nonaqueous⁷⁹ and aqueous media⁸⁰. A common feature of ECL behavior obtained from NPs is their red-shifted ECL maxima compare to their photoluminescence, suggesting that the emitting states are different.¹ This was explained by the fact that photoluminescence response appears from electron transfer mainly from the interior of particles while the ECL occurs at the surface where the surface chemistry has greater influence. ECL of water soluble CdTe NPs has been recently reported where it was shown that the size of NPs has an influence on the ECL behaviour.⁸¹ As finding new luminophores with a high ECL efficiency for bioanalysis is the constant driving force of this area, the family of nanoemitters for ECL has been enlarged from exclusively QDs to other miscellaneous nanomaterials in recent years, with various compositions, sizes and shapes, including metallic nanoclusters,⁸² carbon nanodots,⁸³ metallic oxide semiconductors,⁸⁴ and even organic nanoaggregates.^{85,86}

1.6. ECL applications

Because of very high sensitivity, good selectivity, insensitivity to matrix effects and high dynamic range ECL is a robust detection methodology.⁸⁷ It is widely used in clinical diagnostics, environmental assay such as food and water testing and biowarfare agent detection. Due to high ECL efficiency, the majority of ECL detection systems involve the $\text{Ru}(\text{bpy})_3^{2+}$ luminophore or its derivatives and TPrA or other related amines as co-reactant.⁸⁸

The analytical application is based on the fact that ECL intensity is proportional to the concentration of the ECL luminophore or of concentration of co-reactant, depending on the case. If ECL experiments are carried out in the presence of high and constant concentration of co-reactant, ECL intensity will linearly depend on the concentration of ECL emitter in a wide dynamic range. Alternatively, if the experiments are running in the presence of constant $\text{Ru}(\text{bpy})_3^{2+}$ concentration, ECL signal will show dependence on the co-reactant concentration.

1.6.1. Applications in assays and commercialised ECL systems

The most common and most important commercial applications of ECL are in diagnostic assays. Immunoassays based on ECL detection have several advantages over other immunoassay techniques. No radioactive isotopes are used, thus reducing the problems of sample storage, handling and disposal. The ECL labels are extremely stable, having shelf-lives in excess of 1 year at room temperature. The detection levels are extremely low at sub-picomole, since each label can emit several photons per measurement cycle, and the linear dynamic range extends over 6 or more orders of magnitude. Also, their small size allows multiple labelling of the same molecule without affecting the immunoreactivity or hybridisation of the probes.

A large number of biomolecules such as proteins, DNAs and peptides have no co-reactant functionalities or they can give very poor ECL signal. Thus, their ECL detections are mainly carried out with solid phase ECL assay formats in which biomolecules linked with ECL labels, usually $\text{Ru}(\text{bpy})_3^{2+}$ or its derivatives, are immobilised on a solid substrate and ECL is generated in the presence of a co-reactant, typically TPrA. A lot of works have been done and a lot of commercial systems have been developed for immunoassay and DNA detection.

Sensitive and selective detection of DNA hybridisation has a great importance in genetic disease screening. An ultrasensitive DNA hybridisation detection method based on ECL using polystyrene microspheres/beads (PSB) as the carrier of the ECL label tris(2,2'-bipyridyl)ruthenium(II) tetrakis (pentafluorophenyl)borate ($\text{Ru}(\text{bpy})_3\text{-}[\text{B}(\text{C}_6\text{F}_5)_4]_2$) has been reported.³⁶ With this approach, the ECL intensity was found to be linearly proportional to the DNA concentration in a range of 1.0 fM to 10 nM under optimised conditions.

The ECL system can also be used for protein detection. For example, anti-C-reactive protein (CRP), an acute-phase protein found in human serum, can be determined by a sandwich-type immunoassay which uses ECL as a readout mechanism. Biotinylated CRP species were attached to the surface of streptavidin-coated magnetic beads (MB) and avidin-coated polystyrene microspheres/beads (PSB) entrapping a large number of ECL labels ($\text{Ru}(\text{bpy})_3\text{-}[\text{B}(\text{C}_6\text{F}_5)_4]_2$) to form anti-CRP \leftrightarrow MB and Ru(II)-PSB/avidin \leftrightarrow anti-CRP to form a sandwich-type binding in the presence of analyte CRP.⁸⁹ The ECL intensity was found to be proportional to the analyte CRP over the range of 0.010-10 $\mu\text{g}/\text{mL}$.

The sandwich format is widely used in immunoassays based on recognition properties and antibody/antigen binding. A bead-based platform that exploits ECL to detect three antigens simultaneously has been reported.¹¹ The surface of the microspheres loaded into the wells of an electrode were modified with capture antibodies. Microspheres with different antibodies were encoded with different concentration of Eu^{3+} to enable surface mapping. The bead-based assays were performed by incubating the array first in a sample containing antigen and then in a solution of biotinylated detection antibody that was finally attached to streptavidin-modified $\text{Ru}(\text{bpy})_3^{2+}$ as an ECL label. The ECL response of the beads on the platform was recorded by a CCD camera.

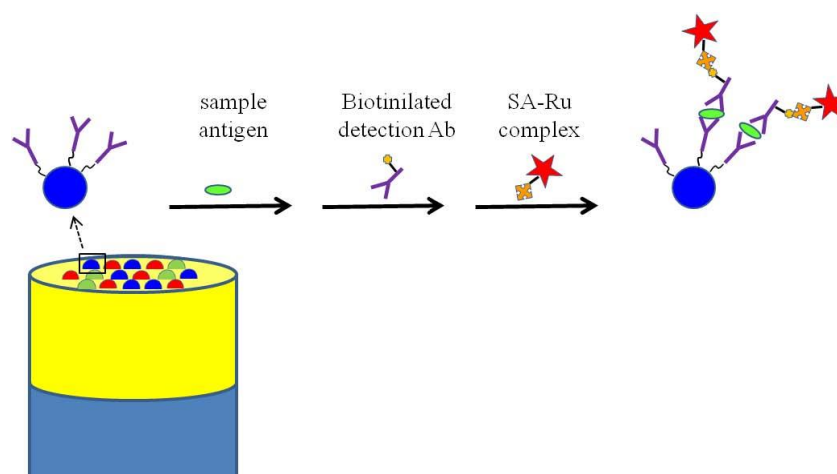


Figure 7. Scheme of a multiplexed bead-based immunoassay on a fiber optic bundle platform¹¹

The ECL imaging can be even developed for single cell analysis. Recently, it has been reported the development of a new transparent electrochemical cell for imaging suitable for single cell analysis.⁹⁰

ECL detection is also widely used in commercialized systems. ECL instrumentation has been commercially available since 1994 and has been rapidly adopted for clinical, industrial and research detection.⁸⁷ The Origen-1 Analyser (IGEN International Inc.)⁸⁷ was the first ECL analyser and has been described by Carter and Bard.⁹¹ Analysers are made for clinical immunoassay testing for small- to medium and for medium- to large-volume laboratories depending on the type.⁹ Completely automated instruments by Roche Diagnostics company, the ELECSYS 10100 and ELECSYS 20100, offer over 150 inexpensive immunoassay tests in

the area of cardiology, thyroid function, oncology, anaemia, fertility, infection diseases and osteoporosis. About 1 billion tests run per year are sold.



Figure 8. Elecsys 2010 system commercialized by Roche Inc.⁹

The ORIGIN Analyser is adapted to measure ECL labels present on the surface of magnetically responsive beads. The principle of operation is as follows. Small magnetic beads are supplied as coated with streptavidin to which biotin molecules are attached, which in turn are bound to a selected antibody or antigen specific for the analyte. The beads are combined with the analyte which binds to this immobilised group on the bead. An antibody labelled with a ruthenium bipyridyl complex is then introduced which also binds to the analyte. The assays are designed so that amount of label on the beads is indicative of the amount of analyte in a sample. The system is consist of a flow cell containing reusable platinum electrode for one side and photomultiplier tube for light detection on the other side of the flow cell. The specific binding and ECL labelling of analytes immobilised on the beads surface is carried out offline prior to introduction of analyte in the flow system. Then each individual sample is drowning into the cell and by application of external magnetic field paramagnetic beads are captured on the electrode surface. By this way, the analyte of interest is separated from the matrix which makes this method very convenient as no pre-treatment of sample is needed. On the other side, labels bounded to the beads are immobilized on the electrode surface which extremely increases the sensitivity of the system. Any unbounded label can be washed out from the cell which reduces background emission.

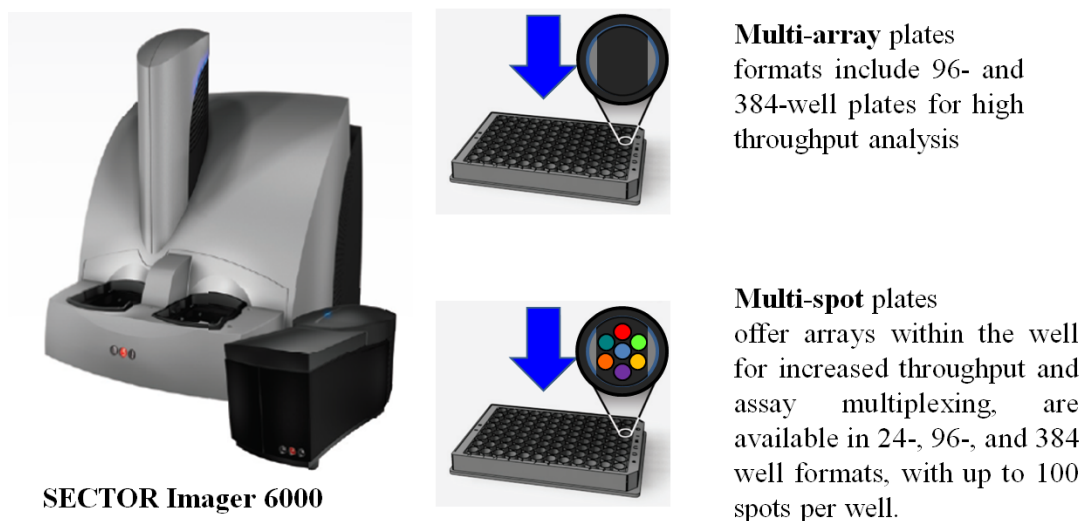


Figure 9. Commercial ECL imager from Meso Scale Discovery. The instrument use ultra-low noise CCD camera and it is suitable for single and multiplexed assay formats.⁸

Another type of commercialised ECL system is provided by Meso Scale Discovery Inc.. ECL measurements in solid phase assays can be carried out on disposable electrodes. The first commercialised ECL instruments based on this concept are offered by Meso Scale Discovery (models Sector HTS Imager and Sector PR).⁸ Assays are carried out on the screen-printed carbon ink electrodes. Multi-Spot plates with patterned microarrays within each plate well are also available which can enable a multiplexed assay.

1.6.2. Application in CE, HPLC and FIA systems

An important feature of ECL detection method is its facility to combine with systems such as capillary electrophoresis (CE), high performance liquid chromatography (HPLC) and flow injection analysis (FIA). The analytes or its derivatives should behave like an ECL co-reactant which often means to have secondary or tertiary amine groups with an α -carbon hydrogen so that efficient ECL can be produced in the presence of $\text{Ru}(\text{bpy})_3^{2+}$.¹ Because tertiary amines can produce sensitive ECL responses a lot of efforts have been made to introduce such a group to initially less or non-ECL sensitive analytes such as amino acids and fatty acids.^{92,93} Amino acids such as proline, valine and leucine can be successfully detected in CE-ECL system with the detection limit in order μM - nM concentration.⁹²

It was found that many compounds are able to quench, inhibit or enhance ECL intensity. For example phenols, ferrocene, anilines and their derivatives can significantly quench the oxidative-reduction ECL by energy or electron transfer between $\text{Ru}(\text{bpy})_3^{2+}$ and the electro-

oxidised species of the quencher.⁹⁴⁻⁹⁶ This strategy has been used in FIA-ECL for tetracycline in Chinese proprietary medicine and noradrenalin and dopamine in commercial pharmaceutical injection samples.⁹⁷

Thermodynamic and kinetic studies can also be realised using CE-ECL system. For example, drug-human serum albumin binding of paracetamol on prolidase activity in erythrocytes and in serum of diabetic patients have been reported.⁹⁸⁻¹⁰⁰ A number of advantages are offered by CE-ECL with respect to other commonly used separation –detection methods such as HPLC using UV-vis or fluorescent detection for this kind of study and include very powerful resolving ability, good selectivity, high sensitivity, easy sample preparation and fast data as generally no sample pre-treatment is needed.^{98,101}

1.7. Conclusion

ECL is a powerful detection method where the analytical signal is the light intensity. The method offers several advantages over other detection methods such as high sensitivity, good selectivity, insensitivity to matrix effects and high dynamic range. As the reaction is initiated and controlled by applying the adequate potential, the method offers the time and position control with a possibility of simultaneous measurements of both experimental parameters, light intensity and Faradaic current. Depending on the reaction mechanism, two ECL pathways may be distinguished: annihilation and co-reactant ECL. Though the first experiments were mainly based on annihilation ECL, the applications were limited by the necessary experimental conditions such as wide potential window and non-aqueous media. The co-reactant ECL is mainly performed in aqueous media often in physiological conditions, thus it is more appropriate for different applications including bio-related systems. Due to its excellent electrochemical and spectroscopic properties, $\text{Ru}(\text{bpy})_3^{2+}$ species and its derivatives are the most used luminophores. It can be used in water or organic solutions or more likely immobilized on the electrode surface. There are several advantages to immobilize luminophores including higher sensitivity due to concentration of emitter centers in the detection region near the electrode surface and less consumption of chemicals, which has a special impact in flow systems. ECL may be coupled with CE, HPLC and FIA for different analysis in the environmental chemistry, for food and water testing and biowarfare agents detection. ECL is also used as a detection method in enzymatic biosensors, in immunoassay and DNA probe analysis where ECL label is attached to the biomolecule. ECL detection is applied in research as well as in commercialized detection systems. Different detection kits provided by Roche Diagnostic and Mesosale Discovery companies offer a large number of fast, reliable and inexpensive assays for clinical diagnostic. ECL applications reported so far indicate the significance of ECL as a general detection method. For this reason, many efforts are made to decipher the ECL phenomena operating in the bead-based assays and to improve and develop new ECL-based detection systems. This is the aim of the work presented in the following chapters.

References

- 1 Miao, W. Electrogenerated Chemiluminescence and Its Biorelated Applications. *Chem. Rev.* **108**, 2506 (2008).
- 2 Richter, M. M. Electrochemiluminescence (ECL). *Chem. Rev.* **104**, 3003 (2004).
- 3 Hu, L. & Xu, G. Applications and trends in electrochemiluminescence. *Chem. Soc. Rev.* **39**, 3275 (2010).
- 4 Bard, A. *Electrogenerated Chemiluminescence*. (Maceler Dekker Inc, New York, 2004).
- 5 Leland, J. K. & Powell, M. J. Electrogenerated Chemiluminescence: An Oxidative-Reduction Type ECL Reaction Sequence Using Tripropyl Amine. *J. Electrochem. Soc.* **137**, 3127 (1990).
- 6 Bertoncello, P. & Forster, R. J. Nanostructured materials for electrochemiluminescence (ECL)-based detection methods: Recent advances and future perspectives. *Biosens. Bioelectron.* **24**, 3191 (2009).
- 7 Martin, A. F. & Nieman, T. A. Glucose quantitation using an immobilized glucose dehydrogenase enzyme reactor and a tris(2,2'-bipyridyl) ruthenium(II) chemiluminescent sensor. *Anal. Chim. Acta* **281**, 475-481 (1993).
- 8 www.mesoscale.com.
- 9 www.roche.com.
- 10 Dennany, L., Forster, R. J. & Rusling, J. F. Simultaneous Direct Electrochemiluminescence and Catalytic Voltammetry Detection of DNA in Ultrathin Films. *J. Am. Chem. Soc.* **125**, 5213 (2003).
- 11 Deiss, F. d. r. *et al.* Multiplexed Sandwich Immunoassays Using Electrochemiluminescence Imaging Resolved at the Single Bead Level. *J. Am. Chem. Soc.* **131**, 6088 (2009).
- 12 Shan, Y., Xu, J.-J. & Chen, H.-Y. Distance-dependent quenching and enhancing of electrochemiluminescence from a CdS:Mn nanocrystal film by Au nanoparticles for highly sensitive detection of DNA. *Chem. Commun.*, 905 (2009).
- 13 Shan, Y., Xu, J.-J. & Chen, H.-Y. Electrochemiluminescence quenching by CdTe quantum dots through energy scavenging for ultrasensitive detection of antigen. *Chem. Commun.* **46**, 5079 (2010).
- 14 Zamolo, V. A. *et al.* Highly Sensitive Electrochemiluminescent Nanobiosensor for the Detection of Palytoxin. *ACS Nano* **6**, 7989-7997 (2012).
- 15 Sun, Y., Zhang, Z. & Xi, Z. Direct electrogenerated chemiluminescence detection in high-performance liquid chromatography for determination of ofloxacin. *Anal. Chim. Acta* **623**, 96 (2008).
- 16 Wang, J., Yang, Z., Wang, X. & Yang, N. Capillary electrophoresis with gold nanoparticles enhanced electrochemiluminescence for the detection of roxithromycin. *Talanta* **76**, 85 (2008).
- 17 Li, J., Xu, Y., Wei, H., Huo, T. & Wang, E. Electrochemiluminescence Sensor Based on Partial Sulfonation of Polystyrene with Carbon Nanotubes. *Anal. Chem.* **79**, 5439 (2007).
- 18 Chi, Y., Dong, Y. & Chen, G. Investigation on the electrochemiluminescent behaviors of oxypurinol in alkaline solution using a flow injection analytical system. *Electrochem. Commun.* **9**, 577 (2007).
- 19 Yin, X.-B., Kang, J., Fang, L., Yang, X. & Wang, E. Short-capillary electrophoresis with electrochemiluminescence detection using porous etched joint for fast analysis of lidocaine and ofloxacin. *J. Chromatogr. A* **1055**, 223 (2004).

- 20 Liu, Z., Qi, W. & Xu, G. Recent advances in electrochemiluminescence. *Chem. Soc. Rev.* **44**, 3117-3142 (2015).
- 21 Harvey, N. Luminescence during Electrolysis. *J. Phys. Chem.* **33**, 1456 (1929).
- 22 Dufford, R. T., Nightingale, D. & Gaddum, L. W. Luminescence of grignard compounds in electric and magnetic fields, and related electrical phenomena. *J. Am. Chem. Soc.* **49**, 1858 (1927).
- 23 Visco, R. E. & Chandross, E. A. Electroluminescence in Solutions of Aromatic Hydrocarbons. *J. Am. Chem. Soc.* **86**, 5350 (1964).
- 24 Santhanam, K. S. V. & Bard, A. J. Chemiluminescence of Electrogenerated 9,10-Diphenylanthracene Anion Radical. *J. Am. Chem. Soc.* **87**, 139 (1965).
- 25 Zweig, A., Maricle, D. L., Brinen, J. S. & Maurer, A. H. Electrochemical Generation of the Phenanthrene Triplet. *J. Am. Chem. Soc.* **89**, 473-474 (1967).
- 26 Silverstein, T. P. Marcus Theory: Thermodynamics CAN Control the Kinetics of Electron Transfer Reactions. *J. Chem. Edu.* **89**, 1159-1167 (2012).
- 27 Tokel, N. E. & Bard, A. J. Electrogenerated chemiluminescence. IX. Electrochemistry and emission from systems containing tris(2,2'-bipyridine)ruthenium(II) dichloride. *J. Am. Chem. Soc.* **94**, 2862 (1972).
- 28 Chang, M.-M., Saji, T. & Bard, A. J. Electrogenerated chemiluminescence. 30. Electrochemical oxidation of oxalate ion in the presence of luminescers in acetonitrile solutions. *J. Am. Chem. Soc.* **99**, 5399 (1977).
- 29 Noffsinger, J. B. & Danielson, N. D. Generation of chemiluminescence upon reaction of aliphatic amines with tris(2,2'-bipyridine)ruthenium(III). *Anal. Chem.* **59**, 865 (1987).
- 30 Montalti, M., Credi, A., Prodi, L. & Gandolfi, T. *Handbook of Photochemistry, Third Edition.* (Taylor & Francis, 2006).
- 31 Innocenzi, P., Kozuka, H. & Yoko, T. Fluorescence Properties of the Ru(bpy)₃²⁺ Complex Incorporated in SolGel-Derived Silica Coating Films. *J. Phys. Chem. B* **101**, 2285 (1997).
- 32 Roda, A. Chemiluminescence and bioluminescence: past, present and future. *Anal Bioanal Chem* **401**, 1457-1458 (2011).
- 33 Haapakka, K. E. & Kankare, J. J. The mechanism of the electrogenerated chemiluminescence of luminol in aqueous alkaline solution. *Anal. Chim. Acta* **138**, 263-275 (1982).
- 34 Miao, W., Choi, J.-P. & Bard, A. J. Electrogenerated Chemiluminescence 69: The Tris(2,2'-bipyridine)ruthenium(II), (Ru(bpy)₃²⁺)/Tri-n-propylamine (TPrA) System Revisited A New Route Involving TPrA⁺ Cation Radicals. *J. Am. Chem. Soc.* **124**, 14478 (2002).
- 35 Zanarini, S. *et al.* Ru(bpy)₃ Covalently Doped Silica Nanoparticles as Multicenter Tunable Structures for Electrochemiluminescence Amplification. *J. Am. Chem. Soc.* **131**, 2260 (2009).
- 36 Miao, W. & Bard, A. J. Electrogenerated Chemiluminescence. 77. DNA Hybridization Detection at High Amplification with [Ru(bpy)₃]²⁺-Containing Microspheres. *Anal. Chem.* **76**, 5379 (2004).
- 37 Sentic, M. *et al.* Mapping electrogenerated chemiluminescence reactivity in space: mechanistic insight into model systems used in immunoassays. *Chem. Sci.* **5**, 2568-2572 (2014).
- 38 Miao, W. & Cynthia, G. Z. in *Handbook of Electrochemistry* (Elsevier, 2007).
- 39 Beideman, F. E. & Hercules, D. M. Electrogenerated chemiluminescence from 9,10-diphenylanthracene cations reacting with radical anions. *J. Phys. Chem. A* **83**, 2203 (1979).

- 40 Faulkner, L. R., Tachikawa, H. & Bard, A. J. Electrogenerated chemiluminescence. VII. Influence of an external magnetic field on luminescence intensity. *J. Am. Chem. Soc.* **94**, 691 (1972).
- 41 Faulkner, L. R. & Bard, A. J. Electrogenerated chemiluminescence. IV. Magnetic field effects on the electrogenerated chemiluminescence of some anthracenes. *J. Am. Chem. Soc.* **91**, 209 (1969).
- 42 Ritchie, E. L., Pastore, P. & Wightman, R. M. Free Energy Control of Reaction Pathways in Electrogenerated Chemiluminescence. *J. Am. Chem. Soc.* **119**, 11920 (1997).
- 43 Tachikawa, H. & Bard, A. J. Electrogenerated chemluminescence. Effect of solvent and magnetic field on ECL of rubrene systems. *Chem. Phys. Lett.* **26**, 246 (1974).
- 44 Yin, X.-B., Dong, S. & Wang, E. Analytical applications of the electrochemiluminescence of tris (2,2'-bipyridyl) ruthenium and its derivatives. *TrAC-Trends Anal. Chem.* **23**, 432-441 (2004).
- 45 Choi, J.-P. & Miao, W. in *Electrogenerated Chemiluminescence* 213-271 (CRC Press, 2004).
- 46 Rubinstein, I. & Bard, A. J. Polymer films on electrodes. 5. Electrochemistry and chemiluminescence at Nafion-coated electrodes. *J. Am. Chem. Soc.* **103**, 5007 (1981).
- 47 Kanoufi, F. d. r., Cannes, C. I., Zu, Y. & Bard, A. J. Scanning Electrochemical Microscopy. 43. Investigation of Oxalate Oxidation and Electrogenerated Chemiluminescence across the LiquidLiquid Interface. *J. Phys. Chem. B* **105**, 8951 (2001).
- 48 Rubinstein, I. & Bard, A. J. Electrogenerated chemiluminescence. 37. Aqueous ecl systems based on tris(2,2'-bipyridine)ruthenium(2+) and oxalate or organic acids. *J. Am. Chem. Soc.* **103**, 512 (1981).
- 49 Rubinstein, I., Martin, C. R. & Bard, A. J. Electrogenerated chemiluminescent determination of oxalate. *Anal. Chem.* **55**, 1580 (1983).
- 50 Kanoufi, F. d. r. & Bard, A. J. Electrogenerated Chemiluminescence. 65. An Investigation of the Oxidation of Oxalate by Tris(polypyridine) Ruthenium Complexes and the Effect of the Electrochemical Steps on the Emission Intensity. *J. Phys. Chem. B* **103**, 10469 (1999).
- 51 White, H. S. & Bard, A. J. Electrogenerated chemiluminescence. 41. Electrogenerated chemiluminescence and chemiluminescence of the Ru(bpy)₃²⁺-S₂O₈²⁻ system in acetonitrile-water solutions. *J. Am. Chem. Soc.* **104**, 6891 (1982).
- 52 Zu, Y. & Bard, A. J. Electrogenerated Chemiluminescence. 66. The Role of Direct Coreactant Oxidation in the Ruthenium Tris(2,2')bipyridyl/Tripropylamine System and the Effect of Halide Ions on the Emission Intensity. *Anal. Chem.* **72**, 3223 (2000).
- 53 Gross, E. M., Pastore, P. & Wightman, R. M. High-Frequency Electrochemiluminescent Investigation of the Reaction Pathway between Tris(2,2'-bipyridyl)ruthenium(II) and Tripropylamine Using Carbon Fiber Microelectrodes. *J. Phys. Chem. B* **105**, 8732 (2001).
- 54 Kanoufi, F. d. r., Zu, Y. & Bard, A. J. Homogeneous Oxidation of Trialkylamines by Metal Complexes and Its Impact on Electrogenerated Chemiluminescence in the Trialkylamine/Ru(bpy)₃²⁺ System. *J. Phys. Chem. B* **105**, 210 (2000).
- 55 Collinson, M. M., Taussig, J. & Martin, S. A. Solid-State Electrogenerated Chemiluminescence from Gel-Entrapped Ruthenium(II) Tris(bipyridine) and Tripropylamine. *Chem. Mater.* **11**, 2594 (1999).
- 56 Smith, P. J. M., C. K. Electrochemical dealkylation of aliphatic amines. *J. Org. Chem.* **34**, 1821-1826 (1969).

- 57 Factor, B. *et al.* Surfactant Chain Length Effects on the Light Emission of Tris(2,2'-bipyridyl)ruthenium(II)/Tripropylamine Electrogenerated Chemiluminescence. *Anal. Chem.* **73**, 4621 (2001).
- 58 Bruce, D., McCall, J. & Richter, M. M. Effects of electron withdrawing and donating groups on the efficiency of tris(2,2[prime or minute]-bipyridyl)ruthenium(ii)/tri-n-propylamine electrochemiluminescence. *Analyst* **127**, 125 (2002).
- 59 Zu, Y. & Bard, A. J. Electrogenerated Chemiluminescence. 67. Dependence of Light Emission of the Tris(2,2')bipyridylruthenium(II)/Tripropylamine System on Electrode Surface Hydrophobicity. *Anal. Chem.* **73**, 3960 (2001).
- 60 Workman, S. & Richter, M. M. The Effects of Nonionic Surfactants on the Tris(2,2'-bipyridyl)ruthenium(II) Tripropylamine Electrochemiluminescence System. *Anal. Chem.* **72**, 5556 (2000).
- 61 Arora, A., J. de Mello, A. & Manz, A. Sub-microliter Electrochemiluminescence Detector-A Model for Small Volume Analysis Systems. *Anal. Commun.* **34**, 393 (1997).
- 62 Milutinovic, M. *et al.* Photopatterning of ultrathin electrochemiluminescent redox hydrogel films. *Chem. Commun.* **47**, 9125 (2011).
- 63 Downey, T. M. & Nieman, T. A. Chemiluminescence detection using regenerable tris(2,2'-bipyridyl)ruthenium(II) immobilized in Nafion. *Anal. Chem.* **64**, 261 (1992).
- 64 Liu, X., Shi, L., Niu, W., Li, H. & Xu, G. Environmentally Friendly and Highly Sensitive Ruthenium(II) Tris(2,2'-bipyridyl) Electrochemiluminescent System Using 2-(Dibutylamino)ethanol as Co-Reactant. *Angew. Chem. Int. Edit.* **46**, 421 (2007).
- 65 Xue, L., Guo, L., Qiu, B., Lin, Z. & Chen, G. Mechanism for inhibition of /DBAE electrochemiluminescence system by dopamine. *Electrochem. Comm.* **11**, 1579-1582 (2009).
- 66 Hu, T., Liu, X., Liu, S., Wang, Z. & Tang, Z. Toward Understanding of Transfer Mechanism between Electrochemiluminescent Dyes and Luminescent Quantum Dots. *Anal. Chem.* **86**, 3939-3946 (2014).
- 67 Stagni, S. *et al.* A New Family of Ruthenium(II) Polypyridine Complexes Bearing 5-Aryltetrazolate Ligands as Systems for Electrochemiluminescent Devices. *Inorg. Chem.* **45**, 695 (2005).
- 68 Bolletta, F., Rossi, A. & Balzani, V. Chemiluminescence on oxidation of tris(2,2'-bipyridine)chromium(II): Chemical generation of a metal centered excited state. *Inorg. Chim. Acta* **53**, L23 (1981).
- 69 Creutz, C., Chou, M., Netzel, T. L., Okumura, M. & Sutin, N. Lifetimes, spectra, and quenching of the excited states of polypyridine complexes of iron(II), ruthenium(II), and osmium(II). *J. Am. Chem. Soc.* **102**, 1309 (1980).
- 70 Shin, I.-S. *et al.* Efficient Electrogenerated Chemiluminescence from Bis-Cyclometalated Iridium(III) Complexes with Substituted 2-Phenylquinoline Ligands. *J. Phys. Chem. C* **111**, 2280 (2007).
- 71 Bruce, D. & Richter, M. M. Green Electrochemiluminescence from Ortho-Metalated Tris(2-phenylpyridine)iridium(III). *Anal. Chem.* **74**, 1340 (2002).
- 72 Doeven, E. H. *et al.* Selective Excitation of Concomitant Electrochemiluminophores: Tuning Emission Color by Electrode Potential. *Angew. Chem. Int. Ed.* **51**, 4354-4357 (2012).
- 73 Zanarini, S. *et al.* Green and Blue Electrochemically Generated Chemiluminescence from Click Chemistry—Customizable Iridium Complexes. *Chem. Eu. J. A* **17**, 4640-4647 (2011).
- 74 Bonacchi, S. *et al.* Luminescent Silica Nanoparticles: Extending the Frontiers of Brightness. *Angew. Chem. Int. Ed.* **50**, 4056-4066 (2011).

- 75 Doeven, E. H. *et al.* A potential-controlled switch on/off mechanism for selective excitation in mixed electrochemiluminescent systems. *Chem. Sci.* **4**, 977-982 (2013).
- 76 Swanick, K. N., Ladouceur, S., Zysman-Colman, E. & Ding, Z. Self-Enhanced Electrochemiluminescence of an Iridium(III) Complex: Mechanistic Insight. *Angew. Chem. Int. Ed.* **51**, 11079-11082 (2012).
- 77 Wu, P., Hou, X., Xu, J.-J. & Chen, H.-Y. Electrochemically Generated versus Photoexcited Luminescence from Semiconductor Nanomaterials: Bridging the Valley between Two Worlds. *Chem. Rev.* (2014).
- 78 Deng, S. & Ju, H. Electrogenerated chemiluminescence of nanomaterials for bioanalysis. *Analyst* **138**, 43-61 (2013).
- 79 Myung, N., Ding, Z. & Bard, A. J. Electrogenerated Chemiluminescence of CdSe Nanocrystals. *Nano Letters* **2**, 1315 (2002).
- 80 Yoonjung, B. & et al. Electrochemistry and electrogenerated chemiluminescence of films of silicon nanoparticles in aqueous solution. *Nanotechnology* **17**, 3791 (2006).
- 81 Liu, X., Jiang, H., Lei, J. & Ju, H. Anodic Electrochemiluminescence of CdTe Quantum Dots and Its Energy Transfer for Detection of Catechol Derivatives. *Anal. Chem.* **79**, 8055 (2007).
- 82 Fang, Y.-M. *et al.* Electrogenerated chemiluminescence from Au nanoclusters. *Chem. Comm.* **47**, 2369-2371 (2011).
- 83 Baker, S. N. & Baker, G. A. Luminescent Carbon Nanodots: Emergent Nanolights. *Angew. Chem. Int. Ed.* **49**, 6726-6744 (2010).
- 84 Liu, X. *et al.* High Electron Transfer Efficiency of Titania Dioxide Nanotube for Low Potential Electrochemiluminescent Biosensing. *Electroanalysis* **23**, 2629-2632 (2011).
- 85 Chang, Y.-L., Palacios, R. E., Fan, F.-R. F., Bard, A. J. & Barbara, P. F. Electrogenerated Chemiluminescence of Single Conjugated Polymer Nanoparticles. *J. Am. Chem. Soc.* **130**, 8906-8907 (2008).
- 86 Omer, K. M. & Bard, A. J. Electrogenerated Chemiluminescence of Aromatic Hydrocarbon Nanoparticles in an Aqueous Solution†. *J. Phys. Chem. C* **113**, 11575-11578 (2009).
- 87 Sigal George, B., Glezer, E., Leland, J., Wohlstadter, J. & Debad, J. in *Electrogenerated Chemiluminescence* 359-396 (CRC Press, 2004).
- 88 Yuan, Y., Han, S., Hu, L., Parveen, S. & Xu, G. Coreactants of tris(2,2'-bipyridyl)ruthenium(II) Electrogenerated Chemiluminescence. *Electrochim. Acta* **82**, 484-492 (2012).
- 89 Miao, W. & Bard, A. J. Electrogenerated Chemiluminescence. 80. C-Reactive Protein Determination at High Amplification with [Ru(bpy)₃]²⁺-Containing Microspheres. *Anal. Chem.* **76**, 7109 (2004).
- 90 Dolci, L. S., Zanarini, S., Ciana, L. D., Paolucci, F. & Roda, A. Development of a New Device for Ultrasensitive Electrochemiluminescence Microscopy Imaging. *Anal. Chem.* **81**, 6234 (2009).
- 91 Carter, M. T. & Bard, A. J. Electrochemical investigations of the interaction of metal chelates with DNA. 3. Electrogenerated chemiluminescent investigation of the interaction of tris(1,10-phenanthroline)ruthenium(II) with DNA. *Bioconjugate Chem.* **1**, 257-263 (1990).
- 92 Li, J., Yan, Q., Gao, Y. & Ju, H. Electrogenerated Chemiluminescence Detection of Amino Acids Based on Precolumn Derivatization Coupled with Capillary Electrophoresis Separation. *Anal. Chem.* **78**, 2694 (2006).
- 93 Morita, H. & Konishi, M. Electrogenerated Chemiluminescence Derivatization Reagent, 3-Isobutyl-9,10-dimethoxy-1,3,4,6,7,11b-hexahydro-2H-pyrido[2,1-a]isoquinolin-2-ylamine, for Carboxylic Acid in High-Performance Liquid

- Chromatography Using Tris(2,2'-bipyridine)ruthenium(II). *Anal. Chem.* **75**, 940 (2003).
- 94 Cui, H., Li, F., Shi, M.-J., Pang, Y.-Q. & Lin, X.-Q. Inhibition of Ru Complex Electrochemiluminescence by Phenols and Anilines. *Electroanal.* **17**, 589 (2005).
- 95 Cao, W., Ferrance, J. P., Demas, J. & Landers, J. P. Quenching of the Electrochemiluminescence of Tris(2,2'-bipyridine)ruthenium(II) by Ferrocene and Its Potential Application to Quantitative DNA Detection. *J. Am. Chem. Soc.* **128**, 7572 (2006).
- 96 McCall, J., Alexander, C. & Richter, M. M. Quenching of Electrogenerated Chemiluminescence by Phenols, Hydroquinones, Catechols, and Benzoquinones. *Anal. Chem.* **71**, 2523 (1999).
- 97 Li, F., Pang, Y.-Q., Lin, X.-Q. & Cui, H. Determination of noradrenaline and dopamine in pharmaceutical injection samples by inhibition flow injection electrochemiluminescence of ruthenium complexes. *Talanta* **59**, 627 (2003).
- 98 Yuan, J. *et al.* Characterization of Prolidase Activity Using Capillary Electrophoresis with Tris(2,2'-bipyridyl)ruthenium(II) Electrochemiluminescence Detection and Application To Evaluate Collagen Degradation in Diabetes Mellitus. *Anal. Chem.* **78**, 2934 (2006).
- 99 Yuan, J., Wei, H., Jin, W., Yang, X. & Wang, E. Kinetic study of paracetamol on prolidase activity in erythrocytes by capillary electrophoresis with $\text{Ru}(\text{bpy})_3^{2+}$ electrochemiluminescence detection. *Electrophoresis* **27**, 4047 (2006).
- 100 Zhao, X. *et al.* Drug-human serum albumin binding studied by capillary electrophoresis with electrochemiluminescence detection. *Electrophoresis* **25**, 3422 (2004).
- 101 Huang, Y., Pan, W., Guo, M. & Yao, S. Capillary electrophoresis with end-column electrochemiluminescence for the analysis of chloroquine phosphate and the study on its interaction with human serum albumin. *J. Chromatogr. A* **1154**, 373 (2007).

Chapter 2:

Mechanistic Insight into Model Systems Used in Electrogenenerated Chemiluminescence Immunoassays via Mapping the Light Distribution in Space

2.1. Introduction

ECL's main characteristics and advantages are its utility for a large variety of biological and medical applications and diagnostics^{1,2}. ECL technology enables researchers to profile biomarkers such as cytokines and intracellular signaling proteins, which has a direct impact on drug discovery and improving human health³. In the appropriate chemical environment, ECL labels generate light upon electrochemical stimulation. Discovery of co-reactant ECL, which enables detection in aqueous medium, incorporated this reaction into bioassays⁴. The system consist of $\text{Ru}(\text{bpy})_3^{2+}$ complex and tri-n-propylamine (TPrA) as a co-reactant, exhibits the highest ECL efficiency⁵. Also, 2-(dibutylamino)ethanol (DBAE) has been reported as more efficient, less toxic, more soluble and less volatile co-reactant than TPrA⁶. Still, the $\text{Ru}(\text{bpy})_3^{2+}$ /TPrA tandem stays the model ECL pair and it is exploited in commercial devices for diagnostic applications such as immunoassays⁷⁻⁹ and DNA analyses^{7,10-13}. More than 30000 ORIGEN analysers by Roche Diagnostic, based on functionalised magnetic microbeads, are placed worldwide³.

Whereas, there is still a lack of understanding the extremely high sensitivity of the bead-based ECL assays¹⁴⁻¹⁶, the number of instruments and assays using ECL as a readout method clearly indicates the need of deciphering the ECL mechanism. Since the first ECL reaction between $\text{Ru}(\text{bpy})_3^{2+}$ and TPrA has been reported⁵, different competitive mechanistic pathways have been proposed to explain the ECL emission for this model system^{2,17-21}. They can be classified into two main groups depending on how $\text{Ru}(\text{bpy})_3^{2+}$ is oxidized: The first one requires explicitly the direct oxidation of ruthenium centres at the electrode surface to generate *in fine* the ECL emission. However, these mechanistic routes cannot account for the excellent sensitivity of the bead-based immunoassays;^{14,22} A second "revisited" route involving the mediated oxidation of $\text{Ru}(\text{bpy})_3^{2+}$ by the cation radical ($\text{TPrA}^{\bullet+}$) has been proposed by Miao *et al*²³. In this path, only the co-reactant TPrA is oxidized at the electrode and the resulting radicals, $\text{TPrA}^{\bullet+}$ and TPrA^\bullet , play the central role in the ECL process. Besides, DBAE is an environmentally friendly co-reactant which could be expanded to bioassays as it shows better performance than TPrA in ECL operated with $\text{Ru}(\text{bpy})_3^{2+}$ solution (not immobilized as for bead-based assays)²⁴⁻²⁶. Therefore, this work aims at deciphering the ECL phenomena operating in bead-based ECL bioassays.

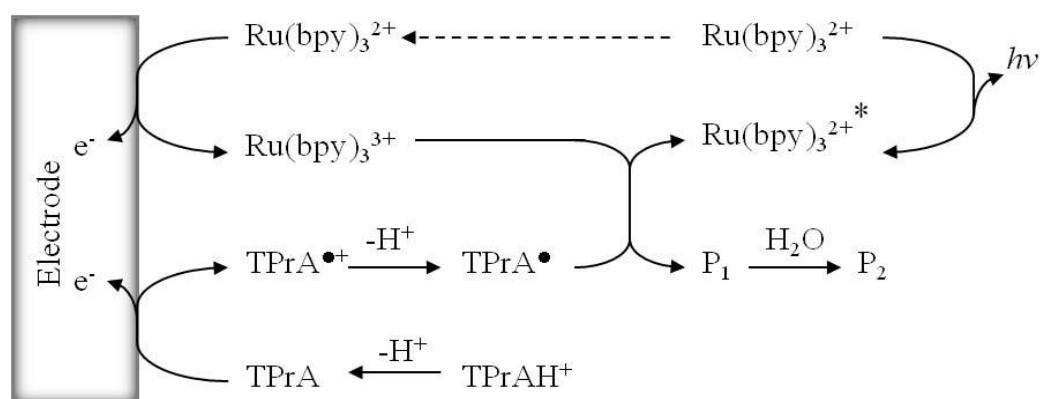
The first part of this chapter deals with already reported studies of reaction mechanism of $\text{Ru}(\text{bpy})_3^{2+}$ /co-reactant system. In the second part, the mechanisms of $\text{Ru}(\text{bpy})_3^{2+}$ co-reactant

systems at the single bead level, with either TPrA or DBAE, will be investigated by imaging the 3D distribution of ECL intensity²⁷.

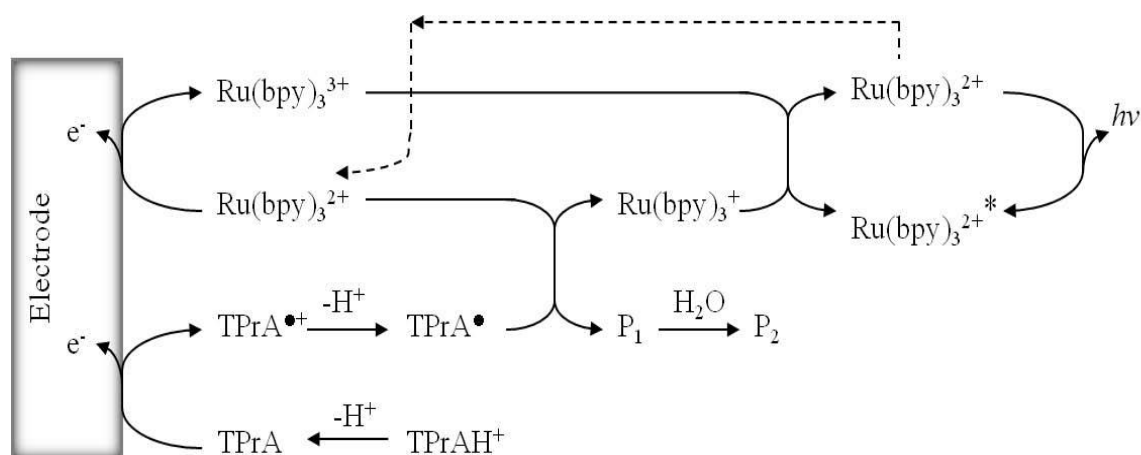
2.2. Reported mechanisms of Ru(bpy)₃²⁺/ TPrA system

The ECL reaction mechanism of dissolved Ru(bpy)₃²⁺ species with TPrA has mainly been investigated by the groups of Leland and of Bard^{5,11,13,18}. According to these studies and other investigations that follow, the mechanistic routes have been established. In order to generate an ECL signal at high efficiency, oxidation of TPrA plays an important role in the ECL mechanism. ECL is produced upon concomitant electrooxidation of Ru(bpy)₃²⁺ and TPrA (Schemes 1 and 2)^{5,19}. Upon oxidation, the short-lived TPrA radical cation (TPrA^{•+}) loses a proton from the α -carbon to form a strong reducing species TPrA[•]^{28,29}. This radical can then reduce Ru(bpy)₃³⁺ to form the excited state Ru(bpy)₃^{2+*} (Scheme 1). Also, the highly reducing agent, TPrA[•] can reduce Ru(bpy)₃²⁺ to Ru(bpy)₃⁺, followed by the annihilation reaction between Ru(bpy)₃³⁺ and Ru(bpy)₃⁺ (Scheme 2)^{5,19}.

Scheme 1:



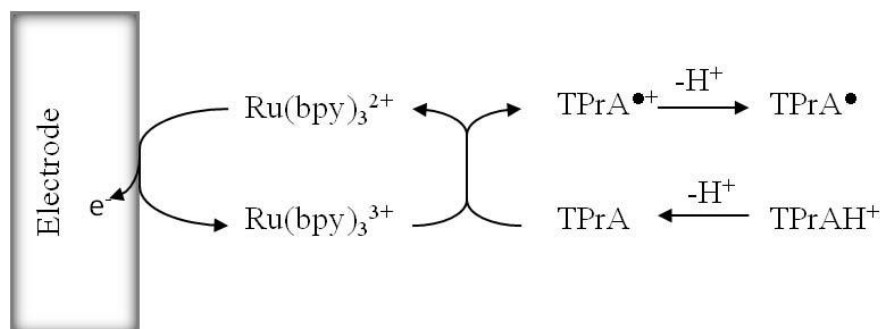
Scheme 2:



The mechanisms were presented in more details in Chapter 1.

It has been reported that TPrA can be oxidized directly at the electrode surface, but also via catalytic homogeneous reaction with $\text{Ru}(\text{bpy})_3^{3+}$ (Scheme 3)^{18,19}:

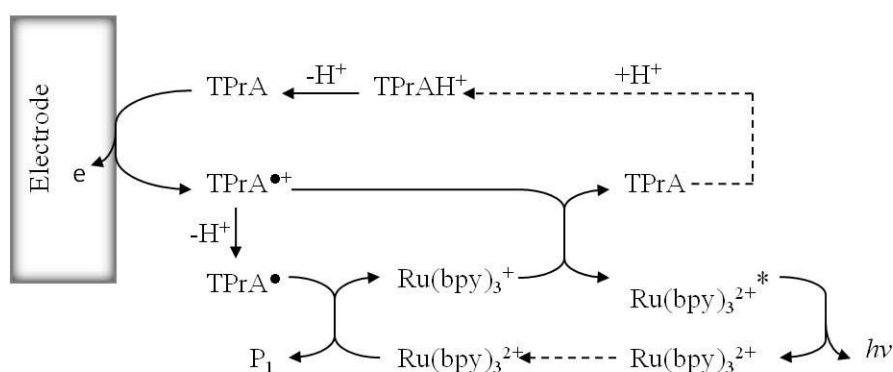
Scheme 3:



It should be noted that, although TPrA can also be oxidized by $\text{Ru}(\text{bpy})_3^{3+}$, this oxidation reaction occurs only when $\text{Ru}(\text{bpy})_3^{2+}$ concentration is high enough. In other words, oxidation of TPrA by $\text{Ru}(\text{bpy})_3^{3+}$ is negligible when the concentration of $\text{Ru}(\text{bpy})_3^{2+}$ is low, as it is the case when ruthenium complex is immobilized in the bead-based assays. The role of direct co-reactant oxidation on the glassy carbon (GC), gold (Au) and platinum (Pt) electrode have been investigated by Zu and Bard¹⁸. In the experiments performed on the GC electrode at the concentration of $1 \mu\text{M}$ $\text{Ru}(\text{bpy})_3^{2+}$, the ECL curve showed two waves. The electrochemical, chemical and spectroscopic behaviors of the second ECL wave at potential (+1.2 V vs. SCE) corresponding to the $\text{Ru}(\text{bpy})_3^{2+}$ oxidation have already been detailed before¹⁸. Therefore, they emphasized on establishing possible mechanism for the first ECL wave which occurs at low-oxidation-potential (at potential less than +1.0 V vs. SCE), compare to the one required for the direct oxidation of $\text{Ru}(\text{bpy})_3^{2+}$ at the electrode surface. The ECL emission of the first wave showed dependence on the electrode material and it was not recorded at Au and Pt electrodes. Due to the formation of surface oxides at Au and Pt electrodes, the direct oxidation of TPrA was significantly blocked. This led to conclusion that the first ECL wave was strongly dependent on direct oxidation of TPrA¹⁸. Further, the ECL spectrum obtained at the potential of the first wave was corresponding to the light emission of $\text{Ru}(\text{bpy})_3^{2+*}$.²³ Because the direct oxidation of TPrA leads to the formation of reducing radicals TPrA^\bullet that could react with $\text{Ru}(\text{bpy})_3^{2+}$ to generate $\text{Ru}(\text{bpy})_3^+$, authors suggested that one possible way to produce $\text{Ru}(\text{bpy})_3^{2+*}$ could be electron transfer from $\text{Ru}(\text{bpy})_3^+$ to some oxidative species¹⁸. Miao and Bard two years later reported the “revisited” route where ECL emission is

completely independent of direct oxidation of $\text{Ru}(\text{bpy})_3^{2+}$ at the electrode surface and involves cation radical $\text{TPrA}^{\bullet+}$. The mechanism is based on the assumption that $\text{TPrA}^{\bullet+}$ through a very reactive intermediate, has a life-time long enough to react itself before it undergoes deprotonation. Namely, the oxidation of deprotonated TPrA generates the cation radical $\text{TPrA}^{\bullet+}$ which loses one proton forming highly reducing agent TPrA^\bullet . This radical it then able to reduce $\text{Ru}(\text{bpy})_3^{2+}$ to $\text{Ru}(\text{bpy})_3^+$. In the same time produced $\text{TPrA}^{\bullet+}$ behaves like strong oxidant and it oxidises $\text{Ru}(\text{bpy})_3^+$ to $\text{Ru}(\text{bpy})_3^{2+*}$ (Scheme 4).

Scheme 4:



To verify this assumption, several experiments were performed. Scanning electrochemical microscopy SECM-ECL has been used to verify whether the light emission occurs without direct oxidation of $\text{Ru}(\text{bpy})_3^{2+}$.²³ Precisely, $\text{Ru}(\text{bpy})_2[\text{bpy}(\text{COOH})_2]^{2+}$, whose ECL behaviour is similar to $\text{Ru}(\text{bpy})_3^{2+}$, in the presence of TPrA, was covalently immobilised on an ITO electrode to serve as a substrate. To avoid the direct oxidation of $\text{Ru}(\text{bpy})_2[\text{bpy}(\text{COOH})_2]^{2+}$, during the course of SECM-ECL experiment, the modified ITO electrode was at an open circuit potential. The working electrode – tip was 1.5 mm diameter hemispherical Au. The tip was withdrawn from the ITO surface to a certain distance while current and ECL curves were monitored during voltammetric cycle between 0 and 1.0 V vs. Ag/AgCl/KCl. It was detected that upon oxidation of TPrA at ~ 0.80 V vs. Ag/AgCl/KCl the ECL signal appears and tracks the tip current during potential cycling. Furthermore, the ECL signal could be detected only within very short distance ($\sim 5\text{-}6 \mu\text{m}$) from the electrode surface and it decreases almost exponentially with increasing the distance. This experiment clearly demonstrates that, by the simple oxidization of TPrA, the formed intermediates, $\text{TPrA}^{\bullet+}$ and TPrA^\bullet , are involved in the ECL generation of $\text{Ru}(\text{bpy})_3^{2+}$.

The maximum distance at which ECL emission was observed was $\sim 5 \mu\text{m}$ and therefore it represents the distance of $\text{TPrA}^{\bullet+}$ diffusion before deprotonation. The half-life of the cation radical was estimated at $\sim 0.2 \text{ ms}$ taking the typical diffusion coefficient of $5 \times 10^{-6} \text{ cm}^2/\text{s}$.

In the same article, the detection of $\text{TPrA}^{\bullet+}$ by using electron spin resonance (ESR) was reported.²³ The investigation was based on the previous studies which have shown that trimethylamine radical cation has a similar lifetime as that estimated for $\text{TPrA}^{\bullet+}$. The ESR spectrum showed good correlation with simulated spectrum indicating the direct evidence for $\text{TPrA}^{\bullet+}$.

The effect of the so-called “revisited” mechanism on the overall ECL signal was reported by Zanarini *et al.*³⁰ In their work, they used silica nanoparticle with a mean size of 18 nm covalently doped with $\text{Ru}(\text{bpy})_3^{2+}$. Self-assembled monolayer (SAM) of covalently doped nanoparticles (DSNP) that can be considered as model systems for probe-target assays was prepared on a gold working electrode. The gold electrodes functionalized with thiol-terminated DSNP SAM were characterized by cyclic voltammetry. The oxidation of $\text{Ru}(\text{bpy})_3^{2+}$ units was not visible and the voltammetric curve was governed by two different phenomena: stripping of the DSNP-SH SAM and formation and reduction of Au oxides on the substrate.

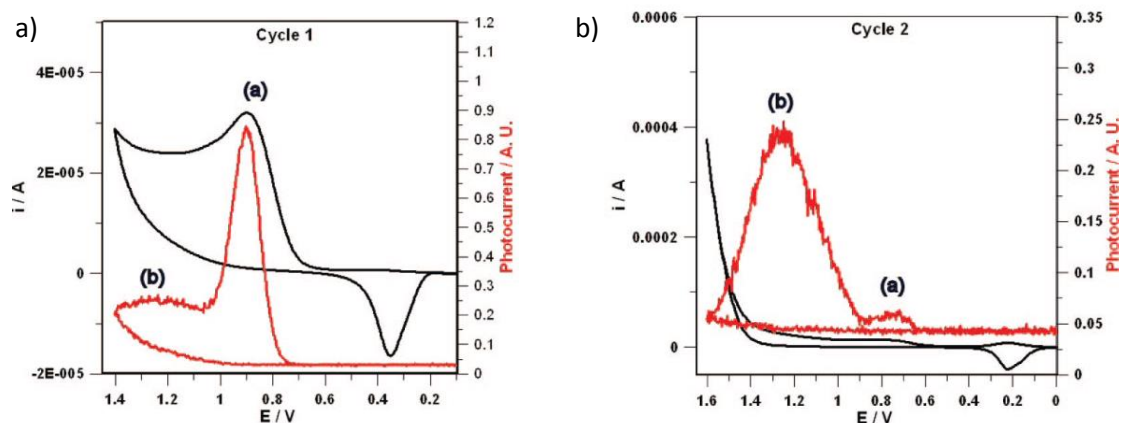


Figure 1. First (a) and second (b) cycle light/current/potential curve of a gold substrate functionalized with DSNP-SH self-assembled layer immersed in a 0.1 M PB (pH 7.5) containing $3 \times 10^{-2} \text{ M}$ TPrA. Scan rate: 0.5 V/s. Potentials are measured vs. saturated Ag/AgCl electrode.³⁰

The ECL intensity curves obtained in the first two cycles were compared (Figure 1). The ECL profile showed two peaks located at +0.91 and +1.23 V vs. Ag/AgCl/KCl, compatible with known mechanism. Such peaks were observed in both cycles. However, while the intensity of

the peak at 1.23 V remained almost unchanged, the first peak decreased by factor of 10 after the first scan. It becomes almost negligible compared with the second one. These results were explained with respect to direct oxidation of TPrA. In the first scan, the Au electrode was covered with hydrophobic SAM which prevents the formation of surface oxides and allows direct oxidation of TPrA leading to the high concentration TPrA^{•+} production. These species can diffuse into the porous silica particles and generate excited state. In the following scans, detachment of the SAM occurs. Therefore, direct oxidation of TPrA becomes less efficient and the ECL profile shows dependence only on direct oxidation of Ru(bpy)₃²⁺ confined in nm scale from the electrode surface. The overall decrease of ECL intensity clearly indicates the importance of the ECL emission on the sensitivity of bead-based assays, when electrochemical oxidation of Ru(bpy)₃²⁺ does not take place.

Still, the electro-oxidation of TPrA itself produce a weak ECL background signal even in the absence of luminophores limiting the sensitivity of ECL analytical methods.³¹ The nature of this reaction is not understood very clearly for many years. Recently, a very interesting and useful research³² has demonstrated that background ECL emission at 630 nm observed during the electrochemical oxidation of TPrA in the presence of dissolved O₂ in solution can be attributed to the ¹Δ_g state of O₂. The formation of the excited state is based on the reaction between dissolved oxygen and two different products of TPrA oxidation: the TPrA[•] radical that reduces O₂ to the superoxide ion and the TPrA^{•+} radical cation that oxidizes this species to singlet O₂. No ECL emission was observed when the same solution was used in the absence of dissolved O₂. These results suggest that the sensitivity of analytical applications of ECL could be improved by the rigorous exclusion of O₂.

The study of ECL mechanism and its influence on ECL emission at the single bead level is of great importance considering numerous bead-based analyses, as mentioned above. ORIGIN Analyser provided by IGEN International, Inc. (now Elecsys, product-line of Roche), is the first commercialized system based on ECL as detection method.³ The use of ECL detection has many advantages over other detection systems especially because of its remarkable sensitivity, negligible auto-luminescent background signal and simplicity in experimental design. The labels are not radioactive and they are stable compared with those of most other chemiluminescent systems. The detection limits for label are extremely low (200 fmol/L) with dynamic range of quantification over six orders of magnitude.⁷ The ORIGIN Analyser is adapted to measure ECL labels presented on the surface of magnetic beads. The instrument

consists of a flow cell containing a reusable platinum electrode and a PMT for light detection (Figure 2).

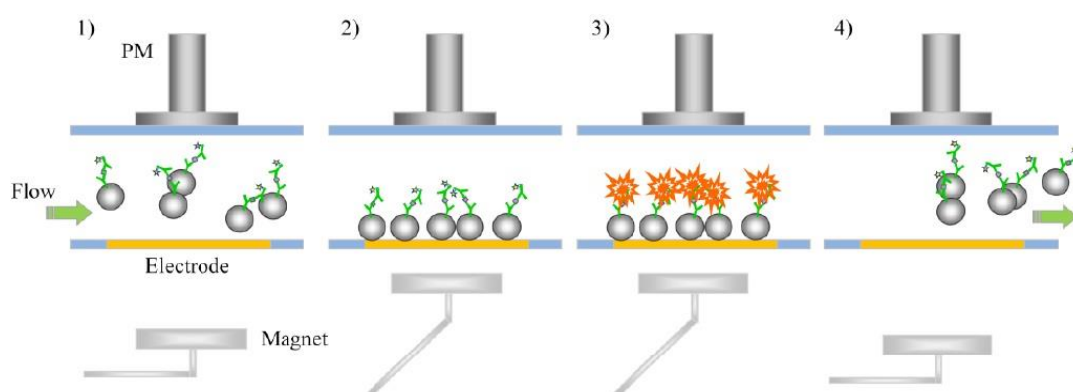


Figure 2. Generic process for measuring magnetic bead-based ECL assays in flow cells. 1) Introduce magnetic beads with bound assay component; 2) Capture magnetic particles with magnetic field, introduce TPrA buffer; 3) Apply potential at electrode to induce ECL; 4) Wash out of the beads.

The ECL labels are usually $\text{Ru}(\text{bpy})_3^{2+}$ derivatives which can bind to biomolecules. The binding of ECL label to the magnetic beads depends on assay format. In sandwich immunoassay, for example, antibody coated magnetic beads are used to bind the detection antigen and secondary ECL labeled antibody. The binding is usually running offline. Then, each individual sample is drawn into the flow cell, where the paramagnetic beads are magnetically captured on the electrode surface. In this way the labels attached to the beads are concentrated on the electrode surface increasing the sensitivity. A solution containing TPrA is then drawn through the flow cell to wash the beads and supply co-reactant for ECL, which is oxidized by applying potential between the working and counter electrodes. The emitted light is detected by PMT. The beads are then washed from the cell, and a cleaning solution is introduced into the cell to leave the surfaces of the electrodes in a reproducible state, ready for the next measurement³³.

Now, there are several commercial systems that are based on ORIGEN technology. These instruments are designed for a variety of applications in life sciences, high-throughput drug screening, and food, water, and animal health testing. Roche Diagnostics and Mesoscale markets different assays for clinical immunoassay testing. These systems feature an expansive menu of immunoassay tests in the areas of cardiology, fertility, thyroid function, oncology, anemia, infectious disease, and osteoporosis^{3,34}.

In the research field, bead-based ECL assays have been also described^{8,11,35-37}. A very sensitive immunoassay based on the similar instrumentation as in commercial systems have been reported. The application of the system was presented on detection of α -fetoprotein (AFP).³⁸ The magnetic beads coated with anti-AFP antibodies was used for binding of AFP in sandwich type immunoassay with Ru(bpy)₃²⁺-NHS labelled secondary anti-AFP antibodies. Employing ECL detection of beads confined to the electrode surface the detection reached sensitivity to the level of 5 pg/mL of the AFP with wide dynamic range.³⁸

2.3. Reported mechanisms of Ru(bpy)₃²⁺ / DBAE system

An extensive research has been focused on exploring effective co-reactants for the sensitive determination of Ru(bpy)₃²⁺, which has important bioanalytical applications for detection of numerous analytes such as oxalate,^{39,40} NADH,⁴¹ glucose,^{42,43} amines,^{5,17} and amino acids⁴⁴. The classic co-reactant used is TPrA, but others have been investigated and found to lead to even higher ECL signals than TPrA. A prime example is DBAE for ECL generation with Ru(bpy)₃²⁺ available in solution. DBAE has found increasing use for ECL applications^{25,45,46}. It is used as co-reactant, not only for Ru(bpy)₃²⁺ but also for its derivatives or QDs, partly applied in quenching techniques.²⁵ The group of Guobao Xu reported an investigation of the ECL of a series of tertiary amines with various substituents whilst keeping the concentration of Ru(bpy)₃²⁺ lower than that of the amine.⁶ Generally, tertiary amines are more effective than secondary amines, primary amines, and other kinds of co-reactants.^{5,17} They reported that the ECL intensity for the Ru(bpy)₃²⁺/DBAE system is close to that of the Ru(bpy)₃²⁺/TPrA system when the concentration of Ru(bpy)₃²⁺ is 1 mM; still, the intensity of the DBAE system is about ten times that of the TPrA system if the concentration of Ru(bpy)₃²⁺ is 1 μ M at Au and Pt working electrode. These results are consistent with findings that direct oxidation of the co-reactant plays an important role at low concentrations of Ru(bpy)₃²⁺ and that electrocatalytic oxidation of the co-reactant by Ru(bpy)₃²⁺ is dominant at high concentrations of Ru(bpy)₃²⁺. ECL of the Ru(bpy)₃²⁺/DBAE system at Pt and GC electrodes was also studied. The ECL of the Ru(bpy)₃²⁺/DBAE system at Pt electrodes is comparable to that at Au electrodes, and is about 100-times stronger than that of the Ru(bpy)₃²⁺/TPrA system at a Pt electrode. The striking difference in ECL intensity can be attributed to the different oxidation rate of DBAE and TPrA at platinum electrodes. An earlier report detailed in paragraph 2.2. by Zu and Bard showed that the ECL intensity of the Ru(bpy)₃²⁺/TPrA system

at Pt electrodes is only about 10% of that at Au electrodes because the growth of anodic oxide films at platinum electrodes significantly inhibited the direct oxidation of TPrA.¹⁸ In contrast, the direct oxidation of DBAE at Pt electrodes is much faster, indicating that hydroxyethyl also catalyzes the direct oxidation of amines at Pt electrodes, and thus dramatically enhance ECL intensity. The ECL of DBAE increases rapidly initially with increasing concentration up to 20 mM, and then it decreases slowly upon further increasing its concentration. The decrease in ECL intensity at high concentrations of DBAE may be attributed to side reactions.^{6,24} In comparison, 20 mM DBAE is more effective than 100 mM N,N-diethylethanolamine and TPrA, despite increases in the ECL of N,N-diethylethanolamine and TPrA upon increasing their concentrations. At the glassy carbon electrode, the intensity of ECL increase with the concentration of DBAE up to just 3 mM and as a result of side reactions at higher concentrations is offset.⁶

Recently, Tang *et al.* studied mechanism of the Ru(bpy)₃²⁺/DBAE ECL system by using quantum dots.²⁵ It has been reported that Ru(bpy)₃²⁺/DBAE system is similar to the mechanism of the Ru(bpy)₃²⁺/TPrA system with regard to the earlier report by Bard and Miao. They showed that the ECL mechanism of the Ru(bpy)₃²⁺/TPrA system involve reduction of Ru(bpy)₃²⁺ by the intermediacy of TPrA cationic radicals to generate the excited state Ru(bpy)₃^{2+*}. The proposed mechanism of the Ru(bpy)₃²⁺/DBAE is based on the fact that DBAE is also an aliphatic tertiary amine and its molecular structure is similar to TPrA. In this way, DBAE is first oxidized at the electrode (~0.60 V vs Ag/AgCl) to form a DBAE^{•+} cationic radical that further deprotonates to a DBAE[•] free radical.²⁴ It is also known that Ru(bpy)₃²⁺ can be oxidized at 1.14 V (vs. Ag/AgCl) to Ru(bpy)₃³⁺. Due to its sufficient reducing ability, DBAE[•] free radicals reduce Ru(bpy)₃³⁺ to generate the excited-state Ru(bpy)₃^{2+*} radicals that subsequently decay into Ru(bpy)₃²⁺ with light emission.⁴ Electron spin resonance (ESR) measurements confirm that oxidation of DBAE can generate the amine cationic radical DBAE^{•+} that subsequently deprotonates to DBAE[•] free radicals.²⁵ When CdSe@ZnS QDs are added into Ru(bpy)₃²⁺/DBAE system, the solution containing DBAE^{•+} cation radicals, the ESR spectrum corresponding to DBAE^{•+} cationic radicals totally disappears. Generated DBAE^{•+} cationic radicals will prefer reacting with QDs - reducing holes of QDs, in competition with Ru(bpy)₃³⁺ reduction. Such a competition is realistic, on the basis of band levels of QDs and redox potentials of DBAE and Ru(bpy)₃²⁺. Finally, ESR measurements have revealed that there is charge transfer occurring between QDs and the radical state of DBAE, leading to ECL quenching of Ru(bpy)₃²⁺/DBAE.

Besides, DBAE is an environmentally friendly co-reactant which could be expanded to bioassays as it shows better performance than TPrA in ECL operated with $\text{Ru}(\text{bpy})_3^{2+}$ solution (not immobilized as for bead-based assays). In order to simulate kinetic parameters, one should take in account that a series of consecutive reactions of short-lived radicals with different redox potentials is taking place within competing ECL mechanisms.^{47,48} Therefore, it is a real task to model the precise values for reactions in solution phase and even more difficult to assume in real practical cases.

2.4. Bead-based Sandwich ECL immunoassay

Since there are numerous examples of bead based assays, the study of ECL mechanism is of great importance for improving the system efficiency and developing new protocols. In the commercial Origen analyzer (see), the $\text{Ru}(\text{bpy})_3^{2+}$ -tagged entities (antibodies) are immobilized on 2.8 μm diameter magnetic beads.³ We performed a sandwich ECL immunoassay exploiting 3- μm polystyrene (PS) beads of size comparable to the ones used in commercialized assays. PS beads were modified with a capture antibody (anti-IL-8) and exposed to a sample containing the antigen and biotinylated detection antibodies. Lastly the streptavidin-modified $\text{Ru}(\text{bpy})_3^{2+}$ -label was attached (Figure 3a). The beads were deposited on a flat glassy carbon (GC) electrode by drop-casting and let to dry on the room temperature, protected from the light. ECL image was recorded with a microscope in a top-view configuration so that the electrode surface was orientated parallel to the microscope objective lens for observation (Scheme 5(A)). To obtain the position of the beads on the surface, the photoluminescent mode was used with excitation at 485 nm and emission at 605 nm. The ECL imaging was realized in the same focal plane without use of excitation light and a sufficient anodic potential of 1.1 V was applied to the modified GC electrode in a solution containing TPrA. A Pt wire and a Ag/AgCl/KCl-electrode were the counter and reference electrode, respectively. To avoid the background ECL from O_2 quenching, buffer solution was deaerated by bubbling nitrogen gas for 30 minutes.³² From the Figure 3b one can see that a single functionalized bead is emitting ECL light.

The ECL light emerges from the entire bead and not only from the region where the bead is in contact with the surface. Concerning the spherical geometry of the beads, only a small part of the bead is in contact with electrode. As the ruthenium label is attached to the bead only the co-reactant radicals resulting from the oxidation step at the electrode diffuse to react with the

label to generate the excited state. Moreover, ECL intensity is not homogeneously distributed over the bead; it appears more intense in the centre. However, such an image does not allow resolving sufficiently the distribution of the ECL intensity.

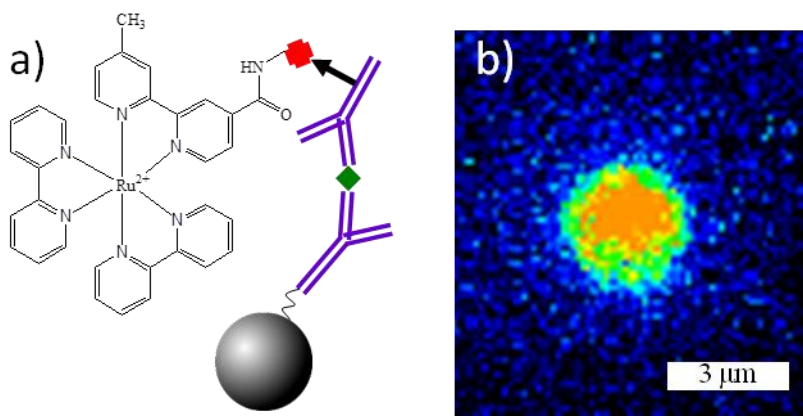
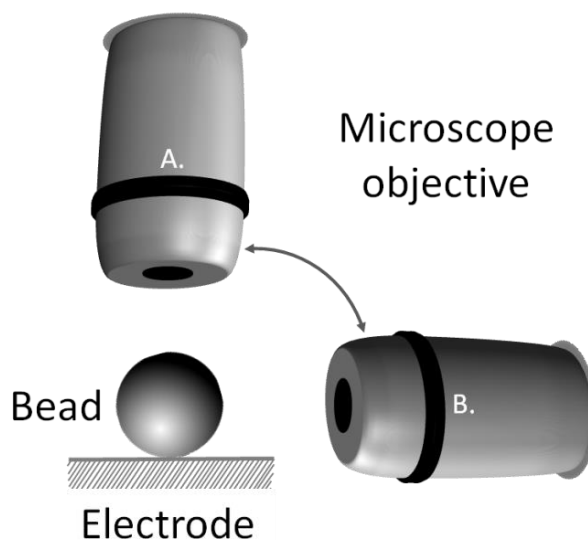


Figure 3. (a) Sandwich immunoassay with PS beads. (b) ECL imaging of a single 3-µm bead using the top-view configuration. ECL images were acquired over a 6 s exposure-time at a potential of 1.1 V vs Ag/AgCl/KCl in a PBS solution containing 100 mM TPrA (pH = 7.4).

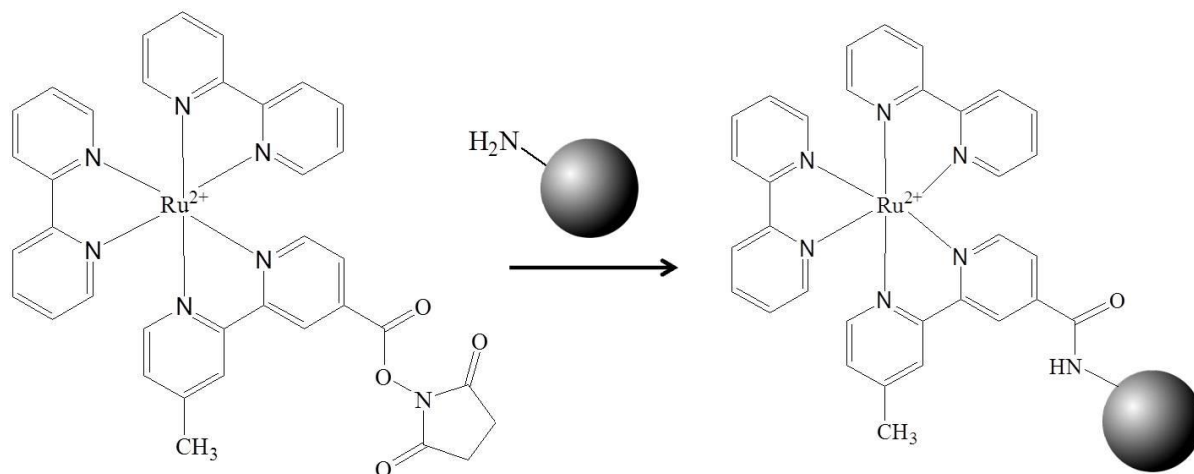
Scheme 5:



Schematic representation of both optical configurations used to image the functionalized bead: top-view (A) and side-view (B).

To improve the spatial resolution of the luminescence phenomenon and to obtain well-resolved ECL patterns, we used in further experiments 12-µm diameter PS beads. To demonstrate the concept, -NH₂ functionalized beads were modified with the same ruthenium

label, $\text{Ru}(\text{bpy})_3^{2+}$ -NHS ester (bis(2,2'-bipyridine)-4'-methyl-4-carboxybipyridine-ruthenium N-succinimidyl ester bis(hexafluorophosphate)) whose ECL behaviour is very similar to that of $\text{Ru}(\text{bpy})_3^{2+}$, *via* an amide-type reaction (Scheme 6).



Scheme 6. Functionalization of beads with a $\text{Ru}(\text{bpy})_3^{2+}$ label *via* the peptide coupling.

2.4.1. 2D ECL Imaging

The photoluminescence (PL) image shows the location of a labelled PS bead (Figure 4a). The PL intensity which reflects the immobilized ruthenium sites was homogeneously distributed over the bead. To study the dependence of the ECL emission on the electrode potential, a series of ECL images were recorded during a cyclic voltammetric scan. By increasing progressively the applied potential from 0.7 V, where no ECL is generated, to 1.2 V, ECL intensity increased progressively with a maximum value obtained at 1.1 V (Figure 4c).²³ Similarly, we observed with a good spatial resolution that the entire beads emit ECL light with a brighter spot in their centre. In fact, they act as an efficient lens focusing the light at their centre. Such a peculiar electromagnetic field distribution that emerges from a dielectric microsphere has been experimentally demonstrated.^{49,50} The light beam emerges from the microsphere with high intensity and low divergence. Such a focusing behaviour concentrates the analytical signal and contributes to the extremely good sensitivity of the bead-based ECL immunoassays. Since DBAE has been reported to produce stronger ECL signal in solution than TPrA (e.g. 6.5-fold higher ECL signal at 20 mM co-reactant concentration)⁶, we tested its performance in the bead-based format (Figure 4b and 5a).

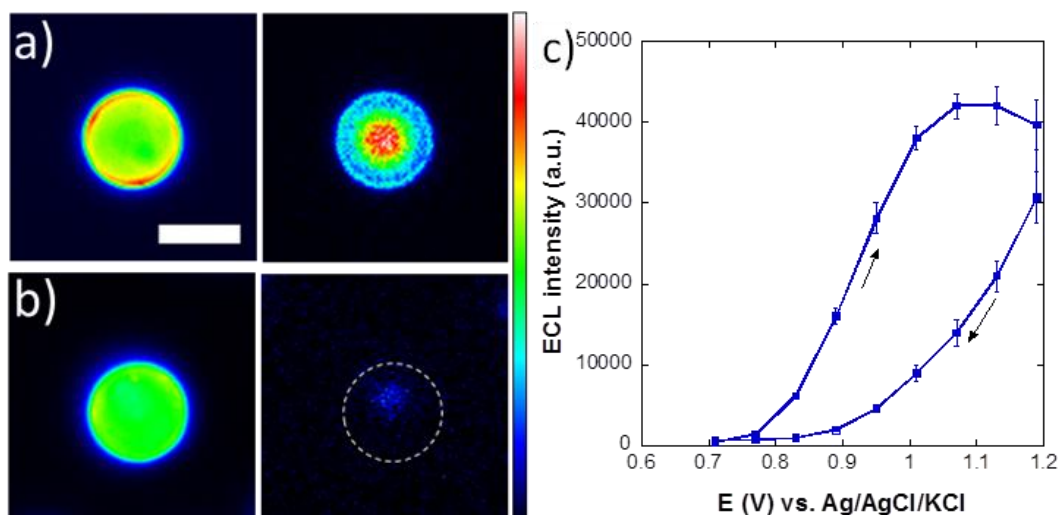


Figure 4. (a-b) Top-view PL (left) and ECL (right) images of 12-µm PS beads functionalized with the ruthenium label. ECL images were recorded in PBS solutions containing (a) 100 mM TPrA or (b) 20 mM DBAE on GC electrodes. The dashed line materializes the position of the bead. Experiments have been performed on more than 50 single beads in each condition. Scale bar: 10 µm. (c) ECL intensity measured on a PS bead as a function of the potential applied to the GC electrode in a PBS solution containing 100 mM TPrA (pH = 7.4).

In our conditions, maximum ECL intensity has been obtained at 1.2 V with a DBAE concentration of 20 mM. ECL emission was located just at the centre of the bead over a ~4-5 µm diameter surface (Figures 4b and 5a,b). Unexpectedly, the ECL intensity was extremely low on GC and on Au electrodes: ECL signals recorded on the functionalized beads were surprisingly 7-fold lower than those collected with TPrA. This difference may be explained by the different experimental conditions since, in previous reports,^{6,24,51} Ru(bpy)₃²⁺ was freely diffusing in solution and could react homogeneously with the DBAE radicals. In the bead-based format, radicals resulting from DBAE oxidation have to diffuse away from the electrode and to react with the immobilized Ru(bpy)₃²⁺ to generate the excited state. Such behaviour highlights the difference in reactivity of both tested co-reactants which depends on the redox potentials and the lifetimes of their radicals. At first sight, both the weaker and lesser expansion of ECL suggest that the DBAE-derived radicals propagate less in solution and are likely less stable than the TPrA ones. Even if the top-view imaging of the bead highlights the non-uniform distribution of ECL intensity over it, it does not give precise localization of the ECL-emitting region on its surface. Indeed, the recorded ECL pattern reflects mainly the optical paths through the beads.

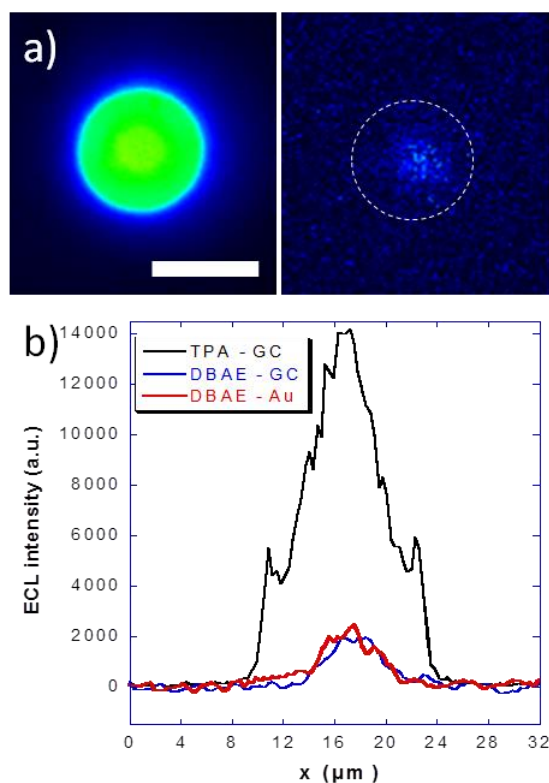


Figure 5. a) Top-view PL (left) and ECL (right) images of a 12- μm PS bead functionalized with the ruthenium label. ECL image was recorded over a 6 s exposure-time in a PBS (pH = 7.4) solution containing 20 mM DBAE on Au electrode poised at 1.2 V vs Ag-AgCl. The dashed line materializes the position of the bead. Scale bar: 10 μm . b) ECL intensity profiles taken along the middle vertical axis of the beads and recorded in 100 mM TPrA on GC electrode (black line) or in 20 mM DBAE on GC (red line) and on Au (blue line) electrodes.

To reconstruct the spatial location and the volumic extension of the ECL-emitting zone, a 3D cartography, as in scintigraphy, can be obtained by changing the angle of observation of the emitting object.

2.4.2. 3D ECL Imaging

Here, we used an orthogonal side-view configuration (position B in Scheme 5), where the working electrode with immobilized beads was orientated so that surface of the electrode was perpendicular toward the microscope objective. It supplements the top-view approach with a 2D ECL mapping normal to the electrode surface. Figure 6 shows the PL image of the bead: the upper part of the image corresponds to the real bead and the lower part to its mirror image formed by the light reflection on the GC surface. PL image precisely defines position of the bead and also its interface with the electrode. As for the top-view images, the ECL experiments with TPrA, did not show light emission before applying sufficiently anodic

potentials (Figure 4). At 1.1 V, an ECL-emitting region was observed at the interface between the GC surface and the bead (*i.e.* $z = 0$); this extends over a $\sim 6 \mu\text{m}$ length knowing that this value integrates also the contribution of the light reflection. Interestingly, there is a second region from where ECL light emerged, located at the top of the PS bead.

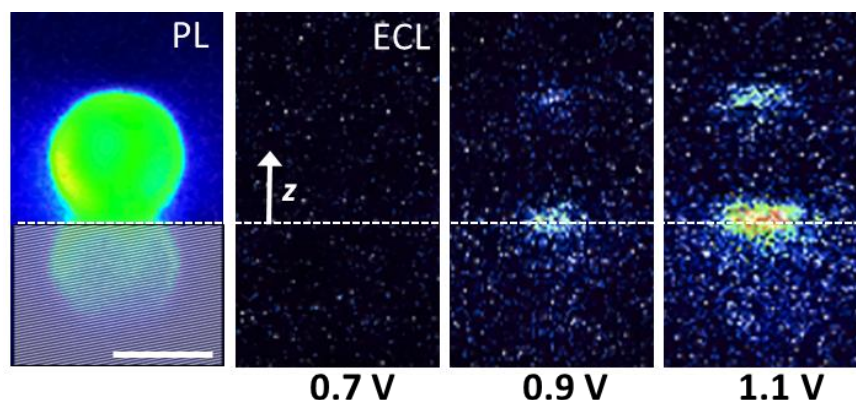


Figure 6. Side-view images of a 12- μm PS bead labelled with the ruthenium complex. The first image is obtained by PL and the following ones by ECL in a PBS solution containing 100 mM TPrA (pH = 7.4). The dashed line materializes the position of the GC electrode surface (*i.e.* $z = 0$) and the hatched zone represents the PL reflection on the electrode surface. Same conditions as in Figure 1. Scale bar: 10 μm .

As discussed previously, it corresponds to the focusing effect of the bead which acts as a lens and does not contain any real chemical information. The ECL-emitting region was confined very close to the electrode surface and extended only over 3-4 μm along z axis. With the side-view configuration, we were not able to record any ECL emission with DBAE even for exposure time of the CCD camera up to 20 s (Figure 7). Again, with DBAE, the extension of the ECL-emitting region is probably too small at the bead/electrode interface and its intensity too low to be imaged in our conditions.

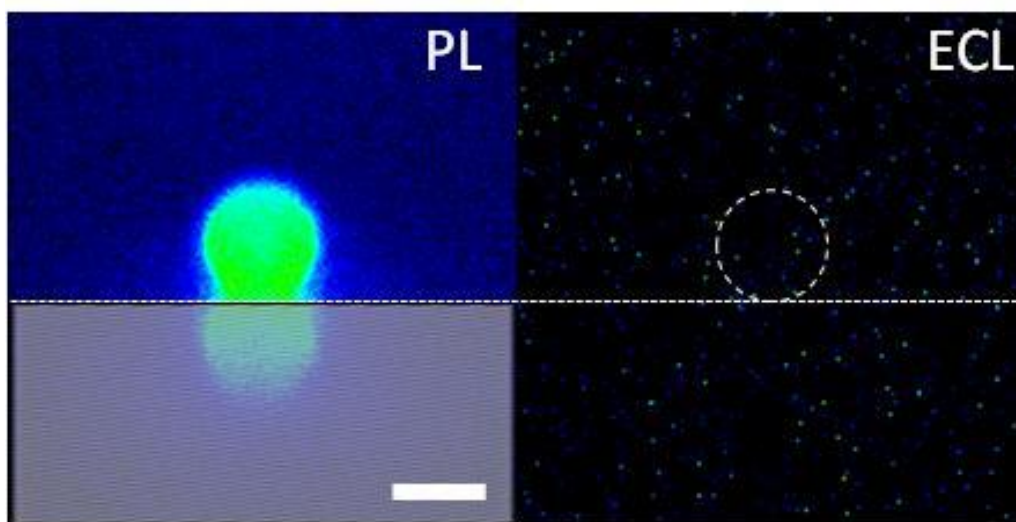
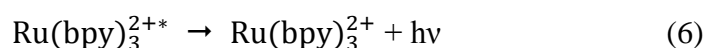
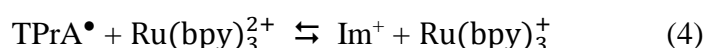


Figure 7. Side-view PL (left) and ECL (right) images of 12- μm PS beads functionalized with the ruthenium label. ECL image was recorded over a 20 s exposure-time at 1.2 V in a PBS (pH = 7.4) solution containing 20 mM DBAE on Au electrode. The dashed line materializes the position of the bead on the electrode surface (*i.e.* $z = 0$) delimited by the dotted line. The hatched zone represents the reflection of the PL on the electrode surface. Same experimental conditions as in Figure 1. Scale bar: 10 μm .

The ECL mechanisms involving the direct oxidation of $\text{Ru}(\text{bpy})_3^{2+}$ may be operative only at nanometric distances (*i.e.* electron tunnelling distance $\sim 1\text{-}2$ nm) which are impossible to resolve with classic optics. The micrometric extension of the ECL region observed in our study with TPrA is consistent with the “revisited” route involving both TPrA radicals:²³



where Im^+ is the iminium product.

$\text{Ru}(\text{bpy})_3^{2+}$ is not oxidized directly at the electrode in this route. The oxidation of deprotonated TPrA generates the cation radical $\text{TPrA}^{\bullet+}$ (reaction 2); it deprotonates rapidly to form locally the free radical TPrA^\bullet ,²³ which is a strong reductant (reaction 3). This radical reduces $\text{Ru}(\text{bpy})_3^{2+}$ to $\text{Ru}(\text{bpy})_3^+$ (reaction 4). Then $\text{TPrA}^{\bullet+}$ oxidizes $\text{Ru}(\text{bpy})_3^+$ to generate the excited state $\text{Ru}(\text{bpy})_3^{2+*}$ (reaction 5) which deactivates through the emission of a photon.

In this path, ECL generation requires the simultaneous presence of both radicals under sufficient fluxes to form the excited state.

Since DBAE is an aliphatic tertiary amine structurally similar to TPrA, it has been proposed to follow mechanisms analogous to TPrA with the formation of radical cation DBAE^{•+} and the reducing intermediate DBAE[•] by deprotonation.⁵¹⁻⁵³ Even if DBAE leads to stronger ECL intensity than TPrA when Ru(bpy)₃²⁺ is in solution,⁶ ECL emission recorded on the modified beads is very low and even undetectable in the side-view configuration. Such an unexpected behaviour might be attributed to the intervention of a much more unstable intermediate (i.e. at least 10 times faster deprotonation rate of DBAE^{•+}) which limits drastically the ECL-emitting zone. Our results show the differential reactivity of both model co-reactants and the importance of inspecting the ECL mechanistic pathways with surface-confined species or read/write approaches. Taking into account the overall mechanistic scheme for TPrA, the concentration profiles of both co-reactant radicals diffusing from the electrode and around the bead were simulated (Figure 8).

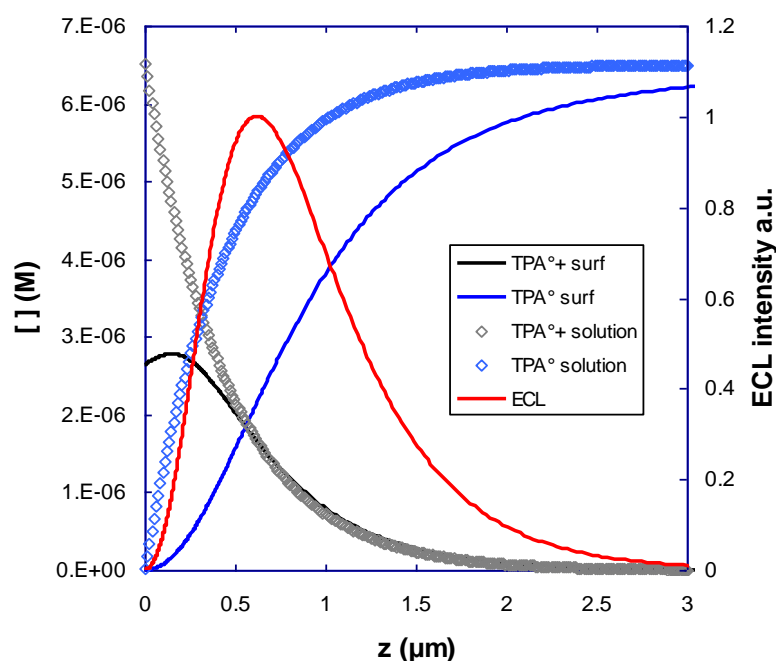


Figure 8. Concentration profiles of TPrA^{•+} (black curve), of TPrA[•] (blue curve) and of the resulting ECL intensity (red curve) with the ruthenium complex immobilized on the bead. The depicted concentration and ECL profiles are simulated with a value of 2920 s⁻¹ for the TPrA^{•+} deprotonation rate constant. A value of 2920 s⁻¹ is extracted from the ECL profile for the rate constant k_3 of the TPrA^{•+} deprotonation (reaction 3). Assuming that this reaction is a first-order process, the half-life time ($\tau_{1/2}$) is $\tau_{1/2} = \ln 2 / k_3$. It gives a value of ~0.24 ms. The concentration profiles along the z axis in the solution, i.e. far from the bead $r > 50 \mu\text{m}$, are depicted by the symbols.

The simulations have been done in collaboration with Dr. Frédéric Kanoufi from Paris Diderot University (for the detail study see supporting information of reference 27). The spatial location and extension of this ECL-emitting region is also confined in the first 3- μm height of the bead next to the electrode, as evidenced by the simulation (Figure 9a). The ECL profile is constrained by the $\text{TPrA}^{\bullet+}$ and TPrA^{\bullet} concentration gradients at the bead surface. Indeed, ECL generation requires the sequential reactions of both reducing and oxidizing TPrA radicals at the same location. Under steady-state, ECL at small z values reflects the TPrA^{\bullet} concentration profile, while the tail of the ECL profile at large z values mimics the distribution of the most chemically unstable radical, here $\text{TPrA}^{\bullet+}$.

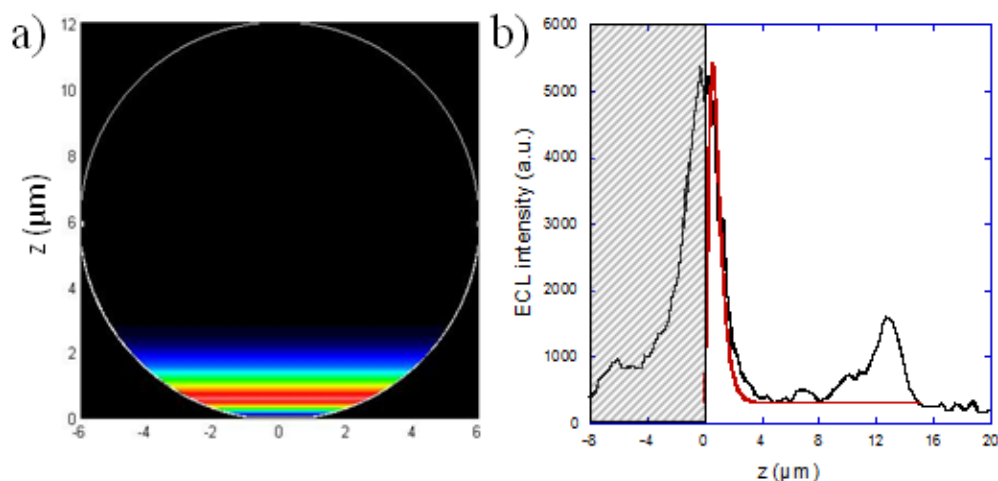


Figure 9. (a) Side-view of the simulated distribution of the generated $\text{Ru}(\text{bpy})_3^{2+*}$ excited state (*i.e.* ECL intensity) at the surface of a 12- μm bead. (b) Comparison of the experimental (black line) and simulated (red line) ECL intensity profiles at the level of a single bead. The experimental data correspond to the PS bead of Figure 3a recorded at 1.1 V. The ECL signals are simulated with a value of 2920 s^{-1} for the $\text{TPrA}^{\bullet+}$ deprotonation rate constant. The hatched zone represents the reflection of the ECL light on the electrode surface.

The key kinetic parameter in this overall process is the rate constant for the deprotonation of the $\text{TPrA}^{\bullet+}$. The position of the maximum ECL intensity and the thickness of this ECL-emitting region depend on the value of this rate constant. If this deprotonation step was slow, then the $\text{TPrA}^{\bullet+}$ may be formed further away from the electrode and it would result in an extended ECL zone. At the opposite, increasing this reaction rate would contract the ECL zone much closer to the electrode (Figure 10). In particular, the bead confines the different reactive species from hindrance of mass transfer^{54,55} allowing for an expansion of the

concentration profiles and of ECL-emitting region to greater domains (larger z values) than those expected from planar diffusion reaction layer conditions (Figure 11).

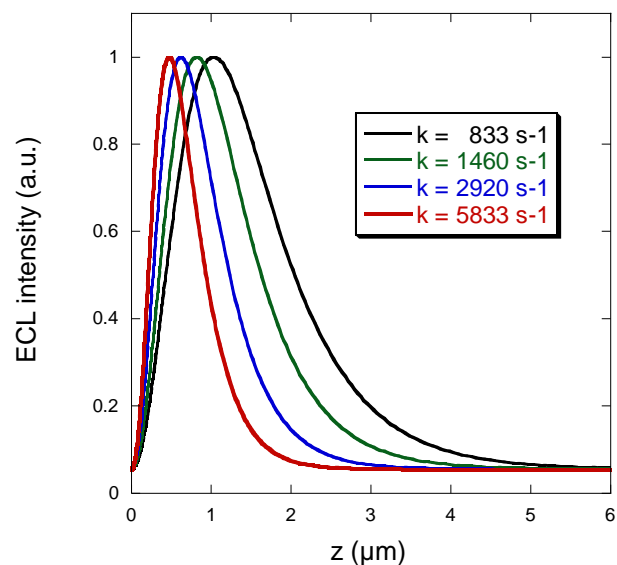


Figure 10. Effect of the kinetic of TPrA^{•+} deprotonation on the normalized ECL intensity profile in the vicinity of a 12- μm diameter bead.

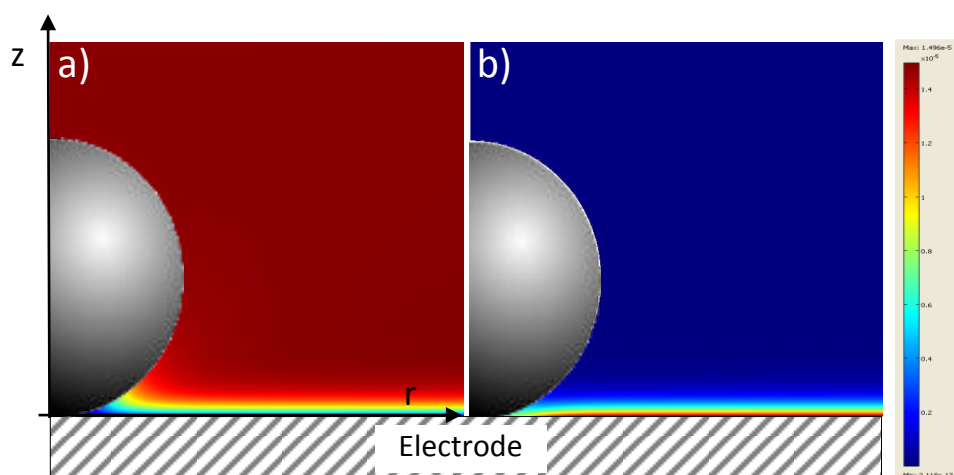


Figure 11. Simulated concentration profiles of (a) TPrA[•] and (b) TPrA^{•+} in the vicinity of a 12- μm diameter bead. The selected value for the TPrA^{•+} deprotonation rate constant was 2920 s^{-1} .

Figure 9b (black line) shows a typical experimental ECL intensity profile taken along the vertical symmetry axis of a PS bead placed on the GC electrode. The ECL-emitting region is clearly visible and is surrounded by 2 bright zones related to optical effects: the mirror image for $z < 0$ and the light focused at the top of the bead (viz. $z \sim 13 \mu\text{m}$), as discussed previously. We just considered the zone of photon production which contains all information on the chemical reactivity. The projection of the simulated ECL profile along the same z symmetry

axis is shown on Figure 9b (red line) and the best fit with the experimental data was obtained for a value of 2920 s^{-1} for the rate constant of the $\text{TPrA}^{\bullet+}$ deprotonation (half-life time of $\sim 0.24 \text{ ms}$). It is in relative good agreement with the value of 3500 s^{-1} reported by Miao *et al.*²³ If the simulated ECL emission profiles fits well with the experimental ones for $z > 0.6 \text{ }\mu\text{m}$, it deviates at the level of the electrode-bead contact ($z < 0.6 \text{ }\mu\text{m}$). Indeed, the revisited route suggests no TPrA^{\bullet} radical at the electrode, then no generation of the luminophore excited state. Experimentally, even if a decrease of intensity was detected for $z < 0.3 \text{ }\mu\text{m}$, the electrode-bead contact region was still illuminated. Eventually, lateral charge propagation between adjacent immobilized ruthenium centres (electron hopping)⁵⁶ would extend the light emission toward the bead-electrode interface without affecting the higher z values (Figure 12). Indeed, for fast surface transformation process,⁵⁷ the reactivity at the bead surface is limited by the 3D spatial distribution of the diffusing radical species. The signature of the $\text{TPrA}^{\bullet+}$ lifetime is then readily obtained from the tail of the ECL distribution.

2.5. Conclusions

In summary, ECL imaging resolved at the single bead level provides a general description of the ECL phenomena operating in bead-based ECL bioassays; it allows deciphering the mechanistic route, testing co-reactant efficiency and showing associated optical focusing effects. Reactivity mapping demonstrates the mechanistic route which leads to ECL emission. Maximum ECL intensity occurs in the micrometric region where concentrations of $\text{TPrA}^{\bullet+}$ and TPrA^{\bullet} radicals are locally the highest. Only the luminophores located in the $3\text{-}\mu\text{m}$ region next to the electrode contribute to the ECL signal and this finite reaction layer defines the optimal size of the functionalized beads for the bioassays. In comparison to bulk situation (*i.e.* freely diffusing $\text{Ru}(\text{bpy})_3^{2+}$ in solution), additional thermodynamic and kinetic criteria are required to select efficient co-reactants in the bead-based bioassays: adequate redox potentials and appropriate deprotonation rate constant to form concentrations gradients of both radicals extending simultaneously over sufficiently long distance in order to excite $\text{Ru}(\text{bpy})_3^{2+}$ -labels located far from the electrode. We also showed the lens effects of the bead which concentrate the ECL emission and thus contribute to increase the collected analytical signal. Finally, the ECL reactivity imaging offers the opportunity to select new co-reactants with improved sensitivity and to develop new analytical strategies.

References

- 1 Bard, A. J. *Electrogenerated Chemiluminescence*. (M. Dekker, New-York, 2004).
- 2 Miao, W. Electrogenerated Chemiluminescence and Its Biorelated Applications. *Chem. Rev.* **108**, 2506-2553 (2008).
- 3 www.roche.com.
- 4 Hu, L. & Xu, G. Applications and trends in electrochemiluminescence. *Chem. Soc. Rev.* **39**, 3275 (2010).
- 5 Leland, J. K. & Powell, M. J. Electrogenerated Chemiluminescence: An Oxidative-Reduction Type ECL Reaction Sequence Using Tripropyl Amine. *J. Electrochem. Soc.* **137**, 3127 (1990).
- 6 Liu, X., Shi, L., Niu, W., Li, H. & Xu, G. Environmentally Friendly and Highly Sensitive Ruthenium(II) Tris(2,2'-bipyridyl) Electrochemiluminescent System Using 2-(Dibutylamino)ethanol as Co-Reactant. *Angew. Chem. Int. Edit.* **46**, 421 (2007).
- 7 Blackburn, G. F. *et al.* Electrochemiluminescence detection for development of immunoassays and DNA probe assays for clinical diagnostics. *Clin. Chem.* **37**, 1534-1539. (1991).
- 8 Deiss, F. *et al.* Multiplexed Sandwich Immunoassays using Electrochemiluminescence Imaging Resolved at the Single Bead Level. *J. Am. Chem. Soc.* **131**, 6088-6089 (2009).
- 9 Muzyka, K. Current trends in the development of the electrochemiluminescent immunosensors. *Biosen. Bioelectron.* **54**, 393-407 (2014).
- 10 Dennany, L., Forster, R. J. & Rusling, J. F. Simultaneous Direct Electrochemiluminescence and Catalytic Voltammetry Detection of DNA in Ultrathin Films. *J. Am. Chem. Soc.* **125**, 5213 (2003).
- 11 Miao, W. & Bard, A. J. Electrogenerated Chemiluminescence. 77. DNA Hybridization Detection at High Amplification with $[\text{Ru}(\text{bpy})_3]^{2+}$ -Containing Microspheres. *Anal. Chem.* **76**, 5379 (2004).
- 12 Kenten, J. H. *et al.* Improved electrochemiluminescent label for DNA probe assays: rapid quantitative assays of HIV-1 polymerase chain reaction products. *Clin. Chem.* **38**, 873-879 (1992).
- 13 Xu, X.-H. & Bard, A. J. Immobilization and Hybridization of DNA on an Aluminum(III) Alkanebisphosphonate Thin Film with Electrogenerated Chemiluminescent Detection. *J. Am. Chem. Soc.* **117**, 2627 (1995).
- 14 Chen, Z. & Zu, Y. Electrogenerated Chemiluminescence of the Tris(2,2'-bipyridine)ruthenium(II)/Tertiary Amine Systems: Effects of Electrode Surface Hydrophobicity on the Low-Oxidation-Potential Emission. *J. Phys. Chem. C* **113**, 21877-21882 (2009).
- 15 Li, F. & Zu, Y. Effect of Nonionic Fluorosurfactant on the Electrogenerated Chemiluminescence of the Tris(2,2'-bipyridine)ruthenium(II)/Tri- n-propylamine System: Lower Oxidation Potential and Higher Emission Intensity. *Anal. Chem.* **76**, 1768-1772 (2004).
- 16 Factor, B. *et al.* Surfactant Chain Length Effects on the Light Emission of Tris(2,2'-bipyridyl)ruthenium(II) / Tripropylamine Electrogenerated Chemiluminescence. *Anal. Chem.* **73**, 4621-4624 (2001).
- 17 Noffsinger, J. B. & Danielson, N. D. Generation of chemiluminescence upon reaction of aliphatic amines with tris(2,2'-bipyridine)ruthenium(III). *Anal. Chem.* **59**, 865 (1987).

- 18 Zu, Y. & Bard, A. J. Electrogenenerated Chemiluminescence. 66. The Role of Direct Coreactant Oxidation in the Ruthenium Tris(2,2')bipyridyl/Tripropylamine System and the Effect of Halide Ions on the Emission Intensity. *Anal. Chem.* **72**, 3223 (2000).
- 19 Kanoufi, F., Zu, Y. & Bard, A. J. Homogeneous Oxidation of Trialkylamines by Metal Complexes and Its Impact on Electrogenenerated Chemiluminescence in the Trialkylamine/Ru(bpy)₃²⁺ System. *J. Phys. Chem. B* **105**, 210-216 (2001).
- 20 Wightman, R. M., Forry, S. P., Maus, R., Badocco, D. & Pastore, P. Rate-Determining Step in the Electrogenenerated Chemiluminescence from Tertiary Amines with Tris(2,2'-bipyridyl)ruthenium(II). *J. Phys. Chem. B* **108**, 19119 (2004).
- 21 Gross, E. M., Pastore, P. & Wightman, R. M. High-Frequency Electrochemiluminescent Investigation of the Reaction Pathway between Tris(2,2'-bipyridyl)ruthenium(II) and Tripropylamine Using Carbon Fiber Microelectrodes *J. Phys. Chem. B* **105**, 8732 (2001).
- 22 Zu, Y. & Bard, A. J. Electrogenenerated chemiluminescence. 67. Dependence of light emission of the tris(2,2')bipyridylruthenium(II)/tripropylamine system on electrode surface hydrophobicity. *Anal. Chem.* **73**, 3960-3964 (2001).
- 23 Miao, W., Choi, J.-P. & Bard, A. J. Electrogenenerated chemiluminescence 69. The tris(2,2'-bipyridine)ruthenium(II), (Ru(bpy)₃²⁺) / tri- n-propylamine (TPrA) system revisited. A new route involving TPrA^{•+} cation radicals. *J. Am. Chem. Soc.* **124**, 14478-14485 (2002).
- 24 Wang, S. *et al.* Electrogenenerated chemiluminescence determination of C-reactive protein with carboxyl CdSe/ZnS core/shell quantum dots. *Phys. Chem. Chem. Phys.* **12**, 10073-10080 (2010).
- 25 Hu, T., Liu, X., Liu, S., Wang, Z. & Tang, Z. Toward Understanding of Transfer Mechanism between Electrochemiluminescent Dyes and Luminescent Quantum Dots. *Anal. Chem.* **86**, 3939-3946 (2014).
- 26 Li, M.-J., Chen, Z., Yam, V. W.-W. & Zu, Y. Multifunctional Ruthenium(II) Polypyridine Complex-Based Core-Shell Magnetic Silica Nanocomposites: Magnetism, Luminescence, and Electrochemiluminescence. *ACS Nano* **2**, 905-912 (2008).
- 27 Sentic, M. *et al.* Mapping electrogenerated chemiluminescence reactivity in space: mechanistic insight into model systems used in immunoassays. *Chem. Sci.* **5**, 2568-2572 (2014).
- 28 Richter, M. M. Electrochemiluminescence (ECL). *Chem. Rev.* **104**, 3003 (2004).
- 29 Portis, L. C., Bhat, V. V. & Mann, C. K. Electrochemical dealkylation of aliphatic tertiary and secondary amines. *J. Org. Chem.* **35**, 2175-2178 (1970).
- 30 Zanarini, S. *et al.* Ru(bpy)₃ Covalently Doped Silica Nanoparticles as Multicenter Tunable Structures for Electrochemiluminescence Amplification. *J. Am. Chem. Soc.* **131**, 2260 (2009).
- 31 Zheng, H. & Zu, Y. Emission of Tris (2,2'-bipyridine) ruthenium (II) by Coreactant Electrogenenerated Chemiluminescence: From O₂-Insensitive to Highly O₂-Sensitive. *J. Phys. Chem. B* **109**, 12049-12053 (2005).
- 32 Senthil Kumar, S. & Bard, A. J. Background Emission of Electrogenenerated Chemiluminescence during Oxidation of Tri-n-propylamine from the Dimeric 1Δg State of O₂. *Anal. Chem.* **85**, 292-295 (2012).
- 33 B. Sigal George, E. G., J. Leland, J. Wohlstader and J. Debat. *Electrogenenerated Chemiluminescence*. 359-396 (CRC Press, 2004).
- 34 www.mesoscale.com.

- 35 Miao, W. & Bard, A. J. Electrogenerated Chemiluminescence. 80. C-Reactive Protein Determination at High Amplification with $[\text{Ru}(\text{bpy})_3]^{2+}$ -Containing Microspheres. *Anal. Chem.* **76**, 7109 (2004).
- 36 Zhou, X., Xing, D., Zhu, D. & Jia, L. Magnetic Bead and Nanoparticle Based Electrochemiluminescence Amplification Assay for Direct and Sensitive Measuring of Telomerase Activity. *Anal. Chem.* **81**, 255 (2008).
- 37 Zhou, X., Xing, D., Zhu, D. & Jia, L. Magnetic beads-based electrochemiluminescence assay for rapid and sensitive detection of telomerase activity. *Electrochem. Commun.* **10**, 564 (2008).
- 38 Namba, Y., Usami, M. & Suzuki, O. Highly Sensitive Electrochemiluminescence Immunoassay Using the Ruthenium Chelate-Labeled Antibody Bound on the Magnetic Micro Beads. *Anal. Sci.* **15**, 1087-1093 (1999).
- 39 Rubinstein, I., Martin, C. R. & Bard, A. J. Electrogenerated chemiluminescent determination of oxalate. *Anal. Chem.* **55**, 1580 (1983).
- 40 Rubinstein, I. & Bard, A. J. Electrogenerated chemiluminescence. 37. Aqueous ecl systems based on tris(2,2'-bipyridine)ruthenium(2+) and oxalate or organic acids. *J. Am. Chem. Soc.* **103**, 512 (1981).
- 41 Downey, T. M. & Nieman, T. A. Chemiluminescence detection using regenerable tris(2,2'-bipyridyl)ruthenium(II) immobilized in Nafion. *Anal. Chem.* **64**, 261 (1992).
- 42 Milutinovic, M., Sallard, S., Manojlovic, D., Mano, N. & Sojic, N. Glucose sensing by electrogenerated chemiluminescence of glucose-dehydrogenase produced NADH on electrodeposited redox hydrogel. *Bioelectrochem.* **82**, 63 (2011).
- 43 Sentic, M. *et al.* Electrochemiluminescent swimmers for dynamic enzymatic sensing. *Chem. Comm.* **50**, 10202-10205 (2014).
- 44 Dennany, L., O'Reilly, E. J., Keyes, T. E. & Forster, R. J. Electrochemiluminescent monolayers on metal oxide electrodes: Detection of amino acids. *Electrochem. Commun.* **8**, 1588 (2006).
- 45 Xue, L., Guo, L., Qiu, B., Lin, Z. & Chen, G. Mechanism for inhibition of /DBAE electrochemiluminescence system by dopamine. *Electrochem. Comm.* **11**, 1579-1582 (2009).
- 46 Kirschbaum, S. K. & Baeumner, A. A review of electrochemiluminescence (ECL) in and for microfluidic analytical devices. *Anal. Bioanal. Chem.*, 1-16 (2015).
- 47 Klymenko, O. V., Svir, I. & Amatore, C. A New Approach for the Simulation of Electrochemiluminescence (ECL). *ChemPhysChem* **14**, 2237-2250, doi:10.1002/cphc.201300126 (2013).
- 48 Amatore, C., Fosset, B., Maness, K. M. & Wightman, R. M. Theory of electrochemical luminescence at double band electrodes. An examination of "steady-state" diffusion at ultramicroelectrodes. *Anal. Chem.* **65**, 2311-2316 (1993).
- 49 Aouani, H. *et al.* Optical-fiber-microsphere for remote fluorescence correlation spectroscopy. *Opt. Express* **17**, 19085 (2009).
- 50 Wenger, J., Gérard, D., Aouani, H. & Rigneault, H. Disposable Microscope Objective Lenses for Fluorescence Correlation Spectroscopy Using Latex Microspheres. *Anal. Chem.* **80**, 6800-6804 (2008).
- 51 Xue, L., Guo, L., Qiu, B., Lin, Z. & Chen, G. Mechanism for inhibition of /DBAE electrochemiluminescence system by dopamine. *Electrochem. Commun.* **11**, 1579-1582 (2009).
- 52 Wang, S. *et al.* Electrochemical and Electrogenerated Chemiluminescent Studies of a Trinuclear Complex, $[\text{((phen)}_2\text{Ru}(\text{dpp}))_2\text{RhCl}_2]^{5+}$, and Its Interactions with Calf Thymus DNA. *Anal. Chem.* **81**, 4068 (2009).

- 53 Parveen, S. *et al.* Electrogenerated chemiluminescence of /2-(dibutylamino)ethanol system. *J. Electroanal. Chem.* **688**, 45-48 (2013).
- 54 Suraniti, E. *et al.* Electrochemical Detection of Single Microbeads Manipulated by Optical Tweezers in the Vicinity of Ultramicroelectrodes. *Anal. Chem.* **85**, 8902-8909 (2013).
- 55 Fosdick, S. E., Anderson, M. J., Nettleton, E. G. & Crooks, R. M. Correlated Electrochemical and Optical Tracking of Discrete Collision Events. *J. Am. Chem. Soc.* **135**, 5994-5997 (2013).
- 56 Amatore, C., Bouret, Y., Maisonhaute, E., Goldsmith, J. I. & Abruña, H. D. Precise Adjustment of Nanometric-Scale Diffusion Layers within a Redox Dendrimer Molecule by Ultrafast Cyclic Voltammetry: An Electrochemical Nanometric Microtome. *Chem. Eur. J.* **7**, 2206-2226 (2001).
- 57 Nunige, S. *et al.* Reactivity of Surfaces Determined by Local Electrochemical Triggering: A Bromo-Terminated Self-Assembled Monolayer. *Angew. Chem. Int. Ed.* **51**, 5208-5212 (2012).

Chapter 3:
**Immunosensing and Mapping the ECL generation with
nanoelectrodes ensembles and arrays**

3.1. Introduction

Since its discovery, ECL has been widely studied and applied, with a focus on development of new and sensitive analytical methods and devices.¹ An important upturn for development of diagnostic biosensors, widening the area of application²⁻⁴, was the discovery of aqueous ECL systems using co-reactants and operating at physiological pH.^{2,5,6} In addition to the already-mentioned benefits of the technique,⁷⁻⁹ deciphering the ECL mechanisms, in particular mechanistic route at low oxidation potentials, brought an essential advantage in development of new analytical strategies with improved sensitivity.¹⁰ Spatial reactivity mapping by ECL imaging resolved at the single bead level pictured how ruthenium centres located at micrometric distances from the electrode generate ECL by oxidation only of co-reactant.¹¹ Also, it highlights the importance of the contribution of the “revisited” route in overall ECL response (signal). On the other side, the booming trend in the use of nanosized devices can further enhance the merits of the technique.^{12,13} Advances in bioelectroanalytical applications of nanostructured electrodes, nanoelectrode ensembles (NEEs) and arrays (NEAs), can further improve the sensitivity of ECL methods due to its known properties, enhanced mass fluxes and dramatic enhancement of the signal-to-background current ratio.¹⁴⁻¹⁷ The group of Prof. Paolo Ugo developed immunosensors for determination of the cancer biomarker HER2 (human epidermal growth factor receptor) and DNA hybridization, immobilizing the biorecognition layer in the vicinity of the nanoelectrodes, precisely on a non-conductive component of the electrodes (e.g. on the polycarbonate, PC of the NEE).¹⁸⁻²⁰ In such arrangements, the enhanced mass transport typical of nanoelectrodes is fully exploited. Moreover, in contrast to the classical biosensor concept²¹⁻²³, in ECL-based biosensors, immobilization of luminophore labeled biomolecule at a distance from the active surface of the nanoelectrodes, enables ECL generation at low oxidation potentials. Applying such lower potentials might avoid damages on sensitive proteins and oligonucleotides, interferences from side reactions particularly in real samples of complex matrix (e.g. blood) and oxide layer formation on Au and Pt electrodes resulting in poor analytical reproducibility⁶. Combining above specified properties of ECL technique and NEEs, herein, we propose design of a novel immunoassay for celiac disease diagnostic utilizing an original detection strategy. Although “the gold standard” for definitive diagnosis of this gluten-dependent autoimmune disorder is still tissue biopsy based on histological changes in small intestinal mucosa, serological test for CD screening based on detection anti-transglutaminase (anti-tTG) type-2 antibodies are less

invasive²⁴. Many trials have been made to develop variety of electrochemical methods^{3,22,23,25} but, so far, no single confirmatory serological method has been adopted for practical use.

Ordered arrays of nanoelectrodes have been used for diverse bioanalytical applications, although detailed electroanalytical characteristics have been described only very recently. For instance, detection of prostates specific antigen and fabrication of multiplex biosensors have been described^{26,27}. Still, a very few studies dealt with the use of NEAs as electrochemical generator of ECL. To this aim, arrays of boron-doped-diamond (BDD) nanodisk and nanoband electrodes with different dimensions and inter-electrode distances were prepared by e-beam lithography²⁸. BDD is a promising material particularly attractive for ECL studies thanks to its high chemical and electrochemical stability, satisfactory electrical conductivity owing to the doping, wide potential window accessible and applications for medical diagnostics.²⁹

Therefore, in the first part of this chapter, nanofabrication techniques, electrochemical behavior and specific advantages of NEEs and NEAs will be described. In the second part, a novel immunoassay for CD diagnostic will be presented. Finally, in the third part ECL imaging and tuning of luminescence with arrays of nanoelectrodes will be demonstrated. The work presented in the following chapter was done in collaboration with Prof. Paolo Ugo from the University Ca' Foscari of Venice (Italy), Department of Molecular Science and Nanosystems.

3.2. Nano-Electrode Ensembles (NEEs) fabrication

Nanoelectrodes may be defined as electrodes having at least one dimension (called critical dimension) in the nanometer range. This determines unique physico-chemical properties described below. The first template synthesis of NEEs for electrochemical use was described by Menon and Martin¹⁴ who deposited gold nanofibres with a diameter as small as 10 and 30 nm within the pores of track-etched polycarbonate (PC) membranes by a chemical (electroless) deposition. The ensemble of metal nanodisc electrodes randomly distributed in the insulating polymer is presented in a schematic diagram of the NEE structure in Figure 1. In comparison, if the ensemble of nanoelectrodes is arranged in an ordered manner, owing to nanometric resolution-fabrication techniques, we can obtain well-ordered arrays in NEAs. Since all nanoelectrodes are interconnected in these systems, they all experience the same applied potential and behave usually as a sum of nanosized-electrochemical sensors.

Membrane-templated synthesis is based on the idea that the pores of a host material can be used as a template to direct the growth of new conductive materials. In the template synthesis of nanoelectrodes, each pore of the membrane is filled with a metal nanowire or nanofibre. Growth of the metal fibres can be achieved by use of both electrochemical³⁰ or electroless^{14,31,32} methods of deposition.

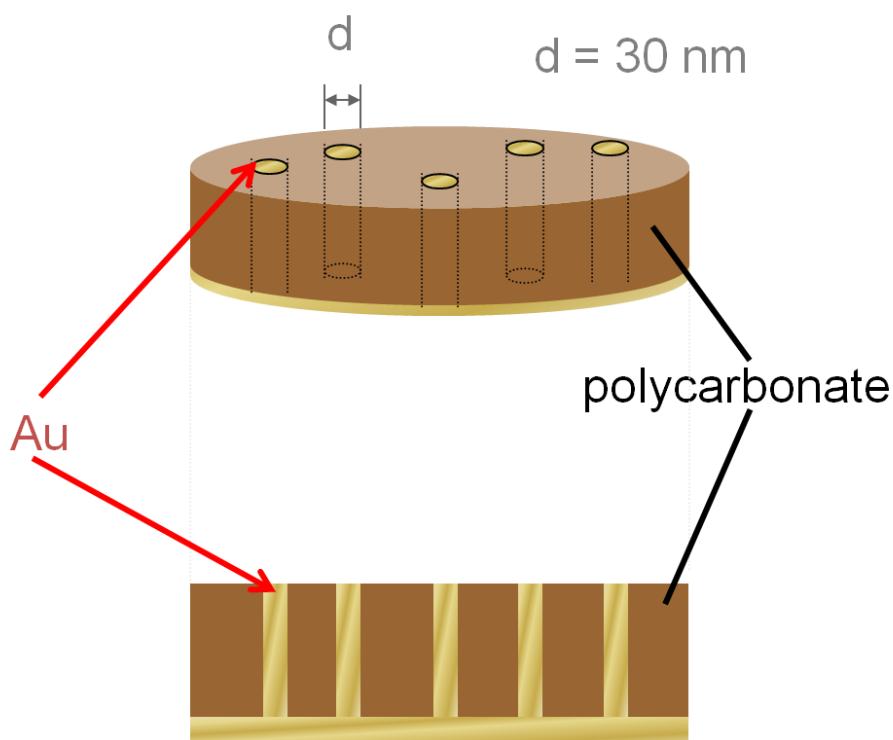


Figure 1. Schematic diagram of a nanoelectrode ensemble in a template membrane.

In both methods of deposition, the pore density of the template determines the number of metal nanoelectrode elements on the NEE surface and, correspondingly, the average distance between them, whereas the diameter of the pores in the template determines the diameter of the individual nanoelectrodes. Track-etched membranes with pore diameters ranging from 10 nm to 10 μm are commercially available. Electrochemical deposition inside the pores of a nanoporous membrane requires that one side of the membrane is conductive. Deposition can be performed under potentiostatic or galvanostatic conditions. In electrochemical template deposition, the coated film is placed in an electrochemical cell, and acts as the cathode whereas the counter electrode is the anode. Electrodeposition of metals has been used to obtain nanowires not only of gold, but also of other materials.

Electroless deposition involves chemical reduction of a metal salt from solution to metal on a surface. The principles of electroless deposition on nanoporous membranes are exemplified by the Au deposition method developed in Charles Martin's laboratory for template fabrication of gold nanowires, nanotubes, and other shaped gold materials¹⁴. The following procedure was used for NEEs exploited in our immunoassays described below.

The process based on an electroless deposition of gold can be divided in four steps:

1. "sensitization" of the membrane, during which Sn^{2+} ions are adsorbed by the substrate;
2. deposition of Ag nanoparticles by reduction of an Ag^+ solution by the adsorbed Sn^{2+} ions;
3. galvanic displacement of the Ag particles by reduction of a Au(I) solution;
4. catalytic reduction of more gold on the deposited Au nuclei, by addition of a reducing agent (formaldehyde).

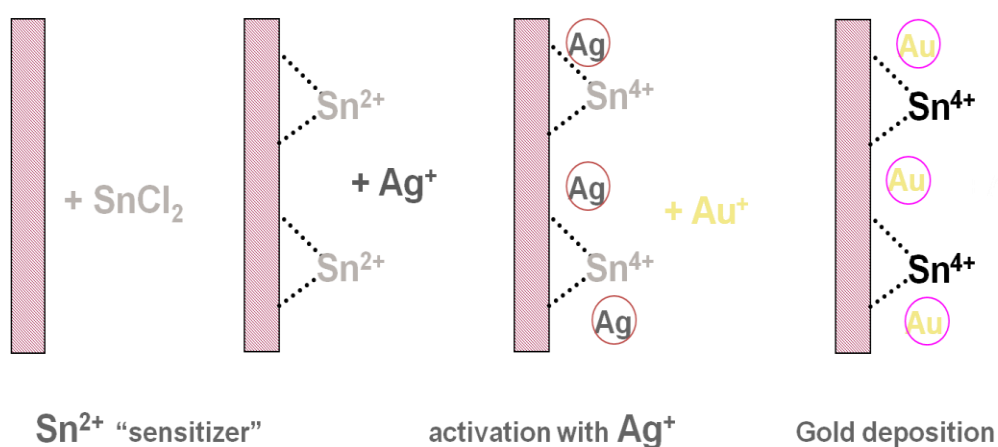


Figure 2. Schematic representation of electroless deposition.

NEEs ready to be used in an electrochemical experiment are shown in Figure 3. The surface of the ensemble exposed to the solution defines the geometric area of the NEE (A_{geom} , area of the nanodiscs plus the insulator area).

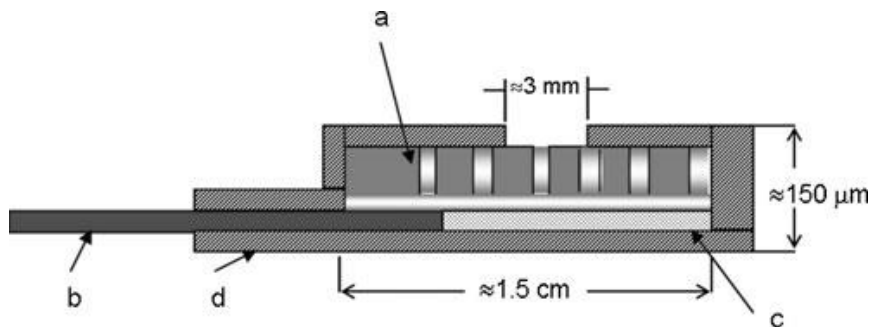


Figure 3. Schematic representation of a NEE section, prepared by using a track-etched polycarbonate membrane as template: (a) track-etched membrane incorporating gold nanofibers or nanowires; (b) copper adhesive tape with conductive glue to connect to instrumentation; (c) aluminium adhesive foil with nonconductive glue; (d) insulating tape. Note: the dimensions of the pores (nanofibres) are only indicative and not to scale³³.

3.3. Nano-Electrode Arrays (NEAs) fabrication

Techniques such as electron beam lithography (EBL)³⁴, ion beam lithography¹², nanoimprint³⁴, enable one to achieve high resolution nanostructuring, i.e. precise positioning and sizing down to a scale of a few nanometres. This spatial resolution capability has been exploited to prepare ordered arrays of nanoelectrodes^{12,34,35}. These techniques generally consist in three successive steps (Figure 4):

- Coating a substrate with irradiation-sensitive polymer layer (resist);
- Exposing the resist to light, electron or ion beams;
- Developing the resist image with a suitable chemical.

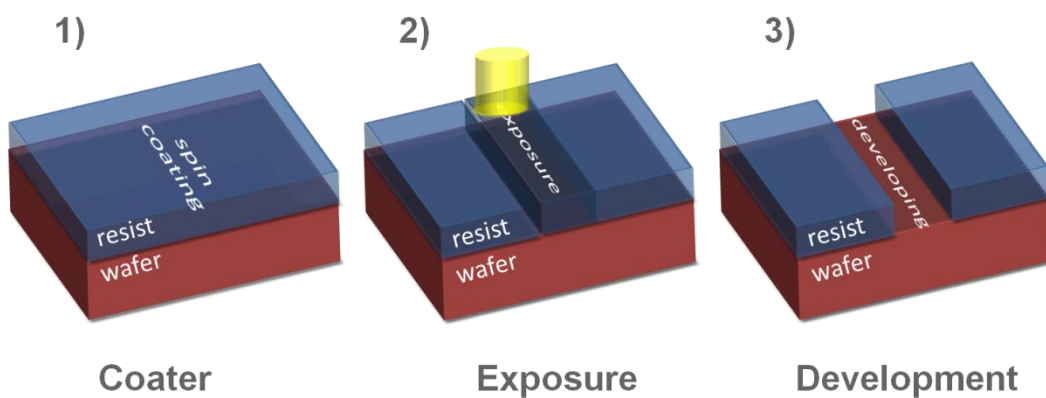


Figure 4. Representation of the main lithographic steps for NEA fabrication.

Exposures can be achieved either by scanning a focused beam, pixel by pixel from a designed pattern, or by exposing through a mask for parallel replication. The response of the resist to the exposure can be either positive or negative, depending on whether the exposed or unexposed portions will be removed from the substrate after development. In case of a so-called “positive resist” the effect of the exposure is the cutting of polymeric chains in smaller molecular weight fragments that are then dissolved in an appropriate developer. In case of a “negative resist” the exposure causes instead the cross-linking of the polymer. Recent study demonstrated that PC, also, can be used as a high-resolution resist for e-beam lithography³⁶. It is worth stressing that PC, in addition to its low cost, has the advantage of being suitable for easy chemical functionalization with biomolecules, by using well-known functionalization procedures, through amide linkage.²⁰ In addition to the characteristics of the electron beam, the success of lithography depends also on the choice of the resist, the subsequent development and post-processing.

3.4. Electrochemistry at nanoelectrode ensembles and arrays

NEE/NEAs can be considered as an assembly of extremely small ultramicroelectrodes separated by an electrical insulator interposed between them³⁷. An ultramicroelectrode is considered as an electrode with at least one dimension comparable or lower than the thickness of the diffusion layer (typically < 25 μm)³⁸. At such small dimensions, edge effects from the electrode become relevant and diffusion from the bulk solution to the electrode surface is described in terms of radial geometry instead of the simpler linear geometry used for larger electrodes (> 100 μm), as illustrated in Figure 5. Linear diffusion at macroelectrodes is characterised by peak-shaped responses in voltammetry, with the peak current (I_p) being given (for a reversible system) by the Randles–Ševčík equation:

$$I_p = 2.69 \times 10^5 n^{3/2} A_{\text{geom}} \nu^{1/2} D^{1/2} c^b \quad (1)$$

where n is the number of electrons transferred, A is the geometric area of the electrode, c^b is the bulk concentration, D is the diffusion coefficient and ν is the voltage scan rate. F , R and T have their usual meanings³⁸.

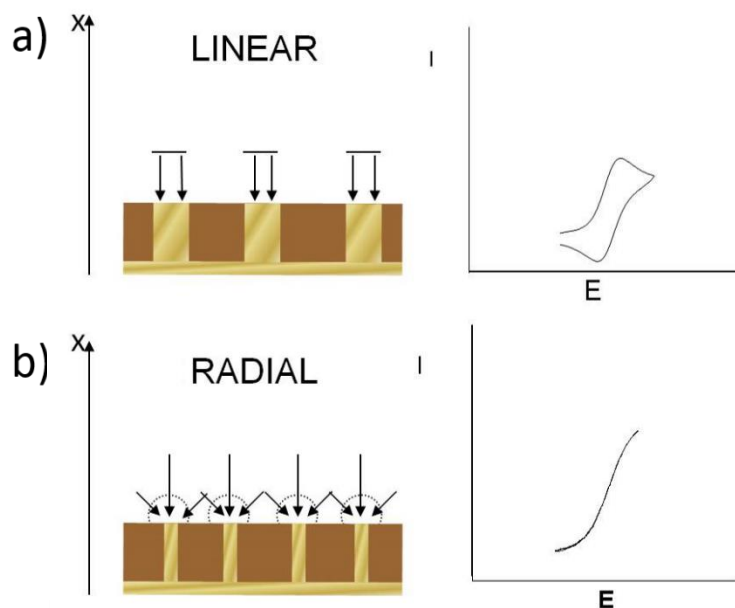


Figure 5. Schematic diagram of linear (a) and radial (b) diffusion geometries occurring at electrode arrays and corresponding current vs. potential (E/I) curves.³⁹

Under radial diffusion conditions the voltammograms' shape is sigmoidal, and the limiting current (I_{lim}) of the plateau, is the crucial analytical parameter directly related to analyte concentration. In fact, due to the small size of the nanoelectrodes in NEE/NEA, a spherical diffusion field (three dimensional) is easily reached and produce steady-state voltammograms (i.e. sigmoidal shape). This voltammogram shape is independent of the nanoelectrode geometry³⁹.

Generally, the nanoelectrode critical parameter (i.e. radius of the disc) is extracted by applying a suitable model for the steady-state current. Figure 6 illustrates the possible diffusion modes and the corresponding steady-state current (limiting current) equations for hemisphere, inlaid disc and recessed disc electrodes geometries¹².

By decreasing the electrode size from micrometer to nanometer scale, the study of faster electrochemical and chemical reactions is possible. This is because at very high rates of mass transport, the electron transfer process is less limited by the mass transport of reactant to the electrode surface^{40,41}. Furthermore, steady-state responses can be reached, which decreases dramatically charging-capacitive currents. The main disadvantage of using individual nanoscale electrodes is the extremely small current that can be achieved with them. For this reason, the development of ensemble of nanoelectrodes operating in parallel has attract a great

deal of interest. Even better performances are available when this ensemble is arranged in an ordered manner with a controlled inter-electrode spacing, more precisely with arrays.

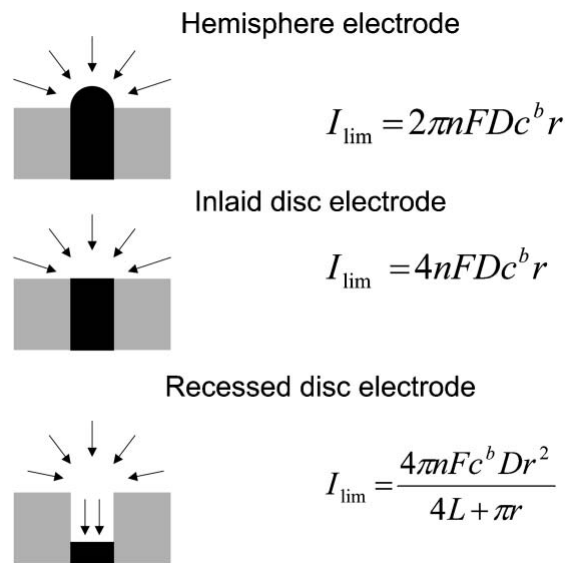


Figure 6. Three main nanoelectrode geometries: hemispherical electrode, inlaid disc electrode and recessed disc electrode; schematic diffusion geometries and the equations for the corresponding steady-state limiting currents: r is the electrode radius and L is the recession depth of the electrode¹².

Moreover, NEE/NEA can exhibit different diffusion regimes. According to the model proposed by Guo and Lindner⁴², diffusion regimes occurring at an array of ultramicroelectrodes can be divided into five categories (Figure 7) depending on the scan rate or the reciprocal distance among the nanoelectrodes:

- (I) planar diffusion toward each microelectrode;
- (II) mixed diffusion over each microelectrode (transition between planar and hemispherical/radial diffusion);
- (III) diffusion toward each hemispherical microelectrode;
- (IV) diffusion mixed with onset of overlap of diffusion layers;
- (V) planar diffusion over the entire array (total overlap diffusion).

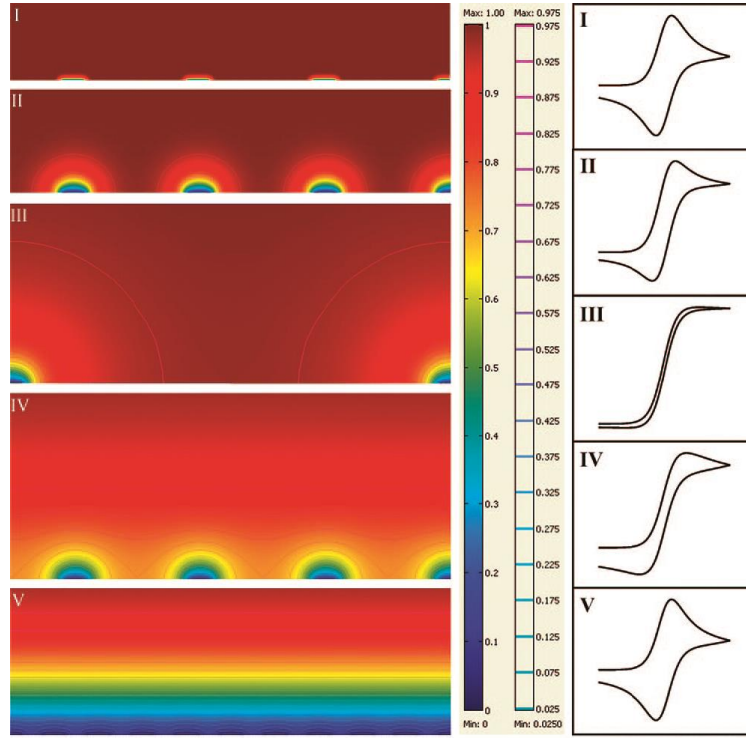


Figure 7. Simulated concentration profiles, with isoconcentration contour lines, over an ultramicroelectrode array representing the five main categories of diffusion modes (forms I to V). In the scale bar next to the figure, the red color represents the bulk concentration and the blue colour represents zero concentration. The second scale bar represents a relative concentration scale for the contour lines. Typical cyclic voltammograms obtained for each diffusion profile are shown at the right proposed by Guo and Linder⁴².

For ultramicroelectrodes, the thickness, $\delta(t)$, of the diffusion layer around the electrode is given by Eq. 2:

$$1/\delta(t) = [1/(\pi Dt)^{1/2}] + 1/r \quad (2)$$

t is the time of the experiment, and r is the radius of the electrode. As the electrode decreases in size, the diffusion layer thickness approaches the electrode dimensions. The steady-state diffusion-controlled limiting current, $I(t \rightarrow \infty)$, is inversely proportional to the diffusion layer thickness, in accordance with Eq. (3):

$$I(t \rightarrow \infty) = nFAc^b/\delta(t \rightarrow \infty) \quad (3)$$

where A is the electrode surface area. Dividing Eq. (3) by A reveals that smaller electrodes will exhibit higher current densities as a consequence of this enhanced mass transport.

As mentioned before, the characteristic of the time-dependent diffusion profile of NEEs/NEAs depends primarily on the relative inter-electrode spacing, d/r (where d is the

centre-to-centre distance between nanoelectrodes and r is their mean radius), as well as the scan rate, which determines the time-constant of the experiment.

In the case of widely spaced electrodes (with a large d/r ratio) or at high scan rates, diffusion of the electroactive species to each individual electrode remains independent of all others and linear diffusion predominates at each nanoelectrode (case I, peak-shaped voltammograms)³⁴. This is the regime that gives the higher Faradic current, therefore this is the regime of choice for obtaining the maximum improvement of detection limits when there are no constraints in increasing the distance between the nanoelectrodes.

When the radial diffusion-boundary layers totally overlap, i.e. when the diffusion hemisphere is larger than the mean hemidistance among the nanoelectrodes, NEEs/NEAs behave as a whole macroelectrode with regard to the Faradic current (total overlap, peak shape voltammograms, case V, but with peak currents much bigger than case I). Therefore, the diffusion-controlled current will be proportional to the geometric area, A_{geom} of the ensemble or array (i.e. active electrode surface as well as inter-electrode insulation, Eq. 4.). The background or charging current instead is proportional only to the active area of the electrode elements, A_{active} , in contrast to the conventional electrodes (CE) (Eq. 6)^{39,43}.

$$\text{Faradaic current at CE/NEE : } I_p = 2.69 \times 10^5 n^{3/2} A_{\text{geom}} v^{1/2} D^{1/2} C_b \quad (4)$$

$$\text{Background (charging) current at NEE : } I_c = A_{\text{active}} v C_d \quad (5)$$

$$\text{Background (charging) current at CE : } I_c = A_{\text{geom}} v C_d \quad (6)$$

By combining Eq. (4)–(6), we can obtain the ratio:

$$(I_p/I_c)_{\text{NEE}} = (I_p/I_c)_{\text{conv}} \times (A_{\text{geom}}/A_{\text{active}}) = (I_p/I_c)_{\text{conv}} / (A_{\text{active}}/A_{\text{geom}}) \quad (7)$$

$$f = \frac{A_{\text{active}}}{A_{\text{geom}}} \quad (8)$$

Where C_d is the double layer capacitance and f is the reciprocal of the fractional electrode area. This means that an effective enhancement of the signal (diffusion-controlled current) to noise (background or charging current) ratio is obtained. This represents an important advantage to the analytical use of NEAs and NEEs because the lowering of the background noise (related to the capacitive current) in an electrochemical measurement improves not only the detection limit but also the precision of the measurement⁴⁴.

In the case where the diffusion hemisphere becomes shorter or the hemidistance among nanodiscs is larger (higher scan rates compare to case V, but lower than in case I), the voltammetric response is dominated by radial diffusion conditions at each element (pure radial conditions, sigmoidal-shap voltammograms, case III). Obviously, intermediate situations can be observed (cases IV and II).

3.5. Bioelectroanalysis and biosensors with NEEs/ NEAs

The improved signal-to-noise ratio typical of NEEs, as detailed in Paragraph 3.3, with detection limits improved 2–3 order of magnitudes with respect to conventional microelectrodes,^{15,43} makes them extremely suitable for detection of electroactive species at low concentrations. Moreover, with the electrodes typically prepared by electroless deposition of gold within the pores of a nanoporous polycarbonate (PC) membrane^{14,15,17}, the pore diameter and pore density of the template determines the number and surface density of Au-nanoelectrodes. NEEs prepared with commercially available template membranes have high nanoelectrode densities, in excess of 10^8 pores cm^{-2} . As a consequence, these NEEs operate in the total-overlap response regime where the products of the electrochemical process are homogeneously diffusing away from the electrodes. Recently, the properties of NEEs were exploited to develop electrochemical biosensors in which high amounts of biorecognition layer is immobilized directly on the PC of the NEE¹⁵. In such a design, a useful electroanalytical signal is assured by the presence in the electrolyte solution of a substrate and/or redox mediator which, diffusing all over the geometric area of the NEE, can shuttle electrons to the redox labels bound onto the biorecognition layer¹³. Exploiting this idea, Pozzi *et al.* developed an immunosensor for determination of the human epidermal growth factor receptor HER2 in which a specific capture agent is bound to the templating PC of a NEE²⁰. In breast cancers, HER2 is over expressed, and causes cancer cells to reproduce uncontrollably. The mechanism for detection of this protein is presented in Figure 8. First, the monoclonal anti-HER2 antibody trastuzumab (commercially Herceptin) is immobilized on the polycarbonate of a NEE. The functionalized NEE is then incubated with the sample to capture the target protein HER2. Finally, the captured protein is reacted with a primary antibody (monoclonal CB-11) and a secondary antibody, labelled with horseradish peroxidase (HRP).

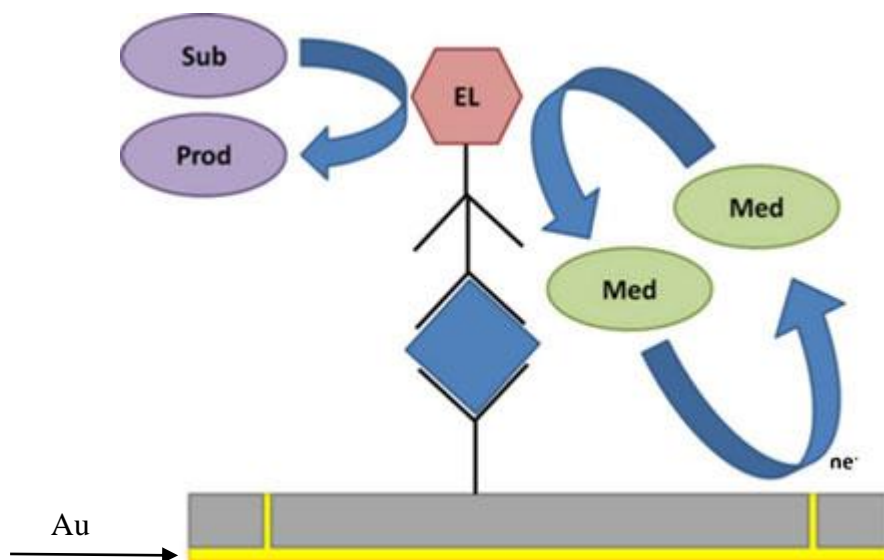


Figure 8. Schematic illustration of the HER2 detection mechanism. A specific antibody is first attached to the polycarbonate to capture the target protein (blue square). A primary antibody binds to the protein and, subsequently, a secondary antibody tethered with the enzyme label (EL)²⁰.

The biosensor is then dipped into phosphate buffer, used as an electrolyte, and containing the HRP substrate (i.e. H_2O_2) and the redox mediator methylene blue, which shuttles electrons from the nanoelectrodes to the active site of HRP. A similar approach has also been applied to the electrochemical detection of DNA sequences for virus genotyping^{18,19} and ligand proteins of interest for cultural heritage diagnostics⁴⁵. In the present work, we capitalized on the listed advantages of both ECL and NEEs properties to develop highly sensitive sensor for detection of celiac disease biomarkers.

Recently, the group of Paolo Ugo reported electrochemical biosensors for medical diagnostics based on BDD NEAs²⁸. Electrodes of BDD offer advantageous properties over conventional electrodes such as high reproducibility, stability, and robustness under extreme conditions. Also, they have shown an extremely wide potential window in aqueous solutions without oxidation of the electrode itself. BDD based NEAs were prepared by electron beam lithography in a thin film of PC. This approach leads to the formation of recessed nanoelectrodes working in pure radial diffusion conditions. When using PC as a novel electron beam resist, this allows the creation of structures of dimensions less than 100 nm; in addition, its chemical stability favors a long-term use for electrochemical detection and the possibility of its functionalization with biological molecules (DNA and proteins). PC surface of NEAs was successfully functionalized with small ss-DNA sequence, confirming the possibility of exploiting these systems as diagnostic biosensors.

E-beam writing of nanodot arrays on PC is briefly presented in Figure 9 and SEM image of prepared NEAs are shown in Figure 10.

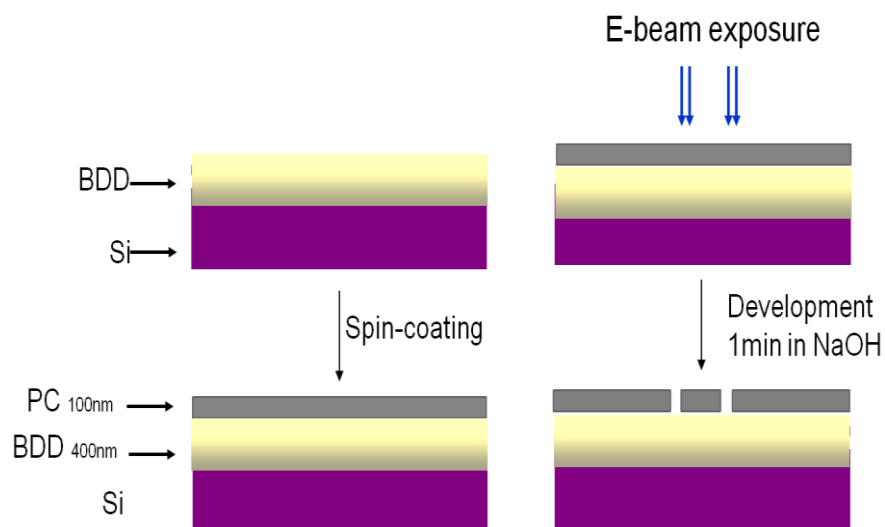


Figure 9. Schematic representation of the steps of E-beam writing of BDD nanodot arrays in a PC substrate.

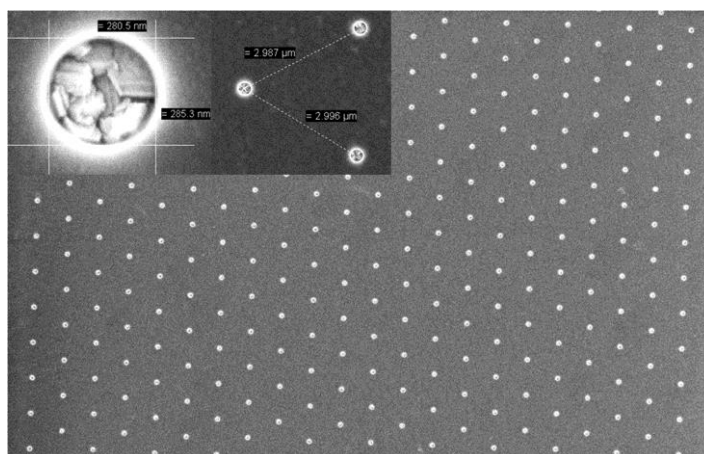


Figure 10. SEM images of a BDD-NEA prepared by e-beam writing; dots-nanoelectrodes are of 140 nm mean-radius and the interspacing distance is $3 \mu\text{m}^{28}$.

Carboxylic groups present on the surface of PC were further exploited for the immobilization of single-stranded DNA modified with fluorescein (using a carbodiimide/succinimide strategy). Before proceeding with the immobilization of the oligonucleotide probes, the carboxylic groups were activated enabling the reaction of $-\text{COOH}$ groups with the amino group of the ss-DNA. A microscopy image in fluorescence of a functionalized array is shown in Figure 11.

The fluorescence signal that can be observed around the nanoelectrodes indicates the successful immobilization of the oligonucleotidic probes in proximity of the nanoelectrodes.

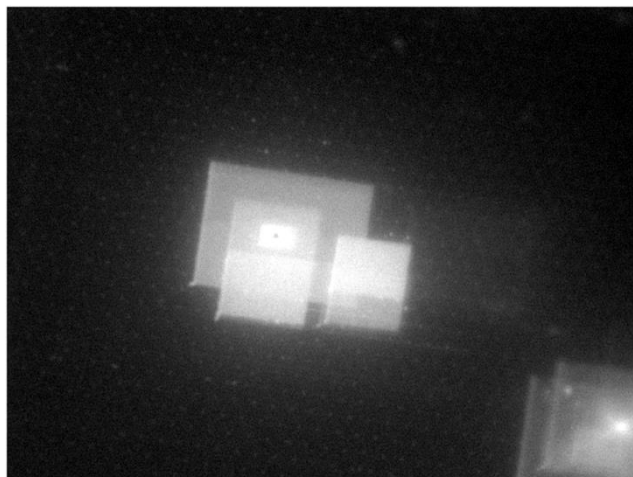


Figure 11. Fluorescence imaging of a NEA²⁸ functionalized by the single-stranded DNA modified with fluorescein

3.6. Highly sensitive ECL Sensor for Celiac Disease Biomarkers

Celiac disease is an autoimmune-mediated disorder that affects the gastrointestinal tract. It is characterized by inflammation of the small intestine upon ingestion of gluten, a protein made up of gliadins and glutenins²⁴. CD has a prevalence of 1% in the general population⁴⁶ with an increasing trend over time with aging⁴⁷. Certain patients can be asymptomatic for years, while clinical conditions of CD vary from mild to severe. Classical symptoms include gastrointestinal complaints (malabsorption, diarrhea) but the extra-intestinal symptoms represent the large majority of the clinical features such as osteoporosis⁴⁸, dermatitis herpetiformis⁴⁹, psychiatric and neurological disorders⁵⁰, arthritis⁵¹, cardiac⁵² and obstetric disorders⁵³. Early diagnosis and treatment with gluten-free diet, reduces the prevalence of CD-associated disorders, as well as mortality. Given the high prevalence of the CD and the implications of detecting it late, several simple, cheaper and rapid immunoassays were developed as a first step towards speeding up CD diagnosis in the physician's office^{54,55}. Tissue transglutaminase (tTG) is the main autoantigen that triggers antibodies production and the determination of the serum concentration of the anti-tTG antibodies, both immunoglobulin IgA and IgG, providing a powerful tool to screen the general population and to identify the individuals⁵⁶. Up-to-now, no single confirmatory serological method has been adopted for practical use, although many trials have been made to develop variety of analytical methods,

including electrochemical ones^{3,22,23,25,57}. Based on its successful use for many serological assays (see Chapters 1 and 2), ECL could be a powerful analytical method for future CD screening⁵⁸.

The principle of using ECL as the detection method of the target analyte anti-tTG combined with nanoelectrode ensembles properties is presented in Figure 12. First, the capturing agent tTG is adsorbed onto the PC surface of a NEE so that, when incubated with the sample, it will react with the target analyte anti-tTG, if present. The biorecognition chain is continued by the reaction of a biotinylated secondary antibody (sec-Ab-Bt) with the captured anti-tTG. Finally, a streptavidin-Ru(bpy)₃²⁺ derivative (SA-Ru(bpy)₃²⁺), used as ECL label, will bind to the sensor in case of positive analytical response. The ECL emission is triggered by addition of a co-reactant, TPrA (see chapter 2). Due to the customized architecture of the biosensor, oxidized TPrA acts both as a co-reactant and a redox mediator. The oxidized radicals generated at the electrodes, TPrA^{•+} and TPrA[•], diffuse toward the PC area of the NEE, to provide *in fine* an ECL signal by reaction with the non-diffusing ruthenium centers.

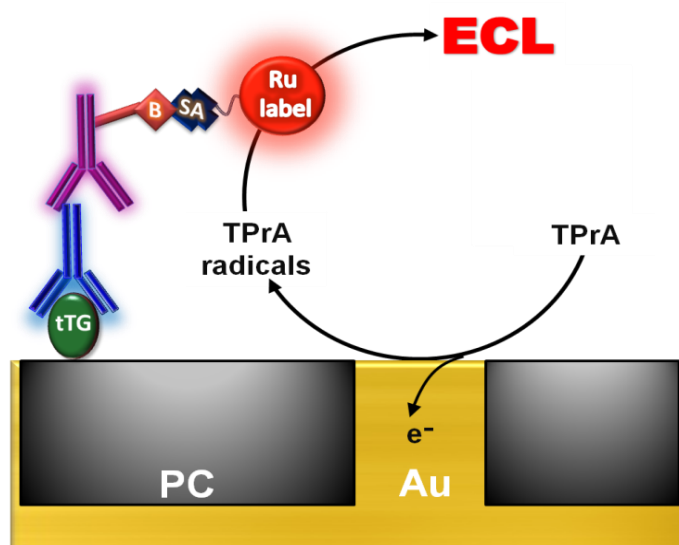


Figure 12. Schematic illustration of the anti-tTG detection mechanism. A capturing agent tTG is first attached to the polycarbonate surface to capture the target analyte anti-tTG (blue antibody). A biotinylated secondary antibody (sec-Ab-Bt, violet antibody) binds to the analyte and, subsequently a streptavidinated Ru(bpy)₃²⁺ derivative (SA-Ru(bpy)₃²⁺), the ECL label.

3.6.1. NEEs characterization

Prior to immunosensor construction, NEEs have been characterized. The FE-SEM images of a NEE prepared by electroless deposition of gold in the pores of track-etched PC filter membrane as a template are shown in Figure 13.^{31,44-46} NEEs were fabricated by H. Habtamu abd M. Ongaro from the University Ca' Foscari of Venice as described in the paragraph 3.2. The pores of the template are filled by Au-nanowires whose upper ends emerge on the surface of the template with the shape of nanodisks of approximately 50 nm diameter.

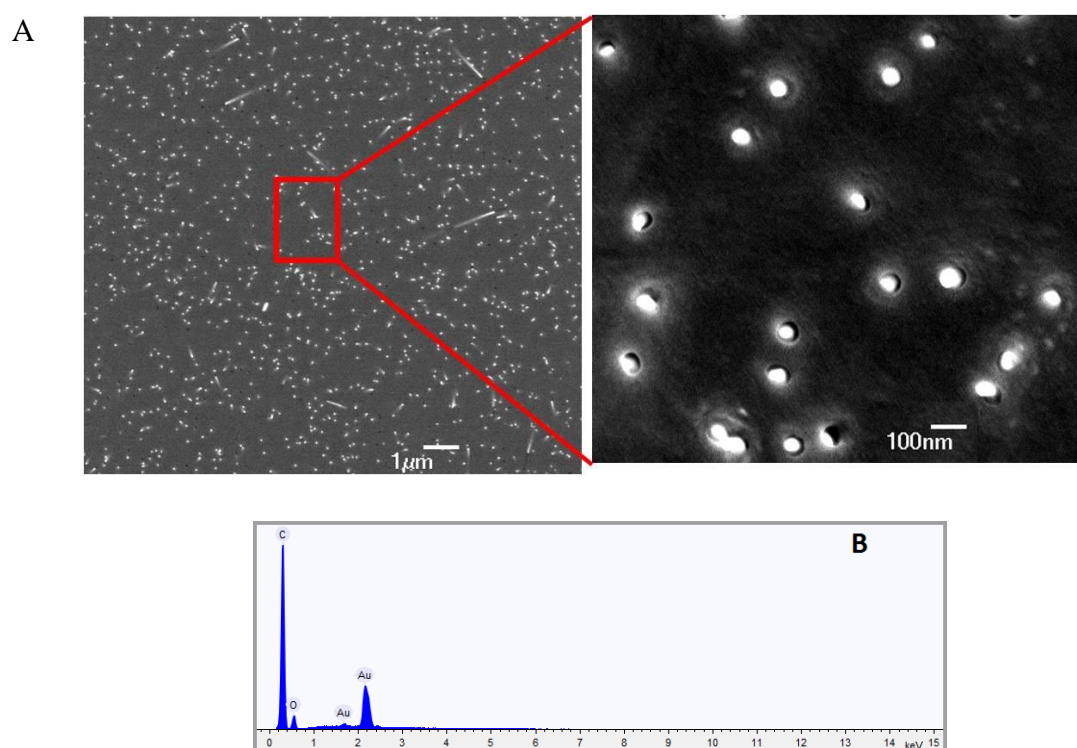


Figure 13. A) Field emission scanning electron microscopy (FE-SEM) images of a NEE at different magnifications. B) A plot of a NEE's surface elemental analysis using scanning electron microscopy-energy dispersive X-ray spectrometry (SEM-EDS).

The distance between the nanoelectrodes is rather variable, between 100 and 400 nm. The density of nanoelectrodes measured from different images is 5×10^8 electrodes.cm⁻². Furthermore, from the Figure 13B is clear that there is no impurities on the surface of the NEEs. All these morphological data substantially match with previous reports¹⁶.

The cyclic voltammetry characterization of the NEEs in 0.1 mM (ferrocenylmethyl) trimethylammonium hexafluorophosphate (FA⁺, PF₆⁻), used as a test redox probe, matches

with the theoretical expectations for NEEs; meaning that with the determined morphological characteristics, NEE operate under total overlap-diffusion condition³¹ (Figure 14).

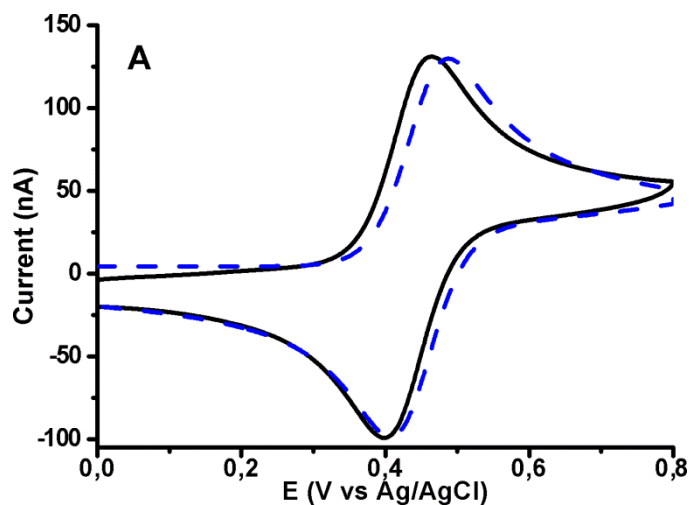


Figure 14. Experimental (solid line) and simulated (dashed line) cyclic voltammograms at a NEE recorded in 100 μM FA^+PF_6^- , 0.05 M phosphate buffer saline pH 6.8 at 50mV/s, A_{geom} is 0.07 cm^2 . Additional parameters used for the digital simulation: $E^\circ = 0.44$ V, $k^\circ = 0.007$ and $D = 4 \times 10^{-6}$ $\text{cm}^2 \text{sec}^{-1}$ where E° is the formal potential, k° and k_{app} are the standard and apparent heterogeneous electron transfer rate constants, respectively, and D is the diffusion coefficient.

3.6.2. Voltammetric and ECL characterization of the immunosensor

The functioning scheme of the sensor was summarized in Figure 12. At first, the tTG antigen is immobilized on the PC component of NEEs *via* formation of an amide bond between the protein and the carboxylic groups present on the PC surface^{18,20,45}. The tTG-NEE is subsequently blocked with 1% bovine serum albumin (BSA) to avoid non-specific binding on free binding sites of the PC and Au surfaces. The blocked tTG-NEE is then incubated with sample solutions eventually containing the anti-tTG. After a thorough washing step with PBS-Tween, the captured primary antibody is coupled with biotinylated goat anti-mouse (or antihuman) secondary antibody. Finally, the reporter Ru(bpy) complex is incorporated *via* biotin-streptavidin affinity binding for the detection and quantification of the analyte. After addition of TPrA to the electrolyte solution, the ECL response is obtained by scanning the potential between 0 and 1.6 V vs Ag/AgCl (scan rate of 100mV/s). Cyclic voltammogram and ECL curves for anti-tTG are presented in Figure 15.

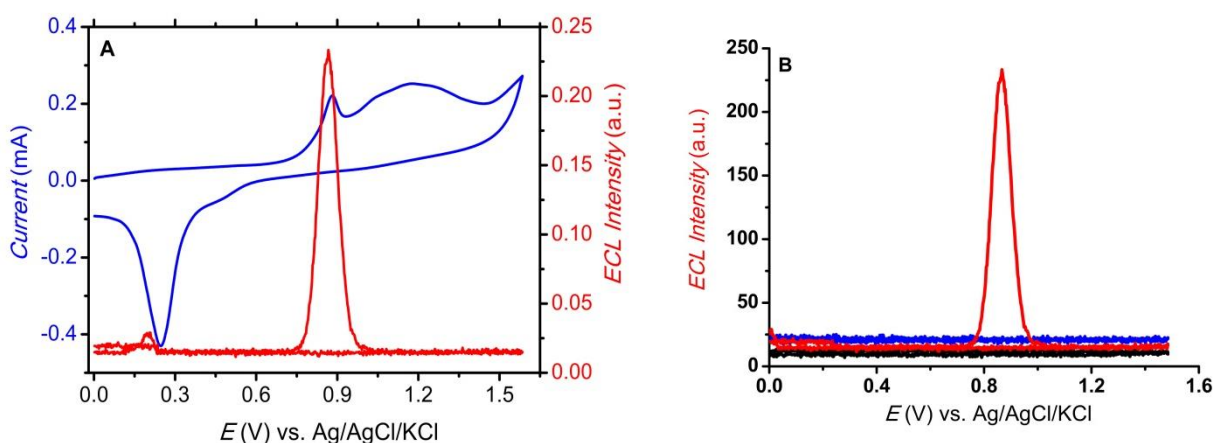


Figure 15. A) Cyclic voltammogram (blue) at scan rate of 100mV/s and the corresponding ECL signal (red) of the anti-tTG immunosensor in solution of 0.1M PBS pH 7.4 containing 0.1M TPrA; B) ECL plots of bare NEE (black), negative control –without anti-tTG (blue) and immunosensor (red) in solution as in A.

The ECL curve in Figure 15A reveals the presence of one intense ECL peak, detected at a potential of +0.87 V vs Ag/AgCl during the course of the anodic scan. This ECL signal is emitted at the reported-oxidation potential of TPrA, but well ahead of the oxidation potential of $\text{Ru}(\text{bpy})_3^{2+}$ ⁵⁹. This matches with a well-defined oxidation peak at 0.9 V on the CV curve. Furthermore, a broad sequential peak appears at 1.17 V, which is at about the usual potential for ruthenium oxidation. In the absence of an ECL emission at the potential of the second peak, results indicate that only the oxidation of co-reactant contributes to the ECL response. Dealing with gold NEEs one can assign this peak at more positive anodic current potential to the well-known Au-oxides formation^{17,60}. To confirm the ECL signal at the potential for oxidation of TPrA and to distinguish the second peak appearance either from non-specific binding of ruthenium label, or from Au-oxide generation, differential pulse voltammetry experiments have been performed. A set of experiments have been done with a bare NEEs only in TPrA or $\text{Ru}(\text{bpy})_3^{2+}$ solution at different concentrations.

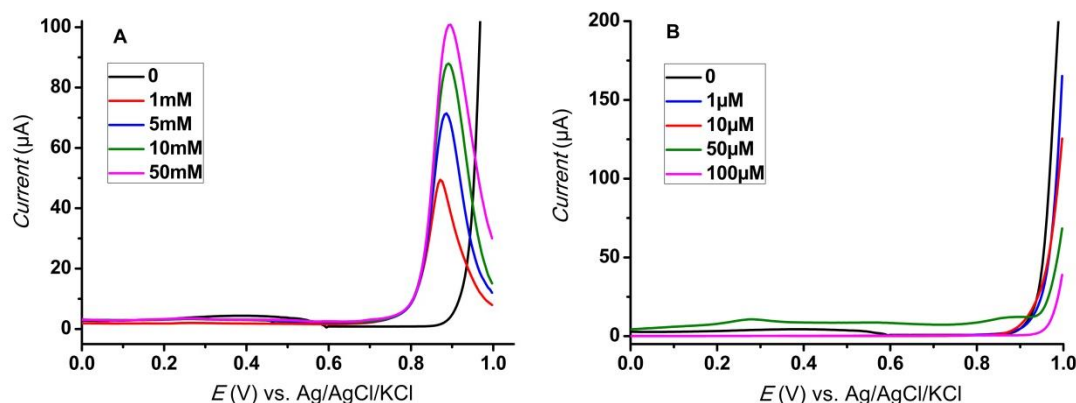


Figure 16. Differential pulse voltammograms recorded at bare NEEs in 0.1M PBS pH 7.4 containing different concentrations of A) TPrA or B) Ru(bpy)₃²⁺.

Differential pulse voltammetry (DPV) was preferred to cyclic voltammetry in order to maximize separation between possibly-overlapping peaks corresponding to the oxidation of ruthenium moiety and gold. The peak in the differential pulse voltammogram for the direct oxidation of TPrA is detected with bare NEEs in TPrA solution. Figure 16A shows that wave peaking at 0.9 V *vs.* Ag/AgCl/KC increases progressively with the TPrA concentration as expected, e.g. in the 1-50 mM range. The current curves for differential pulse voltammograms, running in the presence of different concentrations of Ru(bpy)₃²⁺ dissolved in solution with no TPrA added, confirm also that the ruthenium⁶¹ complex is not oxidized at this potential value (Figure 16B). The increase in anodic current at potential > 0.9 V, detected at the bare NEE in pure electrolyte (black curve), is therefore related to the formation of gold oxides. All results confirm that the current peak detected at 0.9 V in Figure 15A is related to the direct electrochemical oxidation of TPrA.

The absence of measurable ECL at potential greater than +1.0 V on repetitive scanning indicates that direct oxidation of Ru(bpy)₃²⁺ at the surface of the nanodisks is not taking place. All these data lead to the conclusion that electrochemical oxidation of TPrA onto the nanoelectrodes provide a flux of oxidation products, namely TPrA^{•+} radical cations, diffusing from the electrode surfaces. As total overlap-diffusion conditions hold, both the in and out fluxes of reagent and product, respectively, will cover the overall geometric surface of the NEE. While diffusing away from the nanoelectrodes, TPrA^{•+} is deprotonated forming TPrA[•] radical species. Both radical species are involved in the ECL generation, following the “revisited” route operating at low operating potential (LOP)^{10,11,62}. Finally, the ECL signal is

thus obtained by mediated oxidation of the $\text{Ru}(\text{bpy})_3^{2+}$ centers bound to the biorecognition chain by oxidized TPrA products.

To show the effect of concentration of luminophore on ECL response, we performed experiments with ruthenium complex in immobilized form and free diffusive form in the electrolyte solution. The increase in concentration of the luminophore in immobilized state resulted in a corresponding increase in the intensity of the LOP wave unlike the increase in the concentration of the luminophore in the solution enhanced the intensity of the second wave diminishing the intensity of the ECL peak at LOP (Figure 17).

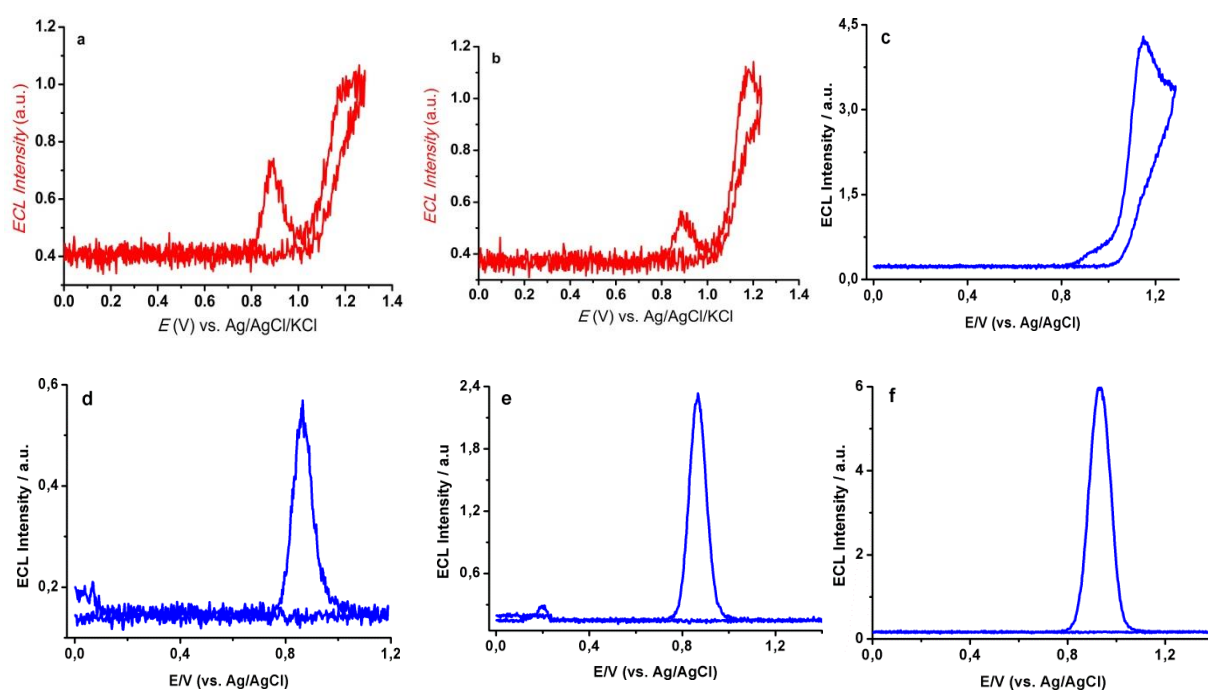


Figure 17. Effect of concentration and immobilization of luminophore on ECL intensity and potential of emission respectively, in 0.1M PBS pH 7.4 containing 0.1M TPrA; a-c) at bare NEE after adding a) 0.5, b) 1.0, and c) 10 μM $\text{Ru}(\text{bpy})_3^{2+}$ in the solution; d-f) at the immunosensor constructed of d) 0.5, e) 1, and f) 10 $\mu\text{g/mL}$ anti-tTG. Scan rate 100mV/s.

3.6.3. Analytical performances of the immunosensor

As standard human anti-tTG is unavailable on the market, the performances of the developed ECL based immunosensor were initially evaluated using serial dilutions of standard mouse anti-tTG IgG antibody. The ECL spectra for concentrations ranging from 1ng/mL to 5 $\mu\text{g/mL}$ are shown in Figure 18A. The ECL peak intensity was observed to increase progressively with the concentration of anti-tTG. The standard calibration curve in Figure 18B was plotted

using mean ECL values of triplicate measurements of different solutions at each concentration.

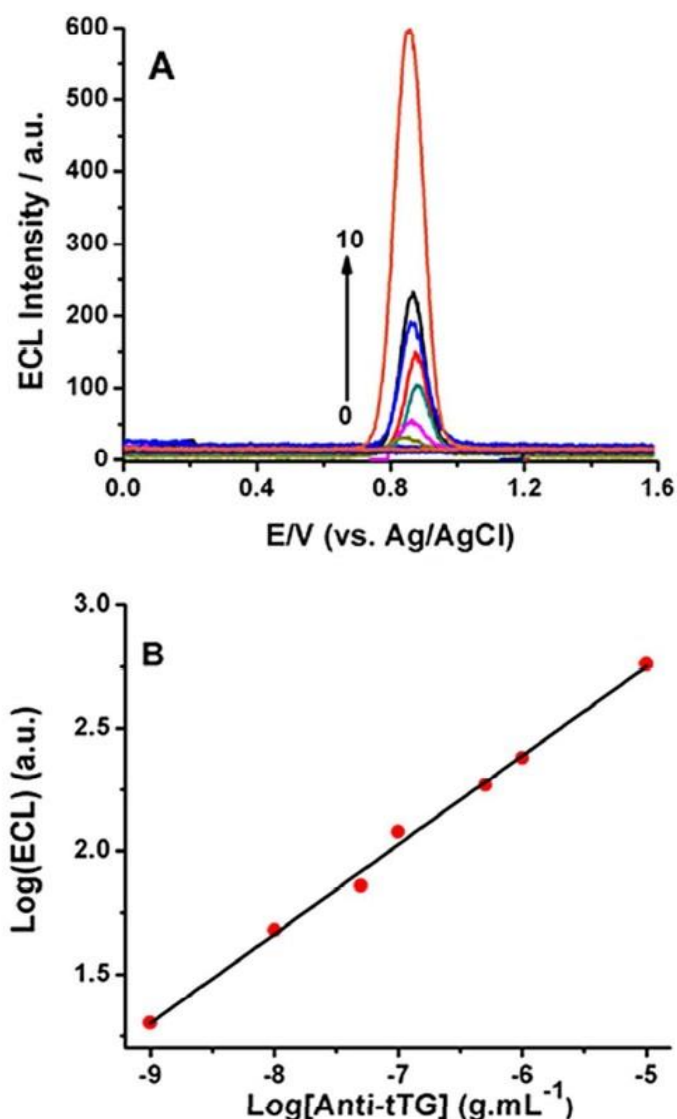


Figure 18. A) ECL response as function of Anti-tTG concentration (0.00, 0.001, 0.01, 0.05, 0.1, 0.5, 1 and 10 μM); B) Calibration curve developed from the average net ECL-peak amplitude ($n=3$). Experimental conditions are same as in Figure 15.

The logarithm of net ECL amplitude was directly proportional to the logarithm of concentration of anti-tTG within a wide range (i.e. 1 ng/mL to 10 $\mu\text{g/mL}$). The plot is linear in a log-log representation following the equation of $\text{Log}(\text{ECL}) = 0.379\text{Log}C + 1.679$ (unit of C is g/mL) with a correlation coefficient of 0.9959 and a limit of detection below 1ng/mL. In most of the ECL measurements using the immunosensor, stable ECL was obtained starting from the third scan.

The above results have shown the efficiency of the proposed immunosensor and correspondingly of its architecture, based on the biosensing protocol on the PC surface and on the ECL initiation at the nanoelectrodes. However, one may expect at least a weak ECL from the luminophores found in close proximity (within electron tunneling distance) from the surface of nanodisks. This may be attributed to one or more of the following reasons: (1) the protein layer formed may be thicker than the electron tunneling distance, (2) the nature of the PC close to the pores may be altered (low opening, deep recess) during industrial manufacturing processes so that biomolecules cannot be attached to the nanodisks, and electrons tunneling doesn't occur. On the other hand, absence of any ECL at the oxidation potential of $\text{Ru}(\text{bpy})_3^{2+}$ confirms that the nonspecific binding on the gold nanodisks is marginal. It further indicates the stability of the platform upon repetitive scans because occurrence of any sort of leaking of the sensor ladder into the electrolyte solution should allow the ruthenium tag to be directly oxidized at the surface of gold, with a resulting ECL emission at potentials > 1.0 V. Also, it supports studies concerning the sufficient stability of TPrA cation radical to react itself before its deprotonation supported in "revisited route". It is found that $\text{TPrA}^{\bullet+}$ can diffuse up to $3\mu\text{m}$ from the site of formation with half-life time of $0.2\text{ ms}^{10,11}$. In our immunosensor platform, the maximum distance of the luminophore corresponds to the vector sum of the distance that the tTG is bound from the Au surface and the contribution from the protein layer formed in the immunosensor construction steps. As the average edge-to-edge distance between the nanodisks is about 170 nm , a biomolecule located exactly at mid-way between two Au nanodisks i.e. 85 nm is the farthest point in platform. Due to the optimum distance of the luminophore from the nanodisks' surface and the excessive production of the radical cation at the interface, sufficient quantity of the two radicals seem to be available at the site of emission. As displayed in Figure 15B, the fact that a bare NEE immersed in PBS buffer containing 0.1 M TPrA didn't show any ECL, indicates that neither TPrA alone nor components of the buffer system used are not implicated for the ECL emission. Also, absence of ECL at the negative control (an immunosensor constructed in the absence of the analyte anti-tTG) implies lack of non-specific binding both on the polycarbonate and nanodisks' surfaces. It also confirms the effectiveness of our blocking step with 1% BSA solution and thorough rinsing with 0.05% Tween 20 surfactant before incubation with the biotinylated secondary antibody.

Reduction of the conventional ECL detection-oxidative potential of the $\text{Ru}(\text{bpy})_3^{2+}/\text{TPrA}$ system by about 300 mV offers the following analytical benefits. First, it significantly reduces

possible interferences from side reactions while dealing with samples of complex matrix like blood. The interferences could provide either background emission or quenching. Second, it reduces the ECL background arising from the reaction between $\text{Ru}(\text{bpy})_3^{3+}$ and hydroxide in aqueous systems⁶³. Third, in the development and use of biosensors, it minimizes electrical damage on susceptible biomolecules and oligonucleotide sequences, and lastly, it reduces the formation of an oxide layer on metal electrode surfaces particularly on Au and Pt, which eventually causes analytical reproducibility problems. Utilization of the nonconductive polymer of the NEEs as a biosensor platform provides other advantages besides maintaining the high signal-to-noise ratio of the electrode. Finally, this approach doesn't need the lengthy surface modification of metal electrode surface to load biorecognition elements.

3.7. Tuning of induced luminescence with arrays of nanoelectrodes (NEAs)

Different types of NEAs with precisely controlled geometries, have been reported for electroanalytical applications²⁸. As introduced above, NEAs offer significant advantages over larger electrodes, such as enhanced mass transport, improved faradic/capacitive currents ratio (i.e. extremely low detection limits), high miniaturization, possibility to be functionalized with various strategies³⁶. Despite such attractive features, no experimental study has ever been reported concerning the use of NEAs with controlled geometry as ECL generators. These observations prompted us to undertake the present study devoted to examine the characteristics of ECL generated by arrays of nanoelectrodes fabricated with a variety, but well-controlled range of geometries. To this aim, arrays of nanodisk and nanoband electrodes, with different dimensions and inter-electrode distances, were prepared by e-beam lithography on a polycarbonate layer deposited on boron-doped-diamond substrates. BDD consists of sp^3 hybridized carbon in a diamond lattice structure, where approximately one carbon atom in a thousand is replaced by an atom of boron. This imparts electrical conductivity to the material, BDD being one of the most attractive carbon substrates for electroanalysis due to the large potential window (up to 3V in aqueous electrolyte solutions), low background current, mechanical durability and resistance to surface fouling⁶⁴⁻⁶⁶. NEAs with 16 different geometries were fabricated on the same BDD sample-substrate (Figure 19) by Dr. Francesca Virgilio and Alessandra Zanut from the University of Trieste. This approach provides a platform of multiple arrays of nanoelectrodes (Multiple Nanoelectrode Array Platform, MNEAP) suitable to capture simultaneously in a single image the ECL emission from the different NEAs. ECL emission was induced using $\text{Ru}(\text{bpy})_3^{2+}$ as the ECL luminophore and

TPrA or dibutylaminoethanol (DBAE) as the co-reactant. Each MNEAP consisted in 16 small arrays of disks and bands. Each line of the sample includes a series of four arrays in which the centre-to-centre distance (for dots) or pitch (for bands) is kept constant, while the radius of disks or bands width is increased. Note that all the arrays are electrically connected by the BDD under-layer. This type of sample was fabricated in order to follow changes in the ECL reaction layer as a function of shape and inter-electrode distance.

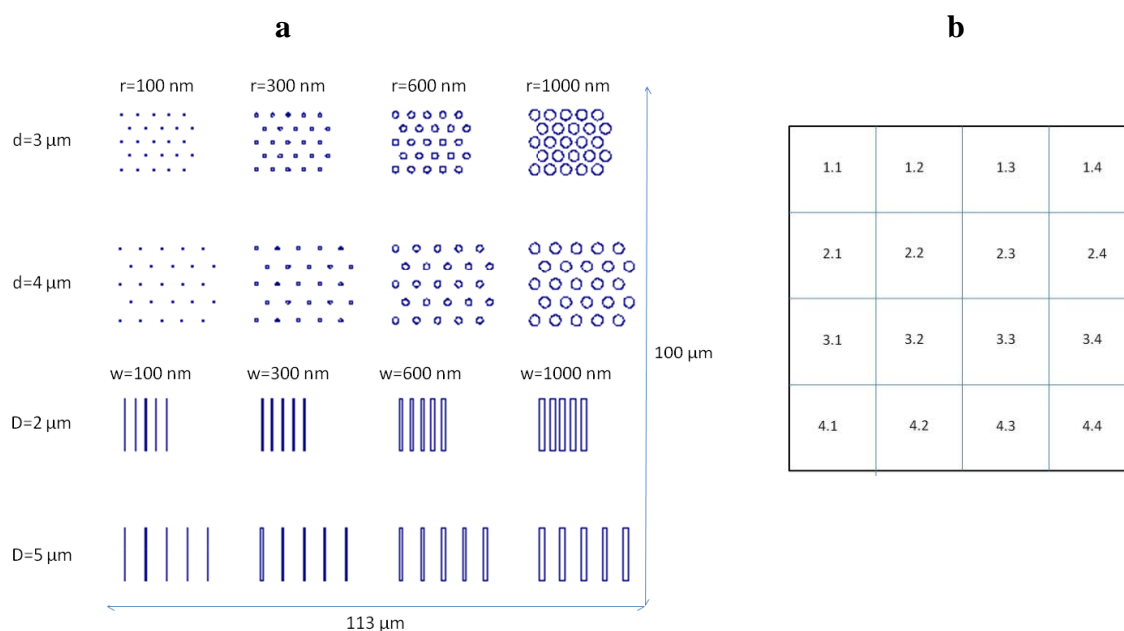


Figure 19. a) Schematic drawing of NEA fabricated for preliminary ECL experiments: r is the individual disk radius, d is centre-to-centre distance between them; D represents the pitch between bands and w is the width of each band; b) Identification key of the NEAs in the platform.

3.7.1. MNEAPs fabrication

The samples were fabricated by the following procedure:

- First, markers were created in order to easily locate the arrays with the microscope. Poly (methilmethacrylate)-coined PMMA 671.05 was spin-coated at 5000 rpm for 1 minute on a BDD substrate and subsequently annealed at 170 °C for 15 minutes. The EBL exposure of marker pattern was done using parameters summarized in Table 1.

Table 1. Summary of the conditions used for markers exposure.

Dose	400 $\mu\text{C}/\text{cm}^2$
Aperture	300 μm (mag 220)
Bake	170 $^{\circ}\text{C}$ for 15 minutes
Current	310 pA
Developer	IBMK:IPA=3:1
Temperature	RT

After development, samples were modified by CVD with 30 nm of chromium followed by lift off in hot $(\text{CH}_3)_2\text{CO}$ in order to obtain BDD substrate with metallic markers. Then, the sample was treated with O_2 plasma for 15 seconds and a layer of PC was deposited on it by spin coating. Structures reported in Figure 19a were exposed by EBL. Process parameters are reported in Table 2.

Table 2. Conditions used for NEA fabrication described in figure 19a exposure.

Resist	PC 3%
Spin Speed	2000 rpm
Bake	180 $^{\circ}\text{C}$ for 30 minutes
Dose	8000 $\mu\text{C}/\text{cm}^2$
Developer	5M NaOH
Temperature	35 $^{\circ}\text{C}$

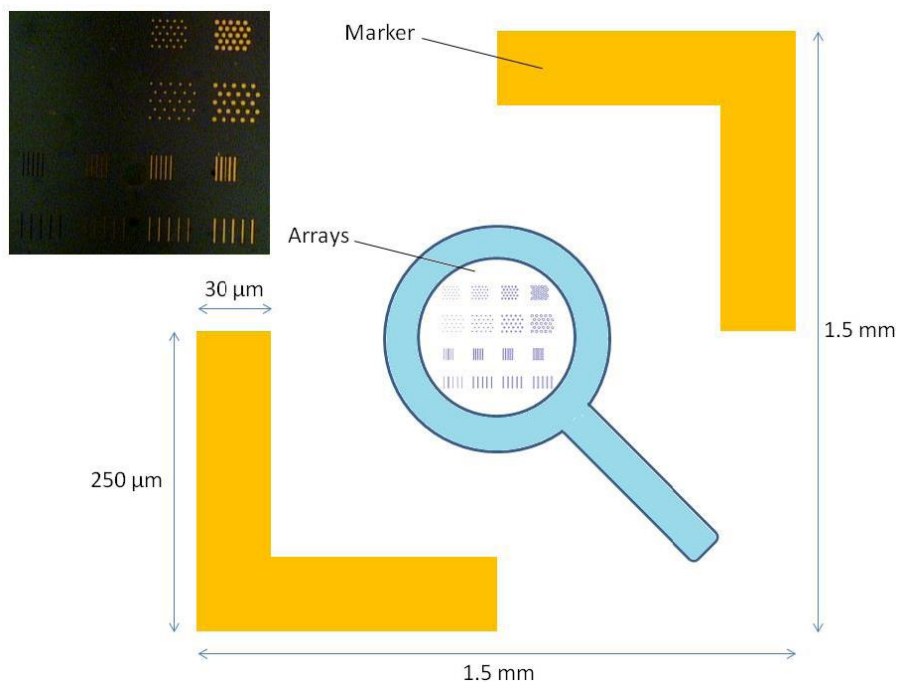


Figure 20. Schematic representation of samples for ECL experiments. Visible Cr marks were made by EBL, metal deposition and lift off. After that, arrays' structures were obtained by lithography on polycarbonate film, inside the field delimited by the marks.

3.7.2. Electrochemical characterization of the MNEAP

For the electrochemical experiments, nanoelectrode arrays assembled as shown in Figure 20 were used as working electrode, while a Pt wire and Ag/AgCl/KCl were the counter and reference electrode, respectively. Figure 21 shows the cyclic voltammetry recorded at the MNEAP in supporting electrolyte in the absence (black line) and presence (blue line) of 1 mM Ru(bpy)₃²⁺.

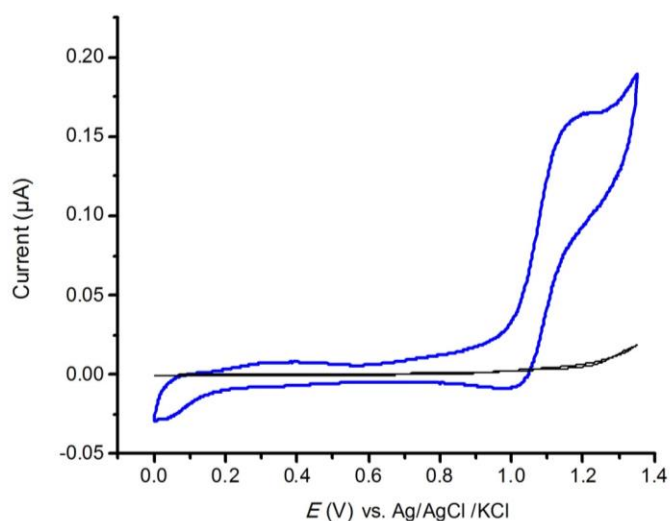


Figure 21. Cyclic voltammogram of the NEAs in 100 mM phosphate buffer (pH=7.4) (black), added with 1mM Ru(bpy)₃²⁺ (blue); scan rate is 10 mV/s.

Note that in all presented measurements, NEAs in the platform are all connected together and all experience the same applied potential. The cyclic voltammograms recorded in the buffer-supporting electrolyte show a very small double layer charging current producing an I vs. E plot with negligible slope up to +1.2 V, as expected for a polarized electrode under negligible ohmic drop effects. The background current starts to increase slowly for $E > 1.2$ V, but keeping a low profile, at least up to 1.35 V; this can be attributed to the oxidation of chloride anions. The current curve in Figure 21 shows the oxidative response of 1 mM $\text{Ru}(\text{bpy})_3^{2+}$ with the appearance of a peak at 1.15 V, associated with a small return-reduction peak at 1.010 V during the reverse scan. These data agree with the occurrence of the one-electron oxidation of $\text{Ru}(\text{bpy})_3^{2+}$. It can be noted that the shape of the cyclic voltammogram is midway between a peak and sigmoidally shaped voltammogram. Explanation lies in the fact that we are recording the signal gathered simultaneously by 16 different NEAs with different geometries. For instance, on the basis of their geometrical features, NEAs in the first line (1.1 – 1.4) are expected to operate under pure radial control conditions while those in the 4th line (4.1- 4.4) should operate under total overlap diffusion. Since all the NEAs are connected together, it is not possible to deconvolute the signal of an individual NEA from the described overall cyclic voltammogram pattern. As a whole, these data demonstrate that: the NEAs are electroactive; no residual PC (which can cause electrical resistance effects) is present on the surface of the nanoelectrodes, the MNEAPs work over a potential window suitable for performing the electrochemical oxidation of $\text{Ru}(\text{bpy})_3^{2+}$.

3.7.3. ECL measurements with the MNEAP

A modified epifluorescence microscope (BX-30, Olympus) was used for bright field (BF) and ECL imaging. BF and ECL emission were collected by a 50X microscope objective and detected by an Electron Multiplying Charge Coupled Device (EM-CCD) Camera (Figure 22). Experiments were done in the direct view of the NEAs. The ECL intensities and ECL profiles were analysed with Image J software.

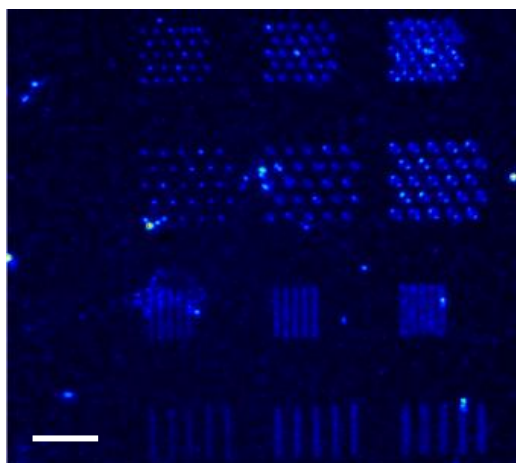


Figure 22. Microscopic bright field imaging (false color), of the MNEA; magnification = 50X, scale bar 12 μ m.

Figure 23 reports the ECL images recorded with the MNEAP at +1.2.V in 1 mM Ru(bpy) $_3^{2+}$ in phosphate buffer after adding increasing TPrA concentrations, from 1 mM to 85 mM. Emitted ECL patterns are indeed clearly detected, with varying intensities for each TPrA concentration. Focusing the attention for instance on the image taken at 10 mM TPrA, it can be noted that the emission patterns are particularly bright and well resolved for the NEAs in the 3rd and 4th columns in the platform matrix, allowing one to clearly recognize the morphological features typical for these arrays. The intensity of emitted ECL increases by enlarging the dimensions of the nanoelectrodes in the array. As shown in particular for the NEAs in column 1 and 2, emission from nanobands is more intense than emission from arrays of nanodisks. Important information are obtained by comparing the ECL in the different boxes. The increase in co-reactant concentration generates a higher ECL intensity, at the same time a shrinking of the radius/width of the bright spots, which corresponds to the shrinking of ECL emitting region.

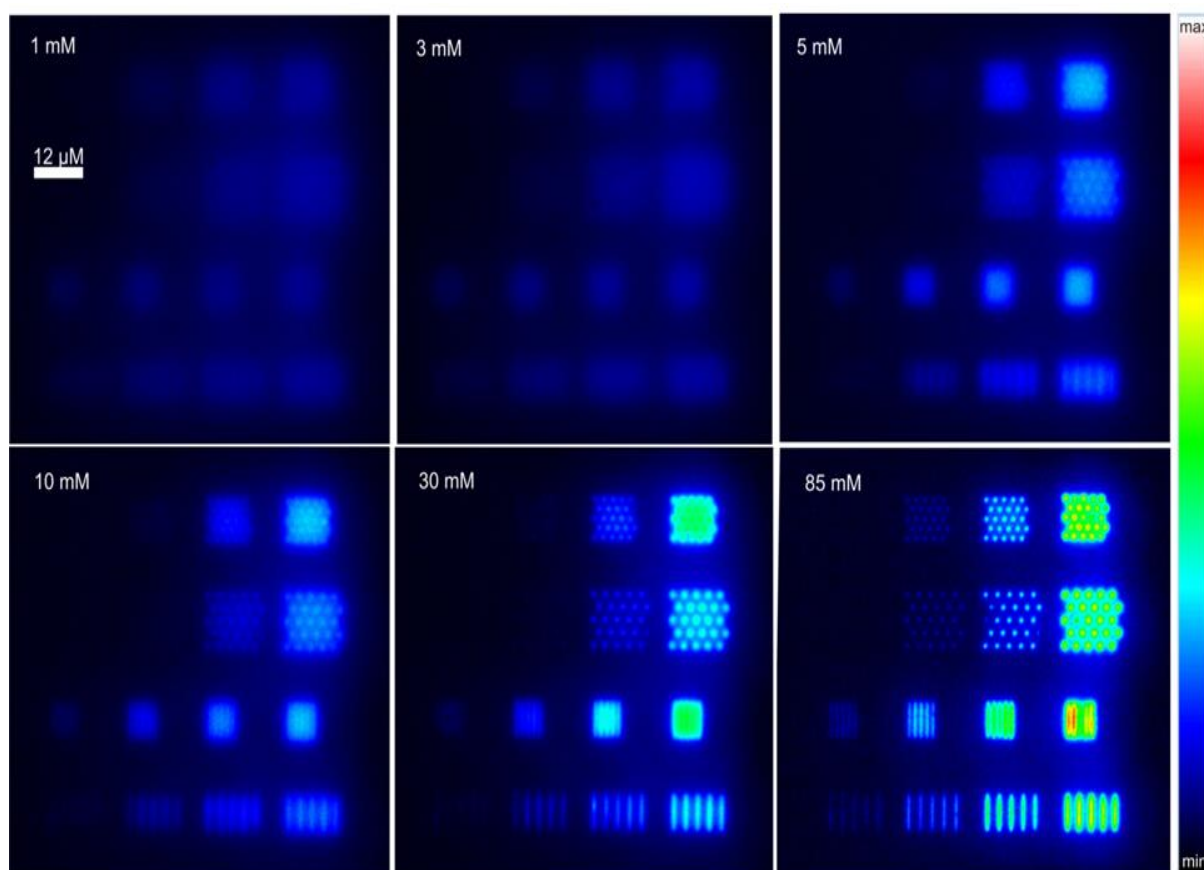


Figure 23. ECL on the MNEA obtained with increasing concentration of TPrA (indicated in top-left corner of each box), during chronoamperometry at 1.2 V vs. Ag/AgCl/KCl; images were acquired with 50X objective at 2 sec. exposure time in normal CCD mode.

Another observed effect is that, by increasing TPrA concentration, the light emission dots or lines are more separated around each electrode element. By comparing carefully the boxes relative to 30 or 85 mM TPrA, one can note that the ECL intensity increases along the lines, i.e. with increasing radius, or band width), and it decreases along column (with increasing space among elements). Note that an increase of the dimension of the elements in NEAs in the same line corresponds also to a decrease of the inter-electrode distance. On the other hand, for NEAs with the same disk radius (lines 1 and 2 in the same column) or band width (lines 3 and 4 in the same column), an increase of the ECL intensity is observed as a consequence of the decrease in spacing between the elements. This can be observed by comparing the emission intensities between NEAs 1.4 vs. 2.4 or 3.4 vs. 4.4. All results suggest that the intensity of emitted chemiluminescence increases for NEAs where the ECL reaction layers between adjacent nanoelectrodes overlap.

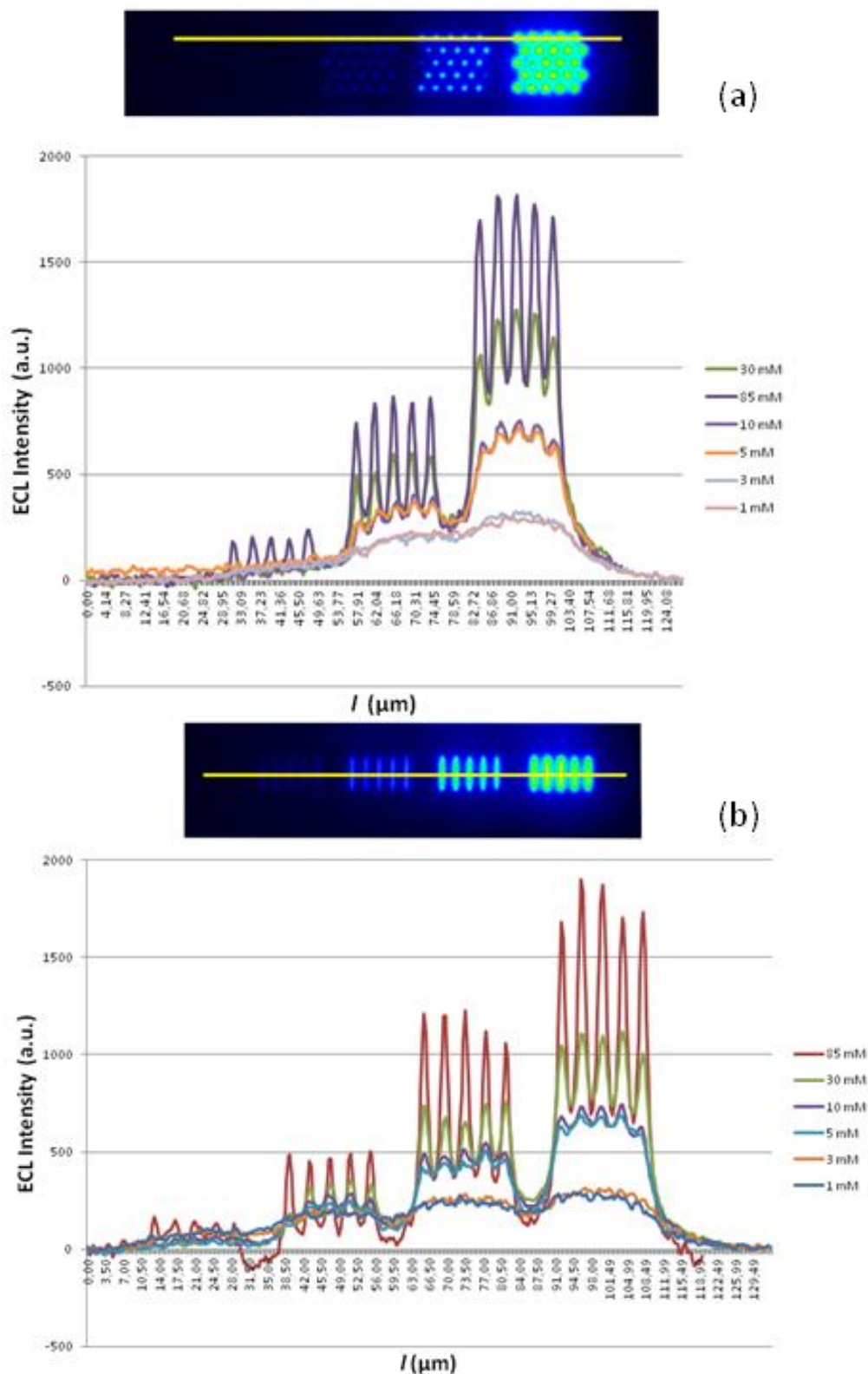


Figure 24. ECL profiles relative to different TPrA concentration for disks (a) and bands (b) in lines 2 and 4 of the MNEAP.

More quantitative information can be obtained by plotting the changes of the ECL intensity profiles with the co-reactant concentration, as shown by the plots reported in Figure 24 for the typical case of NEAs on lines 2 and 4 of the platform. The plots evidence that the peaks are

more defined and well separated at higher co-reactant concentration. Further, it indicates that the ECL-emitting region is more confined. This effect is illustrated by data in Figure 25, where the half-peak widths (HWHM) for the indicated NEAs are plotted as a function of TPrA concentration. It is evident that the width of the luminescence emitting zone at each nanoelectrode scales oppositely with respect to the co-reactant concentration.

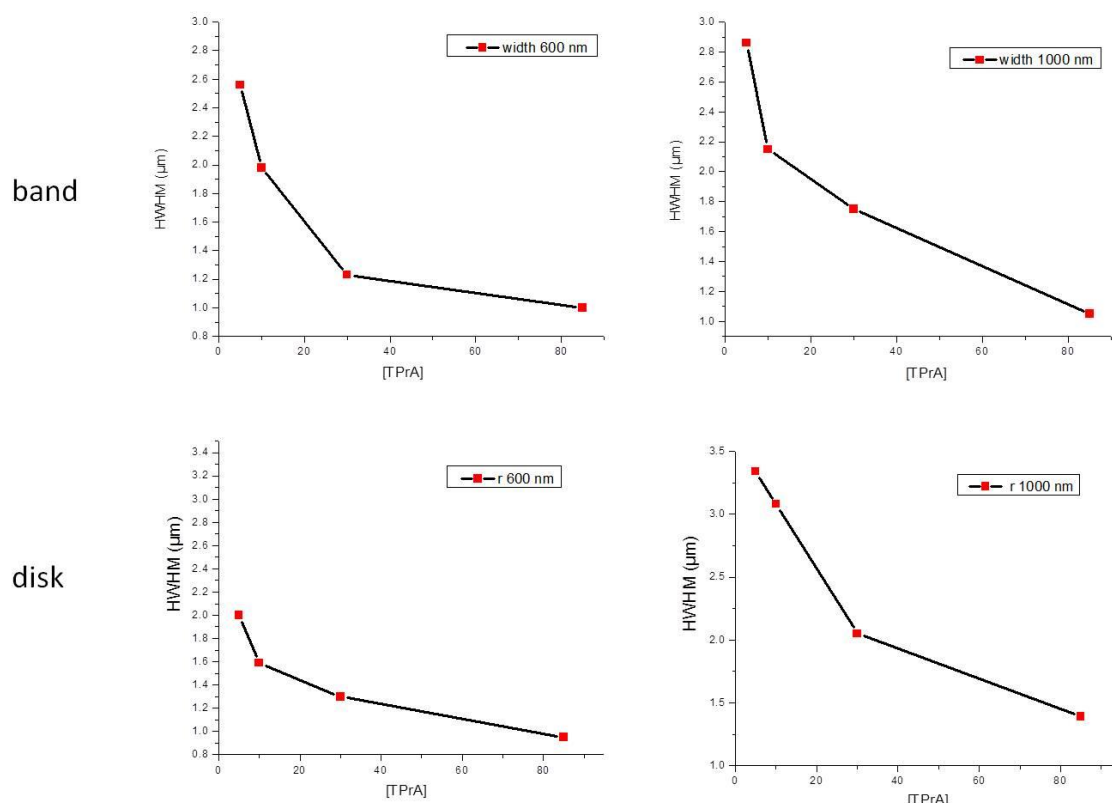


Figure 25. HWHM of ECL profiles for NEAS with period 4 μm at different TPrA concentration.

The trends observed for the arrays of nano-disks agree with the trends expected on the basis of simplified models which correlate the thickness of the ECL emission layer at hemispherical ultramicroelectrodes with the electrode radius and co-reactant concentration according to the following equation :

$$\mu = \left[\frac{1}{r_{av}} + \left(\frac{[TPrA]2k_3}{D} \right)^{1/2} \right]^{-1} \quad (9)$$

where r_{av} is the average apparent radius of a single electroactive dot of the array, k_3 is the reaction apparent rate constant and D is the diffusion coefficient of $\text{Ru}(\text{bpy})_3^{2+/3+}$. D is $5.9 \times 10^{-6} \text{ cm}^2 \text{ s}^{-1}$. The variation of k_3 with pH is related to the acid-base behaviour of TPrA and it is given by $k_3 = k/(1 + 10^{-\text{pH} + \text{p}K_a})$, where k is the intrinsic value of the rate constant. The values of k and $\text{p}K_a$ are respectively $1.3 \times 10^7 \text{ M}^{-1} \text{ s}^{-1}$ and 10.4. At $\text{pH} = 7.5$, k_3 is estimated to be $1.6 \times 10^4 \text{ M}^{-1} \text{ s}^{-1}$.¹ It is worth stressing that this equation holds for arrays where the nanoelectrodes in the same array do not interact, or crosstalk between them, that is when the distance between the nanoelectrodes is much larger than the diameter of the reaction layer. Application of the above equation to ECL from NEAs under reaction-layer overlapping conditions must be taken with caution.

Reaction layers calculated for disks with radius from 100 to 1000 nm and increasing concentration of TPrA are reported in table 3. Data are also plotted for a better visualization in Figure 26.

[TPrA] mol/L	Reaction Layer (μm)			
	r=100 nm	r=300 nm	r=600 nm	r=1000 nm
0,001	0,0977	0,280	0,527	0,812
0,003	0,0961	0,268	0,484	0,714
0,005	0,0951	0,260	0,458	0,659
0,01	0,0932	0,246	0,417	0,578
0,03	0,0888	0,217	0,341	0,441
0,085	0,0824	0,183	0,263	0,319

Table 1. Reaction layers calculated for different TPrA concentration and different disk radius.

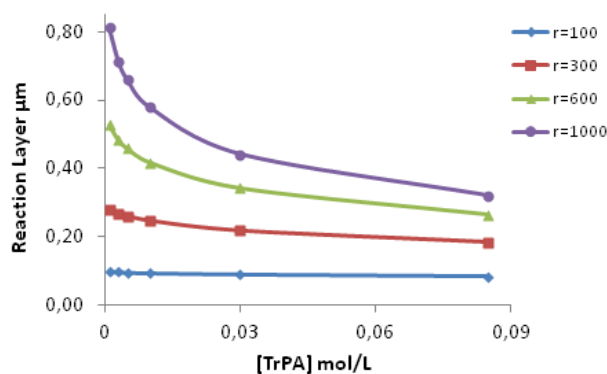


Figure 26. Reaction layers reported as function of TPrA concentrations.

Under such conditions, for small radius disks, the reaction layers do not significantly change by increasing the concentration of TPrA, while the effect is much more pronounced with greater electrode radius, in agreement with our experimental observations.

Similar imaging experiments were performed using another co-reactant, DBAE. As can be seen in Figure 27, comparable concentration of DBAE and TPrA generate higher ECL intensity for the former. The dependence of the emission with DBAE follows the same trend as with TPrA, that is ECL intensity increases by increasing dots radius or band width (along lines), and by decreasing spacing between the elements in the same NEA (along column).

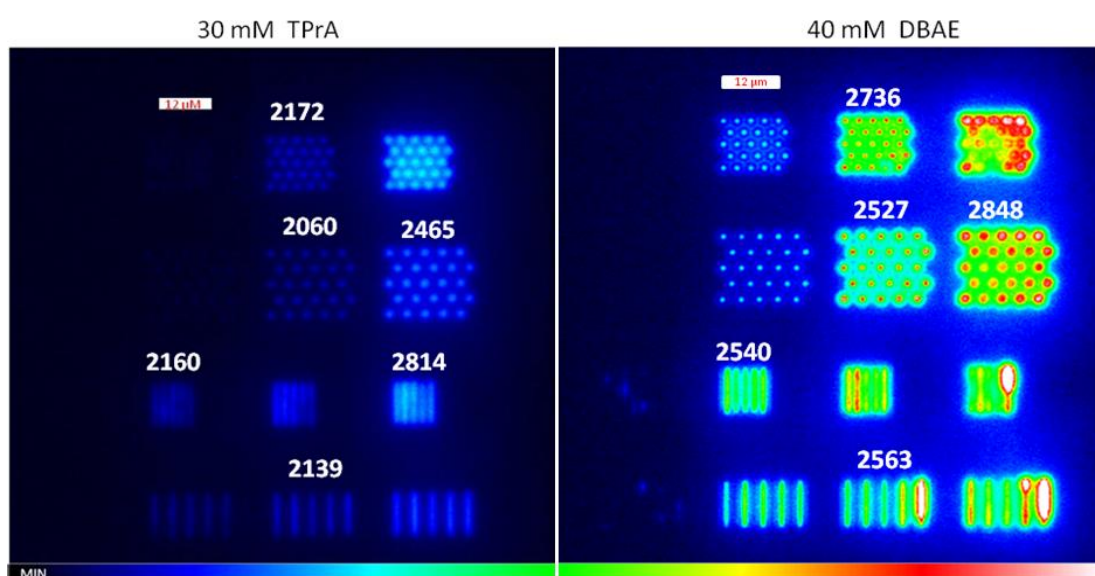


Figure 27. Comparison between ECL images at the MNEA using TPrA and DBAE as co-reactants, during chronoamperometry with potential application at 1.2 V vs. Ag/AgCl/KCl, images acquired with 50X objective and recorded in normal CCD mode with a 2 seconds exposure time,.

This result indicates that DBAE could be an optimal co-reactant in the perspective of coupled NEA/ECL biosensor future development. A more environmentally-friendly co-reactant, DBEA is much less toxic and less volatile than TPrA, and more effective at lower concentration than TPrA. It is also more convenient to prepare DBAE solutions because it has better solubility in aqueous solutions. Due to the higher ECL intensity with respect to TPrA, DBAE could probably allow reaching lower detection limits.

3.8. Conclusion

In the present chapter, we developed a new sensitive and specific anti-tTG ECL immunosensor for diagnosis of celiac disease-CD with limit of detection below 1 ng/mL, using a novel analytical strategy. We exploited the revisited ECL route with TPrA as co-reactant, which enables ECL generation at micrometric distances from the electrode surface at LOP. Using this approach, location of the initial electrochemical step (i.e. oxidation of TPrA) is separated from the biosensing chain and ECL-label, which are immobilized on the non-conductive surface of the NEEs. It therefore minimizes electrical damage on very sensitive biomolecules and oligonucleotide sequences. Also, operating at low oxidation potential allows to reduce possible interferences from side reactions dealing with samples of complex matrix like blood; making this method extremely suitable for serological screening. Furthermore, we studied the characteristics of ECL generated by arrays of boron-doped-diamond nanoelectrodes as a promising materials for biosensing. The arrays of nanodisk and nanoband electrodes were fabricated with different dimensions and inter-electrode distances. The ECL intensity increases with increasing the dimensions of the nanoelectrodes in the array, being more intense at nanobands than at nanodisks. The increase in co-reactant concentration generates a higher ECL intensity, at the same time confining the ECL emitting region around the nanoband and nanodisk arrays. Lastly, ECL emissions based on two different co-reactants, DBAE and TPrA, were compared. The results have shown that DBEA is a more favorable co-reactant in our condition, exhibiting the higher ECL emission at lower concentration in comparison to TPrA.

By using advantages of the electron beam lithography for future analytical platform development, more detailed information on ECL generation should be obtained by writing an ultramicroelectrode on the same PC platform of the NEAs. In such an arrangement ECL reaction layers in different diffusion regimes might be compared at the same time in a single image. Furthermore, PC surface of BDD NEAs was successfully functionalized with small ss-DNA sequence, confirming the possibility of exploiting these systems as diagnostic biosensors. Developing an ECL sensor for biological molecules (DNA and proteins) can possibly reach extremely low detection limits.

References

- 1 Bard, A. J. *Electrogenerated Chemiluminescence*. (M. Dekker, New-York, 2004).
- 2 Rubinstein, I. & Bard, A. J. Electrogenerated chemiluminescence. 37. Aqueous ecl systems based on tris(2,2'-bipyridine)ruthenium(2+) and oxalate or organic acids. *J. Am. Chem. Soc.* **103**, 512 (1981).
- 3 Kergaravat, S. V. *et al.* Electrochemical magneto immunosensor for the detection of anti-TG2 antibody in celiac disease. *Biosen. Bioelectron.* **48**, 203-209 (2013).
- 4 Milutinovic, M., Sallard, S., Manojlovic, D., Mano, N. & Sojic, N. Glucose sensing by electrogenerated chemiluminescence of glucose-dehydrogenase produced NADH on electrodeposited redox hydrogel. *Bioelectrochemistry* **82**, 63-68 (2011).
- 5 White, H. S. & Bard, A. J. Electrogenerated chemiluminescence. 41. Electrogenerated chemiluminescence and chemiluminescence of the Ru(bpy)₃²⁺-S₂O₈²⁻ system in acetonitrile-water solutions. *J. Am. Chem. Soc.* **104**, 6891 (1982).
- 6 Zu, Y. & Bard, A. J. Electrogenerated chemiluminescence. 66. The role of direct coreactant oxidation in the ruthenium tris (2,2') bipyridyl/triethylamine system and the effect of halide ions on the emission intensity. *Anal. Chem.* **72**, 3223-3232 (2000).
- 7 Blackburn, G. F. *et al.* Electrochemiluminescence detection for development of immunoassays and DNA probe assays for clinical diagnostics. *Clin. Chem.* **37**, 1534-1539 (1991).
- 8 Staffilani, M. *et al.* Multimetallic ruthenium (II) complexes as electrochemiluminescent labels. *Inorg. Chem.* **42**, 7789-7798 (2003).
- 9 Wei, H. & Wang, E. Electrochemiluminescence of tris (2, 2'-bipyridyl) ruthenium and its applications in bioanalysis: a review. *Luminescence* **26**, 77-85 (2011).
- 10 Miao, W., Choi, J.-P. & Bard, A. J. Electrogenerated Chemiluminescence 69: The Tris(2,2'-bipyridine)ruthenium(II), (Ru(bpy)₃²⁺)/Tri-n-propylamine (TPrA) System Revisited A New Route Involving TPrA^{•+} Cation Radicals. *J. Am. Chem. Soc.* **124**, 14478-14485 (2002).
- 11 Sentic, M. *et al.* Mapping electrogenerated chemiluminescence reactivity in space: mechanistic insight into model systems used in immunoassays. *Chem. Sci.* **5**, 2568-2572 (2014).
- 12 Arrigan, D. W. M. Nanoelectrodes, nanoelectrode arrays and their applications. *Analyst* **129**, 1157-1165 (2004).
- 13 Ongaro, M. & Ugo, P. Bioelectroanalysis with nanoelectrode ensembles and arrays. *Anal. Bioanal. Chem.* **405**, 3715-3729 (2013).
- 14 Menon, V. P. & Martin, C. R. Fabrication and Evaluation of Nanoelectrode Ensembles. *Anal. Chem.* **67**, 1920-1928 (1995).
- 15 Brunetti, B., Ugo, P., Moretto, L. M. & Martin, C. R. Electrochemistry of phenothiazine and methylviologen biosensor electron-transfer mediators at nanoelectrode ensembles. *J. Electroanal. Chem.* **491**, 166-174 (2000).
- 16 Moretto, L. M., Pepe, N. & Ugo, P. Voltammetry of redox analytes at trace concentrations with nanoelectrode ensembles. *Talanta* **62**, 1055-1060 (2004).
- 17 Pereira, F. C., Moretto, L. M., De Leo, M., Zanoni, M. V. B. & Ugo, P. Gold nanoelectrode ensembles for direct trace electroanalysis of iodide. *Anal. Chim. Acta* **575**, 16-24 (2006).
- 18 Silvestrini, M., Fruk, L. & Ugo, P. Functionalized ensembles of nanoelectrodes as affinity biosensors for DNA hybridization detection. *Biosen. Bioelectron.* **40**, 265-270 (2013).

- 19 Silvestrini, M. & Ugo, P. Ensembles of nanoelectrodes modified with gold nanoparticles: characterization and application to DNA-hybridization detection. *Anal. Bioanal. Chem.* **405**, 995-1005 (2013).
- 20 Mucelli, S. P., Zamuner, M., Tormen, M., Stanta, G. & Ugo, P. Nanoelectrode ensembles as recognition platform for electrochemical immunosensors. *Biosens. Bioelectron.* **23**, 1900-1903 (2008).
- 21 Miao, W. & Bard, A. J. Electrogenerated Chemiluminescence. 80. C-Reactive Protein Determination at High Amplification with [Ru(bpy)₃]²⁺-Containing Microspheres. *Anal. Chem.* **76**, 7109 (2004).
- 22 Dulay, S., Lozano-Sánchez, P., Iwuoha, E., Katakis, I. & O'Sullivan, C. K. Electrochemical detection of celiac disease-related anti-tissue transglutaminase antibodies using thiol based surface chemistry. *Biosens. Bioelectron.* **26**, 3852-3856 (2011).
- 23 Giannetto, M. *et al.* An amperometric immunosensor for diagnosis of celiac disease based on covalent immobilization of open conformation tissue transglutaminase for determination of anti-tTG antibodies in human serum. *Biosens. Bioelectron.* **62**, 325-330 (2014).
- 24 Guandalini, S. & Assiri, A. Celiac disease: a review. *JAMA pediatrics* **168**, 272-278 (2014).
- 25 Pividori, M., Lermo, A., Bonanni, A., Alegret, S. & Del Valle, M. Electrochemical immunosensor for the diagnosis of celiac disease. *Anal. Biochem.* **388**, 229-234 (2009).
- 26 Tiroj, N., Jaroenapibal, P., Shi, H., Yeh, J. I. & Beresford, R. Microfluidic chip-based nanoelectrode array as miniaturized biochemical sensing platform for prostate-specific antigen detection. *Biosens. Bioelectron.* **26**, 2927-2933 (2011).
- 27 Arumugam, P. U. *et al.* Wafer-scale fabrication of patterned carbon nanofiber nanoelectrode arrays: A route for development of multiplexed, ultrasensitive disposable biosensors. *Biosens. Bioelectron.* **24**, 2818-2824 (2009).
- 28 Virgilio, F., Prasciolu, M., Ugo, P. & Tormen, M. Development of electrochemical biosensors by e-beam lithography for medical diagnostics. *Microelectron. Eng.* **111**, 320-324 (2013).
- 29 Xiao, L., Streeter, I., Wildgoose, G. G. & Compton, R. G. Fabricating random arrays of boron doped diamond nano-disc electrodes: Towards achieving maximum Faradaic current with minimum capacitive charging. *Sens. Actuators, B* **133**, 118-127 (2008).
- 30 Penner, R. M. & Martin, C. R. Preparation and electrochemical characterization of ultramicroelectrode ensembles. *Anal. Chem.* **59**, 2625-2630 (1987).
- 31 Gilliam, R., Thorpe, S. & Kirk, D. A nucleation and growth study of gold nanowires and nanotubes in polymeric membranes. *Appl. Electrochem.* **37**, 233-239 (2007).
- 32 De Leo, M. *et al.* Towards a better understanding of gold electroless deposition in track-etched templates. *Chemistry of Materials* **19**, 5955-5964 (2007).
- 33 Ugo, P. & Moretto, L. M. in *Handbook of Electrochemistry* (ed Cynthia G. Zoski) 678-XVI (Elsevier, 2007).
- 34 Sandison, M. E. & Cooper, J. M. Nanofabrication of electrode arrays by electron-beam and nanoimprint lithographies. *Lab on Chip* **6**, 1020-1025 (2006).
- 35 Godino, N., Borrisé, X., Muñoz, F. X., del Campo, F. J. & Compton, R. G. Mass Transport to Nanoelectrode Arrays and Limitations of the Diffusion Domain Approach: Theory and Experiment. *J. Phys. Chem. C* **113**, 11119-11125 (2009).
- 36 Moretto, L., Tormen, M., De Leo, M., Carpentiero, A. & Ugo, P. Polycarbonate-based ordered arrays of electrochemical nanoelectrodes obtained by e-beam lithography. *Nanotechnol.* **22**, 185305 (2011).

- 37 Henstridge, M. C. & Compton, R. G. Mass Transport to micro-and nanoelectrodes and their arrays: a review. *Chem. Rec.* **12**, 63-71 (2012).
- 38 Bard, A. J. & Faulkner, L. R. *Electrochemical Methods: Fundamentals and Applications*. (Wiley, 2000).
- 39 Ugo, P., Moretto, L. M. & Vezzà, F. Ionomer-Coated Electrodes and Nanoelectrode Ensembles as Electrochemical Environmental Sensors: Recent Advances and Prospects. *ChemPhysChem* **3**, 917-925 (2002).
- 40 Penner, R. M., Heben, M. J., Longin, T. L. & Lewis, N. S. Fabrication and Use of Nanometer-Sized Electrodes in Electrochemistry. *Science* **250**, 1118-1121 (1990).
- 41 Mirkin, M. V., Fan, F.-R. F. & Bard, A. J. Scanning electrochemical microscopy part 13. Evaluation of the tip shapes of nanometer size microelectrodes. *J. Electroanal. Chem.* **328**, 47-62 (1992).
- 42 Guo, J. & Lindner, E. Cyclic Voltammograms at Coplanar and Shallow Recessed Microdisk Electrode Arrays: Guidelines for Design and Experiment. *Analytical Chemistry* **81**, 130-138 (2009).
- 43 Ugo, P., Moretto, L. M., Bellomi, S., Menon, V. P. & Martin, C. R. Ion-Exchange Voltammetry at Polymer Film-Coated Nanoelectrode Ensembles. *Anal. Chem.* **68**, 4160-4165 (1996).
- 44 Moretto L.M., P. S., Scrosati B., Ugo P., in “Nanomaterials” 1, ed. Lin Y. and Nalwa H.S. & (2009).
- 45 Bottari, F., Oliveri, P. & Ugo, P. Electrochemical immunosensor based on ensemble of nanoelectrodes for immunoglobulin IgY detection: Application to identify hen's egg yolk in tempera paintings. *Biosen. Bioelectron.* **52**, 403-410 (2014).
- 46 Tommasini, A. *et al.* Mass screening for coeliac disease using antihuman transglutaminase antibody assay. *Arch. Dis. Child.* **89**, 512-515 (2004).
- 47 Lohi, S. *et al.* Increasing prevalence of coeliac disease over time. *Aliment. Pharmacol. Ther.* **26**, 1217-1225 (2007).
- 48 Bianchi, M. & Bardella, M. Bone and celiac disease. *Calcified tissue int.* **71**, 465-471 (2002).
- 49 Bolotin, D. & Petronic-Rosic, V. Dermatitis herpetiformis: part I. Epidemiology, pathogenesis, and clinical presentation. *J. Am. Acad. Dermatol.* **64**, 1017-1024 (2011).
- 50 Hadjivassiliou, M. *et al.* Gluten sensitivity: from gut to brain. *Lancet Neurol.* **9**, 318-330 (2010).
- 51 Lepore, L. *et al.* Prevalence of celiac disease in patients with juvenile chronic arthritis. *Jour. Pediatr.* **129**, 311-313 (1996).
- 52 Frustaci, A. *et al.* Celiac disease associated with autoimmune myocarditis. *Circulation* **105**, 2611-2618 (2002).
- 53 Ludvigsson, J. F., Montgomery, S. M. & Ekbom, A. Celiac disease and risk of adverse fetal outcome: a population-based cohort study. *Gastroenterology* **129**, 454-463 (2005).
- 54 Korponay-Szabó, I. R. *et al.* Population screening for coeliac disease in primary care by district nurses using a rapid antibody test: diagnostic accuracy and feasibility study. *Bmj* **335**, 1244-1247 (2007).
- 55 Nemeč, G. *et al.* Looking for celiac disease: diagnostic accuracy of two rapid commercial assays. *Am. J. Gastroenterol.* **101**, 1597-1600 (2006).
- 56 Di Simone, N. *et al.* Anti-tissue transglutaminase antibodies from celiac patients are responsible for trophoblast damage via apoptosis in vitro. *Am. J. Gastroenterol.* **105**, 2254-2261 (2010).
- 57 Neves, M. M., González-García, M. B., Nouws, H. P. & Costa-García, A. Celiac disease detection using a transglutaminase electrochemical immunosensor fabricated

- on nanohybrid screen-printed carbon electrodes. *Biosen. Bioelectron.* **31**, 95-100 (2012).
- 58 www.roche-diagnostics.com.
- 59 Miao, W., Choi, J.-P. & Bard, A. J. Electrogenerated chemiluminescence 69. The tris(2,2'-bipyridine)ruthenium(II), (Ru(bpy)₃²⁺) / tri- n-propylamine (TPrA) system revisited. A new route involving TPrA^{•+} cation radicals. *J. Am. Chem. Soc.* **124**, 14478-14485 (2002).
- 60 Zu, Y. & Bard, A. J. Electrogenerated Chemiluminescence. 66. The Role of Direct Coreactant Oxidation in the Ruthenium Tris(2,2')bipyridyl/Tripropylamine System and the Effect of Halide Ions on the Emission Intensity. *Anal.Chem.* **72**, 3223 (2000).
- 61 Nepomnyashchii, A. B., Kolesov, G. & Parkinson, B. A. Electrogenerated Chemiluminescence of BODIPY, Ru(bpy)₃²⁺, and 9,10-Diphenylanthracene Using Interdigitated Array Electrodes. *ACS Appl. Mater. Inter.* **5**, 5931-5936 (2013).
- 62 Hu, L. & Xu, G. Applications and trends in electrochemiluminescence. *Chem. Soc. Rev.* **39**, 3275 (2010).
- 63 Li, M.-J., Chen, Z., Yam, V. W.-W. & Zu, Y. Multifunctional ruthenium (II) polypyridine complex-based core-shell magnetic silica nanocomposites: magnetism, luminescence, and electrochemiluminescence. *ACS nano* **2**, 905-912 (2008).
- 64 Simm, A. O. *et al.* Boron-doped diamond microdisc arrays: electrochemical characterisation and their use as a substrate for the production of microelectrode arrays of diverse metals (Ag, Au, Cu) via electrodeposition. *Analyst* **130**, 1303-1311 (2005).
- 65 Honda, K., Yoshimura, M., Rao, T. N. & Fujishima, A. Electrogenerated chemiluminescence of the ruthenium Tris (2,2') bipyridyl/Amines system on a boron-doped diamond electrode. *J. Phys. Chem. B* **107**, 1653-1663 (2003).
- 66 Honda, K. *et al.* Hydroxyl radical-related electrogenerated chemiluminescence reaction for a ruthenium tris (2,2') bipyridyl/co-reactants system at boron-doped diamond electrodes. *Electroch. Acta* **51**, 588-597 (2005).

Chapter 4:
**Electrogenerated chemiluminescent swimmers driven
by bipolar electrochemistry**

4.1. Introduction

The design and study of objects that can move in a controlled way and perform tasks at small scales is of crucial importance for many potential applications ranging from micromotors to nanomedicine¹. Micromotors are microscale devices designed to perform selected mechanical movements (e.g., rotation, rolling, shuttling, delivery) in response to specific stimuli¹. Intensive studies have been performed in order to imitate biomotors² by developing molecular motors³ and also synthetic micro- and nano-motors^{4,5}. Generally, there are three methods to induce the motion of these objects according to the type of energy input that they use: (1) Biochemical fueling which is based on the object functionalization with catalytically active enzymes, converting natural fuel into kinetic energy^{6,7}; (2) The most developed, chemical fueling, for objects of different design usually with the catalytic site for the decomposition of hydrogen peroxide to water and oxygen gas⁸; (3) Physical fueling which implies applying an external electric⁹ or magnetic field¹⁰.

Bipolar electrochemistry (BE), as a driving force for the object's motion is a complementary approach to physical fueling¹¹. It triggers electrochemical reactions on a conducting object placed in an electric field (EF), named bipolar electrode (BPE), at its extremities (poles) in the absence of a direct ohmic contact¹². More specifically, when a sufficient EF is applied in an electrolyte solution in which a BPE is immersed, the potential difference between the BPE and the solution drives oxidation and reduction reactions concomitantly¹³. This wireless concept enables mobile electrodes, dubbed microswimmers, to move freely in solution by generating an asymmetric reactivity on its surface. Kuhn and co-workers used BE for the translation, rotation, and levitation of swimmers¹⁴⁻¹⁷. Still, the observation of such swimmers is generally a challenge and usually requires an efficient microscopy set up¹⁸ or swimmers tagged with fluorescent molecules^{19,20} to monitor their motion. In this context, it would be helpful if the swimmer could also act as an autonomous light source, with the photon emission being intrinsically coupled to the motion. As a widely used electrochemical process that has the advantage of not requiring an excitation light source, ECL can be coupled to BPE²¹⁻²³. The combination of ECL and BE has already been used for analytical purposes¹². Manz and co-workers exploited ECL generation at the anodic pole of a BPE for the detection of amines²⁴. Crooks and co-workers²⁵⁻²⁷ have developed it for many analytical purposes.

Herein, we propose an original approach, a first example of a propulsion mechanism for a swimmer, with simultaneous light emission, based on the synergetic action of BE²⁸. Another

ECL swimmer based on luminol as a luminophore, allows to tune the wavelength of light emission²⁹. Furthermore, we expanded the swimmer concept by developing ECL-emitting bioswimmers for enzymatic glucose sensing²⁸. The concomitant oxidation of the luminophore and of the enzymatically-produced reduced form of nicotinamide adenine dinucleotide (NADH) leads to ECL emission via the classic co-reactant pathway with a direct glucose-dependant light intensity^{30,31}. Due to the dependence of ECL intensity on glucose concentration, this approach is also suitable to monitor the spatial distribution of variations in glucose concentration.

The first part of this chapter deals with principles of BE and motion generation of motors triggered by BE. In the second part, a light-emitting electrochemical swimmer approach will be presented. Finally, in the third part, the design of dynamic systems driven by BE used for the first time to perform an analytical task will be described to monitor the glucose concentration.

4.2. Bipolar electrochemistry

4.2.1. Definition of bipolar electrode

Although the phenomenon of BE has been known for a long time, since the 1960s, it has been exploited for a few industrial applications³². The most relevant industrial application exploited BPEs under the name of fluidized bed electrodes for designing industrial reactors for applications such as electrosynthesis, water splitting, and also for increasing fuel cell performances³³⁻³⁵. In the present decade, BE reveals attractive features for applications in the field of materials science and analysis in general, especially for surface modification at the submicron scale and sensing in microfluidic systems³⁶. By using BPEs, analyte separation and detection becomes possible based on miniaturized systems¹². The term “bipolar electrode” is employed for any object exhibiting at the same time oxidation and reduction reactions. In other words, a BPE is acting as an anode and a cathode at the same time^{11,13} in contrast to conventional electrochemical experiments, where cathodes and anodes are physically separated. BPEs can be conducting objects exhibiting a chemical anisotropy designed in order to promote oxidation and reduction reactions at the same time when exposed to an external EF³⁷.

4.2.2. Polarization of a conducting object in an open configuration

To present the basic concept behind BE, we will consider the situation depicted in Figure 1, where a conducting object is immersed in a homogeneous electrolytic solution exposed to an external EF, applied between the feeder electrodes (i.e. anode and cathode)¹¹. The current flowing through the solution, I_{tot} , is divided into two fractions in the vicinity of the BPE. A fraction of the current, I_{bps} , called by-pass current will flow through the solution via the migration of charged species, whereas the current fraction, I_{be} , will flow through the BPE via electronic conduction and it represents faradaic current. Consequently, we can write the following equation:

$$I_{be} = I_{tot} - I_{bps} \quad (1)$$

It follows that the ratio I_{be}/I_{bps} is correlated with the respective resistance of the object R_{be} and the solution R_s ¹².

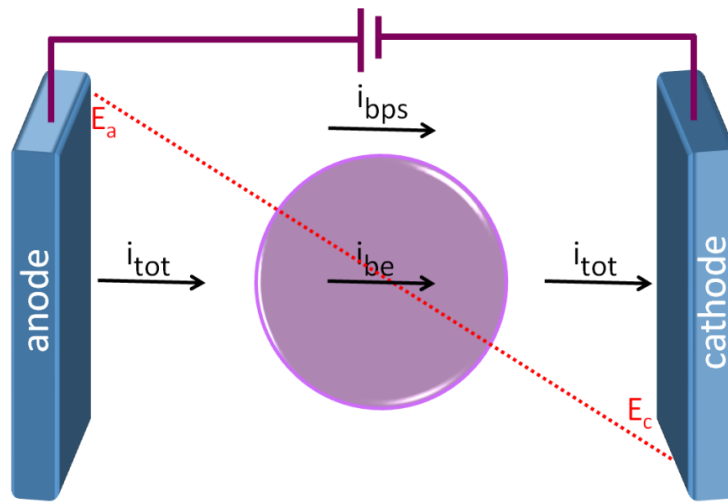


Figure 1. Scheme of a spherical BPE placed in solution in an EF. E_a is the potential of the anode, E_c the potential of the cathode. I_{tot} is the current passing through the solution before and after reaching the BPE, I_{bps} is the current passing through the solution around the BPE - by-passing current, and I_{be} is the current passing through the BPE – faradaic current.

Therefore, working with a highly resistive solution and with a highly conductive object will result in minimizing I_{bps} . Thus, almost all the current passing through the system will flow through the conducting object. With E_a and E_c being the potentials of the “feeder electrodes,” the value of the imposed electric field \mathcal{E} , can be calculated as:

$$\mathcal{E} = \frac{E_a - E_c}{L} \quad (2)$$

with L being the distance between the feeder electrodes. The imposed polarization potential $E = (E_a - E_c)$, given by the difference of the solution potential value with respect to the conducting object arises and drops linearly through the electrolytic solution. It means that the two feeder electrodes have the same geometry and that EF distortions due to the reactions at the feeder electrodes are neglected. In Figure 2, the solution potential distributions in the cell for two object morphologies, one linear and one spherical respectively, is shown.

Considering a constant EF, the value of E varies along the object/solution interface and can be calculated at a position x as: ²

$$\mathcal{E} = Ex \quad (3)$$

in the case of a linear object (Figure 2a) and:

$$\mathcal{E} = E \frac{d}{2} \cos \theta \quad (4)$$

for the spherical object, with d being the object diameter.

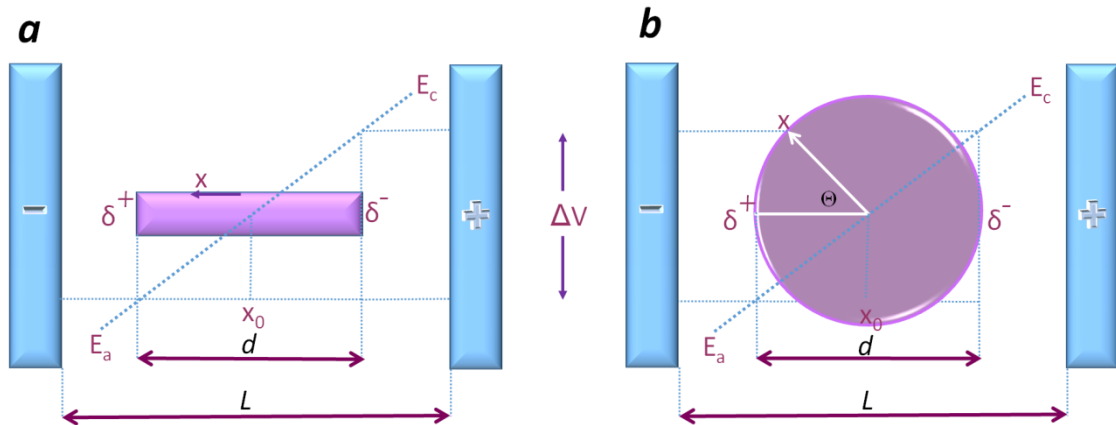


Figure 2. Scheme for the polarization of a linear (a), and spherical (b) conductive objects localized between two feeder electrodes within the electric field. L is the distance between the feeder electrodes, d characteristic object dimensions, x_0 middle of the BPE, δ^- and δ^+ , cathodic pole and anodic pole of the BPE, respectively.

It follows that polarization potential difference ΔV occurs between the extremities of the object and the solution, increasing from the x_0 location towards both ends of the object reaching its maximum at the extremities of the BPE, as shown in Figure 2a and b. The maximum polarization potential difference ΔV is given by the following equation:

$$\Delta V = \mathcal{E} d \quad (5)$$

If the maximum polarization ΔV is important enough, oxidation reactions can happen at the anodic pole of the conducting object coupled with reduction reactions at the cathodic pole in order to respect the electroneutrality within the object:



n_1 and n_2 being the number of electrons involved for each electrochemical reactions and the two redox couples red 1/ox 1 and red 2/ox 2 with a standard potential E_1^0 and E_2^0 , respectively. Therefore, the resulting asymmetric reactivity at the object's surface explains its name as BPE. ΔV quantifies the driving force for the reactions at the extremities of the object. It is clear that a minimum potential value is needed in order that oxidation and reduction reactions take place at both sides of the polarized poles. The theoretical threshold value is equal to the difference of standard potentials of the involved redox couples, $|E_1^0 - E_2^0|$. Therefore, a fine control of the localization of the electrochemical reactions along a BPE surface is enabled by tuning the EF as an easily controllable parameter.

4.2.3. The case of closed bipolar electrochemistry

The BPE can be any kind of conductive material with any characteristic dimensions and geometry. Still it is important to notice that a smaller object will require a higher external EF to be polarized enough in order to induce redox reactions (Eq. 5.). Also, it should be pointed out that the described system refers to the so called “open” BE configuration, where current can flow through both the electrolytic solution and the BPE. However, several reports describe the use of “closed” BE configuration, where the solutions contacting the BPE are divided into two independent compartments, physically separating anode and cathode³². The only current path between both compartments is in this latter case through the BPE.

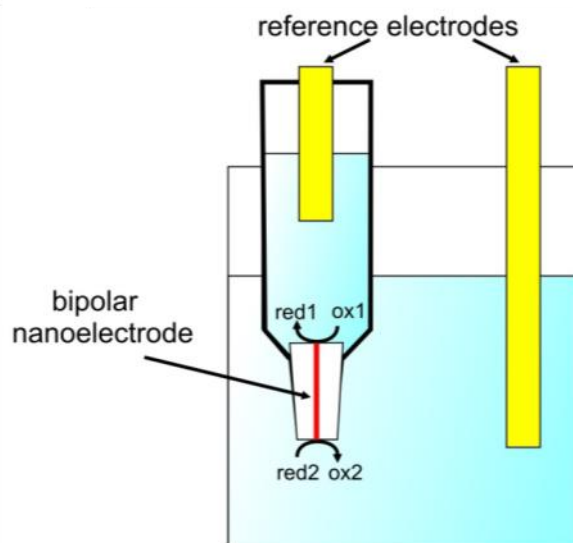


Figure 3. Scheme of the bipolar nanoelectrode in the closed bipolar configuration.³⁸

In Figure 3 is presented an example of a closed BPE demonstrated by Zhang and co-workers³⁸. They showed that certain types of carbon microfiber electrodes, which are commonly used in several fields of bioelectrochemistry, as well as metal microelectrodes obtained by encapsulating a wire in a glass capillary³⁹, actually work as closed BPEs. In this case, the electrochemical current would pass through the BPEs and can be directly measured due to the absence of the ionic current path, providing information on the rates of the faradaic processes³⁹.

4.3. Applications of bipolar electrochemistry coupled to ECL

ECL has been widely used as an analytical technique due to its high specificity, sensitivity and low signal-to-noise ratio²³. The direct optical readout can be obtained using just a CCD camera making this technique a tool-of-choice for collecting information on processes occurring at BPEs. ECL/BE coupling has been applied for EF mapping⁴⁰, microfluidic integrated circuits⁴¹, and analytics^{27,42,43}. A decade ago, Manz *et al.* were the first to report an ECL detection system coupled to BE²⁴. They have used micro-fabricated U-shaped platinum BPE in a separation channel of a glass chip. On a Pt cathodic leg the reduction of O₂ or H₂O occurred, while a Pt anodic leg was used for the detection of ruthenium complexes in μM range following electrophoretic separation. More importantly, separation and detection of three amino acids, acting as ECL co-reactants, from a mixture have been reported by using this technique. Similar approach has been reported by Wu *et al.* for sensitive cell analysis using an indium tin oxide (ITO) BPE as a platform for detection of folate receptors (FR) on a cell membrane⁴⁴. FR is a tumor marker for tumor diagnosis, expressed on tumor cells with

high level which mediates folic acid into cells. Sensor is based on its high affinity to folic acid and the inhibition of the ECL signal at the anodic part of BPE leads to a decrease in ECL intensity. The same authors reported also an ultra sensitive ECL biosensor for the detection of a nucleic acid target at femtomolar concentration in tumor cells⁴⁴.

Jusková *et al.* presented ECL generation from 50 μM gold platelets suspension in fused silica capillary⁴⁵. The ECL signal of freely moving and thus disposable BPEs, has been recorded with a photomultiplier tube as shown in Figure 4.

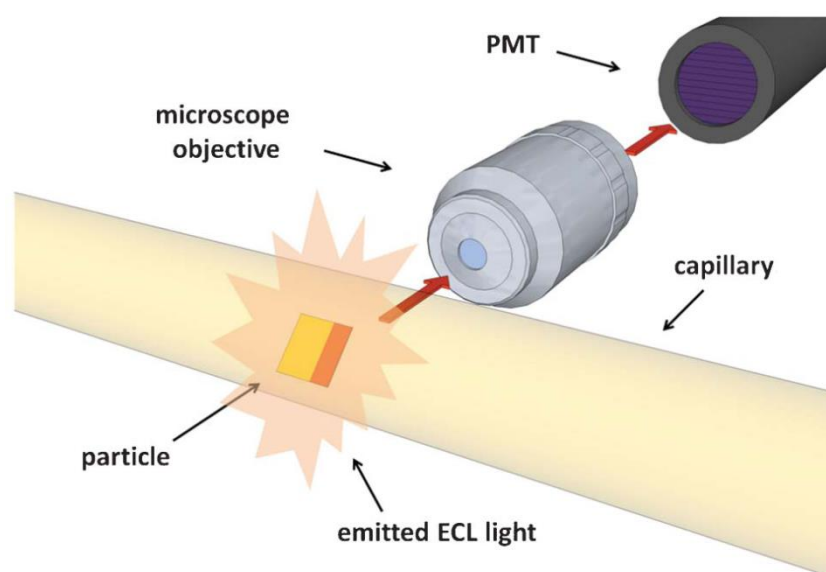


Figure 4. Schematic illustration of a detection system. The particle, 50 μM gold plate, was positioned inside the transparent capillary filled with the ECL reactants. The application of electrical voltage across the capillary resulted in the ECL reaction accompanied by light emission collected by the PMT⁴⁵.

In all above described ECL/BE systems, detection reaction and ECL signal readout take place at the same pole of BPEs, making the accessible analytes in that way limited to species that participate or compete with the ECL-producing reaction. Crooks and co-workers demonstrated that electroactive analytes could be detected by exploiting the fact that the same current passes at the anodic and cathodic poles of BPE. The analyte of interest is reduced at the cathodic pole of a single or arrays of BPEs located in microfluidic devices⁴². As a consequence, faradaic reaction at the cathodic pole triggers light emission at the anodic pole by the corresponding oxidation of ECL reagents. Indeed, in this indirect detection scheme, there is a direct correlation between the number of electrons involved in the reduction and the

ECL photon flux. In the first study considering this method, benzyl viologen has been detected⁴². By changing the length and the geometry of the BPE, authors demonstrated the influence on sensitivity enhancement of the method achieving limits of detection up to nM range.

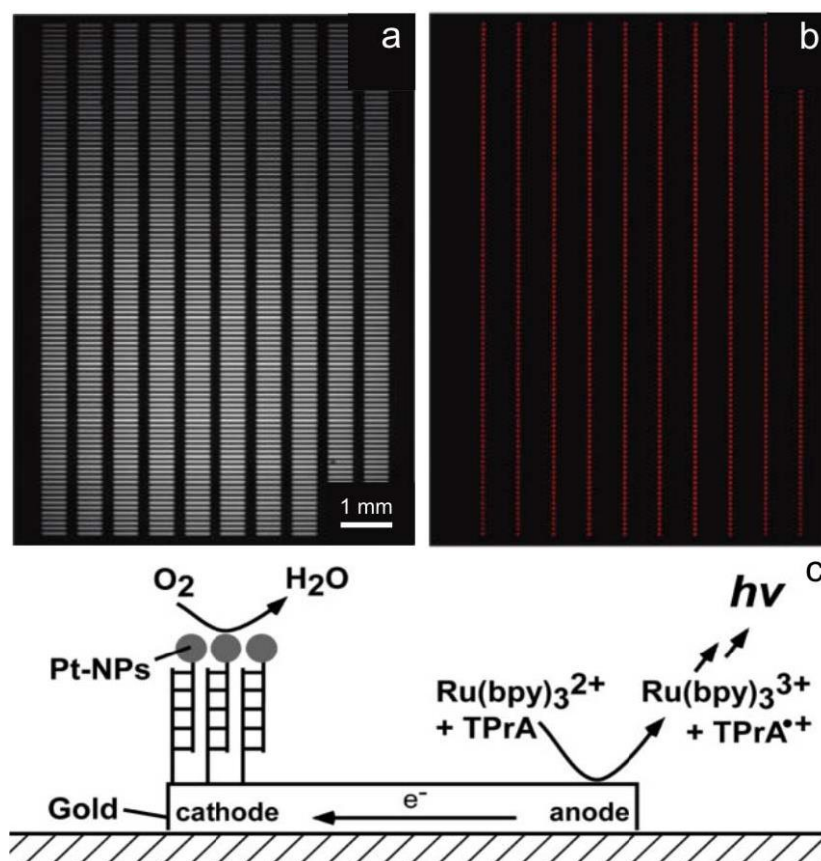


Figure 5. Indirect ECL detection. a) Image of a 1000 Au BPE array with corresponding b) ECL emission⁴⁶. c) Scheme of a bipolar DNA sensing platform²⁷.

Furthermore, the same group enhanced the ECL emission from a BPE array⁴⁶. In this case ECL was generated simultaneously at the anodic poles of 1000 BPEs, as shown in Figure 5a and b. A DNA sensing platform, based on a 1 mm long gold microband covered with a specific oligonucleotide, was designed using indirect an approach²⁷. The hybridization with the Pt NP-labelled complementary oligonucleotide led to O₂ reduction at the cathodic pole of the BPE and simultaneous ECL emission at the opposite side (Figure 5c). Under the same experimental conditions, no ECL emission was observed without hybridization. A theoretical

framework for further understanding ECL generation at a BPE has been reported by Mavré *et al.*⁴⁷.

Chang *et al.* designed a two-channel sensor that enables communication between separated sensing and reporting microchannels via one or more BPEs (Figure 6a)⁴⁸. The sensing channel was filled with conventional electroactive species, such as $\text{Fe}(\text{CN})_6^{3-}$, while the reporting channel with an ECL mixture, and the intensity of ECL was found to be increased with $\text{Fe}(\text{CN})_6^{3-}$ concentration (Figure 6b and c) with a detection limit of 0.32 mM. This type of sensor allows detecting glycosylated hemoglobin and reporting its presence by ECL. The key advantage of this configuration is the physical separation of the ECL reporting mixture and the solution containing the target, thus preventing chemical interference between the two channels.

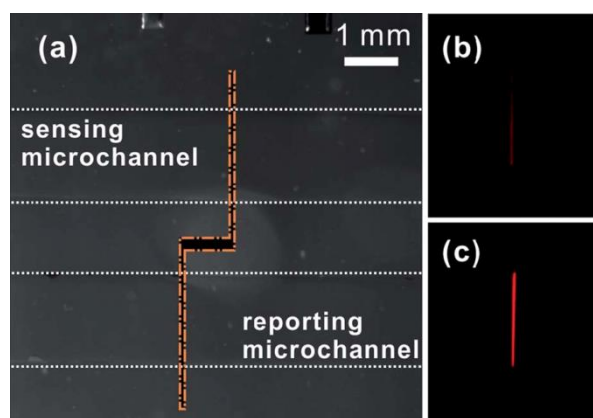


Figure 6. Image of an interchannel BPE spanning a two-channel configuration, the dashed white lines outline the two microchannels, and the orange line emphasizes the location of the BPE. The sensing microchannel was filled with the target molecule $\text{Fe}(\text{CN})_6^{3-}$ and the reporting microchannel was filled with the ECL mixture. ECL images obtained with (b) 0.1 mM and (c) 5 mM $\text{Fe}(\text{CN})_6^{3-}$ present in the reporting channel⁴⁸.

Wang's team reported a novel style of dual-channel ECL based bipolar configuration by using two-direction driving electrodes (only one kind of driving electrode such as driving anode or driving cathode was inserted into both ends of an individual channel as shown in Figure 7)⁴⁹. The BPE is positioned between two channels, and thus a high current efficiency approaching 100% in theory was achieved. More importantly, the background signal from the integrated driving electrodes was completely eliminated, when this unique design was used to construct

an ECL sensing platform. The mechanism, ECL behavior and potential distribution of this design have been investigated in details.

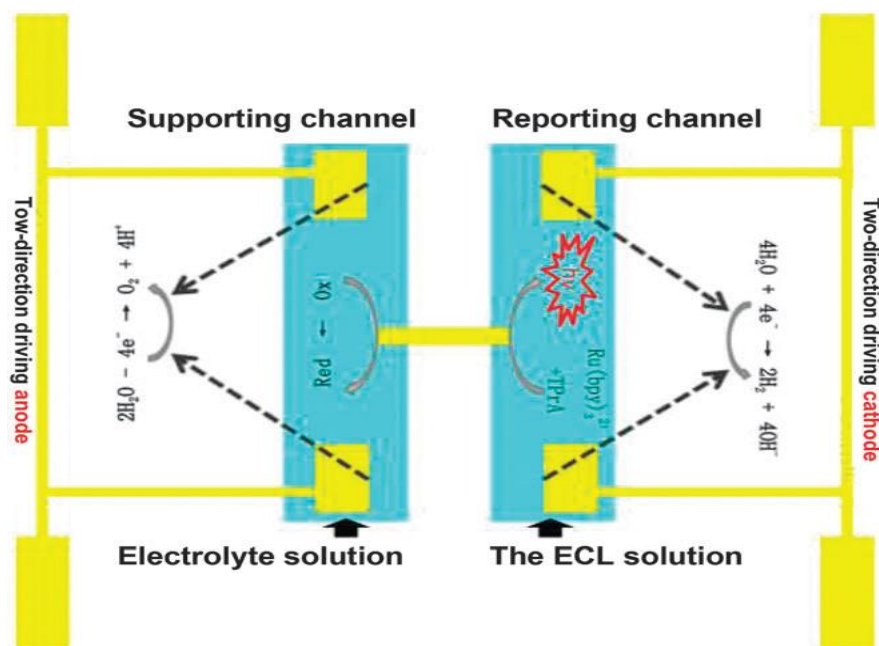


Figure 7. Schematic illustration of the fundamental principle of the dual-channel bipolar ECL sensor⁴⁹.

The applicability of the device was demonstrated by detecting TPrA, dopamine, H₂O₂ and Fe(CN)₆³⁻, with a detection limit of 0.1 μM, 0.2 nM, 2.5 μM and 0.04 mM, respectively⁴⁹. The proposed sensing platform holds promising potential for designing electrochemical or ECL devices with high integration, high automation and high throughput.

4.4. Bipolar electrochemistry for motion generation

The spatial selectivity that BE provides has been recently applied to analytical chemistry,^{12,36} materials science,⁵⁰⁻⁵⁴ and also to propel “swimmers”⁵⁵. Advantages of this technique regarding motors are the motion control provided by the field strength/direction and its versatility, because any kind of conducting object can theoretically act as a swimmer³⁷. Designing such objects, which can mimic the propulsion of biological systems^{2,56-58} in artificial and biological environments has moved to the forefront of science over the last decade⁵⁹⁻⁶¹. The spontaneous hydrolysis of adenosine triphosphate (ATP), which supplies biomolecular motors with energy in natural systems, has been mimicked in most of the strategies developed to generate motion with micro-objects⁶². The concept is based on the use

of a chemical fuel to generate self-electrophoresis or bubble propulsion^{18,62-64}. The most commonly used chemical fuel is H₂O₂. In Figure 8 is presented autonomous motion of platinum-loaded polymer “stomatocytes”⁶². The catalytic decomposition of the fuel from the entrapped Pt-NPs discharges a fast moving jet of gases through an outlet, which in turn generates thrust by jet propulsion.

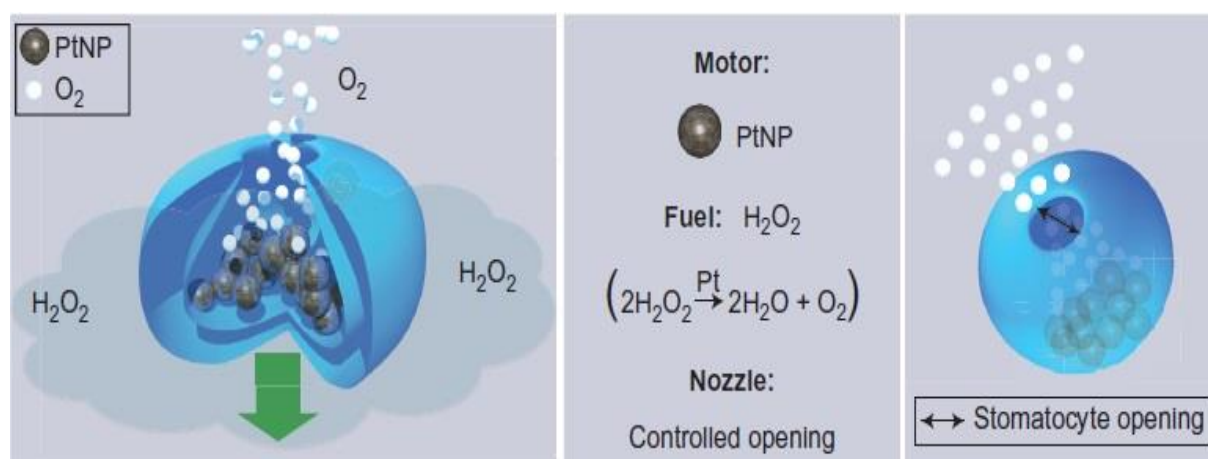


Figure 8. Autonomous movement of artificial stomatocytes (blue) is made possible by entrapping catalytic nanoparticles (grey, here Pt-NPs) through control of the opening and adding the appropriate fuel (here H₂O₂). Left panel, side view of the system; middle panel, analogy with a miniature propellant; right panel, view of the opening of the stomatocyte⁶².

To mimic biomotors, Mallouk, Sen *et al.* were the first to use self-powered nanorods as nanomotors⁶⁵ and Schmidt *et al.* bipolar micro-motors⁶⁶. Wang’s group further improved efficiencies of bimetallic BPEs as nano-motors achieving speeds of 150 $\mu\text{m}\cdot\text{s}^{-1}$ ⁶⁷. The classic strategies are based on using chemically powered motors⁶⁰ and magnetically driven motors having a catalytic or a magnetic extremity, respectively⁶⁸. A fuel induces motion, by reacting at a precise area on the motor composed of an efficient catalyst, e.g. platinum, nickel or metal pairs and alloys⁶⁹. Wang’s group also reported detection of Ag⁺ in a H₂O₂ solution using Au-Pt nano-motors extending the use of motors for sensing⁷⁰. Different applications of such motors have been also reported: isolation of biologically relevant species (e.g. cancer cells, DNA, and RNA)⁷¹⁻⁷³ or pollution remediation⁷⁴. In these cases, bipolar behavior of motors originates from its hybrid composition. BE through electrodeposition offers an attractive approach for the synthesis of highly asymmetric structures appealing for a use as synthetic motors such as “Janus” and “patchy” particles (JPs)⁷⁵.

A motion of a carbon microtubes with an electrochemically generated Pt tip on one side moving in H_2O_2 solution has been reported by Fattah, Kuhn *et al.* (see Figure 9a)⁷⁶. The motion was induced by the generation and release of O_2 bubbles, due to the catalytic decomposition of H_2O_2 at the Pt surface. The same group reported also the synthesis of JPs containing a ferromagnetic part enabling magnetically driven motion⁷⁷. Carbon microtubes modified at one extremity with a Ni particle were rotated using an external magnetic field, as shown in Figure 9b. In all presented examples, the motion of the objects differs in various characteristics, while keeping asymmetry as a common parameter (in shape or composition).

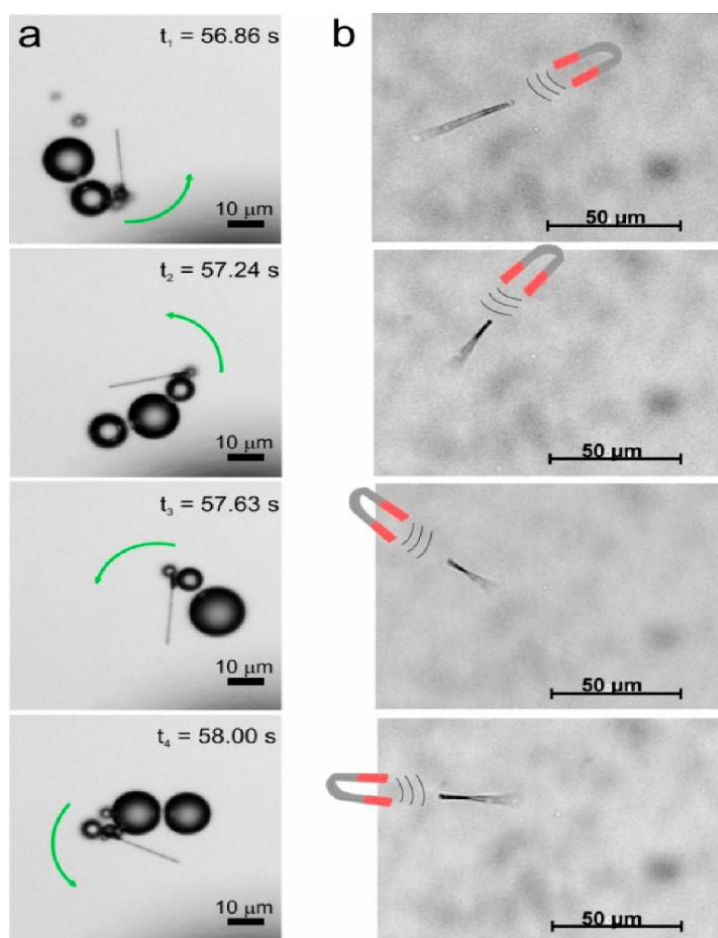


Figure 9. Series of optical micrographs showing (a) rotation of a carbon microtube, modified at one extremity with platinum, in a H_2O_2 solution.⁷⁶ (b) Rotation of a carbon microtube, modified at one extremity with nickel, under the influence of an external magnetic field.⁷⁷

In the following paragraph, motion of objects which exhibit asymmetric electroactivity induced by BE will be presented.

4.4.1. Translation, rotation and levitation of motors by BE

Due to the versatility of BE, any kind of conducting object can be propelled, there is no topological limitation in terms of size and shape³⁶. Since it provides a direct electrochemical break of symmetry, it is an appealing alternative to other existing propulsion mechanisms.

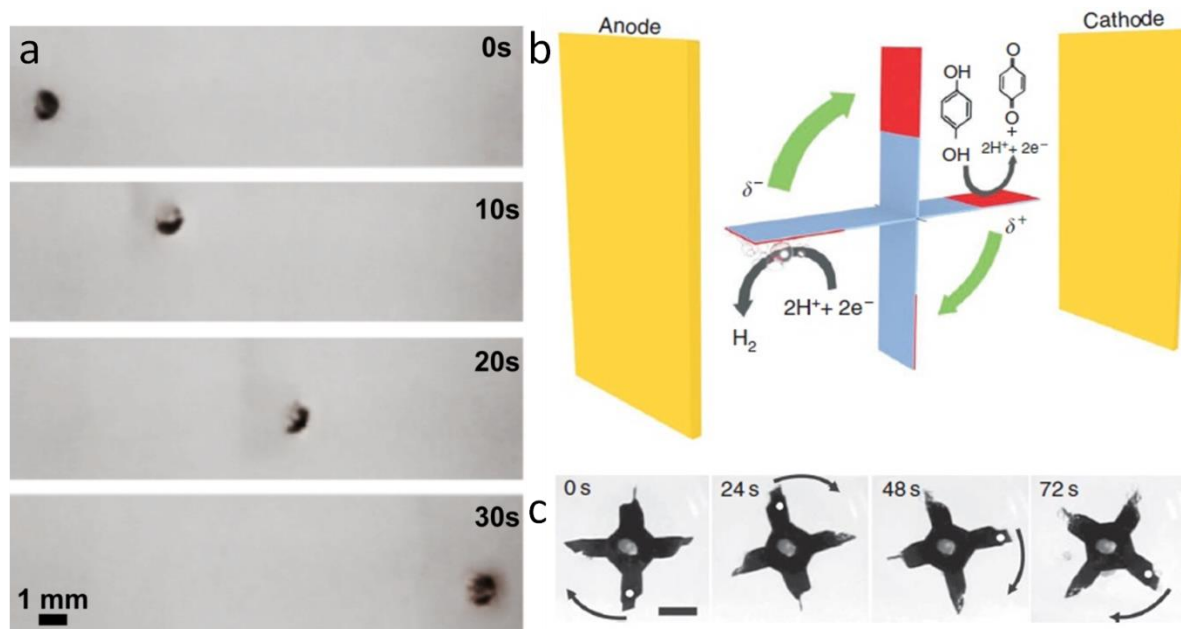


Image 10. a) Translational motion of a metal bead propelled by the production of H_2 bubbles. b) Scheme of a vertical rotor powered by the reduction of protons coupled to hydroquinone, together with the corresponding real-time optical micrographs c), scale bar 0.5 cm^{14} .

Kuhn and co-workers used the strategy for asymmetric bubble production based on water electrolysis at the opposite poles of a spherical metallic BPE¹⁴. The BPE can move because the formation of H_2 bubbles is twice as high as the amount of O_2 . To accelerate the BPEs, the O_2 evolution need to be suppressed and this is possible by addition of molecules which are easier to oxidize than water. This was accomplished by adding hydroquinone to the solution achieving translational motion of 1 mm and 275 μm spheres in polydimethylsiloxane (PDMS) microchannels (Figure 10a and 10b). Using the same principle, rotational motion was demonstrated using an alternative motor design based on a carbon-doped polycarbonate cross covered with an insulating polymer everywhere except at its ends. Generation of gas bubbles at the active ends enabled horizontal and vertical motion, although the vertical one was more efficient due to the buoyancy of the exerted gas (Figure 10c).

The same authors reported the levitation of particles in capillaries¹⁶. To generate the levitation of a conducting bead, the external feeder electrodes are polarized at the capillary entrances in such a way that the H₂ bubbles are generated underneath the bead. As a consequence, motion is generated in the direction opposite of the bubble release. The BPE bead was used as a lifter for a small cargo. Interestingly, using a conically shaped capillary the periodic bubble accumulation and release implied a yo-yo alternating motion (repeating levitation-fall cycle of the bead) instead of a continuous motion.

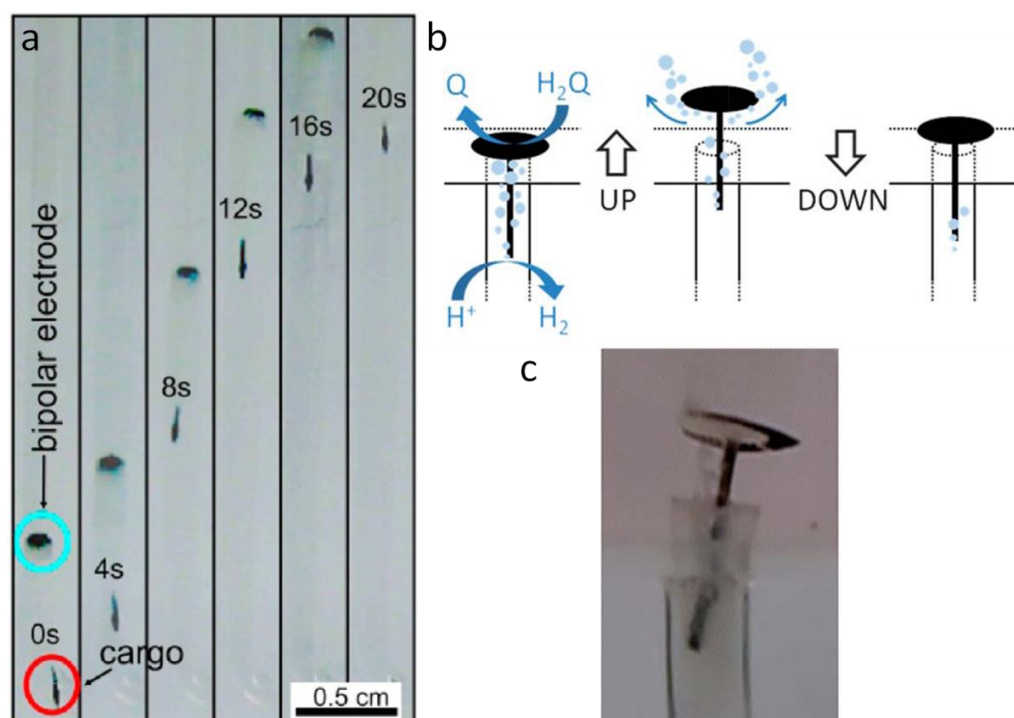


Figure 11. a) Series of optical micrographs showing cargo lifting of a polymer capsule by a glassy carbon bipolar electrode during the levitation.¹⁶ b) Schematic illustration of the 3-step mechanism leading to the motion of the valve together with the corresponding real-time optical micrographs c).¹⁵

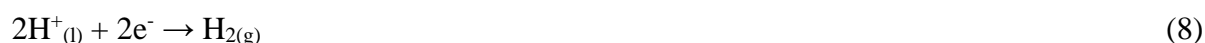
Bouffier and Kuhn showed also that BPEs can operate as a wireless electrochemical valve, where electrogenerated H₂ bubbles cause the valve to lift and open (Figure 11b and c)¹⁵. One can imagine interesting applications of this motors for example by using of cargo lifting concept in miniaturized detection systems and lab on a chip devices.

4.5. Lightening up bipolar swimmers

The intrinsic redox asymmetry provided by BE makes this phenomenon very suitable for the generation of bubble-induced motion of electrically conducting particles. Still, tracking such moving objects in real time is a challenge and therefore tremendous effort has been made to design particles with specific optical, in many cases fluorescent, properties⁷⁸. Here, we will

present an original approach of autonomous motion of the moving object monitored with light emission produced by ECL. In this case, BE is not only the asymmetric driving force for the particle propulsion but is also responsible for the light emission, combining in a synergetic way both redox reactions on the same object²⁸.

As in previous cases, the motion is here induced by the release and evolution of H₂ bubbles due to the reduction of water at the cathodic pole of the bipolar swimmer^{14,16}, which proceeds according to the following equation:



Because of charge neutrality during BE, water or a sacrificial molecule such as hydroquinone must be oxidized simultaneously at the anodic pole, generating oxidation products such as O₂ or benzoquinone. These anodic reactions are not useful in the context of propulsion and can therefore be replaced by electrochemical reactions, leading to ECL emission. As discussed in Chapter 1, ECL is an electrochemical process which produces light and that can be triggered at an anodic potential. The ECL mechanism of the model TPrA/Ru(bpy)₃²⁺ system depends on several experimental parameters like the surface hydrophobicity,⁷⁹ the electrode material, the concentration ratio, the pH or the presence of surfactant⁸⁰. In brief, it is based on the two following reactions:



The formed reactive radical cation TPrA^{•+} fastly undergoes reaction of deprotonation forming a highly reducing agent TPrA[•] (tri-propylamine radical). Both TPrA^{•+} and TPrA[•] react with ruthenium complexes to populate the excited state thus, producing light⁸¹. As depicted in Figure 12, the synergetic reduction of H₂O at the cathodic pole and simplified oxidative ECL mechanism at the anodic pole can induce the simultaneous motion and light emission on a bipolar swimmer.

To estimate the minimum ΔV which is required to generate simultaneously the gas bubbles and ECL, the corresponding redox reactions have been first characterized by cyclic voltammetry. The three-electrode system consisted in a home-made glassy carbon (GC) electrode as working electrode, composed of the same material as the swimmer, a Ag/AgCl/KCl 3 M saturated reference electrode and a platinum wire counter-electrode. GC

has been chosen as the swimmer material because of its low density (1.4 g cm^{-3}) compared to many other conducting materials, like metals. This decreases the force needed to overcome gravity for an object with a given volume.

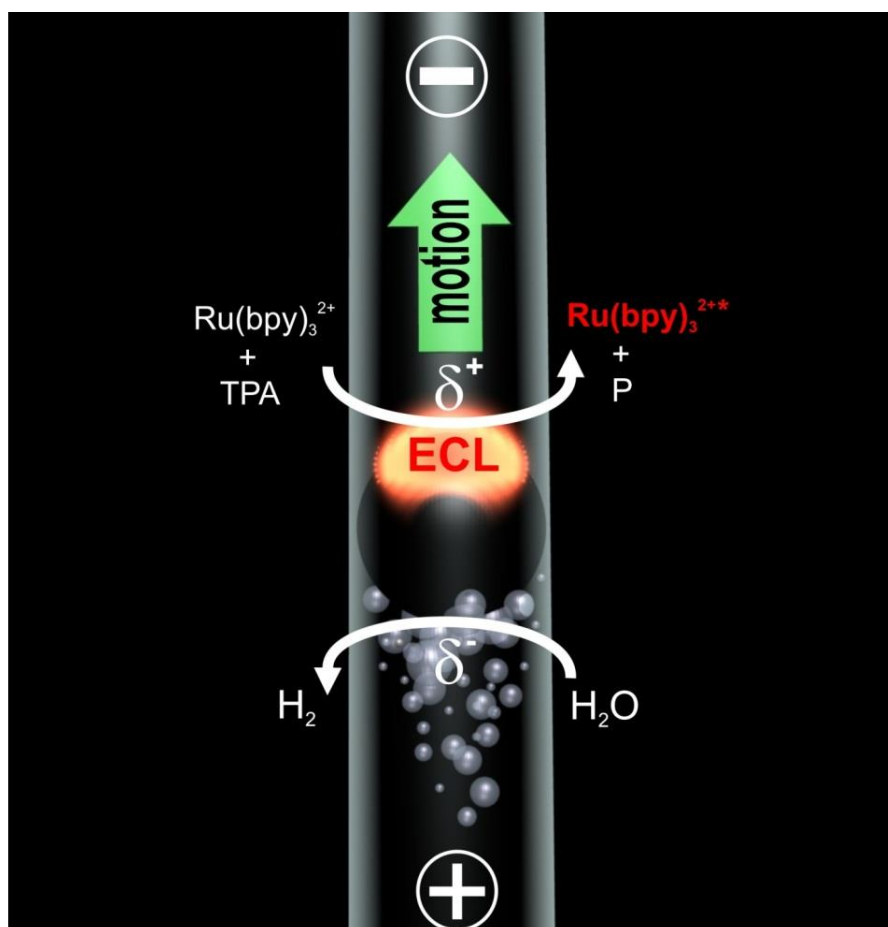


Figure 12. Light emitting electrochemical swimmer. The synergistic reduction of H_2O at the cathodic pole (bottom of the bead) and oxidative ECL mechanism at the anodic pole (top of the bead) induce the simultaneous motion and light emission²⁸.

This electrochemical measurement has been combined with a simultaneous monitoring of the ECL intensity by using a photomultiplier tube. Typical voltammetric and ECL responses of 0.5 mM tris(2,2'-bipyridyl)dichlororuthenium(II) hexahydrate in the presence of 100 mM TPrA with 100 mM phosphate buffer (PBS, $\text{pH}=7.4$) are presented in Figure 13.

From these curves, the potential values for which the different redox reactions are occurring at the swimmer surface can be easily extracted. Water reduction (reaction 8) takes place at $-1.1 \text{ V vs. Ag/AgCl}$ and ECL emission occurs at 1 V vs. Ag/AgCl . Based on these experimentally determined values, one can conclude that the coupling of water reduction and ECL emission

at the reactive poles of a BPE is possible only if the polarization potential ΔV between both extremities of the BPE is at least equal to $\Delta V_{min} = 2.1$ V. Equation (5) thus states that for a BPE having a diameter d of about 1 mm, the electric field E has to be, in a first order approximation, at least equal to 21 V cm^{-1} .

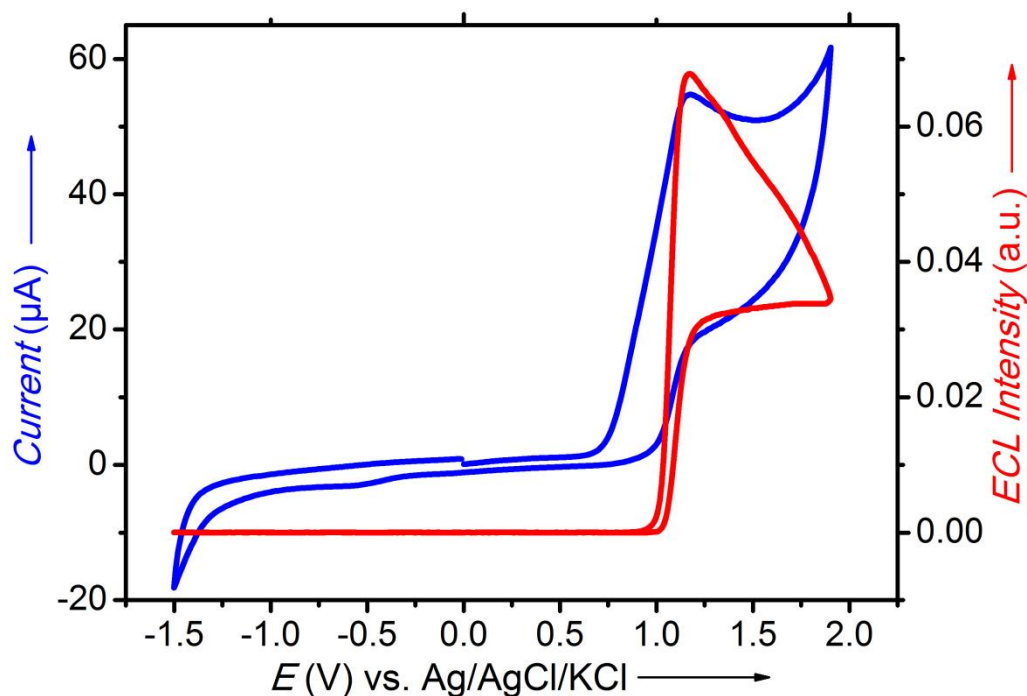


Figure 13. Cyclic voltammogram (blue) and ECL signal (red) of $0.5 \text{ mM Ru(bpy)}_3^{2+}$ in the presence of 100 mM TPrA with $100 \text{ mM phosphate buffer (pH=7.4)}$ on a home-made glassy carbon electrode at a scan rate of 100 mV/s .²⁸

The bipolar experiments for levitation were achieved in glass U-shaped capillaries (Figure 14a), that were made by manual shaping of Pasteur pipettes with a Bunsen burner. A few drops of surfactant were carefully added into the cell to prevent the formation of large gas bubbles. The cell was maintained with its arms in a vertical position and the GC bead with a diameter $d \approx 1$ was then inserted into one arm of the cell. Due to the slightly conical shape of the capillary, the bead dropped until it was stopped by the surrounding capillary walls. The feeder electrodes (Pt wires) were inserted into the top part of the cell and were polarized in such a way that the H_2 flow is generated underneath the bead, as illustrated in Figure 12 and Figure 14b. The ECL was recorded using a digital camera (Sony, Cyber-shot). The length of the U-cell being 9.8 cm between the two electrode positions and the applied voltage was equal to 250 V , corresponding to a global electric field of $E = 25.5 \text{ V cm}^{-1}$. This electric field value

is superior to the theoretical threshold value of 21 V cm^{-1} previously calculated and therefore leads to the synergetic levitation/ECL emission of the GC bead under these conditions, as demonstrated by Figure 14b.

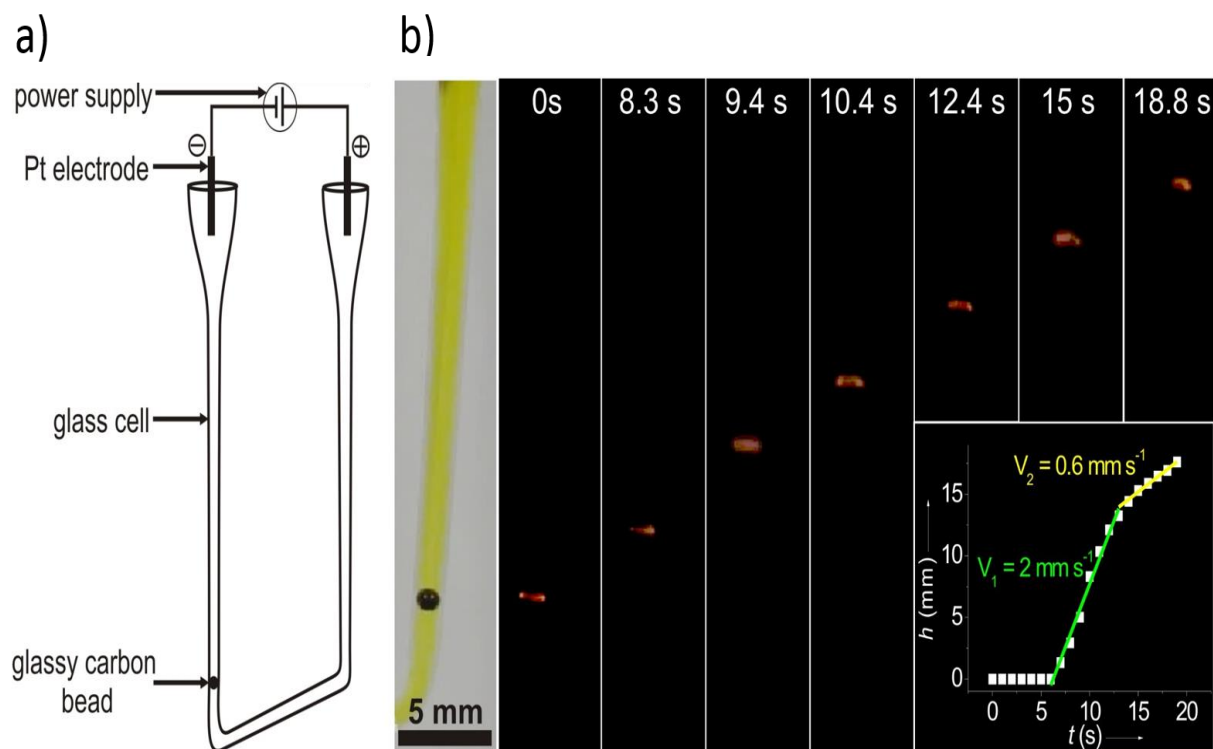


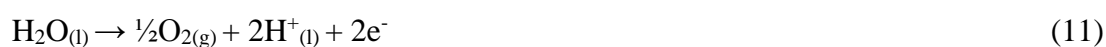
Figure 14. a) Scheme of the set-up used for static and levitation experiments. b) Levitation of a light-emitting glassy carbon bead. Series of optical micrographs showing the levitation of a GC bead in a U-cell filled with PBS (100 mM) containing $0.5 \text{ mM Ru(bpy)}_3^{2+}$, 100 mM TPrA and few drops of surfactant under the influence of a 25.5 V cm^{-1} external electric field. The left micrograph presents the bead position under white light and others micrographs where taken in the dark. Inset: Plot showing the height evolution h as a function of time t .²⁸

The left picture of Figure 14b, obtained under ambient light, shows the GC bead in the capillary. The bead is totally spherical but appears slightly stretched along its equatorial axis due to an optical effect, generated by the cylindrical shape of the capillary. The light was then turned off and the appropriate EF imposed. The ECL generated at the anodic pole of the BE is bright and could be instantaneously observed with the naked eye (Figure 14b). The initial time $t = 0 \text{ s}$ is defined as the time when the camera focused on the ECL signal, allowing its visualization properly. After 6 s the levitation starts due to H_2 bubble production underneath the bead, a phenomenon that could be clearly observed when the ambient light was turned on during the bead motion. The surfactant that was added to the solution promotes a

homogeneous formation of the H₂ bubbles and facilitates their continuous release from the bead surface, generating a more uniform motion⁸².

The inset of Figure 14b shows the height evolution h of the bead during the time t . Height h was defined as the distance between the equatorial axis of the immobilized bead on the left picture and the center of the ECL emitting area during the motion. This curve can be divided into three distinct parts, from which the speed can be extracted based on the slope. In the first part of the curve, the bead did not move. This part corresponds to the period of bubble accumulation underneath the bead for the generation of a sufficiently high buoyancy to overcome gravity. After this initial phase, the change in height was linear for seven seconds at a speed $v_1 = 2 \text{ mm s}^{-1}$ or approximately two body-lengths per second. Finally, because the shape of the cell arm is slightly conical (see left picture of Figure 14b), the space between the bead and the glass walls became larger as the bead rise, thus allowing the bubbles to escape partially from below the bead, which lead to a decrease of the speed during the third phase ($v_2 = 0.6 \text{ mm s}^{-1}$). The levitation was stopped by switching off the EF. This caused the bead to drop and a new rise could be triggered by reapplying the EF. The height and speed of levitation is comparable to the ones described in paragraph 4.4.1 without ECL¹⁶, showing that the ECL mechanism does not affect the bead propulsion. According to Figure 14b, the ECL profile should follow the shape of the anodic pole, leading to a lightened hemisphere at the top of the bead. This was the case at certain moments of the experiment, but during the run a more ring-like ECL shape was also observed. To understand these changes, we further investigated parameters affecting the ECL profile at GC beads in more details.

pH is a crucial parameter for the ECL mechanism to occur. Indeed, ECL is known to be effective at $\text{pH} > 5.5$, with a maximum intensity at $\text{pH} 7.5$ (see paragraph 1.4.1.3). TPrA is insoluble at higher pH and is protonated at lower pH (as well as TPrA^{•+}) which inhibits the ECL mechanism⁸³. This is the reason for using PBS buffer in the reported experiments, ensuring a constant pH value of 7.4 under normal conditions. But, depending on the applied potential, water may also be oxidized at the anodic hemisphere of the bead following the reaction:



The oxidation wave corresponding to this reaction can be observed on Figure 13. It starts at a more anodic potential than the ECL reactions, around 1.5 V vs. Ag/AgCl. The theoretical

polarization voltage required for achieving simultaneously water reduction (reaction 8) at the cathodic pole and ECL emission and water oxidation (reaction 11) at the anodic pole corresponds then to $1.5 + 1.1 = 2.6$ V. This value fits with the value of ΔV applied for Figure 14b. This suggests that water oxidation occurs at the very top of the bead where the polarization potential is the highest, inducing therefore a local pH decrease.

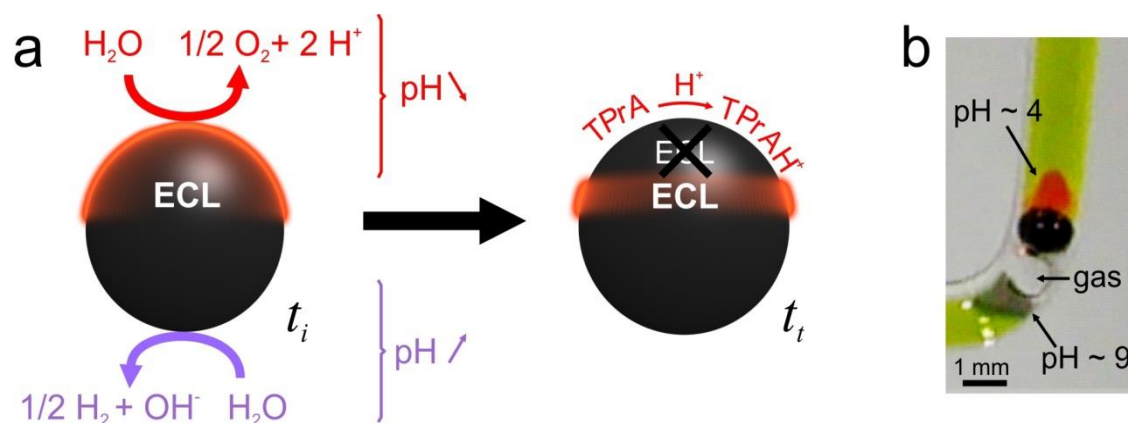


Figure 15. pH control of the ECL shape. a) Mechanism responsible for the shape of the ECL-emitting region on the bead. b) Optical micrograph of a GC bead in the U-cell filled with 100 mM PBS containing 0.5 mM $\text{Ru}(\text{bpy})_3^{2+}$, 100 mM TPrA and a universal pH indicator under the influence of a 25.5 V cm^{-1} external electric field.²⁸

To check such a pH variation, experiments were performed in the presence of a pH indicator. A GC bead was submitted to the same electric field than previously. The medium was also identical except that no surfactant was added and a few drops of a universal pH indicator were added to the solution. Figure 15b shows clearly that, during these experiments, pH variations are occurring at the reactive poles of the BE. Indeed, one can observe that water reduction which produces the H_2 gas bubble also induces an expected pH increase (reaction 8) up to a value about 9. It is worth noting that in this particular case, the absence of surfactant caused the H_2 accumulation, producing the bubble that can be seen at the bottom of the bead. At the top of the bead, the pH reaches a value of 4, confirming that water oxidation (reaction 11) also takes place at the anodic pole. This experiment confirmed that ECL reactions are in competition with water oxidation at the anodic pole of the bead. As depicted in Figure 15a, this reaction directly influences the ECL process since it induces locally a pH decrease, leading to TPrA protonation, which finally causes the ECL quenching at the top part of the bead, thus creating an ECL ring instead of the hemispherical shape.

To precisely capture the ECL profile around the GC bead during BE, additional experiments were performed with the BPE placed in front of a microscope (objective x5) equipped with a CCD camera. To avoid bead motion, which is useless for these experiments, they were carried out in the absence of surfactant. We investigated the influence of parameters such as applied voltage and buffer capacity which directly affect the pH gradient around the bead and thus the ECL profile. Surprisingly, ECL has been observed at global EFs as low as 6.2 V cm^{-1} . This is due to the fact that, in this particular case, the bead is touching the capillary walls, leaving only a very thin layer of liquid between the bead and the walls. The configuration present here is intermediate between the classical cases of open and closed BEs, presented in paragraph 4.2.2. and 4.2.3. The electrical resistance of the liquid thin layer is much higher than the resistance of the solution in the rest of the capillary, leading to a locally increased potential drop that can drive the two redox reactions.

During these experiments, the desired voltage was applied, directly generating the initial ECL shape. As shown in Figure 16, the ECL-emitting region does not expand into the solution surrounding the bead. It is confined to the bead surface by the high TPrA concentration which limits the thickness of the ECL reaction layer. This initial shape changes rapidly to a transient state (typically after a few seconds). Two representative times are now considered, as they correspond to the two characteristic ECL shapes. The first one is the initial time t_0 which corresponds to the first ECL shape obtained once the desired voltage is reached. The second, t_t , corresponds to the transient shape. The images obtained at t_0 and t_t for two buffer concentrations for applied voltages of 60 V, 75 V and 100 V are shown on Figure 16. As expected, the direct consequence of the increase of the potential applied between the feeder electrodes is a shift of the ECL boundary towards the equatorial axis of the bead. Indeed, the region where the potential is anodic enough to generate ECL expands towards the middle of the bead. As shown by Figure 16a, c, g and i, hemispherical ECL shapes are generated at the initial stage t_0 with experimental conditions such as 100 mM PBS and $E = 60 \text{ V}$ or 75 V . With 60 V, this shape remains roughly the same during the whole experiment but with 75 V, it changes quickly to an ECL ring that is shown in Figure 16d. Such a behavior can be rationalized by means of the mechanism previously discussed and illustrated in Figure 16a. At 60 V, the driving force is not sufficient to generate a pH change at the top of the bead, so the ECL shape remains hemispherical. On the contrary, an external voltage of 75 V is high enough to induce proton formation at a sufficient rate to decrease the pH after a given time (t_t).

at the anodic pole when using a 100 mM PBS solution. Therefore the formation of an electrogenerated pH gradient limits the ECL region to a ring shape.

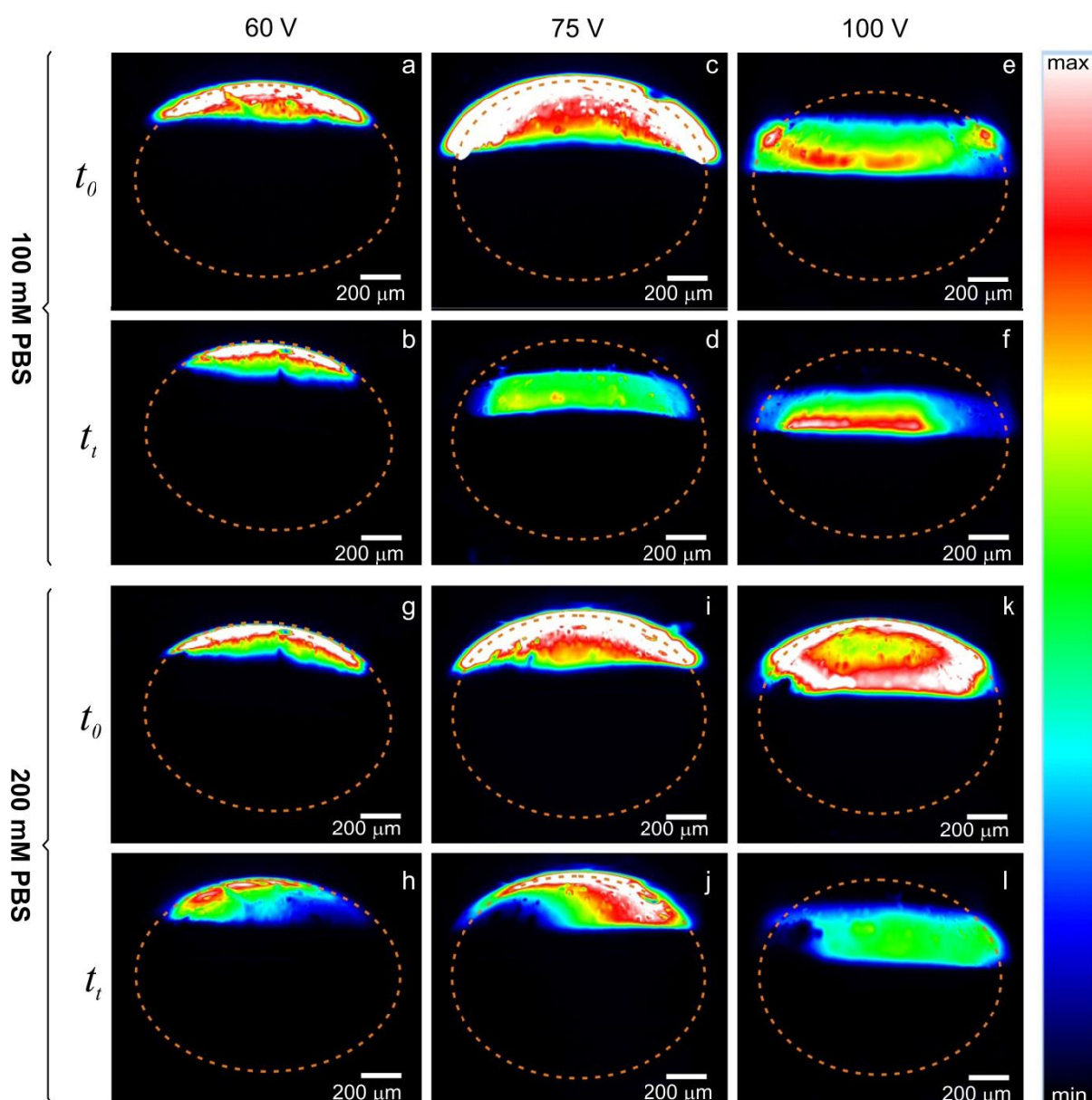


Figure 16. CCD images showing the ECL intensity profiles on a GC bead in a U-cell filled with PBS containing 0.5 mM $\text{Ru}(\text{bpy})_3^{2+}$ and 100 mM TPrA, at $t = t_0$ applying 60 V, 75 V and 100 V between the feeder electrodes. The six top pictures were obtained using a PBS concentration of 100 mM and the six bottom ones with a PBS concentration of 200 mM.²⁸

This general trend is confirmed by Figure 16e which shows that, when applying 100 V, the ring is instantaneously generated at t_0 . The influence of the buffer capacity on these experiments was also investigated. At higher buffer capacity (200 mM PBS), the ECL shape

remains hemispherical up to a voltage of 75 V even after a few seconds (Figure 16j). Under these conditions, no ECL ring was observed because the buffer capacity is strong enough to avoid TPrA protonation, promoting ECL emission all over the anodic pole. Also at this buffer concentration, the initial ECL (at t_0) shape using 100 V is hemispherical (Figure 16k), which was not the case at 100 mM PBS (Figure 16e), confirming once again a pH based mechanism.

These experiments demonstrate clearly that the control of the ECL shape on a BPE in these static experiments can be fine-tuned using easily controllable parameters such as EF value or buffer concentration. In this case, the ECL ring corresponds ideally to the area of the anodic pole where the polarization potential is strong enough to generate ECL emission, but where the water oxidation rate is not efficient enough to protonate TPrA or its radicals. In the case of swimmer motion the situation becomes more complicated, because proton diffusion, convection due to bubbles formation and motion of the bipolar swimmer have a strong impact on the concentration gradients of the involved species and thus on the final ECL shape. Nevertheless, the mechanism inducing the ECL profile changes from hemispherical to ring shapes can be rationalized in terms of local pH variations, which occur in the vicinity of the swimmer during its motion.

This work presents the first synergetic action of BE in terms of simultaneous propulsion and ECL generation, leading *in fine* to the first example of a swimmer which is intrinsically coupled with a chemical light source. In the reported experiments, ECL provides a direct monitoring of the object motion, which is very useful when dealing with autonomous swimmers.

The versatility of BE coupled to ECL allows imagining other types of swimmers based on the same principle. The following work showed that this methodology can be generalized with another ECL system based on luminol (5-Amino-2,3-dihydro-1,4-phthalazine-dione or 3-aminophthalhydrazide), allowing tuning the wavelength of light emission²⁹. Luminol and its derivatives⁸⁴ are widely used in biochemical and clinical analysis such as enzymatic assays and immunoassays^{85,86}. Blue ECL emission is achieved in alkaline solution in the presence of H_2O_2 . Moreover, the previously described bipolar swimmer was reported in neutral solutions with cathodic bubbles generation (H_2 evolution). In contrast, this first example in an alkaline solution proceeds through a mechanism based on H_2O_2 consumption as presented in Figure

17a. H₂O₂ oxidation allows the light emission at the same BPE pole (anode) than the bubble production as following:

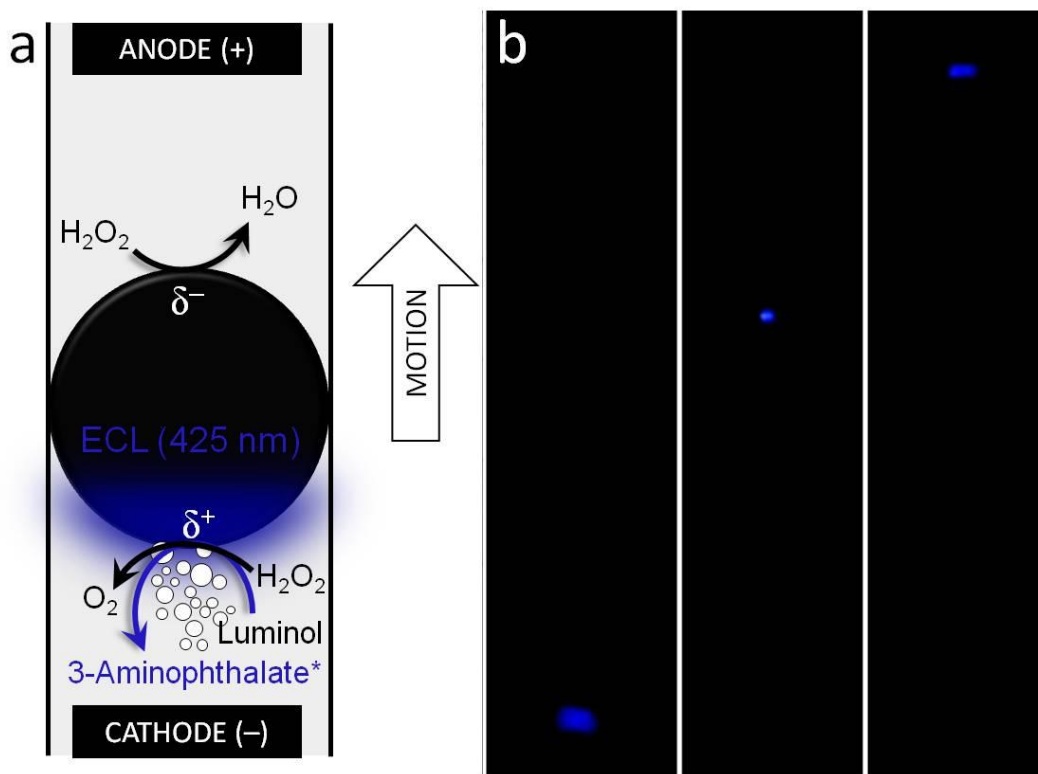


Figure 17. Blue bipolar emitting swimmer a) Scheme showing the electrochemical reactions occurring for the motion of the blue ECL swimmer. b) Corresponding series of optical micrographs showing the levitation of a 1 mm GC bead in a capillary filled with sodium hydroxide (0.1 M) containing 1% H₂O₂ and 0.01 M luminol under the influence of a 25 V cm⁻¹ external electric field.²⁹

These oxidation reactions are compensated with the reduction of hydrogen peroxide at the cathodic pole:



The corresponding redox reactions have been first characterized by cyclic voltammetry simultaneously with ECL recording using the three-electrode system consisted in a home-made GC electrode as working electrode, like for the ruthenium emitting swimmer. Hydrogen peroxide is essentially electro-oxidized to oxygen at ~ + 0.5 V and reduced to hydroxide anions at ~ - 1.25 V vs. Ag/AgCl (Figure 18 a). Both processes are irreversible and involve

two electrons. A cyclic voltammogram recorded with a 10^{-2} M luminol solution in NaOH (0.1 M) with H_2O_2 exhibits the irreversible oxidation of luminol centered at +0.3 V vs. Ag/AgCl (Figure 18 b). As expected, the oxidation step is responsible for the ECL process starting right at the foot of the anodic wave and with a maximum intensity observed at + 0.5 V vs. Ag/AgCl.

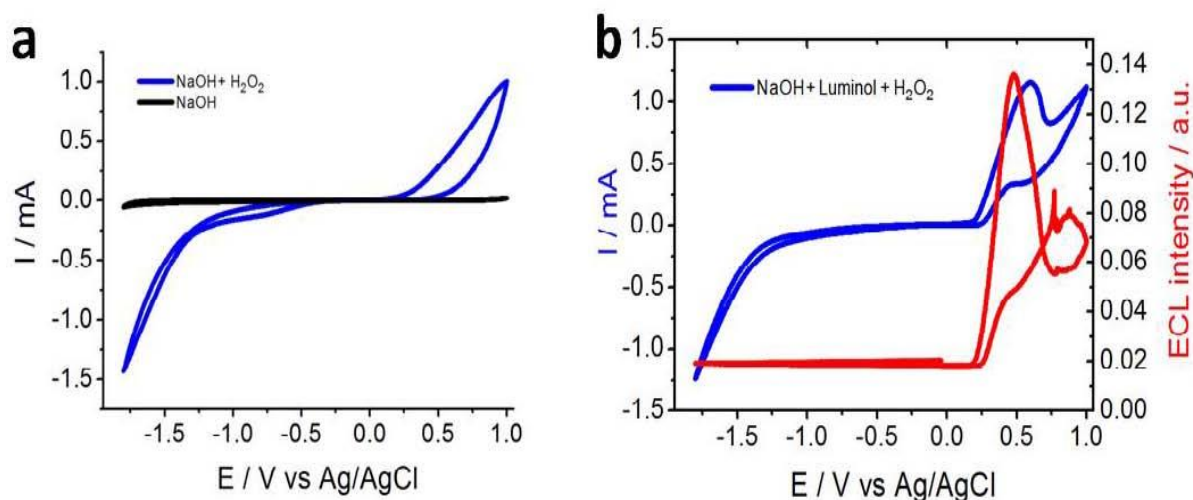


Figure 18. Cyclic voltammograms recorded in 0.1 M sodium hydroxide with and without 1% H_2O_2 (a) and with 0.01 M luminol combined with ECL detection (b). Scan rate 0.1 V/s.

The generation of oxygen bubbles arises from H_2O_2 oxidation but, in addition the decomposition of luminol produces also N_2 bubbles (reaction 13) which can contribute to the propulsion of the BPE. It is noteworthy that the connection of the feeder electrodes to the power supply is opposite to the previous report based on the ECL of $\text{Ru}(\text{bpy})_3^{2+}$. The reason is obvious because the first ECL system was exploiting hydrogen evolution (i.e. proton reduction) located on the cathodic pole of the BE facing the feeder anode. For the levitation experiments, a typical voltage of 250 V over a distance of 10 cm was applied (electric field of 25 V/cm^{-1}). After switching off the light, the vertical motion of the bead could be easily followed due to luminol ECL (Figure 17b). As a general trend the swimmer progressively slows down during the course of vertical motion due to the slightly conical shape of the bipolar cell, which favors the escape of bubbles from underneath the carbon bead after reaching a certain height in the capillary. An average speed of about 0.1 mm s^{-1} has been observed. This finding opens the door to the possible design in the near future of functional systems combining multi-wavelength light emission.

4.6. Light emitting swimmers for enzymatic glucose sensing

BE offers the possibility to design such swimmers in a very straightforward way as the simple application of an EF across the solution promotes localized oxygen or hydrogen evolution, leading *in fine* to a motion driven by gas bubble production¹⁴⁻¹⁷. The asymmetric redox activity induced on the BPE is also used to activate other functions such as the above presented ECL emission. Since, ECL is a very sensitive analytical method that benefits from various advantages including a remarkable signal-to-noise ratio²², monitoring ECL intensity during the swimmer run can be exploited as a useful analytical signal. In model $\text{Ru}(\text{bpy})_3^{2+}$ / TPrA system, only the ECL luminophore is regenerated during the process, whereas the co-reactant is consumed by the electrochemical reactions²⁸. Nevertheless, ECL provides high sensitivity and selectivity detection with wide linear dynamic range for numerous co-reactants. Milutinovic and co-workers reported a sensing approach based on an electrodeposited ECL exhibiting redox hydrogel using glucose dehydrogenase as a model system⁸⁷. They have shown that the intensity of the ECL of reduced NADH produced by the enzymatic activity varies with the enzyme substrate concentration. In dehydrogenase-type enzyme-catalyzed reactions, the addition of β -nicotinamide adenine dinucleotide (NAD^+) is required as a co-factor for the enzymatic reaction^{88,89}. Under substrate oxidation, NAD^+ is simultaneously reduced to NADH, the reduced form of the co-factor, acting in this way as an ECL co-reactant. Numerous examples of dehydrogenase-based ECL detection have been reported with such systems based on alcohol dehydrogenase⁹⁰⁻⁹² and glucose dehydrogenase^{88,93}. ECL light emission is a valuable analytical signal because the NAD^+ does not promote ECL in contrast to its reduced form NADH, in the case of a simultaneous presence of the enzyme and its substrate. It is noteworthy that using NADH as the co-reactant, the ECL-active form of the co-reactant is regenerated by the enzymatic reaction. Herein we present an ECL-emitting bioswimmer for glucose sensing *via* concomitant oxidation of $\text{Ru}(\text{bpy})_3^{2+}$ and of the enzymatically-produced NADH for the first time⁹⁴.

In Figure 19, the principle of the swimmer which generates ECL emission only in the presence of glucose is presented. The set-up for the BE experiments were achieved using a similar protocol like for the levitation of ruthenium or luminol ECL swimmers (Figure 14a).

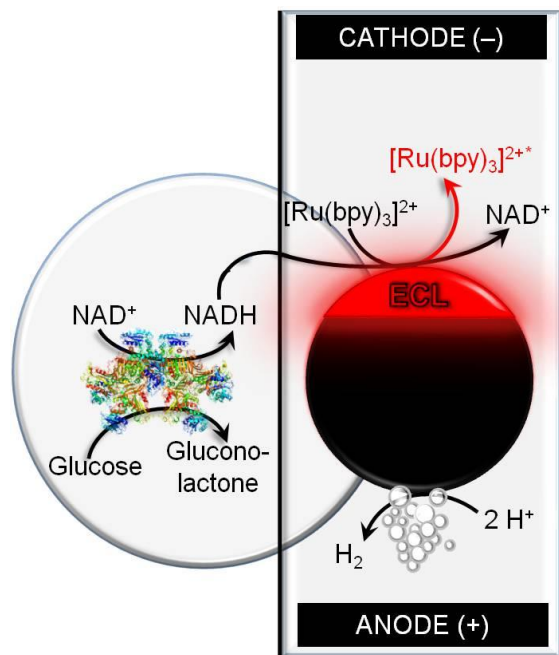


Figure 19. Schematic illustration of enzyme-driven ECL observed on a bipolar swimmer. Glucose is oxidized by glucose dehydrogenase (GDH) with NAD^+ as a co-factor. The enzymatically-produced NADH behaves as an *in situ* co-reactant for the ECL generation.⁹⁴

A GC bead with a diameter $d \approx 1$ mm was inserted into one arm of the U-capillary. The propulsion mechanism is based on the cathodic H_2 bubbles evolution (reaction 8). In the absence of glucose, the only reactions occurring at the anodic pole of the swimmer are the oxidation of the ruthenium complex as well as of water according to the reactions 10 and 11, respectively. Thus, the oxidation of $\text{Ru}(\text{bpy})_3^{2+}$ does not generate any ECL since the enzymatic co-factor remains in the ECL-inactive NAD^+ form. Accordingly, ECL emission occurs when the enzymatic system is turned on in the presence of glucose substrate. Indeed, GDH oxidizes glucose to gluconolactone with the concomitant conversion of NAD^+ to NADH (Figure 18). In that case, the electron transfer (ET) reactions occurring on the anodic BPE pole are the mono-electronic oxidation of $\text{Ru}(\text{bpy})_3^{2+}$ (reaction 10) and of NADH to the corresponding cation radical (reaction 15), which can promote the whole sequence of reactions leading to ECL emission:



Since NAD^+ is regenerated at the end of the ECL mechanism, it is thus available to react again with the enzyme and the process is catalytic. Therefore, a difference in glucose concentration should be easy to distinguish by measuring the ECL intensity.

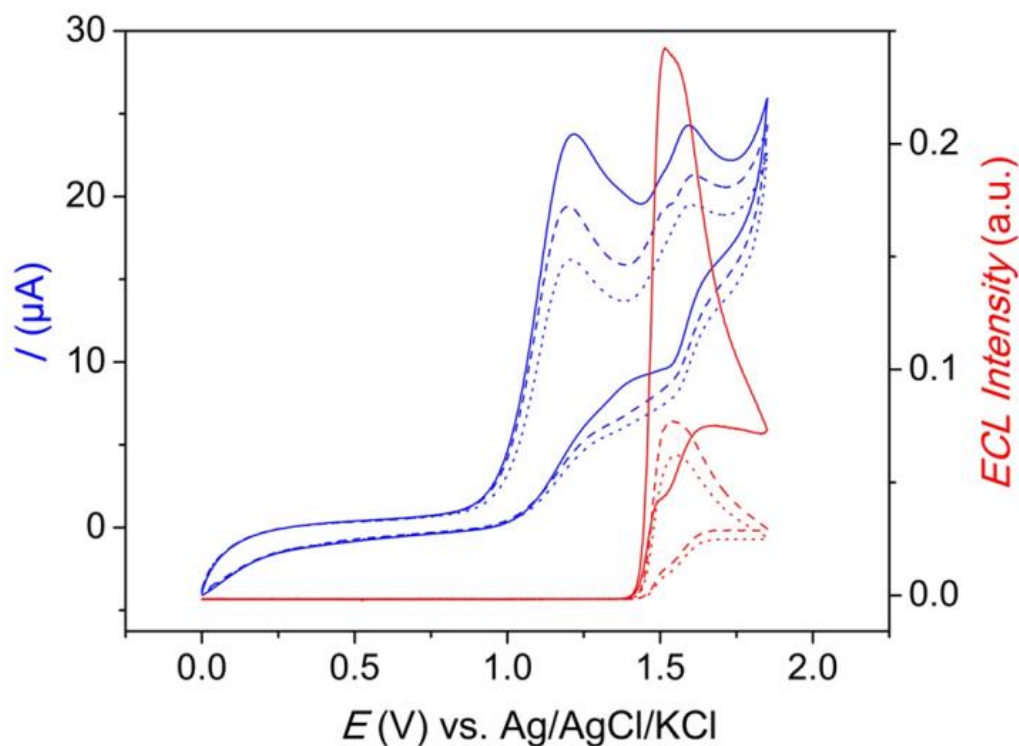


Figure 20. Cyclic voltammograms (blue lines) and ECL signals (red lines) of 1.5 mM $\text{Ru}(\text{bpy})_3^{2+}$ in the presence of $10 \text{ U}\cdot\text{mL}^{-1}$ GDH, 10 mM NAD^+ and various glucose concentrations (5 mM, dotted lines; 10 mM, dashed lines and 40 mM, solid lines) in 100 mM PBS solution (pH 7.4). A GC electrode (same material as the swimmer) was used to record both current and ECL. Scan rate 0.05 V s^{-1} .⁹⁴

Figure 20 gathers the cyclic voltammograms (blue lines) and the corresponding ECL intensity (red lines) of a series of solutions containing various amounts of glucose. These data were recorded 30 minutes after mixing GDH, NAD^+ and glucose in 100 mM PBS solution (pH 7.4). NADH oxidation occurs first and the ET is irreversible with an anodic peak centered at $\sim 1.2 \text{ V vs. Ag/AgCl}$. The oxidation of $\text{Ru}(\text{bpy})_3^{2+}$ takes place at slightly more anodic potential ($\sim 1.55 \text{ V vs. Ag/AgCl}$). A careful examination of the ECL signal recorded during the cyclic voltammogram shows that the emission perfectly matches with the potential region where $\text{Ru}(\text{bpy})_3^{2+}$ is oxidized. The ECL mechanism clearly involves a reaction between both intermediate species formed by the oxidation of NADH and $\text{Ru}(\text{bpy})_3^{2+}$. Increasing the glucose concentration from 5 to 40 mM results in raising the level of NADH in solution. This

increase can be monitored by measuring the ECL intensity with a photomultiplier tube. Indeed, the ECL intensity is dependent on the initial glucose content.

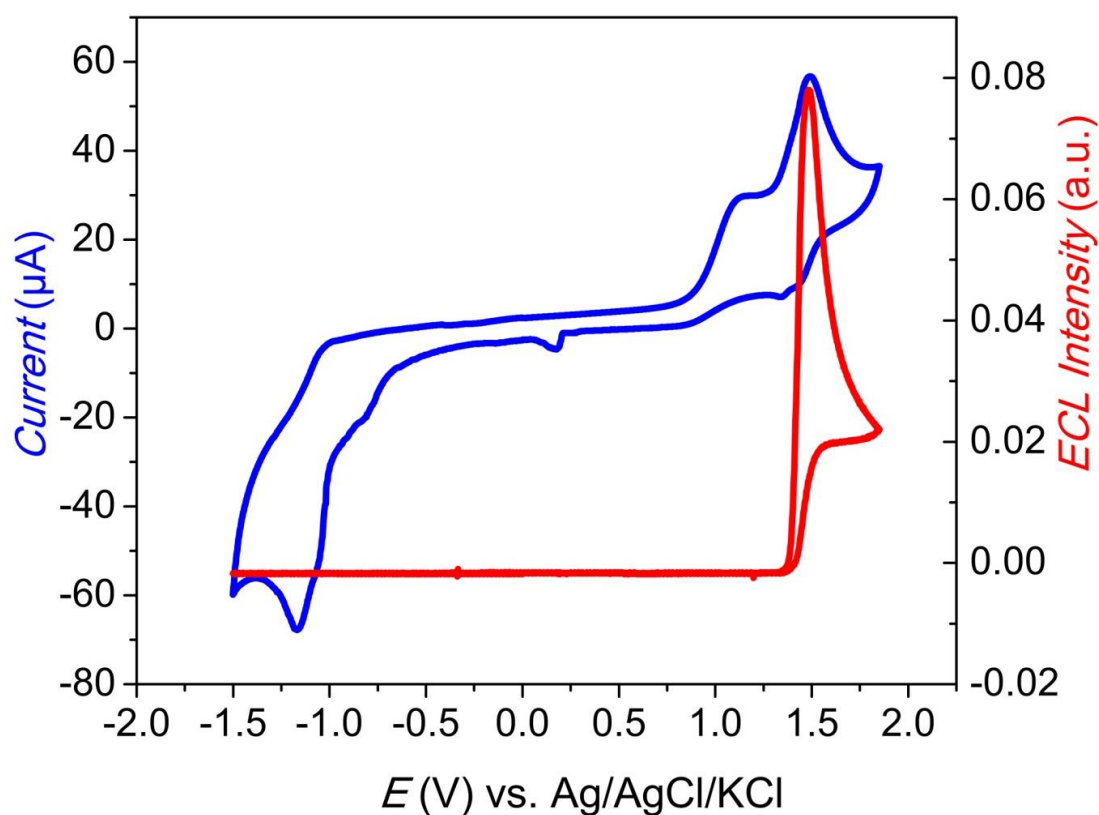


Figure 21. Cyclic voltammogram (blue) and ECL signal (red) of 100 mM PBS solution (pH=7.4) containing 10 U.mL⁻¹ GDH, 1.5 mM Ru(bpy)₃²⁺, 10 mM NAD⁺, 10 mM glucose and a few drops of surfactant recorded on a home-made GC electrode at a scan rate of 0.05 V.s⁻¹.

The minimum ΔV for which the different redox reactions are occurring at the swimmer surface is calculated using equation 5 and extracted from simultaneous recording of cyclic voltammogram and ECL emission on a home-made GC electrode, as for other ECL swimmers (Figure 21). Water reduction takes place at -0.75 V vs. Ag/AgCl/KCl whereas ECL emission occurs at 1.55 V vs. Ag/AgCl/KCl. The electric field \mathcal{E} has to be, in a first order approximation, at least 21.7 V.cm⁻¹ as the calculated polarization potential ΔV_{min} is 2.3 V for the bead with the diameter of 1 mm.

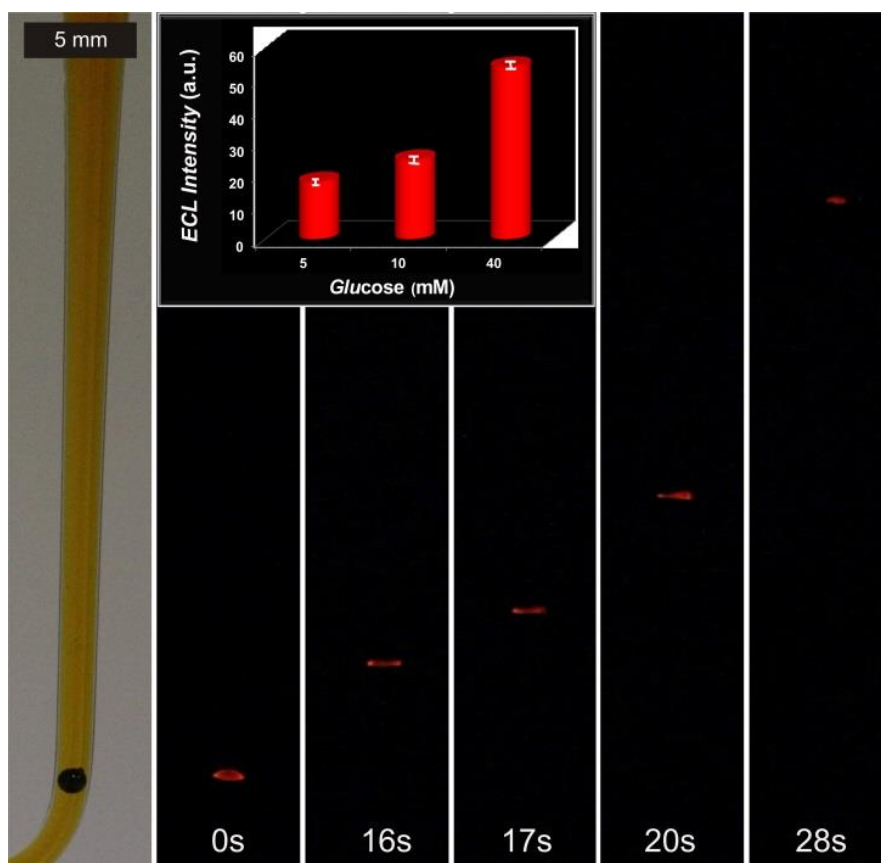


Figure 22. ECL sensing and reporting of glucose concentration during the swimmer motion. Series of optical micrographs showing a GC bead emitting ECL at different times during its motion. The GC bead is positioned in a U-shaped cell, filled with 100 mM PBS solution (pH 7.4) containing $10 \text{ U}\cdot\text{mL}^{-1}$ GDH, $1.5 \text{ mM Ru}(\text{bpy})_3^{2+}$, 10 mM NAD^+ , 40 mM glucose and a few drops of surfactant under the electric field of 23 V cm^{-1} . The left image is recorded under white light whereas the others images were taken in the dark. Inset: Plot showing the dependence of the ECL signal on the glucose concentration.

Figure 22 shows the BE-induced levitation of an ECL bioswimmer. The application of a sufficient EF drives the asymmetric electrochemical reactions on both poles of the bead. On the anodic pole, ECL is generated. The ECL emission is clearly visible by the naked eye in the presence of glucose and the position of the bead could be recorded by using a commercial camera during the rise of the swimmer. A negative control experiment recorded without any glucose in solution does not produce any measurable light emission. Such an approach, also called photoscropy is becoming increasingly popular as it is easy and cheap to perform^{85,95}. The ECL intensity monitored at the top of the bead is proportional to the glucose concentration as reported in the Figure 20. One can note that the shape of the ECL emission evolves with time as detailed above. Nevertheless, the overall intensity was analysed (Image J software) and this reveals a direct relationship between glucose concentration and the relative

luminescence signal. Indeed, the ECL intensity reflects the local NADH concentration which is directly related to the enzymatic activity and thus to the concentration of the substrate. Therefore, in the present case, the ECL swimmer is a dynamic reporter of the local concentration of glucose. Due to the dependence of ECL intensity on glucose concentration, this approach is also suitable to monitor the spatial distribution of variations in glucose concentration.

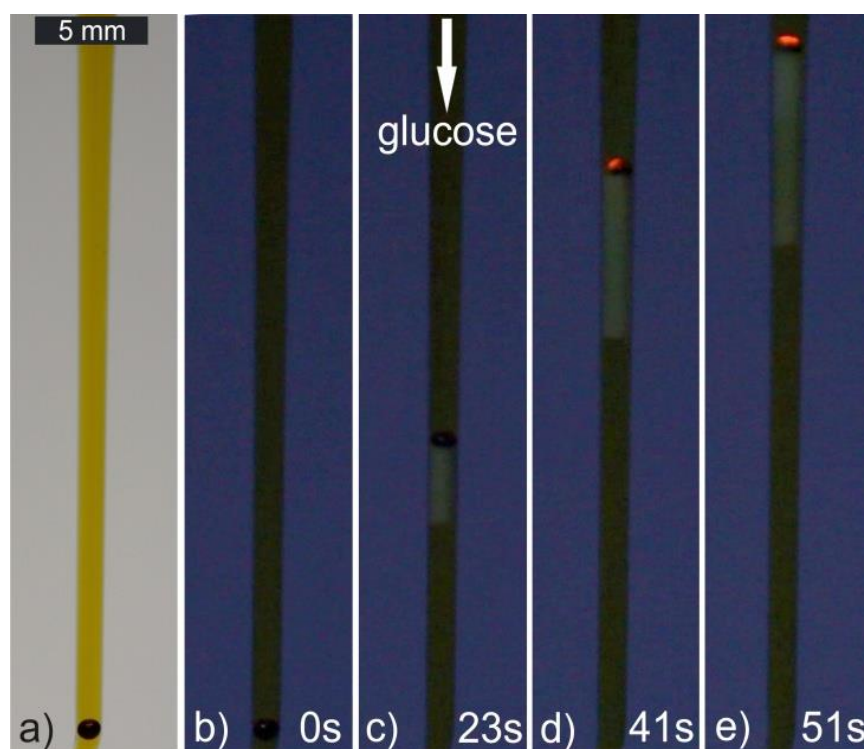


Figure 23. Images illustrating the switching-on of ECL during the swimmer motion in a vertical glucose concentration gradient. The U-shaped cell is filled with 100 mM PBS solution (pH 7.4) containing 2.5 mM $\text{Ru}(\text{bpy})_3^{2+}$, 10 $\text{U}\cdot\text{mL}^{-1}$ GDH and 10 mM NAD^+ . The same solution but containing in addition 40 mM glucose was introduced at the top of the capillary. The established vertical concentration gradient is revealed by ECL. The left image (a) is recorded under ambient light before applying the electric field. The other images (b-e) were taken after the application of the electric field (23 V cm^{-1}) under low external white light illumination in order to image the bead motion during the ECL sensing of glucose.⁹⁴

In other words, if the swimmer moves in inhomogeneous media, then ECL will only be activated at locations where the analyte is present. To demonstrate this ability to switch on the ECL, the GC bead was positioned in a capillary filled with a PBS solution containing the ECL reporter, the enzyme and the co-factor. Another solution containing glucose in addition was introduced dropwise at the very top of the capillary (arrow on Figure 23c). This generates a vertical concentration gradient where the higher amount of glucose and thus of NADH is

localized at the top part. As previously, the GC bead is initially positioned at the bottom of the capillary as observed under white light (Figure 23a). As soon as a sufficient EF is turned on, proton reduction is promoted underneath the BPE. This is clearly visible in Figure 23c where a train of bubbles can be seen below the bead which is moving up. As soon as the GC bead reaches the location where glucose is present in solution, ECL is switched on, thus demonstrating the possibility of dynamic glucose detection (Figure 23d). As the swimmer is moving towards a region of higher glucose concentration (top of the capillary), its ECL intensity increases (Figure 23e). This experiment demonstrates the combined local enzymatic sensing and ECL reporting of an analyte in space and time.

4.7. Conclusion

In conclusion, we have demonstrated the first example of a propulsion mechanism for a swimmer that is coupled with a chemical light source due to the synergetic action of BE in terms of simultaneous ECL generation and H₂ bubble production from water splitting. By closely controlling the applied voltage, surfactant concentration, and capacity of the buffer to maintain a certain pH, we were able to avoid oxidation of water at the anodic pole and control and maximize the ECL intensity generated from a ruthenium complex. Also, luminol based ECL swimmer in the presence of H₂O₂ is demonstrated, tuning the wavelength of emission with also a redox-driven motion resulting from O₂ bubbles evolution. Furthermore, the design of dynamic systems driven by BE for sensing of glucose in a concentration gradient explored by the ECL swimmer is described for the first time. This contribution demonstrates that the development of such ECL swimmers could lead to bioanalytical applications, allowing the study of locally inhomogeneous samples. In that context, combining BE and ECL offers a unique analytical platform based on the design of smart dynamic systems for a straightforward visual readout. Finally, such ECL swimmers resemble biological systems and may be considered as an artificial analogue of bioluminescent fishes or marine creatures.

References

- 1 Guix, M., Mayorga-Martinez, C. C. & Merkoçi, A. Nano/micromotors in (bio) chemical science applications. *Chem. Rev.* **114**, 6285-6322 (2014).
- 2 Van den Heuvel, M. G. & Dekker, C. Motor proteins at work for nanotechnology. *Science* **317**, 333-336 (2007).
- 3 von Delius, M. & Leigh, D. A. Walking molecules. *Chem. Soc. Rev.* **40**, 3656-3676 (2011).
- 4 Ebbens, S. J. & Howse, J. R. In pursuit of propulsion at the nanoscale. *Soft Matter* **6**, 726-738 (2010).
- 5 Mallouk, T. E. & Sen, A. Powering nanorobots. *Sci. Amer.* **300**, 74-79 (2009).
- 6 Pantarotto, D., Browne, W. R. & Feringa, B. L. Autonomous propulsion of carbon nanotubes powered by a multienzyme ensemble. *Chem. Commun.* **0**, 1533-1535 (2008).
- 7 Mano, N. & Heller, A. Bioelectrochemical Propulsion. *J. Am. Chem. Soc.* **127**, 11574-11575 (2005).
- 8 Ismagilov, R. F., Schwartz, A., Bowden, N. & Whitesides, G. M. Autonomous Movement and Self-Assembly. *Angew. Chem. Int. Ed.* **41**, 652-654 (2002).
- 9 Calvo-Marzal, P. *et al.* Propulsion of nanowire diodes. *Chem. Commun.* **46**, 1623-1624 (2010).
- 10 Chang, S. T., Paunov, V. N., Petsev, D. N. & Velev, O. D. Remotely powered self-propelling particles and micropumps based on miniature diodes. *Nat. Mater.* **6**, 235-240 (2007).
- 11 Loget, G. & Kuhn, A. Shaping and exploring the micro-and nanoworld using bipolar electrochemistry. *Anal. Bioanal. Chem.* **400**, 1691-1704 (2011).
- 12 Mavré, F. *et al.* Bipolar Electrodes: A Useful Tool for Concentration, Separation, and Detection of Analytes in Microelectrochemical Systems. *Anal. Chem.* **82**, 8766-8774 (2010).
- 13 Fosdick, S. E., Knust, K. N., Scida, K. & Crooks, R. M. Bipolar electrochemistry. *Angew. Chem. Int. Ed.* **52**, 10438-10456 (2013).
- 14 Loget, G. & Kuhn, A. Electric field-induced chemical locomotion of conducting objects. *Nat. Commun.* **2**, 535 (2011).
- 15 Bouffier, L. & Kuhn, A. Design of a wireless electrochemical valve. *Nanoscale* **5**, 1305-1309 (2013).
- 16 Loget, G. & Kuhn, A. Bipolar electrochemistry for cargo-lifting in fluid channels. *Lab Chip* **12**, 1967-1971 (2012).
- 17 Roche, J. *et al.* Wireless powering of e-swimmers. *Sci. Rep.*, 6705 (2014).
- 18 Laocharoensuk, R., Burdick, J. & Wang, J. Carbon-nanotube-induced acceleration of catalytic nanomotors. *ACS Nano* **2**, 1069-1075 (2008).
- 19 Ghosh, A. & Fischer, P. Controlled propulsion of artificial magnetic nanostructured propellers. *Nano Lett.* **9**, 2243-2245 (2009).
- 20 Ebbens, S. J. & Howse, J. R. Direct observation of the direction of motion for spherical catalytic swimmers. *Langmuir* **27**, 12293-12296 (2011).
- 21 Bard, A. J. Electrogenerated Chemiluminescence. *Maceler Dekker Inc, New York* (2004).
- 22 Miao, W. Electrogenerated chemiluminescence and its biorelated applications. *Chem. Rev.* **108**, 2506-2553 (2008).
- 23 Liu, Z., Qi, W. & Xu, G. Recent advances in electrochemiluminescence. *Chem. Soc. Rev.* **44**, 3117-3142 (2015).

- 24 Arora, A., Eijkel, J. C., Morf, W. E. & Manz, A. A wireless electrochemiluminescence detector applied to direct and indirect detection for electrophoresis on a microfabricated glass device. *Anal. Chem.* **73**, 3282-3288 (2001).
- 25 Zhan, W., Alvarez, J. & Crooks, R. M. A two-channel microfluidic sensor that uses anodic electrogenerated chemiluminescence as a photonic reporter of cathodic redox reactions. *Anal. Chem.* **75**, 313-318 (2003).
- 26 Chow, K.-F., Mavr , F., Crooks, J. A., Chang, B.-Y. & Crooks, R. M. A large-scale, wireless electrochemical bipolar electrode microarray. *J. Am. Chem. Soc.* **131**, 8364-8365 (2009).
- 27 Chow, K.-F., Mavr , F. & Crooks, R. M. Wireless electrochemical DNA microarray sensor. *J. Am. Chem. Soc.* **130**, 7544-7545 (2008).
- 28 Sentic, M., Loget, G., Manojlovic, D., Kuhn, A. & Sojic, N. Light Emitting Electrochemical "Swimmers". *Angew. Chem. Int. Ed.* **51**, 11284-11288 (2012).
- 29 Bouffier, L. *et al.* Lighting up redox propulsion with luminol electrogenerated chemiluminescence. *ChemElectroChem* **1**, 95-98 (2014).
- 30 Downey, T. M. & Nieman, T. A. Chemiluminescence detection using regenerable tris (2, 2'-bipyridyl) ruthenium (II) immobilized in Nafion. *Anal. Chem.* **64**, 261-268 (1992).
- 31 Martin, A. F. & Nieman, T. A. Glucose quantitation using an immobilized glucose dehydrogenase enzyme reactor and a tris (2, 2'-bipyridyl) ruthenium (II) chemiluminescent sensor. *Anal. Chim. Acta* **281**, 475-481 (1993).
- 32 Goodridge, F. Some recent developments of monopolar and bipolar fluidized bed electrodes. *Electrochim. Acta* **22**, 929-933 (1977).
- 33 Fleischmann, M., Ghoroghchian, J., Rolison, D. & Pons, S. Electrochemical behavior of dispersions of spherical ultramicroelectrodes. *J. Phys. Chem.* **90**, 6392-6400 (1986).
- 34 Beck, T. R., Rousar, I. & Thonstad, J. Energy efficiency considerations on monopolar vs bipolar fused salt electrolysis cells. *Metall. Mater. Trans. B* **25**, 661-668 (1994).
- 35 Yang, J., Zhang, Q., Wang, H. & Liu, Y. Establishment and verification of mathematical model for current leakage in bipolar multi-compartment cell. *Trans. Nonferrous Met. Soc. China* **5**, 29-35 (1995).
- 36 Loget, G., Zigah, D., Bouffier, L., Sojic, N. & Kuhn, A. Bipolar Electrochemistry: from materials science to motion and beyond. *Acc. Chem. Res.* **46**, 2513-2523 (2013).
- 37 Loget, G. & Kuhn, A. Bipolar electrochemistry in the nanosciences *Electrochemistry: Nanosystems Electrochemistry*, (Eds.: R. Compton, J. Wadhawan), RSC, Vol. 11 (2012).
- 38 Guerrette, J. P., Oja, S. M. & Zhang, B. Coupled Electrochemical Reactions at Bipolar Microelectrodes and Nanoelectrodes. *Anal. Chem.* **84**, 1609-1616 (2012).
- 39 Cox, J. T., Guerrette, J. P. & Zhang, B. Steady-State Voltammetry of a Microelectrode in a Closed Bipolar Cell. *Anal. Chem.* **84**, 8797-8804 (2012).
- 40 Fosdick, S. E., Crooks, J. A., Chang, B.-Y. & Crooks, R. M. Two-Dimensional Bipolar Electrochemistry. *J. Am. Chem. Soc.* **132**, 9226-9227 (2010).
- 41 Chang, B.-Y., Crooks, J. A., Chow, K.-F., Mavr , F. o. & Crooks, R. M. Design and operation of microelectrochemical gates and integrated circuits. *J. Am. Chem. Soc.* **132**, 15404 (2010).
- 42 Zhan, W., Alvarez, J. & Crooks, R. M. Electrochemical Sensing in Microfluidic Systems Using Electrogenerated Chemiluminescence as a Photonic Reporter of Redox Reactions. *J. Am. Chem. Soc.* **124**, 13265-13270 (2002).
- 43 Chow, K.-F., Chang, B.-Y., Zacco, B. A., Mavr , F. o. & Crooks, R. M. A Sensing Platform Based on Electrodissolution of a Ag Bipolar Electrode. *J. Am. Chem. Soc.* **132**, 9228-9229 (2010).

- 44 Wu, M.-S., Qian, G.-s., Xu, J.-J. & Chen, H.-Y. Sensitive Electrochemiluminescence Detection of c-Myc mRNA in Breast Cancer Cells on a Wireless Bipolar Electrode. *Anal. Chem.* **84**, 5407-5414 (2012).
- 45 Juskova, P., Neuzil, P., Manz, A. & Foret, F. Detection of electrochemiluminescence from floating metal platelets in suspension. *Lab Chip* **13**, 781-784 (2013).
- 46 Chow, K.-F., Mavr , F., Crooks, J. A., Chang, B.-Y. & Crooks, R. M. A large-scale, wireless electrochemical bipolar electrode microarray. *J. Am. Chem. Soc.* **131**, 8364-8365 (2009).
- 47 Mavr , F. o. *et al.* A Theoretical and Experimental Framework for Understanding Electrogenenerated Chemiluminescence (ECL) Emission at Bipolar Electrodes. *Anal. Chem.* **81**, 6218-6225 (2009).
- 48 Chang, B.-Y., Chow, K.-F., Crooks, J. A., Mavre, F. & Crooks, R. M. Two-channel microelectrochemical bipolar electrode sensor array. *Analyst* **137**, 2827-2833 (2012).
- 49 Zhang, X., Chen, C., Li, J., Zhang, L. & Wang, E. New insight into a microfluidic-based bipolar system for an electrochemiluminescence sensing platform. *Anal. Chem.* **85**, 5335-5339 (2013).
- 50 Ishiguro, Y., Inagi, S. & Fuchigami, T. Gradient doping of conducting polymer films by means of bipolar electrochemistry. *Langmuir* **27**, 7158-7162 (2011).
- 51 Loget, G. *et al.* Versatile procedure for synthesis of Janus-type carbon tubes. *Chem. Mater.* **23**, 2595-2599 (2011).
- 52 Fattah, Z., Garrigue, P., Lapeyre, V., Kuhn, A. & Bouffier, L. Controlled Orientation of Asymmetric Copper Deposits on Carbon Microobjects by Bipolar Electrochemistry. *J. Phys. Chem. C* **116**, 22021-22027 (2012).
- 53 Kumsapaya, C. *et al.* Wireless Electrografting of Molecular Layers for Janus Particle Synthesis. *Chem. Eur. J.* **19**, 1577-1580 (2013).
- 54 Loget, G. & Kuhn, A. Bulk synthesis of Janus objects and asymmetric patchy particles. *J. Mater. Chem.* **22**, 15457-15474 (2012).
- 55 Loget, G. & Kuhn, A. Bipolar electrochemistry for cargo-lifting in fluid channels. *Lab Chip* **12**, 1967-1971 (2012).
- 56 Schliwa, M. & Woehlke, G. Molecular motors. *Nature* **422**, 759-765 (2003).
- 57 Goel, A. & Vogel, V. Harnessing biological motors to engineer systems for nanoscale transport and assembly. *Nat. Nanotechnol.* **3**, 465-475 (2008).
- 58 Hess, H., Bachand, G. D. & Vogel, V. Powering Nanodevices with Biomolecular Motors. *Chem. Eur. J.* **10**, 2110-2116 (2004).
- 59 Dreyfus, R. *et al.* Microscopic artificial swimmers. *Nature* **437**, 862-865 (2005).
- 60 Wang, Y. *et al.* Bipolar electrochemical mechanism for the propulsion of catalytic nanomotors in hydrogen peroxide solutions. *Langmuir* **22**, 10451-10456 (2006).
- 61 Manesh, K. M. *et al.* Template-Assisted Fabrication of Salt-Independent Catalytic Tubular Microengines. *ACS Nano* **4**, 1799-1804 (2010).
- 62 Wilson, D. A., Nolte, R. J. & van Hest, J. C. Autonomous movement of platinum-loaded stomatocytes. *Nat. Chem.* **4**, 268-274 (2012).
- 63 Solovev, A. A. *et al.* Self-Propelled Nanotools. *ACS Nano* **6**, 1751-1756 (2012).
- 64 Gao, W., Pei, A. & Wang, J. Water-driven micromotors. *ACS Nano* **6**, 8432-8438 (2012).
- 65 Paxton, W. F. *et al.* Catalytic Nanomotors: Autonomous Movement of Striped Nanorods. *J. Am. Chem. Soc.* **126**, 13424-13431 (2004).
- 66 Sanchez, S., Solovev, A. A., Mei, Y. & Schmidt, O. G. Dynamics of Biocatalytic Microengines Mediated by Variable Friction Control. *J. Am. Chem. Soc.* **132**, 13144-13145 (2010).

- 67 Demirok, U. K., Laocharoensuk, R., Manesh, K. M. & Wang, J. Ultrafast Catalytic Alloy Nanomotors. *Angew. Chem. Int. Ed.* **47**, 9349-9351 (2008).
- 68 Paxton, W. F., Sundararajan, S., Mallouk, T. E. & Sen, A. Chemical Locomotion. *Angew. Chem. Int. Ed.* **45**, 5420-5429 (2006).
- 69 Fournier-Bidoz, S., Arsenault, A. C., Manners, I. & Ozin, G. A. Synthetic self-propelled nanorotors. *Chem. Commun.*, 441-443 (2005).
- 70 Kagan, D. *et al.* Chemical Sensing Based on Catalytic Nanomotors: Motion-Based Detection of Trace Silver. *J. Am. Chem. Soc.* **131**, 12082-12083 (2009).
- 71 Balasubramanian, S. *et al.* Micromachine-Enabled Capture and Isolation of Cancer Cells in Complex Media. *Angew. Chem. Int. Ed.* **50**, 4161-4164 (2011).
- 72 Kagan, D. *et al.* Functionalized Micromachines for Selective and Rapid Isolation of Nucleic Acid Targets from Complex Samples. *Nano Lett.* **11**, 2083-2087 (2011).
- 73 Wu, J. *et al.* Motion-based DNA detection using catalytic nanomotors. *Nat Commun* **1**, 36 (2010).
- 74 Guix, M. *et al.* Superhydrophobic alkanethiol-coated microsubmarines for effective removal of oil. *ACS Nano* **6**, 4445-4451 (2012).
- 75 Du, J. & O'Reilly, R. K. Anisotropic particles with patchy, multicompartiment and Janus architectures: preparation and application. *Chem. Soc. Rev.* **40**, 2402-2416 (2011).
- 76 Fattah, Z. *et al.* Straightforward single-step generation of microswimmers by bipolar electrochemistry. *Electrochim. Acta* **56**, 10562-10566 (2011).
- 77 Loget, G. *et al.* Single point electrodeposition of nickel for the dissymmetric decoration of carbon tubes. *Electrochim. Acta* **55**, 8116-8120 (2010).
- 78 Ghosh, A. & Fischer, P. Controlled propulsion of artificial magnetic nanostructured propellers. *Nano Lett.* **9**, 2243-2245 (2009).
- 79 Zu, Y. & Bard, A. J. Electrogenenerated chemiluminescence. 67. Dependence of light emission of the tris (2, 2') bipyridylruthenium (II)/tripropylamine system on electrode surface hydrophobicity. *Anal. Chem.* **73**, 3960-3964 (2001).
- 80 Workman, S. & Richter, M. M. The effects of nonionic surfactants on the tris (2, 2'-bipyridyl) ruthenium (II)-tripropylamine electrochemiluminescence system. *Anal. Chem.* **72**, 5556-5561 (2000).
- 81 Miao, W. Electrogenenerated Chemiluminescence and Its Biorelated Applications. *Chem. Rev.* **108**, 2506-2553 (2008).
- 82 Loget, G. & Kuhn, A. Bipolar electrochemistry for cargo-lifting in fluid channels. *Lab on a Chip* (2012).
- 83 Leland, J. K. & Powell, M. J. Electrogenenerated Chemiluminescence: An Oxidative-Reduction Type ECL Reaction Sequence Using Tripropyl Amine. *J. Electrochem. Soc.* **137**, 3127-3131 (1990).
- 84 Tian, D., Zhang, H., Chai, Y. & Cui, H. Synthesis of N-(aminobutyl)-N-(ethylisoluminol) functionalized gold nanomaterials for chemiluminescent bio-probe. *Chem. Commun.* **47**, 4959-4961 (2011).
- 85 Chen, X.-m. *et al.* Recent advances in electrochemiluminescent enzyme biosensors. *Tr. Anal. Chem.* **30**, 665-676 (2011).
- 86 Chai, Y., Tian, D., Wang, W. & Cui, H. A novel electrochemiluminescence strategy for ultrasensitive DNA assay using luminol functionalized gold nanoparticles multi-labeling and amplification of gold nanoparticles and biotin-streptavidin system. *Chem. Commun.* **46**, 7560-7562 (2010).
- 87 Milutinovic, M., Sallard, S., Manojlovic, D., Mano, N. & Sojic, N. Glucose sensing by electrogenerated chemiluminescence of glucose-dehydrogenase produced NADH on electrodeposited redox hydrogel. *Bioelectrochemistry* **82**, 63-68 (2011).

- 88 Martin, A. F. & Nieman, T. A. Glucose quantitation using an immobilized glucose dehydrogenase enzyme reactor and a tris(2,2'-bipyridyl) ruthenium(II) chemiluminescent sensor. *Anal. Chim. Acta* **281**, 475 (1993).
- 89 Song, L., Ahn, S. & Walt, D. R. Fiber-Optic Microsphere-Based Arrays for Multiplexed Biological Warfare Agent Detection. *Anal. Chem.* **78**, 1023 (2006).
- 90 Zhang, L., Xu, Z., Sun, X. & Dong, S. A novel alcohol dehydrogenase biosensor based on solid-state electrogenerated chemiluminescence by assembling dehydrogenase to Ru(bpy)₃²⁺-Au nanoparticles aggregates. *Biosens. Bioelectron.* **22**, 1097 (2007).
- 91 Jia, T.-t. *et al.* Electrogenerated chemiluminescence ethanol biosensor based on alcohol dehydrogenase functionalized Ru(bpy)₃²⁺ doped silica nanoparticles. *Biosens. Bioelectron.* **25**, 263 (2009).
- 92 Zhang, L., Xu, Z. & Dong, S. Electrogenerated chemiluminescence biosensor based on Ru(bpy)₃²⁺ and dehydrogenase immobilized in sol-gel/chitosan/poly(sodium 4-styrene sulfonate) composite material. *Anal. Chim. Acta* **575**, 52 (2006).
- 93 Martin, A. F. & Nieman, T. A. Chemiluminescence biosensors using tris(2,2'-bipyridyl)ruthenium(II) and dehydrogenases immobilized in cation exchange polymers. *Biosens. Bioelectron.* **12**, 479 (1997).
- 94 Sentic, M. *et al.* Electrochemiluminescent swimmers for dynamic enzymatic sensing. *Chem. Commun.* **50**, 10202-10205 (2014).
- 95 Doeven, E. H. *et al.* Red–Green–Blue Electrogenerated Chemiluminescence Utilizing a Digital Camera as Detector. *Anal. Chem.* **86**, 2727-2732 (2014).

GENERAL CONCLUSIONS

In the frame of the present doctoral thesis, my work was focused on the study of ECL and its application in the development of new analytical techniques and objects. Fundamentals of ECL have been introduced in the first chapter. ECL technology is a highly innovative detection technology for heterogeneous bead-based immunoassays. Since the launch of the first ECL analyzer in 1996, ECL technology has continued to set the standard in immunochemistry. Generally, the first steps in the development of new ECL assays and in the selection of new efficient co-reactants are the understanding of ECL mechanisms operating in such bead-based assays.

In the second part of the thesis, we presented a new approach to investigate the competitive ECL mechanistic routes by imaging the distribution of the ECL intensity at the level of single beads. The reaction mechanisms between the $\text{Ru}(\text{bpy})_3^{2+}$ luminophore with two model co-reactants (tri-*n*-propylamine, TPrA, and 2-(dibutylamino)ethanol, DBAE) were investigated. A sandwich immunoassay is performed by exposing the 3- μm beads to a detection antibody conjugated with a $\text{Ru}(\text{bpy})_3^{2+}$ complex to simulate the labelled beads which are used in bioassays. The spatial resolution of the luminescence phenomenon was improved using in further experiments 12- μm diameter polystyrene (PS) beads to obtain well-resolved ECL patterns, functionalized with the same ruthenium label *via* a peptidic bond. Two optical configurations were used to image the functionalized beads from different angles. Investigating the 3D ECL patterns recorded on such beads provides a global description of the ECL phenomenon. Mapping the ECL reactivity on one bead demonstrates the generation of the excited state at micrometric distance from the electrode by reaction of surface-confined $\text{Ru}(\text{bpy})_3^{2+}$ with diffusing TPrA radicals. The signature of the $\text{TPrA}^{\bullet+}$ cation radical lifetime is obtained from the ECL profile. Unlike with $\text{Ru}(\text{bpy})_3^{2+}$ solution, DBAE generates very low ECL intensity in the bead-based format suggesting more instable radical intermediates. The lens effect of the bead which concentrates the ECL emission and thus contributes to increase the collected analytical signal was also shown. The 3D imaging approach offers the opportunity to select new co-reactants with improved sensitivity and to develop new analytical strategies.

Third part of the thesis discussed the excellent electrochemical properties of nanoelectrode ensembles and arrays for bioanalytical applications. We developed an ECL

immunosensor for coeliac disease (CD) diagnosis *via* immobilization of bio-recognition elements on the polycarbonate (PC) surface of membrane templated nanoelectrode ensembles. CD is an auto-immune disorder where the blood anti-tissue transglutaminase (anti-tTg) antibodies level is abnormally high. Since ECL could be generated at micrometric distances from the electrode surface at low-oxidation potentials with TPrA as co-reactant, we were able to separate the location of the initial electrochemical step (i.e. oxidation of TPrA) from the ECL-emitting region where the luminophore used as a label is immobilized on the non-conductive surface. To this aim, the immunosensor platform was established by immobilizing the capturing agent tTG on PC component of a NEE so that, when incubated with the sample, it reacts with the target protein anti-tTG. Thus it allows the immobilization of a streptavidin-modified ruthenium-based ECL label *via* reaction with a suitable biotinylated secondary antibody. Upon addition of TPrA, ECL emission was initiated solely *via* its direct electrochemical oxidation. The sensor allows the ECL determination of anti-tTG with a detection limit lower than 1ng/mL. Furthermore, ECL imaging was used for the characterization of ECL generation at boron-doped diamond NEAs. This approach provides a platform of multiple arrays of nanoelectrodes suitable to study changes in reaction layers of the system $\text{Ru}(\text{bpy})_3^{2+}/\text{TPrA}$ as a function of the geometry and of the spacing of arrays elements.

Finally, in the last part of the thesis, the wireless characteristics of bipolar electrochemistry (BE) were exploited as driving force for controlled motion of swimmers. We presented the synergetic action of bipolar electrochemistry in terms of simultaneous bubble production and ECL generation, leading to the first example of a propulsion mechanism for a swimmer that is coupled with a chemical light source. Bipolar swimmers were driven by either H_2 or O_2 evolution with emission from ruthenium complex or luminol luminophores. We moved forward the application of BE swimmers in analytical science by using ECL light as an analytical signal. The swimmers concept for enzymatic glucose sensing was then demonstrated. The concomitant oxidation of the luminophore and of the enzymatically produced NADH led to the ECL emission with a direct glucose-dependent light intensity. The local sensing and reporting of glucose in a concentration gradient was explored by the ECL swimmer. Such a dynamic sensing approach combines in a synergetic way the wireless propulsion with the enzymatic selectivity using ECL as a readout method at the level of moving objects.

Résumé

Dans le cadre de ma thèse, mon travail a été axé sur l'étude de l'ECL et son application dans le développement de nouvelles techniques d'analyse. Les notions de base de l'ECL ont été introduites, notamment les aspects théoriques, dans le premier chapitre. La technologie ECL est une technologie très innovante de détection pour les immunoessais hétérogènes à base de billes fonctionnalisées. Depuis le lancement du premier analyseur ECL en 1996, cette technologie a continué à établir la norme en immunochimie. En général, la première étape dans le développement de nouveaux immunoessais ECL et la sélection de nouveaux co-réactifs est la compréhension des mécanismes ECL qui se produisent dans de tels dosages utilisant les billes comme support.

Dans la deuxième partie de ma thèse, une nouvelle approche est présentée pour étudier les voies mécanistiques en compétition pour aboutir à l'émission ECL. Elle est basée sur l'imagerie de la distribution de l'intensité ECL au niveau d'une bille individuelle. Les mécanismes réactionnels entre le luminophore $\text{Ru}(\text{bpy})_3^{2+}$ et deux co-réactifs modèles (tri-*n*-propylamine, TPrA, and 2-(dibutylamino)ethanol, DBAE) ont été étudiés. Un dosage immunologique de type sandwich est réalisé, en exposant les particules de 3 μm de diamètre à un anticorps de détection conjugué à un complexe de $\text{Ru}(\text{bpy})_3^{2+}$, afin de simuler les billes marquées qui sont utilisés dans des essais biologiques. La résolution spatiale du phénomène de luminescence a été améliorée en utilisant par la suite des billes de polystyrène (PS) de 12 μm de diamètre, fonctionnalisées avec le même marqueur par une liaison peptidique, pour obtenir des motifs ECL bien résolus. Deux configurations optiques ont été utilisées pour réaliser l'imagerie des billes fonctionnalisées sous des angles différents. Les images enregistrés sur ces billes fournissent une description globale du phénomène ECL. La cartographie de la réactivité ECL sur une telle particule démontre la génération de l'état excité à une distance micrométrique de l'électrode, par la réaction du $\text{Ru}(\text{bpy})_3^{2+}$ confiné à la surface avec les radicaux issus de l'oxydation de la TPrA qui diffusent. La signature de la durée de vie du cation radical $\text{TPrA}^{\bullet+}$ est obtenue à partir du profil ECL. Par contre, la DBAE génère une très faible intensité ECL à la base de la bille, ce qui suggère l'existence d'intermédiaires radicalaires nettement plus instables. Les effets de lentille de la bille, qui concentrent l'émission ECL et contribuent ainsi à augmenter le signal analytique ont également été montrés. Cette approche d'imagerie offre la possibilité de sélectionner de

nouveaux co-réactifs donnant une meilleure sensibilité et de développer de nouvelles stratégies d'analyse.

La troisième partie de la thèse discute des propriétés électrochimiques remarquables des ensembles de nanoélectrodes (NEE) pour les applications bioanalytiques. Nous avons développé un immunocapteur ECL pour le diagnostic de la maladie coeliaque (coeliac disease, CD) *via* l'immobilisation des éléments de bio-reconnaissance sur le polycarbonate (PC) d'un ensemble de nanoélectrodes. La CD est une maladie auto-immune où le niveau d'anticorps anti-transglutaminase tissulaire (anti-tTG) dans le sang est anormalement élevé. L'ECL pouvant être générée à des distances micrométriques de la surface de l'électrode, à des potentiels d'oxydation bas avec la TPrA comme co-réactif, nous avons été en mesure de séparer l'emplacement de l'étape électrochimique initiale (à savoir l'oxydation de TPrA) de la région luminescente où le luminophore est immobilisé sur la surface non-conductrice. Dans ce but, la plate-forme de l'immunocapteur a été réalisée en immobilisant l'agent de capture tTG sur la composante PC du NEE de sorte que, lorsqu'incubée avec l'échantillon, il réagit avec la protéine cible anti-tTG marquée avec un anticorps secondaire portant le luminophore $\text{Ru}(\text{bpy})_3^{2+}$. Lors de l'addition de TPrA, l'émission ECL a été initiée uniquement par son oxydation électrochimique directe. Le capteur permet la détermination de l'anticorps anti-tTG avec une limite de détection inférieure à 1 ng/mL. En outre, l'imagerie ECL a été utilisée pour la caractérisation de la génération ECL au niveau de réseaux de nanoélectrodes de diamant dopé. Cette approche fournit une plate-forme de multiples matrices de nanoélectrodes adaptées pour étudier les changements dans les couches réactionnelles du système $\text{Ru}(\text{bpy})_3^{2+}/\text{TPrA}$ en fonction de la géométrie et de l'espacement des éléments de l'ensemble.

Enfin, dans la dernière partie de la thèse, l'adressage électrochimique sans contact direct qui est une des caractéristiques remarquables de l'électrochimie bipolaire a été exploité comme force motrice pour induire le mouvement contrôlé de nageurs. De plus, elle permet simultanément la production de bulles et la génération d'ECL, menant au premier exemple d'un mécanisme de propulsion pour un nageur qui est couplé avec une source luminescente. Les nageurs bipolaires sont mus soit par la production d' H_2 ou d' O_2 couplée respectivement avec l'émission ECL d'un complexe de ruthénium ou du luminol. Nous avons étendu les propriétés de ce type de nageurs en utilisant l'ECL comme signal analytique. Le concept des nageurs analytiques pour la détection enzymatique de glucose a également été démontré. L'oxydation concomitante du luminophore et du NADH produit par voie enzymatique conduit

à une émission ECL avec une intensité lumineuse directement dépendante du glucose. La détection locale du glucose dans un gradient de concentration a été réalisée par ce type de nageurs ECL. Une telle approche de détection dynamique combine la propulsion sans contact avec la sélectivité enzymatique, en utilisant l'ECL comme méthode de lecture au niveau des objets en mouvement.

PERSPECTIVES

ECL can be easily combined with other technologies since the direct optical readout can be performed just with a PMT or costumer mobile cameras. A wide variety of possibilities can be considered coupling ECL with bipolar electrochemistry. It should be noted that even though the phenomenon of BE is known for a very longtime, its applications started to be very popular in the last decade. It has regained considerable attention, especially in the field of micro- and nanoscience. Therefore, in this upstream research field there is a place for innovations, especially linked to ECL. The ECL-swimmer concept described in the Chapter 4, is already expanded for analytical monitoring of a glucose concentration. A glass capillary has been used as a bipolar electrochemical cell for a single moving swimmer. Versatility of BE allows as to imagine and construct very different types of cells and accordingly to use a various materials different in size and shape as a BPE.

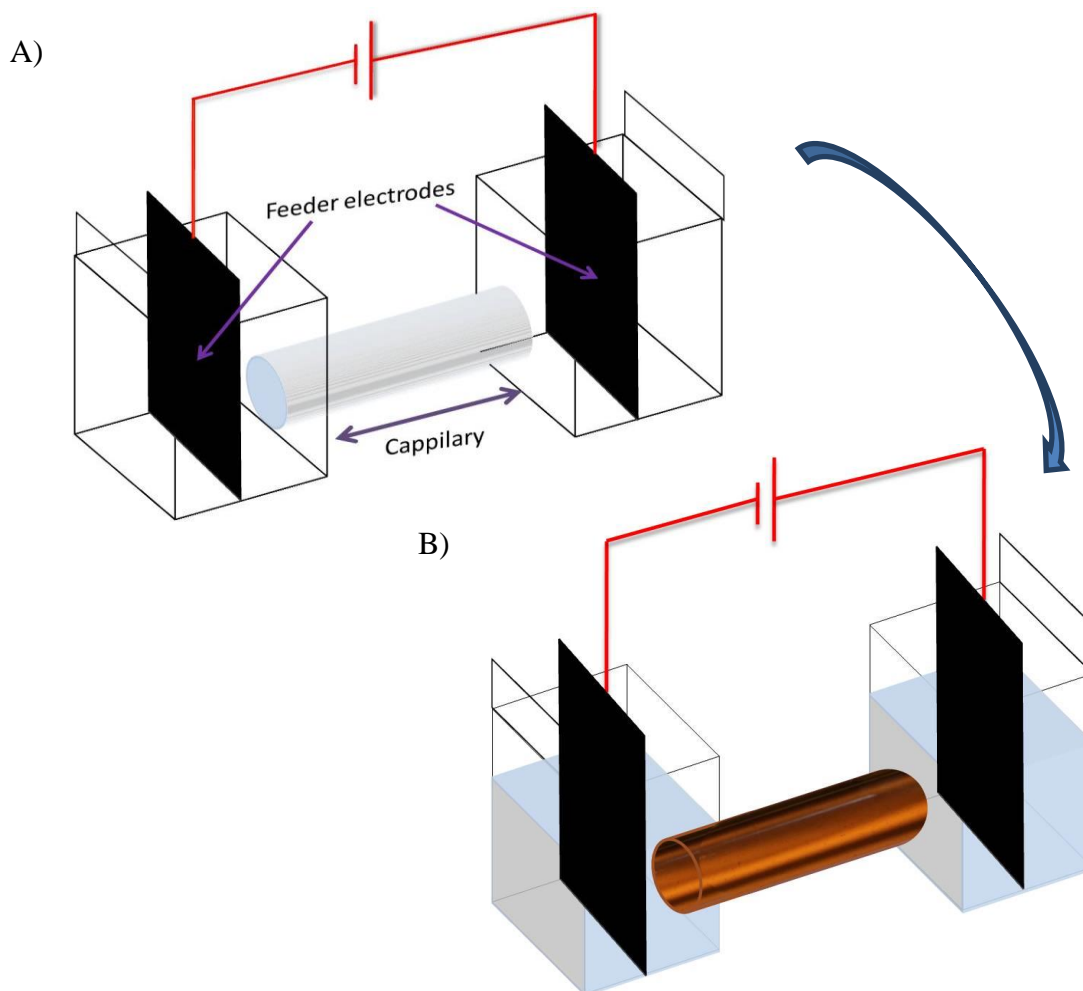


Figure 1. A) Scheme of bipolar cell. B) Capillary filled with ECL reagents and reservoir chambers with supporting electrolyte connected with the capillary.

In Figure 1A schematic illustration for possible cell construction is presented. Length of the capillary as well as diameter are optional, depending on the experiment set-up. A reservoir chambers are connected with capillary and feeder electrodes are placed within them. Filling only the capillary with ECL reagents a background signal from the feeder electrode is avoided (Figure 1B). By increasing the size of the bipolar cell one can imagine more than one BPE electrode placed within the capillary to experience the ECL signal. Reducing the size of the BPEs and going to micro and nano-scale, a big amount of conducting objects can emit ECL at same time in a wireless manner (Figure 2). Correspondingly, reducing the size of BPEs will increase the needed electric field and the resistance, operating in this case in an open bipolar configuration (in agreement with Eqn 3 and 4 in the Chapter 4). Filling the reservoir compartments with agarose gel in supporting electrolyte can decrease the resulting ohmic heating and therefore to prolong the reaction time. For the same reason a different co-reactants can be exploited. For example lower concentrations of DBAE are required with DBEA diffusing in solution than with TPrA to obtain the same ECL intensities. Never less, it is oxidized at lower potential than TPrA.

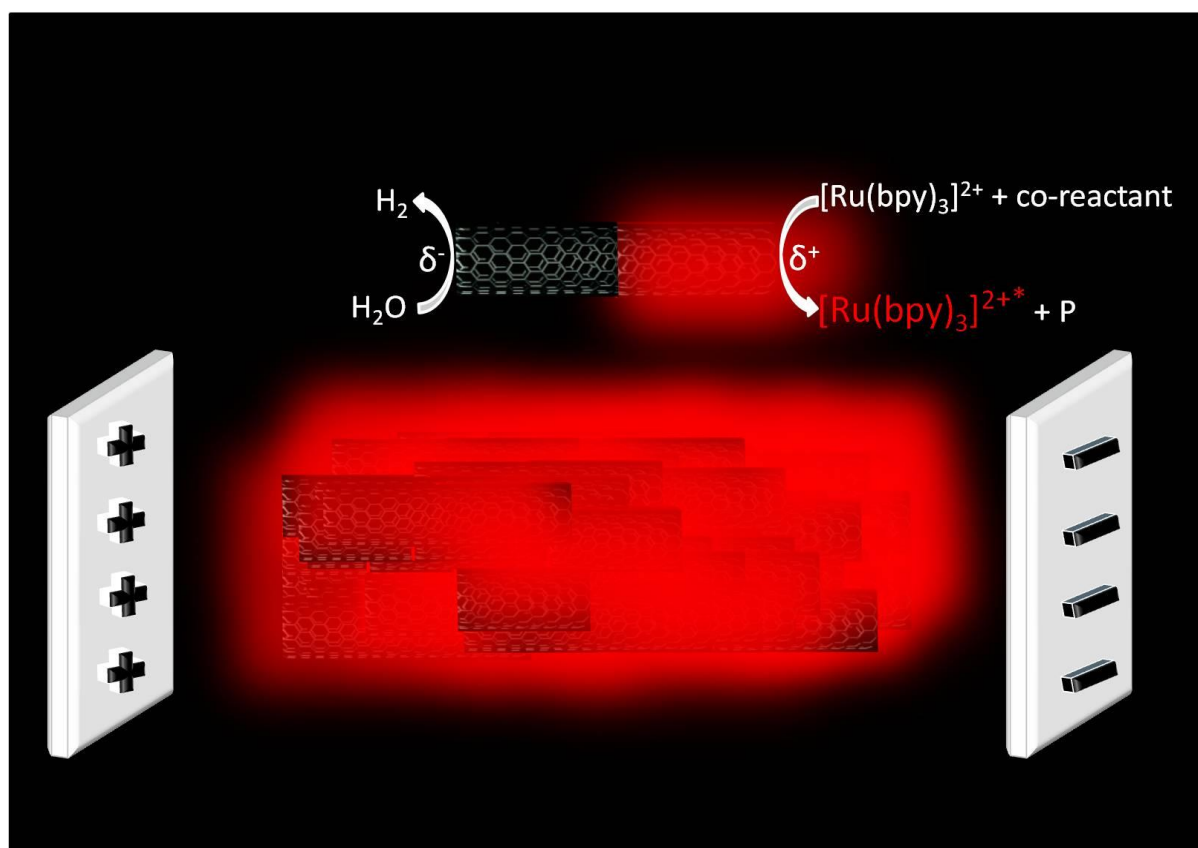


Figure 2. Schematic illustration of ECL generation from the CNTs. The CNTs are polarized by the electric field generated between the feeder electrodes and redox reactions are triggered at the opposite sides of the object: reduction of oxygen at the cathodic pole (left) and oxidation of the ECL reagents at the anodic pole (right) leading to light emission.

If the whole capillary is filled with the BPEs, microbeads or nanotubes, and each BPE generates the ECL signal at the same time it can lead to “3D ECL” emission. Since the concept of bio-swimmers for the enzymatic glucose sensing is demonstrated, this set-up can open the door for a whole range of new applications of ECL such as high-sensitivity analysis or optical tracking of nanomotors.

APPENDIX

Materials. All chemicals were of analytical reagent grade and were used as received. Solutions were prepared using Milli-Q water (resistivity = 18 M Ω cm). Tri-n-propylamine \geq 98%, tris(2,2'-bipyridyl) dichlororuthenium(II) hexahydrate, luminol (3-aminophthalhydrazide, 97%), bis(2,2'-bipyridine)-4'-methyl-4-carboxybipyridine-ruthenium N-succinimidyl ester-bis(hexafluorophosphate), sodium phosphate dibasic heptahydrate, sodium phosphate monobasic monohydrate, glucose dehydrogenase, universal indicator solution pH 3-10, (EC1.1.1.47, from *Thermoplasma acidophilum*), β -nicotinamide adenine dinucleotide hydrate (NAD⁺), β -nicotinamide adenine dinucleotide reduced dipotassium salt (NADH), streptavidin from *Streptomyces avidinii*, Tween 20, bovine serum albumin, and biotinylated goat anti-human secondary antibody were purchased from Sigma. D-(+)-Glucose anhydrous and hydrogen peroxide solution (30%) were from Fluka. Sodium hydroxide (purum) was purchased from Acros. Capture antibody specific for interleukin 8 (IL-8), the complementary biotinylated detection antibody and IL-8 recombinant protein were obtained from R&D Systems, Inc. (Minneapolis, MN). Polystyrene (PS) beads were purchased from Kisker Biotech GmbH & Co. Surfactant Gojo NXT was used. Glassy carbon beads (spherical powder 630–1000 nm, type 2) were purchased from Alfa Aesar. Gold electroless plating solution (Oromerse Part B, Technic Inc.) and hydrophilic track-etched PC filter membranes (47 mm diameter, 6 μ m thickness) with a nominal pore diameter of 30 nm, pore density 6×10^8 pores/cm² were used for manufacturing NEEs.

Apparatus. All electrochemical and ECL experiments were performed with a μ -Autolab Type III and PGSTAT30 electrochemical stations. ECL intensity was measured using Hamamatsu photomultiplier tube R4632. Imaging instrumentation was an epifluorescence microscope Olympus BXFM-ILHSPU equipped with an Electron Multiplying Charge Coupled Device (EM-CCD) Camera (Hamamatsu, 9100-13). The motion of the beads was recorded using a consumer digital cameras (Sony, Cyber-shot and Canon60 D). The electric field was applied with two high power suppliers: Electrometer 6517B from Keithley and Microcomputer electrophoresis direct current DC power supply E862 from Consort.

Chapter 2.

2.1. Immunoassay with 3- μm diameter PS beads

Antigen storage aliquots were prepared in PBS 1x/BSA 0.1% and detection antibody storage aliquots were prepared in tris-buffered saline (TBS StartingBlock). Each washing step was done in 100 μL of TBS with 1% Tween 20. The assay was performed by incubating for 2 hours the microbeads functionalized with a capture antibody (anti-IL-8) first in a sample containing antigen (dilute to the appropriate concentration with PBS StartingBlock) and washed. Then they were incubated for 30 min. in 50 μL of the detection antibodies solution (3 $\mu\text{g}/\text{mL}$ of antibody in PBS StartingBlock) and washed. Beads were then incubated in a solution of biotinylated detection antibody and washed again. Finally, the ECL label was attached to formed immunocomplex by exposing the beads to a solution containing a streptavidin-modified $\text{Ru}(\text{bpy})_3^{2+}$ complex. The streptavidin-modified ruthenium complex used as a label was synthesized according to the procedure described by Deiss *et al.*¹ Beads were then washed for the last time and immobilized on the electrode surface for ECL imaging.

2.2. Functionalization of the 12- μm diameter beads with the ruthenium label

The surface of the PS beads with $-\text{NH}_2$ groups allows further functionalization with the ruthenium label. 10 μL of beads suspension (2.5%) was washed with PBS, $\text{pH}=7.4$ and re-suspended in 1 mL of PBS. In the same time, 1 mg of $\text{Ru}(\text{bpy})_3^{2+}$ -NHS ester (bis(2,2'-bipyridine)-4'-methyl-4-carboxybipyridine-ruthenium N-succinimidyl ester-bis(hexafluorophosphate)) was dissolved in 100 μL of dimethyl sulfoxide and this solution was added to the beads suspension. This mixture was incubated on $+4^\circ\text{C}$ for 3 hours with continuous stirring. After the incubation the beads were washed from reaction solution with PBS 10-15 times by the centrifugation for 10 min at 10000 rpm to separate the beads from the solution. Finally, beads were suspended in 1 mL PBS and kept at 4°C .

2.3. PL and ECL imaging

The PL and ECL imaging were performed using horizontal epifluorescence microscope. Figure 1 presents scheme of the epifluorescence microscope that was used.

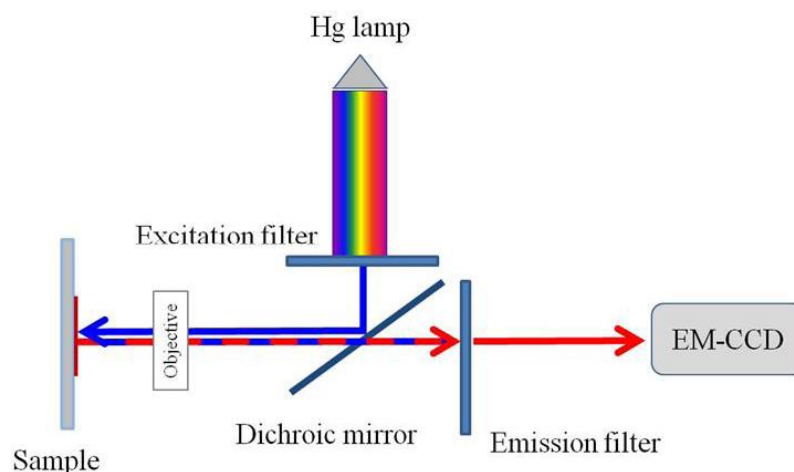


Figure 1. Scheme of epifluorescence microscope

The microscope was equipped with mercury lamp. Specific set of filters was used to select the excitation and emission wavelength of $\text{Ru}(\text{bpy})_3^{2+}$ -fluorophore. Only the light that correspond to the excitation of luminophore passes through and is reflected by dichroic mirror toward the sample. A dichroic mirror (dichroic beam splitter) reflects shorter wavelengths of light and allows longer wavelengths to pass. A dichroic mirror is required because the objective acts as both a condenser lens (excitation light) and objective lens (emission light) therefore the beam splitter isolates the emitted light from the excitation wavelength. The wavelength at which a beam splitter allows the longer wavelengths to pass must be set between the excitation and emission wavelengths so that excitation light is reflected and emission light is allowed to pass through it (Figure 3). In all experiments the set of filters which correspond to ruthenium complex as luminophore was used. The components of the set and the transmission spectra of the filters are presented in Table 1 and Figure 2 respectively.

Filter type	Label	Wavelength
Excitation filter	485DF22	485 nm
Dicroic filter	540DRLP	540 nm
Emission filter	605DF50	605 nm

Table 1. Set of filters for ruthenium complex PL imaging

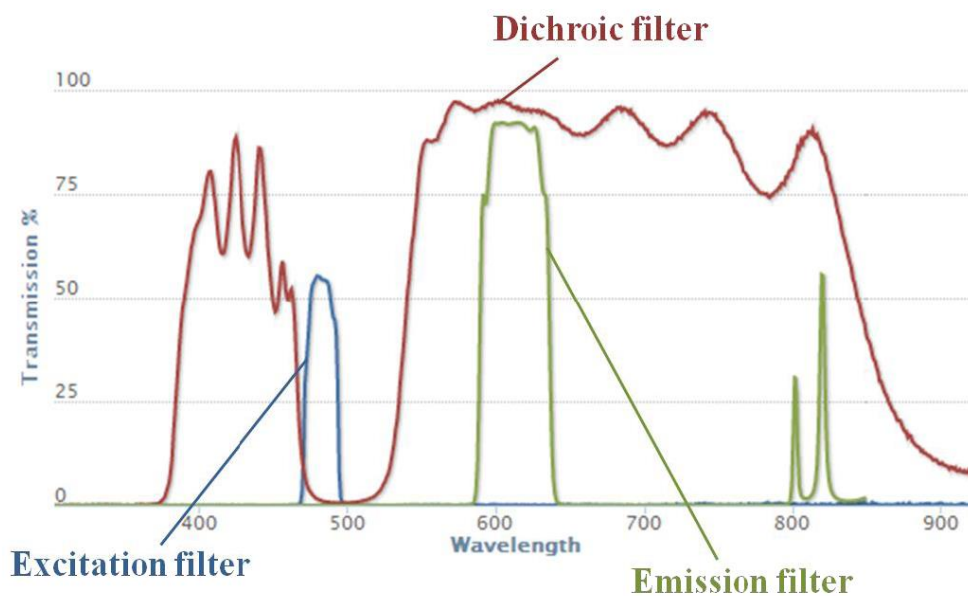


Figure 2. Transmission spectra of the set of filters for ruthenium complex fluorophore (from www.omegafilters.com).

The microscope was equipped with 5x, 10x, 20x, 50x and 100x (Olympus) from which last three were long working distance objectives. The detection was provided by Electron Multiplying CCD (Hamamatsu EM-CCD digital camera).

The PL imaging was often performed just before ECL imaging (to allow the comparison of the two images) thus the experimental set-up was the same. The three-electrode home-made cell with transparent window was placed in front of microscope objective. TPrA was dissolved in PBS by addition of H_3PO_4 (to adjust the pH to 7.4) and deaerated with Ar for 30 min.² The electrodes were connected to potentiostat. For PL imaging no potential was applied. In contrast, for ECL imaging there is no need of excitation light source but the application of the potential is required. The ECL reaction was generated by applying constant potential at 1.2 V vs. Ag/AgCl/KCl and the emitted light was detected by the EM-CCD. No filter was used to diminish the loss of emitted light. For ECL imaging, the whole set-up including microscope and camera was placed in dark box to avoid surround light which intensity may be higher than ECL to reach the detector. Also, images with no application of potential were recorded to check that there is no background light.

Chapter 3.

3.1. Labeling Streptavidin with Ru(bpy)₃Cl₂ (SA-Ru)

The modification was done as was reported by Deiss *et al.*¹ with some modifications. Briefly: A 1 mg Streptavidin was dissolved in 1mL of Milli-Q water. 100 μL of this solution was added in to 810 μL of water and 90 μL of 1x PBS pH 7.4 and mixed with 1 mg of Bis(2,2'-bipyridine)-4'-methyl-4-carboxybipyridine-ruthenium N-succinimidyl esterbis(hexafluorophosphate), which was dissolved in 100 μL of dried DMSO. The mixture was kept at 4 °C on continuous stirring for 4h. Then it was purified by dialysis in PBS (1x) using Slide-A-Lyzer Dialysis Cassettes 10k molecular weight cut off from Thermo Scientific for about 16h. The Ru-SA complex was stored at +4 °C until used.

3.2. Fabrication of the NEEs

The Au NEEs were prepared by electroless deposition of gold in the pores of track-etched PC filter membrane as a template. In this particular work, a membrane with average pores density of 6×10^8 per cm^2 and average pore diameter 30 nm was used. During the electroless deposition of gold from a solution, each pore of the PC membrane was filled with a metal nanowire whose head is exposed to the electrolyte solution so that the surface of the NEE is composed of millions of randomly spaced gold nanodisks. The membrane bearing the nanodisks was assembled in to electrodes of suitable geometry and size.

3.3. Preparation of the immunosensor and analytical protocol

A 10μL 10μg/mL tTG solution was dropped on the NEE and incubated for 2 h at 25°C. The tTG-NEE was subsequently blocked with 1% BSA for 30 min followed by incubation with 10μL standard solution of anti-tTG in 1x PBS pH 7.4 for 60 min. After washing with PBS (1x) pH 7.4 containing 0.05% Tween 20, the captured primary antibody was coupled with biotinylated Goat anti-mouse (or antihuman) secondary antibody for 60 min. It was further incubated for 30 min at +4 °C with ruthenium complex tagged streptavidin solution. In all the procedures, wet filter paper was put in the incubation container and sealed to avoid evaporation of the solution, incubations were made at 25°C except the last step and all incubations were followed by thorough rinsing with buffer solution. Finally, the biosensor was dipped in a three-electrode electrochemical cell containing 0.1 M TPrA in 0.1 M PBS pH 7.4 previously deaerated with nitrogen for 20 minutes.² ECL and cyclic voltammetry were recorded concurrently at scan rate of 100mV/s.

3.3. PL and ECL Imaging

PL and ECL imaging was realized by the same epifluorescence microscope like the one described in the paragraph above. The setup was similar like for the top view ECL imaging of the beads. The three-electrode homemade cell with transparent window was placed in front of the microscope objective (Figure 3) using a three-axis submicron manipulator (MDT616, Thorlabs) for the alignment. The ECL images of the samples were recorded in PBS solution (pH 7.4) containing 1 mM $\text{Ru}(\text{bpy})_3^{2+}$ in the presence of different concentrations of co-reactants. In particular TPrA and DBAE were used. The ECL reaction was generated by applying a constant potential at 1.2 V vs. Ag/AgCl/KCl using chronoamperometry and the emitted light was detected by the EM-CCD.

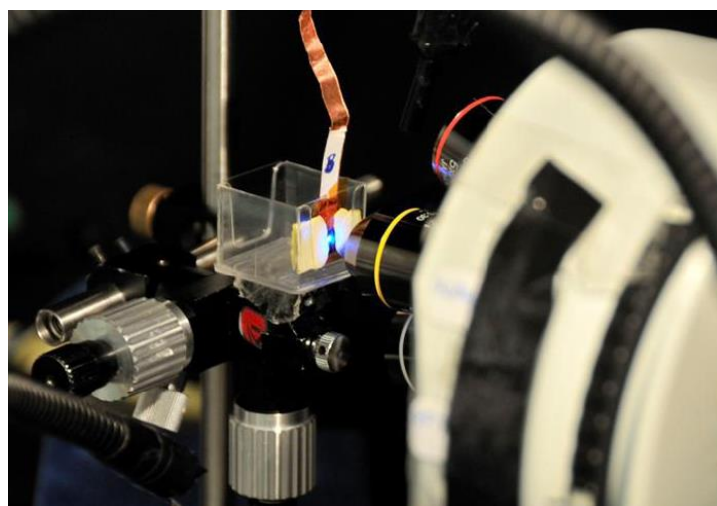


Figure 3. Assembled array and empty cell used for the measurements; Cell is positioned in front of the microscope objective for imaging.

(1) Deiss, F. *et al.* Multiplexed Sandwich Immunoassays Using Electrochemiluminescence Imaging Resolved at the Single Bead Level. *J. Am. Chem. Soc.* **131**, 6088 (2009).

(2) Senthil Kumar, S. & Bard, A. J. Background Emission of Electrogenenerated Chemiluminescence during Oxidation of Tri-n-propylamine from the Dimeric $^1\Delta_g$ State of O_2 . *Anal. Chem.* **85**, 292-295 (2012).

Collaborations

Pr. Neso Sojic and Pr. Dragan Manojlovic supervised my thesis research work.

The following co-workers contributed in collaborations in different projects of this thesis.

Dr. Milena Milutinovic contributed in design of the experimental set-up and electrochemical cells used for PL and ECL imaging and in functionalization of the 12- μm diameter beads with the ruthenium label. Pr. Frédéric Kanoufi from Paris Diderot University performed the simulations of ECL profiles and concentration profiles of TPrA^{•+} and TPrA[•].

Dr. Stéphane Arbault helped in the different imaging experiments and to interpret the data.

Dr. Bertrand Goudeau designed and installed the protective dark box in which the whole set-up for ECL imaging including epifluorescence microscope and EM-CCD camera was placed.

The work presented in the third chapter was realized in collaboration with Pr. Paolo Ugo from the University Ca' Foscari of Venice, Department of Molecular Science and Nanosystems.

Dr. Michael Ongaro and Henok Habtamu from the University Ca' Foscari of Venice fabricated the gold NEEs used as platform for ECL CD immunosensor.

Henok Habtamu performed the FE-SEM experiment (Figure 13 in paragraph 3.6.1.); experimental and simulated cyclic voltammograms and SEM-EDS experiment presented in Figure 14 of paragraph 3.6.1.; ECL measurements presented in Figure 15B of paragraph 3.6.2. and in Figure 18 of paragraph 3.6.3. (from which the calibration curve was obtained).

Dr. Francesca Virgilio and Alessandra Zanut fabricated the BDD NEAs used for ECL imaging presented in paragraph 3.7.

The work presented in chapter IV was realized in collaboration with Pr. Alexander Kuhn.

Dr. Gabriel Loget designed the bipolar U-cell used for the levitation experiments performed in Chapter 2 and contributed in movie recording from which the pictures of Figure 14 in paragraph 5.2. were extracted; in experiment presenting influence of pH on ECL mechanism presented in Figure 15 of the paragraph 5.2..

Dr. Laurent Bouffier and Dr. Dodzi Zigah recorded the movie from which the pictures of Figure 17 of paragraph 4.5. were extracted.

All these collaborators are warmly acknowledged for their inputs and support.

List of Publications That Came out of This Thesis

Light-emitting Electrochemical ‘Swimmers’, *Angew. Chem. Int. Ed.*, 2012, 51, 11284–11288,
M. Sentic, G. Loget, D. Manojlović, A. Kuhn, N. Sojic.

Lighting up redox propulsion with luminol electrogenerated chemiluminescence,
ChemElectroChem, 2014, 1, 95-98

L. Bouffier, D. Zigah, C. Adam, M. Sentic, Z. Fattah, D. Manojlović, A. Kuhn, N. Sojic.

Mapping the Electrogenerated Chemiluminescence Reactivity in Space: Mechanistic
Insight into Model Systems Used in Immunoassays, *Chem. Sci.*, 2014, 5, 2568-2572

M. Sentic, M. Milutinovic, F. Kanoufi, D. Manojlović, S. Arbault, N. Sojic.

Light emitting swimmers for dynamic enzymatic glucose sensing,

Chem.Comm., 2014, 50, 10161-10328, *HOT paper, Inside Cover Article*,

M.Sentic, L. Bouffier, S. Arbault, D. Manojlović, A. Kuhn, N. Sojic.

3D Electrogenerated Chemiluminescence: from Surface-Confined Reactions to Bulk
Emission. *Chem. Sci.*, 2015, 6, 4433-4437, *Back cover*,

M. Sentic, S. Arbault, L. Bouffier, D. Manojlovic, A. Kuhn, N. Sojic.

A sensitive electrochemiluminescent detection of coeliac disease biomarkers at gold
nanoelectrode ensembles. *under review Anal. Chem*,

H.B. Habtamu, M. Sentic, S. Arbault, D. Manojlović, L. De Leo, T. Not, N. Sojic, P. Ugo.

Patent

Method for generating light by electrochemiluminescence by a dispersion of electrically
conductive particles in a solvent. *WO 2015155491 / WO 2015-FR50983*.

N. Sojic, A. Kuhn, M. Sentic, S. Arbault, L. Bouffier.